

Towards a fundamental understanding of plasma – TiO₂ catalyst interaction for greenhouse gas conversion

Proefschrift voorgelegd tot het behalen van de graad van doctor in de wetenschappen aan de Universiteit Antwerpen te verdedigen door

Stijn Huygh



Promotoren

Prof. dr. Erik Neyts

Prof. dr. Annemie Bogaerts

Faculteit Wetenschappen
Departement Chemie
Antwerpen 2017

 Universiteit
Antwerpen

**Towards a fundamental understanding
of plasma – TiO₂ catalyst interaction
for greenhouse gas conversion**

**Inzicht in plasma – TiO₂ katalysator
interactie voor de omzetting van
broeikasgassen**

Proefschrift voorgelegd tot het behalen
van de graad van doctor in de wetenschappen
aan de Universiteit Antwerpen
te verdedigen door

Stijn Huygh

Promotoren: Prof. Dr. Erik Neyts
Prof. Dr. Annemie Bogaerts

Antwerpen, 2017

Table of Contents

Acknowledgments	VII
Chapter 1 Greenhouse gases and greenhouse gas reforming.....	1
1.1. Greenhouse gases	2
1.2. Greenhouse gas reforming.....	4
1.2.1. Steam Methane Reforming	4
1.2.2. Partial Oxidation of Methane	5
1.2.3. Autothermal Reforming.....	5
1.2.4. Dry reforming of Methane.....	6
1.2.5. Plasma-Assisted Methane reforming.....	7
1.3. Plasma-catalysis.....	8
1.3.1. Plasma.....	8
1.3.2. Catalysis	9
1.3.3. Plasma-catalysis	10
1.4. Aim of this Ph.D. thesis	17
Chapter 2 Theoretical Models.....	19
2.1. Classical Molecular dynamics simulations.....	20
2.1.1. Introduction	20
2.1.2. Model	23
2.1.3. ReaxFF	26
2.1.4. Principle of ReaxFF	28
2.1.5. The ReaxFF force field	28
2.1.6. Force field development	38

2.2.	Quantum chemistry	40
2.2.1.	Many-body problem.....	41
2.2.2.	Hartree-Fock Theory	44
2.2.3.	Density Functional Theory	47
Chapter 3	Development of a ReaxFF reactive force field for intrinsic point defects in Titanium Dioxide	55
3.1.	Introduction	56
3.2.	Computational Methods	58
3.2.1.	ReaxFF	58
3.2.2.	Training set	58
3.2.3.	Force field fitting.....	59
3.3.	Results and Discussion	60
3.3.1.	Equations of state and relative phase stability	61
3.3.2.	TiO ₂ clusters.....	66
3.3.3.	Point defects.....	70
3.3.4.	Oxygen adsorption	79
3.3.5.	Application to oxygen vacancy migration	82
3.4.	Conclusions	86
Chapter 4	Adsorption of C and CH _x radicals on anatase (001) and the influence of oxygen vacancies	87
4.1.	Introduction	88
4.2.	Computational details	91
4.3.	Oxygen vacancy formation energies	93

4.4.	Adsorption of CH _x radicals (x = 0 - 3) on anatase (001) ..	95
4.4.1.	Adsorption of CH _x radicals (x = 0 - 3) on a stoichiometric anatase (001) surface.	96
4.4.2.	Adsorption on a reduced anatase (001) surface	102
4.4.3.	Effect of oxygen vacancy defects on the distribution of adsorbed CH _x (x = 0 - 3) radicals.....	131
4.5.	Conclusions	136
Chapter 5 How Oxygen Vacancies Activate CO ₂ Dissociation on TiO ₂ Anatase (001).....		
		139
5.1.	Introduction	140
5.2.	Computational details	142
5.3.	Results and discussion.....	144
5.3.1.	CO ₂ adsorption on the oxidized (non-defective) anatase (001) surface.....	144
5.3.2.	CO ₂ adsorption on a reduced (defective) anatase (001) surface	147
5.3.3.	CO ₂ adsorption at 300 K on anatase (001)	159
5.3.4.	CO ₂ dissociation on anatase (001).....	161
5.4.	Conclusion.....	170
Chapter 6 Insight in the surface reactions of the plasma-catalytic dry reforming of methane on anatase (001)		
		173
6.1.	Introduction	174
6.2.	Computational details	176
6.3.	Results and discussion.....	178

6.3.1.	CH _x (x = 1 - 3) dehydrogenation	178
6.3.2.	Hydrogen diffusion	182
6.3.3.	CH _x (x = 1 - 3) dehydrogenation reactions	183
6.3.4.	Formation and desorption of value-added chemicals	190
6.4.	Conclusion.....	205
	Critical assessment.....	209
	Summary	213
	Samenvatting	219
	List of publications.....	225
	List of conference contributions.....	227
	References	229
	Appendix.....	259

Acknowledgments

I would like to thank everybody who has helped me on the way of finishing my Ph.D.

Foremost, I would like to express my utmost appreciation for everything my two supervisors, Prof. Erik Neyts and Prof. Annemie Bogaerts, have done for me over the last years. Erik and Annemie, thank you for all the opportunities you have given me. Your support on the scientific, as well as on the social level has made it possible to complete my PhD. The freedom and guidance you gave me, allowed me to conquer the obstacles I have encountered in the last years.

I would also like to thank Prof. A. C. T. van Duin, who has given me the opportunity to perform a research stay of one month to his group. The discussions I had with you have learned me a lot.

My gratitude also goes towards the Research Foundation – Flanders (FWO), who have provided the funding that have made my research possible. They are also one of the managing partners of the Flemish Supercomputer Center (VSC), who have provided the infrastructure needed to perform this PhD.

I am glad to have met all the people who have been present in PLASMANT over the years. A special thanks goes to Johan, Alp, Samira, Christof, Yannick, Charlotte, Steven and Vincent who all have contributed to the enjoyable atmosphere in the office.

My thanks to Luc, Nelly and Ingrid for all the help on technical, and administrative problems over the years.

Not only have there been a lot of people who have made my research possible. There have also been a lot of people who have supported me in my personal life, and whose friendship has been really important for me. Thank you all for your support, your listening ears and for all the relaxing times we had.

Also my family (not only by blood) has been a huge support for me. Thank you for being there for me, and listening to me rambling on about my research. A special thanks goes towards my parents, who have made me to who I am. Your support and your belief in me throughout my life means so much to me. There is one person of whom I wish he could be here; whom I wish I could make proud with this moment. *Vake*, my godfather, thank you for who you were.

There is one last person I would like to thank. She has meant everything to me in the last 9 years, and has supported me no matter what. Lotte, your listening ear, your unconditional support, your comforting words in difficult times, and so much more are a big part of what made me who I am today.

Chapter 1 Greenhouse gases and greenhouse gas reforming

1.1. Greenhouse gases

One of the major concerns of the current era is global warming caused by the increasing emission of greenhouse gases in the atmosphere. The Intergovernmental Panel on Climate Change, IPCC, reported in 2014 that each decade in the last 30 years has been successively warmer than any of the other decades since 1850.¹ The global average land-ocean surface temperature has increased with 0.87 °C over the period 1880 to 2015.^{1,2} This increase has led to an increase of sea level with 178 mm in the past hundred years.³

Most climate scientists agree that the main cause of the climate change is the anthropogenic extension of the greenhouse effect.^{1,4,5} The natural occurrence of the greenhouse effect is necessary to sustain life as we know it. The temperature of the earth's surface would decrease from 15 °C to -15 °C if the greenhouse effect were not present.⁶ The name greenhouse effect originates from the similarity with a "normal" greenhouse, although the underlying mechanism is quite different. The earth (surface-atmosphere system) is heated by the absorption of short-wave radiation originating from the sun, and cooled by emitting infrared (long-wave) radiation. If the earth would not be a *greenhouse* then the equilibrium surface temperature would be approximately -15 °C. However, the earth's atmosphere contains so-called greenhouse gases. These gases are relatively transparent to the incoming short-wave radiation, but efficiently absorb the outgoing long-wave radiation. Afterwards these gases will re-radiate this long-wave radiation isotropically, resulting in a part of the radiation being re-emitted to the earth's surface. This results in an equilibrium surface temperature of 15 °C.

There are various gases that contribute to the greenhouse effect. Each one has a specific global warming potential (GWP), which is a measure for the

extent that each molecule contributes to the greenhouse effect. The GWP of CO₂ is used as reference value and set equal to one. A summary of the GWPs, accumulated over 20 and 100 years, as published by the IPCC¹, is given in Table 1, together with the average lifetime and the percentage contribution to the total annual greenhouse gas emission in 2010 based on the CO₂ equivalent emission. No single lifetime can be defined for CO₂ due to the different rates of CO₂ uptake by different removal mechanisms. The main contributors to the greenhouse effect are CO₂, mainly emitted through fossil fuel combustion and industrial processes, and CH₄ originating from decomposition in landfills, agriculture, ruminant digestion and manure of domestic livestock.

Table 1. Average lifetime, cumulative GWP over 20 years (GWP₂₀) and 100 years (GWP₁₀₀) and the percentage contribution of the different greenhouse gases in CO₂ equivalent emission (weighed with GWP₁₀₀).¹

	Lifetime (yr)	GWP ₂₀	GWP ₁₀₀	percentage contribution CO ₂ equivalent emission (%)
CO ₂	No single lifetime	1	1	72
CH ₄	12.4	84	28	20
N ₂ O	121.0	264	265	5.0
CF ₄	50,000.0	4880	6630	2.2

Different strategies can be devised to decrease the concentration of CO₂ and CH₄ in the atmosphere, in order to mitigate the effect of greenhouse gases on the global climate. The most obvious strategy is a reduction of the emission itself, by the increased use of CO₂ neutral technologies (photovoltaics, wind energy, biogas, etc.). This reduction strategy alone will not suffice to achieve a strong decrease of the greenhouse gas concentration, as the global population will keep increasing, and countries

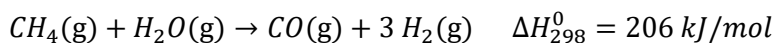
and their economies will keep developing. This strategy should be combined with carbon capture and long-term storage⁶ and/or the conversion of the greenhouse gases into value-added chemicals by the use of different conversion techniques including plasma-conversion⁷⁻¹⁴ and heterogeneous catalysis on reactive catalyst surfaces¹⁵. The conversion strategy combines the strong mitigation of the greenhouse gas effect with the conversion of greenhouse gases into value-added chemicals, by activation of the gas in a plasma or on the catalyst surface.

1.2. Greenhouse gas reforming

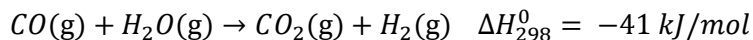
CO₂ and methane are amongst the main causes of the currently observed global climate change. Only about 1% of the natural gas that is harvested is chemically utilized, while the rest is burned, which leads to the conversion of methane into CO₂.¹⁶ It would be more opportune to utilize these gases for other industrial processes.

1.2.1. Steam Methane Reforming

One of the possibilities to utilize greenhouse gases is steam methane reforming (SMR). In this process methane is converted to carbon monoxide and molecular hydrogen. Approximately half of the hydrogen produced worldwide originates from the SMR, partial oxidation and autothermal reforming,¹⁷ of which SMR is the most common¹⁸ and produces hydrogen at the lowest operational and production costs¹⁹. To reform methane to syngas (CO + H₂) the following reaction is used:



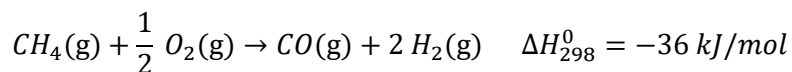
This strongly endothermic reaction can be combined with the exothermic Water Gas Shift (WGS) reaction to adjust the H₂/CO ratio and to increase the H₂ yield.



As there are severe limitations in mass and heat transfer, conventional steam reformers are limited by the use of pelletized catalysts, which have a typical effectiveness factor of 5% or less.²⁰ Therefore, kinetics are usually not the limiting factor in steam reformer reactors,²¹ which allows the use of less effective and less expensive nickel catalysts in contrast to the more effective and more expensive rhodium and platinum catalysts.

1.2.2. Partial Oxidation of Methane

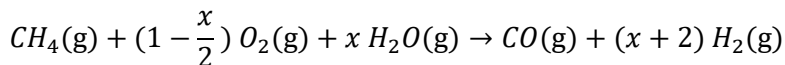
Partial oxidation of methane can be accomplished with or without the use of a catalyst. However, the non-catalytic version requires temperatures >1400 K and pressures ranging from 50-70 atm to obtain large conversions of methane.¹⁷ During the partial oxidation of methane a sub-stoichiometric amount of O₂ is used to obtain syngas as main product instead of CO₂.



It is possible to lower the reaction temperature to 1000 – 1300 K by the use of a catalyst.¹⁷ However, due to the exothermic nature of the reaction there is a risk of hot spots, and coke formation is also proven to deactivate the catalyst. Especially the used nickel catalyst has a strong tendency to form coke. The operation cost of the reactor is lower than for SMR, however the post-processing makes this technology more expensive.¹⁷

1.2.3. Autothermal Reforming

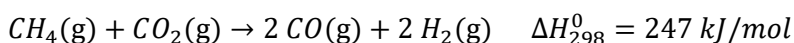
A combination of steam methane reforming and the partial oxidation of methane is called the autothermal reforming of methane. In this process methane is mixed with steam and O₂, which causes methane to be oxidized by either O₂ or H₂O. The overall reaction can be summarized as follows:



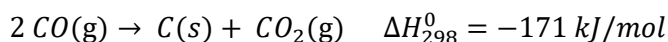
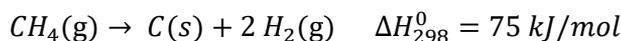
This reaction has the advantages that the partial oxidation provides the heat for the SRM reaction, it is less expensive and simpler than SRM,¹⁷ and the resulting H₂/CO ratio can be tuned by changes in the feed gas composition, thus allowing a more versatile reaction process. Steam reforming of methane typically results in a H₂/CO ratio of 3, which is not suitable for processes such as Fischer-Tropsch synthesis.

1.2.4. Dry reforming of Methane

A highly attractive process from an environmental point of view is the dry reforming of methane or the CO₂ reforming of methane. In this process two greenhouse gases are converted to syngas, which can be utilized for chemical synthesis of fuels through the Fischer-Tropsch synthesis due to the high CO/H₂ ratio.²² Furthermore, the combination of CO₂ and methane allows the utilization of low-grade natural gas obtained as by-product at oil platforms, which is otherwise flared, and at the same time allows the use of biogas as a renewable energy source. The overall reaction is as follows:



This reaction is highly endothermic, thus high temperatures and a catalyst are required to obtain significant conversions of methane. The main issue concerning the dry reforming of methane is coke formation, which is caused by methane decomposition and the Boudouard reaction.²³



Temperatures of 1023 K and above favour the DRM reaction over the possible side reactions.²³

1.2.5. Plasma-Assisted Methane reforming

Conventional methods, such as steam reforming and dry reforming, have their disadvantages, in particular requiring high temperatures and thus a high energy input. Apart from the high energy requirement, other challenges are present in an industrial setup, such as sintering, sulphur poisoning, coke formation and maintaining a sufficiently high activity.²⁴ A method that is proposed to overcome these challenges is plasma-catalysis. In plasma-catalysis one combines a plasma with a catalyst, where one hopes to combine the advantages of both.

The input gas stream will be modified by both the plasma and the catalyst. In the gas phase the plasma will induce plasma chemical reactions, while the heterogeneous catalyst will lower the activation barrier for surface processes. The catalyst and the plasma will influence each other, thereby possibly leading to synergistic effects. The plasma will change the gas mixture to a highly active and complex mixture of molecules, atoms, radicals, excited species, electrons and ions, thus leading to a change in the catalytic processes happening on the surface. The presence of a catalyst in the plasma discharge will also lead to a modification of the plasma properties. However, due to the complexity of this system the exact mechanisms and interactions between the plasma and the catalyst are far from understood.^{13,25,26} Experimental studies can be used to better understand how the plasma influences the catalyst, and vice versa. However, most measurements disturb the plasma, thus change its properties. Also information on the atomic and molecular level, which can give more fundamental insight in mechanisms in the plasma-catalytic system, is difficult to obtain. Therefore, theoretical models can be used as a

complementary technique to gain a deeper fundamental understanding of the system.

1.3. Plasma-catalysis

1.3.1. Plasma

A plasma is a gaseous state of matter, which is partially or completely ionised. It is sometimes referred to as the fourth state of matter, next to the three other observable states of matter in everyday life, i.e., solid, liquid and gas. Just as the gaseous state of matter it has no fixed shape or volume, but a plasma consists of a larger variety of species than a gas. A plasma consists of atoms, molecules, excited species, ions, radicals and freely moving electrons. Due to the free charge carriers, i.e., (positive and negative) ions and electrons, a plasma is electrically conductive, and highly responsive to electromagnetic forces. Although many charged species are present in a plasma, it is quasineutral, i.e., the charges compensate each other.

Plasmas can be categorized in various ways. First, there exist naturally occurring and man-made plasmas. Some examples of the former are lightning, flames, the northern lights, the sun and the solar corona. Man-made plasmas are generated by adding energy to a gas. The additional energy can be added as heat or by applying an electric field. This will cause the gas to become ionized, breaking it down into electrons and ions. These artificial plasmas can be divided in two groups based on their thermodynamic equilibrium. When all plasma species are in thermal equilibrium, i.e., they have a similar temperature in the order of 10,000 K and above, the plasma is categorized as a thermal plasma. If, however, there is no thermal equilibrium, i.e., the electrons have a significantly higher temperature than the heavy particles (300 – 1000 K), of the plasma

is called a non-thermal plasma. As this plasma contains species (ions, electrons, excited states, and radicals), which are not present in a gas at these gas temperatures, it provides access to chemical processes that normally do not occur in thermal equilibrium at these “low” temperatures.²⁵ Non-thermal plasmas can for example be generated in a dielectric barrier discharge (DBD) reactor. This reactor has been frequently used as possible alternative to classical reforming, both in a pure plasma setup^{12,27–33}, as in a plasma-catalytic setup^{34–37}.

1.3.2. Catalysis

The term catalysis was first used by the Swedish chemist Jöns Jacob Berzelius in 1835, after the first observations of catalytic processes by sir Humphry Davy in 1817 and by Johan Wolfgang Döbereiner in 1823. The former found that heated platinum could bring about combustion of alcohol, ether, coal gas and methane at temperatures below their ignition temperature.²⁵ The latter stated that “finely divided platinum powder causes hydrogen gas to react with oxygen gas by mere contact to water whereby the platinum itself is not altered.”¹⁴ The Nobel Prize winner in chemistry of 1909, Wilhelm Ostwald, defined catalysis, focused more on chemical kinetics. He defined a catalyst as “A substance which affects the rate of a chemical reaction without being part of its end products.”. Around 80% of all industrial processes make use of catalysts, which is equivalent to a monetary value of 20 trillion dollar each year of products resulting from catalysed processes.³⁸ Two examples of very important industrialized catalytic processes are the Haber-Bosch process and the Fischer-Tropsch process. The Haber-Bosch process, which fixates nitrogen in ammonia by the use of hydrogen gas, has been developed by two Nobel Prize winners in Chemistry. Fritz Haber received his prize for the “synthesis of ammonia by its elements” in 1918, while Carl Bosch received his prize for “the invention and development of chemical high pressure methods” in 1931.

The developments of Bosch resulted in the possibility to realize the industrialization of the Haber-Bosch process. The Fischer-Tropsch synthesis is a series of chemical reactions that converts carbon monoxide into liquid hydrocarbons by the use of hydrogen.

Nowadays, a catalyst is defined by IUPAC as “A substance that increases the rate of a reaction without modifying the overall standard Gibbs energy change in the reaction. The catalyst is both a reactant and a product of the reaction.”.³⁹ Apart from increasing the rate of a reaction by lowering the energy barrier of the reaction, a catalyst can also increase the selectivity by favouring certain reaction pathways over others.

1.3.3. Plasma-catalysis

Until now we have discussed plasma and catalysis separately. However, the hybridisation of these two techniques can lead to synergistic effects, i.e., the combination of a plasma with a catalyst leads to better results than the sum of their individual results. There exist two possible ways to configure a plasma-catalytic setup. In the first, the catalyst is directly introduced in the discharge region of the plasma. This setup is commonly called single-stage plasma-catalysis. The second possible configuration is that the catalyst is placed behind the plasma discharge region, i.e., downstream of the plasma, which is called two-stage plasma-catalysis. In this two-stage plasma-catalytic setup the plasma acts as a means to change the gas composition, and thus changes the availability of the reactants for the catalytic reactions. The complexity of this system is much reduced compared to the single-stage setup, as short-lived plasma species, i.e., electrons, ions, radicals and excited species, do not reach the catalyst surface. Apart from the change in feed gas there will not be any influence of the plasma on the catalyst, and vice versa.

If one thinks about catalysis, one normally envisages the role of the catalyst to lower the activation energy of the rate-limiting reaction step. However, one can also use the catalyst as a way to control the reaction products, by favoring certain reaction pathways over others. In a single-stage plasma-catalytic setup the plasma is used as a means to strongly activate the gas at reduced temperatures by electron impact reactions, while the role of the catalyst is to lower the activation barrier and to control the end-products.

As previously mentioned, the combination of catalysis with a plasma can lead to synergism. Synergism has been reported for volatile organic compounds, NO_x and O_3 abatement.^{40–46} Other studies also reported synergism for both plasma-assisted steam and dry reforming of methane^{34,47–57}, although there are also studies that report that the introduction of a catalyst in the plasma setup reduces the conversion of methane and sometimes also of CO_2 ^{36,58–60}. However, synergism is a relative concept as one can find synergism in different properties of the plasma-catalytic setup. For instance, Sentek et al.³⁶ reported a slightly lower methane conversion in a packed DBD than without packing. However, the product selectivity changed and significantly less solid deposition was formed. Also Tu et al.⁵⁸, Song et al.⁵⁹ and Gallon et al.⁶⁰ reported a lower conversion, but also a change in product selectivity. This change in product selectivity and the reduced solid deposition can be effects one wants to pursue.

It is clear that plasma-catalysis holds great potential in the field of environmental chemical processes. In order to fully employ this potential, a fundamental understanding is needed of the processes that are taking place in plasma-catalysis, especially the interactions of the plasma with the catalyst and the interactions of the catalyst with the plasma. The plasma will change the gas composition by creating reactive species nearby

the catalyst, and might change the physicochemical properties by ion, electron or photon interactions.^{13,14,25,61} On the other hand, the catalyst can change the electronic properties of the plasma and increase the retention time of the generated plasma species.^{13,14,25,61} An overview of various effects of the catalyst on the plasma and vice versa presented in literature is given below.

1.3.3.1. Plasma-catalytic interactions: effects of the catalyst on the plasma

Change in discharge type

The introduction of (catalytic) pellets in the discharge region can change the type of discharge that is occurring in the plasma. It has been reported that the discharge type changes from typical filamentary discharges in “air” to streamers that will propagate over the surface (surface flashover), i.e., surface discharges, and a possible combination with microdischarges and filamentary discharges.^{13,25,41,58,62,63} The so-called surface discharge results in higher electron impact ionization and dissociation rates, thereby resulting in a higher production and concentration of reactive species. There also exists a possibility to generate microdischarges in sufficiently large pores, resulting in a greater discharge per volume and thus increasing the average density of the discharge.⁴¹ Hensel et al.⁶⁴ studied the microdischarge formation inside porous ceramic materials. A sufficiently large pore is required to form microdischarges. They reported that only surface discharges were formed for small pores (0.8 μm) and only when the pore sizes was increased above 15 μm they found “leakage” of the surface discharge into the pores, and stable microdischarges were obtained, corresponding to Paschen’s law, i.e., at atmospheric pressure pore

sized of several micrometers are required. Zhang et al.^{65,66} studied the microdischarge formation inside catalyst pores by two-dimensional fluid modelling for various pore sizes in the μm -range. They reported noticeable changes in the ion density for 10 μm pores, while an increase in electron density is only observed for pore-sizes above 200 μm . The required pore-size for microdischarge formation in the catalyst pore also shows a dependency on the dielectric constants, for $\epsilon_r = 50$ enhanced ionization was observed at 10 μm and above, while for $\epsilon_r = 300$ a pore size of 100 μm was required. For example TiO_2 is reported to have a dielectric constant between 40 – 100, while SrTiO_3 has a dielectric constant equal to 300.^{67,68}

Electric field enhancement

The presence of a catalytic material in the plasma discharge induces a packed bed effect. This effect is not directly related to the catalytic activity of the material and can be considered as a physical effect. The introduction of dielectric materials, such as glass beads or ferroelectric materials, leads to the same effect. The field enhancement is a result of nano-features (i.e., local roughness and curvature), charge accumulation and polarization effects when dielectric materials are inserted in the discharge region.^{13,14,69,70} The enhanced electric field leads to an increase in the high-energy tail of the electron energy distribution function, which changes the rate of electron impact dissociation and ionization reactions.⁷¹ The plasma gas composition is thus changed by the presence of the catalyst. The magnitude of the change in electric field is determined by the curvature, dielectric constant and the contact angle of the pellets.⁷²

Increased retention time of plasma species

The presence of the catalyst will increase the retention time of reactants and products in the plasma discharge region, as these can adsorb on the catalyst surface and can therefore lead to higher efficiency of the plasma as compared to the pure plasma system.^{13,41}

1.3.3.2. Plasma-catalytic interactions: effects of the plasma on the catalyst

Changes in the surface properties of the catalyst

The presence of surface discharges leads to a change in physicochemical properties of the catalyst surface. The adsorption probability is increased at the catalyst surface if one compares plasma-catalysis with thermal catalysis. It has been suggested that the adsorption-desorption equilibrium at the surface of microporous materials is greatly influenced by the discharge.⁷³ This has been associated with the change in electric surface properties by the discharge, thereby affecting the van der Waals interactions, which in turn affect the adsorption-desorption equilibrium.¹³ As described in section 1.3.3.1, a longer retention time, caused by the higher adsorption probability, results in higher efficiency of the chemical processes. It is key for catalytic reactions to occur that the molecule is adsorbed at the surface, no matter if the reaction mechanisms follow a Langmuir-Hinshelwood, an Eley-Rideal or a Mars-van Krevelen mechanism. Thus a higher adsorption probability can lead to a higher catalytic activity. The change in surface area of the catalyst is a second possible influence on the adsorption probability at the catalyst surface, apart from the change in adsorption-desorption equilibrium. The plasma can give rise to the formation of

smaller nanoparticles, i.e., a higher degree of dispersion, and thus to a larger total surface area.⁷⁴⁻⁷⁶ The higher dispersion and formation of smaller nanoparticles can lead to reduced coke formation on the catalyst surface, which prevents catalyst deactivation. Indeed, it has been shown by Martinez that increasing the Ni dispersion leads to a higher coke resistance in dry reforming of methane.⁷⁷ Tu et al.⁷⁸ investigated the reduction of a NiO catalyst to its metallic form by the use of a plasma. Not only is it possible to fully reduce a metal oxide to its metallic form, but also partial oxidation and reduction is possible. This has been found by for example Demidyuk et al.⁷⁹ and Guo et al.⁸⁰. The former found an increase in oxidation state of manganese in alumina supported MnO_x , while the latter found a decrease in oxidation state of manganese.

Hot spot formation

The thermal catalytic activity at temperatures typically found in non-thermal plasmas is negligible, as these temperatures are too moderate.^{13,41} The enhanced thermal catalytic activity in plasma-catalysis might be attributed to hot spots formed on the catalyst surface. These hot spots are typically found in the vicinity of sharp edges and pores as the microdischarges are stronger at these structures with high curvature, due to the presence of an enhanced electric field. These hotspots could locally thermally activate the catalyst.

Electron-hole generation

In the plasma, photons and electrons are present, which can induce electronic excitations. This in turn can initiate “photocatalytic” reactions. However, the photocatalytic effect triggered by the plasma generated photons is not well understood. It has been reported that plasma generated photons activate the TiO₂ photocatalyst.^{81,82} However, it has also been suggested that the UV intensity generated in a plasma is significantly lower than that emitted from UV lamps, indicating that the effect of photons is actually negligible.³⁷ The photocatalytic activity is assigned to the generation of electron-hole pairs by the aid of highly energetic electrons from the plasma discharge.^{37,83–85} Thus the hybridization of the plasma-catalytic system makes it in principle possible to perform “photocatalytic” reactions without the necessity of an external UV-source.

Change in available reaction pathways

The plasma composition deviates significantly from the feed gas composition, due to the generation of (reactive) plasma species. These species consist of molecules, atoms, radicals, electronically and vibrationally excited species, ions, and electrons. Due to the change in gas mixture a larger variety of reactants is available compared to a thermal setup. Consequently, new available reaction pathways on the catalyst arise.

1.4. Aim of this Ph.D. thesis

The aim of this dissertation is to gain insight in the plasma-surface reactions by applying computational models. The interactions of plasma gas-phase species with an anatase catalytic surface are studied.

In Chapter 3 a classical reactive force field is developed for the study of intrinsic point defects in titanium dioxide. The developed force field is applied to study the diffusion of oxygen vacancies on the surface.

In Chapter 4, the influence of oxygen vacancies on the adsorption of methane derived radicals on an anatase (001) surface is studied, using DFT calculations. A significant influence is found on the adsorption distribution and strength of the radicals on the surface.

In Chapter 5, the reduction of CO₂ on anatase (001) is studied by means of DFT calculations. The results in this chapter show a strong activation for CO₂ reduction by the presence of oxygen vacancies.

In Chapter 6, the surface reactions of plasma-catalytic dry reforming of methane on anatase (001) is studied with DFT simulations. The hydrogenation and dehydrogenation of adsorbed methane derived radicals is investigated. The adsorption, desorption and formation of formaldehyde, methanol, methane, CO, H₂, water, ethane and ethene is studied in a temperature range of 300 – 1000 K.

Chapter 2

Theoretical Models

2.1. Classical Molecular dynamics simulations

The first part of this thesis focusses on the use of classical physics to describe how a molecular system will behave without predetermining reaction pathways. Every property will – in principle – follow self-consistently from the simulation. During my Ph.D. research, we developed a classical molecular dynamics force field. In the next section, we will therefore give an introduction to classical molecular dynamics, followed by the explanation of the model and the used force field fitting method.

2.1.1. Introduction

Classical Molecular dynamics (MD) simulations are used to determine statistical and dynamical properties of a classical many-body system. Classical in this context means that the nuclei will move according to the laws of classical physics. For many systems this is a good approximation. However, when the translational or rotational motion of light atoms and/or molecules (He, H₂, D₂) or the vibrational movement with a frequency ν for which $h\nu > k_B T$ are considered including quantum effects may be important.⁸⁶

MD is a simulation technique in which the evolution of a given set of interacting atoms is followed through time and space. The classical equations of motion, such as the equations of Newton, allow following the evolution by integrating these equations. We know Newton's Laws of motion as follows:

The first law states that if no force is exerted on a particle, then this particle has to be at rest or move at a constant velocity.

The second law states that a change in the velocity vector (magnitude or orientation) has to be induced by a force. This change has to be parallel to the vector sum of all forces exerted on the particle.

$$F_i = m_i a_i$$

For a molecular system this equation is valid for every atom i with an atomic mass m_i , an acceleration a_i , and a force F_i exerted on that atom by the interaction with the other atoms.

The third Newton's law states that the mutual action of two particles upon each other is always equal, and orientated in opposite direction.

Molecular Dynamics simulations are deterministic, in contrast to Monte Carlo methods, which use random numbers. Thus for a given set of atoms, atomic positions and velocities, the evolution of the system as function of time is in principle predetermined at the start of the simulation. MD simulations are used to determine the dynamical trajectory of atoms, but as MD is a statistical method also macroscopic properties of the system can be determined. A set of configurations distributed according to a statistical distribution function is calculated. The collection of all configurations that are obtained by integrating the equations of motion is the ensemble of that calculation. An example of an ensemble is the canonical ensemble, for which the number of atoms (N), the volume (V) and the temperature (T) is kept constant. In this so called NVT-simulation the phase space probability density is given by the Boltzmann distribution:

$$\frac{e^{-H(\Gamma)}}{e^{k_B T}}$$

Where $H(\Gamma)$ is the Hamiltonian, and Γ is the considered point in the 6N-dimensional phase space (3N coordinates and 3N momenta). In this type of simulation the energy change caused by endothermic and exothermic

processes is compensated by absorption of energy or releasing energy from/to the “environment” by using a thermostat. This thermostat rescales the velocities of the atoms so that the kinetic energy of the system corresponds to the desired temperature.

$$\frac{3}{2}Nk_bT = \frac{1}{2}\sum_i m_i v_i^2$$

The natural ensemble of MD simulations is the microcanonical ensemble. In this ensemble the number of atoms (N), the total energy (E) and the Volume (V) are kept constant. While the total energy is constant, the kinetic and potential energy are allowed to freely interchange, so the temperature can increase or decrease, depending on the occurring reactions being exo- or endothermic.

Most of the time one is interested in the global system properties rather than the individual trajectories. To calculate a physical quantity in statistical mechanics one calculates the average over all microsystems of the ensemble, which are distributed according to the ensemble’s characteristic phase space. However, in MD simulations one integrates over time instead of taking an instantaneous average over all microsystems. If the system is in thermodynamic equilibrium and is ergodic, then the instantaneous average over all microsystems is equal to the time average of a microsystem of that ensemble. This only holds if the simulation is long enough. Ergodicity means that the system will go through all points of the phase space if the simulation runs long enough. As the simulation only runs for a finite amount of time and it is hard to assess if this simulation time is sufficiently long, the results of the simulation need to be approached with some caution.

2.1.2. Model

To perform a simulation a model is needed for the system. One of the important parts of the model in MD-simulations is the interatomic potential or the force field $V(\mathbf{r}_1, \dots, \mathbf{r}_N)$, which is function of the atomic coordinates. This potential determines the potential energy of the system for every given configuration. The potential is independent of the used coordinate system, as the interaction between the atoms is independent of the used coordinate system. As the potential determines the forces acting on each atom in the system, it also determines the acceleration and therefore, the positions and velocities of the atoms. The forces are derived from the potential as the negative gradient of the potential

$$\mathbf{F}_i = -\nabla_{\mathbf{r}_i} V(\mathbf{r}_1, \dots, \mathbf{r}_n)$$

This definition implies a conservative force, thus the work done in moving an atom is independent of the path taken. A very simple way to describe the potential energy is by the use of pairwise interactions.

$$V(\mathbf{r}_1, \dots, \mathbf{r}_n) = \sum_i \sum_{j>i} \phi(|\mathbf{r}_i - \mathbf{r}_j|)$$

In the second sum operator $j>i$ makes sure that all interactions are counted only once. While such potentials are computationally very cheap, they are only suitable for the simplest of systems. Metals and semiconductors, for instance, are not well described at all by pairwise interactions. With increasing computer power, more complicated (and also bigger) systems can be calculated in a more accurate way. This has caused an evolution of the use of two-particle interatomic potentials of a very simple analytical form, such as the Morse⁸⁷ and Lennard-Jones⁸⁸ potentials, to more complex potentials which account for many-particle interactions, which in some cases can give results of a comparable accuracy as quantum mechanical results. As large and complex systems can be

simulated by these potentials in an accurate way, they constitute a link between experiments and theory, and allow research in novel areas.

While classical MD is a very powerful technique, a few limitations need to be considered as well:

Classical Mechanics

Systems at an atomic level follow the laws of quantum mechanics rather than the classical laws, which are only an approximation. So it is important to check if the classical equations of motion are an acceptable approximation to the reality. A simple test to validate the classical approach is the *de Broglie thermal wavelength*:

$$\Lambda = \sqrt{\frac{h^2}{2\pi M k_B T}}$$

where M is the atomic mass, h the Planck constant and k_B the Boltzmann constant. The classical equations of motion are justified when the *de Broglie thermal wavelength* $\Lambda \ll a$, with a the smallest average distance between the atoms. For example for titanium dioxide containing O and Ti the *de Broglie thermal wavelengths* are 0.25 Å and 0.15 Å at 300 K, respectively. These values are at least eight times smaller than the average distance in for example rutile, where the average interatomic distance is 1.956 Å.⁸⁹ However, for light systems containing hydrogen atoms, which have a *de Broglie wavelength* of 1.0 Å, and for systems at very low temperatures one has to account for quantum effects. But in practice it is found that systems containing H atoms still give reasonable results, so can still be simulated, albeit with caution.⁸⁶

Finite time

Classical MD can be used to simulate hundreds up to millions of atoms over a period of time of several picoseconds to microseconds. Whether this is long enough to study a specific process, depends on the properties one wants to study. If the simulated time is significantly larger than the relaxation time of the studied property, then MD is trustworthy. For example for diffusion of small molecules, or reactions with small barriers there is no problem. However, for phenomena such as phase transitions, for which the relaxation time is very large one has to be very careful.

The interatomic potential

One of the major concerns for a molecular dynamics simulation is how accurate the forces are. The interactions between atoms in MD are described by the forces that are exerted on the atoms. The atoms then move under the influence of these instantaneous forces. When atoms move, their relative positions change and therefore also the forces on these atoms. As the forces determine the complete evolution of the system, and therefore the studied properties, the forces have to be very accurate in order to obtain a realistic result and to avoid artefacts in the properties caused by the forces.

Thus, the simulation will only be realistic if the calculated interatomic forces are similar to the real interatomic forces. This will make the system behave as it would in reality. The accuracy of the forces is inherently linked to the used interatomic potential or force field to describe the behaviour of the material under the given conditions.

It is, therefore, of the utmost importance to make sure that the used force field is developed for a system similar to the system under study, to check results with other methods, and/or develop an accurate force field for the system based on more accurate methods. If this is neglected, then the artefacts caused by the force field will corrupt the real processes and will prevent the simulation to have any scientific value.

2.1.3. ReaxFF

The accuracy and speed of modern quantum mechanical codes allows them to be used to accurately determine the ground state geometry and energy for “small” molecular systems. However, even with the tremendous amount of computing power available nowadays it is very difficult to study dynamical properties of large molecules and solid state systems with the use of quantum mechanical methods, as the necessary computing power and time increase rapidly with the number of atoms. The use of classical molecular dynamics allows simulation of these processes in a limited amount of time, even with the use of a desktop computer. It is therefore desirable to develop interatomic potentials that are as accurate as possible. Indeed, it is of the utmost importance that the used interatomic potential is capable of accurately describing the considered properties of and events in the system under study. In this thesis, a parameter set is developed for the ReaxFF potential, which is a generic bond order dependent force field.⁹⁰ This force field allows calculations on large systems, while maintaining an accuracy comparable to quantum mechanical methods.

Before the development of the ReaxFF force field in 2001, already other interatomic potentials existed, for example MM3^{91–93}, which gives an accurate description for geometries, conformational energy differences and enthalpies of formation. On the other hand, also generic force fields exist,

such as DREIDING⁹⁴ and UFF⁹⁵, which allow simulations of different classes of compounds. However, often these potentials are not capable of describing the chemical reactivity, as bond breaking and formation causes the energy to change as a function of the a priori undetermined atomic coordination.

In contrast to such potentials, also so-called reactive potentials exist, in which bond breaking and formation is accounted for. An example is the Brenner potential, which can accurately describe the ground state of carbohydrates. However, long distance interactions, such as the van der Waals and Coulomb interactions, are not incorporated in the Brenner force field. It is formulated in a way that allows bond breaking and formation, but the energy pathways of reactions are generally poorly described. Improvements have been applied to the Brenner force field⁹⁶ such as addition of torsion interactions and long distance non-bonding interactions, which improve the force field but do not solve the fundamental problems of the dissociation and reaction energy pathways.

A different bond-order dependent force field is the BEBO method, which is based on the Pauling relationship⁹⁷ between the bond length and bond order. The method assumes that the lowest energy pathway is the one for which the total bond order is maintained. The partial bond order n_i is calculated as follows:

$$n_i = e^{-(r_i - r_s)/a}$$

where r_s is the single bond length between the considered elements and a a constant which can be determined empirically. This method is mostly used for reactions where hydrogen atom transfer occurs.

The above mentioned force fields are capable of describing the ground state geometries of complex molecules; they are, however, not capable of accurately describing the chemical behaviour of reactions in these systems.

2.1.4. Principle of ReaxFF

ReaxFF is a generic bond order dependent reactive interatomic potential, which incorporates both short range and long range interactions (van der Waals and Coulomb forces).⁹⁰ Dissociation and reaction pathways used for the parameterisation of the force field are typically derived from quantum mechanical calculations. ReaxFF incorporates the central-force formalism to describe the continuous energy pathway of dissociation of molecules, including non-bonding interactions and Coulomb forces and to accurately describe the complex system local perturbations, through the incorporation of bond, angle, and torsion terms. When dissociation of a bond occurs, all the bonding energy terms, such as the bond, angle and torsion terms, go to zero without causing any discontinuities in the energy.

2.1.5. The ReaxFF force field

In the ReaxFF formalism the total energy is divided in several partial energy contributions. These are the bonding energy, atom over- and undercoordination, valence angle, penalty energy, torsion angle energy, conjugation energy, van de Waals energy and Coulomb energy.

$$E_{system} = E_{bond} + E_{over} + E_{under} + E_{val} + E_{pen} + E_{tors} + E_{conj} \\ + E_{vdWaals} + E_{coulomb}$$

The description of the formalism follows that of the original carbohydrate force field first proposed in 2001 by van Duin et al. As the force field is generic, the description can be transferred to other systems, and only the parameter set is system-dependent.

2.1.5.1. Bond order and bond energy

The bond order in ReaxFF is based on the bond length of the considered bond. The bond order BO'_{ij} between two atoms i and j is determined by:

$$BO'_{ij} = \exp \left[p_{bo,1} \cdot \left(\frac{r_{ij}}{r_0} \right)^{p_{bo,2}} \right] + \exp \left[p_{bo,3} \cdot \left(\frac{r_{ij}}{r_{0,\pi}} \right)^{p_{bo,4}} \right] + \exp \left[p_{bo,5} \cdot \left(\frac{r_{ij}}{r_{0,\pi\pi}} \right)^{p_{bo,6}} \right]$$

where r_{ij} is the interatomic distance between the atoms. The equation consists of three exponential terms which describe the σ -bond, the first and the second π -bond, respectively. For example for the carbon-carbon bond the parameters included in this general form are chosen in a way that the bond order of the σ -bond becomes 1 for interatomic distance smaller than ~ 1.5 Å and becomes negligible above ~ 2.5 Å. For the second term, the first π -bond, the bond order becomes 1 below ~ 1.2 Å and is negligible above ~ 1.75 Å, and for the third term, the second π -bond, the bond order becomes 1 for interatomic distances below ~ 1.0 Å and is negligible above ~ 1.4 Å. For atoms between which no double or triple bonds are formed, the last term(s) can be neglected. For the C-C bond the bond order as function of the bond length is shown in Figure 1.

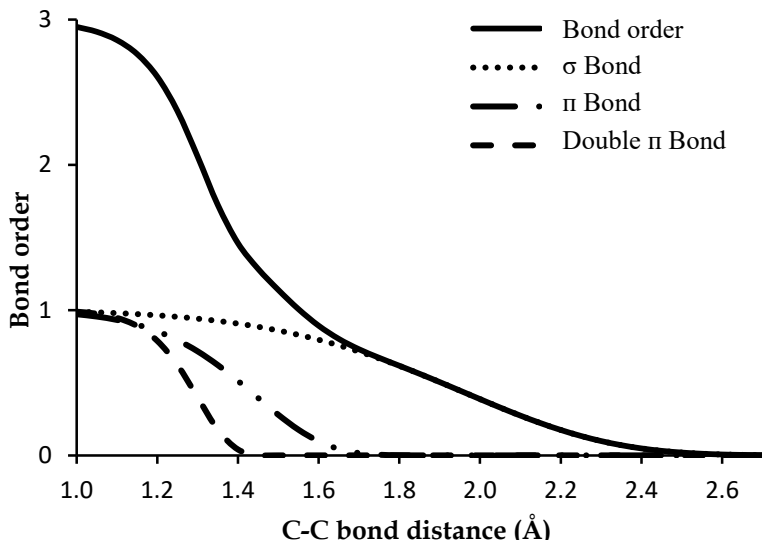


Figure 1. Bond order in function of the carbon-carbon interatomic distance.

The bond order BO'_{ij} is subsequently corrected for overcoordination and possible residual 1-3 bond orders. The latter is done for all atoms and with the correction factor $f_1(\Delta_i, \Delta_j)$. The overcoordination correction is only applied for bonds with two atoms that are not hydrogen atoms and with correction factors $f_4(\Delta'_i, BO'_{ij})$ and $f_5(\Delta'_j, BO'_{ij})$. Thus one obtains the corrected bond order BO_{ij} by multiplying the original obtained bond order BO'_{ij} with the correction factors $f_1(\Delta_i, \Delta_j)$, $f_4(\Delta'_i, BO'_{ij})$ and $f_5(\Delta'_j, BO'_{ij})$.

$$BO_{ij} = BO'_{ij} \cdot f_1(\Delta_i, \Delta_j) \cdot f_4(\Delta'_i, BO'_{ij}) \cdot f_5(\Delta'_j, BO'_{ij})$$

Where:

$$f_1(\Delta_i, \Delta_j) = \frac{1}{2} \cdot \left(\frac{Val_i + f_2(\Delta'_i, \Delta'_j)}{Val_i + f_2(\Delta'_i, \Delta'_j) + f_3(\Delta'_i, \Delta'_j)} + \frac{Val_j + f_2(\Delta'_i, \Delta'_j)}{Val_j + f_2(\Delta'_i, \Delta'_j) + f_3(\Delta'_i, \Delta'_j)} \right)$$

$$f_2(\Delta'_i, \Delta'_j) = \exp(-\lambda_1 \cdot \Delta'_i) + \exp(-\lambda_1 \cdot \Delta'_j)$$

$$f_3(\Delta'_i, \Delta'_j) = \frac{1}{\lambda_2} \cdot \ln \left\{ \frac{1}{2} \cdot [\exp(-\lambda_2 \cdot \Delta'_i) + \exp(-\lambda_2 \cdot \Delta'_j)] \right\}$$

$$f_4(\Delta'_i, BO'_{ij}) = \frac{1}{1 + \exp(-\lambda_3 \cdot (\lambda_4 \cdot BO'_{ij} \cdot BO'_{ij} - \Delta'_i)) + \lambda_5}$$

$$f_5(\Delta'_j, BO'_{ij}) = \frac{1}{1 + \exp(-\lambda_3 \cdot (\lambda_4 \cdot BO'_{ij} \cdot BO'_{ij} - \Delta'_j)) + \lambda_5}$$

In these equations Val_i is the valence of atom i , so for example for carbon and hydrogen Val_i is equal to 4 and 1, respectively. Δ'_i is the deviation of the total non-corrected bond order of atom i with respect to its valence.

$$\Delta'_i = \sum_{j=1}^{n_{bond}} BO'_{ij} - Val_i$$

Once the bond order BO_{ij} has been obtained, the bonding energy can be calculated as follows:

$$E_{bond} = -D_e \cdot BO_{ij} \cdot \exp \left[p_{be,1} \left(1 - BO_{ij}^{p_{be,1}} \right) \right]$$

2.1.5.2. Over- and undercoordination

Even after correction of the bond orders for overcoordination, it is still possible to have residual overcoordination. For example, carbon may not have a bond order larger than 4 (except for hypervalent molecules). If residual overcoordination occurs, it should be penalised by an additional overcoordination term.

Overcoordination

If $\Delta_i > 0$, then atom i is overcoordinated as the total bond order is larger than the valence. An overcoordination term E_{over} is then added to the total energy.

$$E_{over} = p_{over} \cdot \Delta_i \cdot \left(\frac{1}{1 + \exp(\lambda_6 \cdot \Delta_i)} \right)$$

This term quickly drops to zero once the system becomes undercoordinated. Δ_i is calculated in the same manner as Δ'_i , however with the use of corrected bond orders BO_{ij} .

Undercoordination

For an undercoordinated atom, for which Δ_i is negative, an energy contribution is added to account for the resonance of the π -electrons between bonded undercoordinated atomic centers. The energy contribution is given by:

$$E_{under} = -p_{under} \cdot \frac{1 - \exp(\lambda_7 \cdot \Delta_i)}{1 + \exp(-\lambda_8 \cdot \Delta_i)} \cdot f_6(BO_{ij,\pi}, \Delta_j)$$

Where

$$f_6(BO_{ij,\pi}, \Delta_j) = \frac{1}{1 + \lambda_9 \cdot \exp(\lambda_{10} \cdot \sum_{j=1}^{neighbours(i)} \Delta_j \cdot BO_{ij,\pi})}$$

$$BO_{ij,\pi} = \exp \left[p_{bo,3} \cdot \left(\frac{r_{ij}}{r_{0,\pi}} \right)^{p_{bo,4}} \right] + \exp \left[p_{bo,5} \cdot \left(\frac{r_{ij}}{r_{0,\pi\pi}} \right)^{p_{bo,6}} \right]$$

With this formulation one makes sure that this undercoordination term will only contribute to the total energy if the bond between the undercoordinated centers has a partly π -bonding character ($BO_{ij,\pi} > 0$).

2.1.5.3. Valence angle terms

Just as with the energy contribution of the bond energy, it is important that the contribution of the valence angle energy drops to zero if the bond order drops to zero without causing any discontinuities. E_{val} is the

distortion contribution to the energy associated with the deviation of the valence angle Θ_{ijk} compared to the equilibrium value Θ_0 . The factor $f_7(BO_{jk})$ makes sure that this local perturbation will disappear upon bond dissociation without causing any discontinuities in the total energy. The factor $f_8(\Delta_j)$ makes sure that the effects on E_{val} of the over- or undercoordination of the central atom j are correctly described. The angles in the equations concerning the valence angle energy contribution are all expressed in radians. The equation for the valence angle energy is as follows:

$$E_{val} = f_7(BO_{ij}) \cdot f_7(BO_{jk}) \cdot f_8(\Delta_j) \cdot \left\{ k_a - k_a \exp \left[-k_b (\Theta_0 - \Theta_{ijk})^2 \right] \right\}$$

where

$$f_7(BO_{ij}) = 1 - \exp(-\lambda_{11} \cdot BO_{ij}^{\lambda_{12}})$$

$$f_8(\Delta_j) = \frac{2 + \exp(-\lambda_{13} \cdot \Delta_j)}{1 + \exp(-\lambda_{13} \cdot \Delta_j) + \exp(p_{v,1} \cdot \Delta_j)} \cdot \left[\lambda_{14} - (\lambda_{14} - 1) \cdot \frac{2 + \exp(\lambda_{15} \cdot \Delta_j)}{1 + \exp(-\lambda_{15} \cdot \Delta_j) + \exp(-p_{v,1} \cdot \Delta_j)} \right]$$

The equilibrium value Θ_0 for the valence angle of atoms i , j and k , is described as function of the sum of the π -bond orders around the central atom j . Apart from the effects of the π bonding character on the equilibrium valence angle, the equation ensures that the effects of over- or undercoordination and free electron pairs are taken into account.

The equilibrium valence angle is calculated as follows:

$$\Theta_0 = \pi - \Theta_{0,0} \cdot \{1 - \exp[-\lambda_{18} \cdot (2 - SBO2)]\}$$

where

$$SBO = \Delta_{j,2} - 2 \cdot \left\{ 1 - \exp \left[-5 \cdot \left(\frac{1}{2} \Delta_{j,2} \right)^{\lambda_{16}} \right] \right\} + \sum_{n=1}^{neighbours(j)} BO_{jn,\pi}$$

$$\Delta_{j,2} = \Delta_j \text{ if } \Delta_j < 0$$

$$\Delta_{j,2} = 0 \text{ if } \Delta_j \geq 0$$

$$SBO2 = 0 \text{ if } SBO \leq 0$$

$$SBO2 = SBO^{\lambda_{17}} \text{ if } 0 < SBO < 1$$

$$SBO2 = 2 - (2 - SBO)^{\lambda_{17}} \text{ if } 1 < SBO < 2$$

$$SBO2 = 2 \text{ if } SBO > 2$$

An extra penalty term E_{pen} to describe the stability of a system with two double bonds around the central atom j (e.g., an allene), is added to the total energy. The influence of over- and undercoordination is described with $f_9(\Delta_j)$.

$$E_{pen} = \lambda_{19} \cdot f_9(\Delta_j) \cdot \exp \left[-\lambda_{20} \cdot (BO_{ij} - 2)^2 \right] \cdot \exp \left[-\lambda_{20} \cdot (BO_{jk} - 2)^2 \right]$$

where

$$f_9(\Delta_j) = \frac{2 + \exp(-\lambda_{21} \cdot \Delta_j)}{1 + \exp(-\lambda_{21} \cdot \Delta_j) + \exp(\lambda_{22} \cdot \Delta_j)}$$

2.1.5.4. Torsion angle terms

Just as all other bonding energy contributions the torsion angle energy will drop to zero without energy discontinuities if bond dissociation occurs in one of the bonds related to the considered torsion angle. The torsion

angle energy contribution E_{tors} for a system with a torsion angle ω_{ijkl} is given by:

$$E_{tors} = f_{10}(BO_{ij}, BO_{jk}, BO_{kl}) \cdot \sin(\Theta_{ijk}) \cdot \sin(\Theta_{jkl}) \cdot \left[\frac{1}{2} V_2 \cdot \exp\left\{ p_l (BO_{jk} - 3 + f_{11}(\Delta_j, \Delta_k))^2 \right\} \cdot (1 - \cos(2 \cdot \omega_{ijkl})) + \frac{1}{2} V_3 \cdot (1 + \cos(3 \cdot \omega_{ijkl})) \right]$$

where

$$\begin{aligned} f_{10}(BO_{ij}, BO_{jk}, BO_{kl}) &= [1 - \exp(-\lambda_{23} \cdot BO_{ij})] \cdot [1 - \exp(-\lambda_{23} \cdot BO_{jk})] \cdot [1 - \exp(-\lambda_{23} \cdot BO_{kl})] \end{aligned}$$

$$f_{11}(\Delta_j, \Delta_k) = \frac{2 + \exp[-\lambda_{24} \cdot (\Delta_j + \Delta_k)]}{1 + \exp[-\lambda_{24} \cdot (\Delta_j + \Delta_k)] + \exp[\lambda_{25} \cdot (\Delta_j + \Delta_k)]}$$

$f_{10}(BO_{ij}, BO_{jk}, BO_{kl})$ is the factor that makes sure that upon bond dissociation of one of the bonds E_{tors} drops to zero. The valence angle dependent factor $\sin(\Theta_{ijk}) \cdot \sin(\Theta_{jkl})$ makes sure that the E_{tors} will drop to zero if one of the valence angles Θ_{ijk} and Θ_{jkl} reaches 180° . If a central double bond exists between atom j and k ($BO_{jk} = 2$), then the $V_2 - \cosine$ term will be maximized, and will drop off very quickly if the BO_{jk} starts deviating from 2. An extra term $f_{11}(\Delta_j, \Delta_k)$ is added to prevent that E_{tors} becomes unrealistically large for systems containing two overcoordinated atoms. This makes sure that the influence of the BO_{jk} on the $V_2 - \cosine$ term is reduced for overcoordinated atoms j and k . This corresponds to $\Delta_j > 0$ and $\Delta_k > 0$.

2.1.5.5. Conjugated systems

The local perturbation described by E_{conj} will be most important for systems which have sequential bonds with a bond order of about 1.5, like benzene. This term will increase the overall stability of the system, as highly conjugated systems are very stable. This stabilisation is added by the following energy contribution:

$$E_{conj} = f_{12}(BO_{ij}, BO_{jk}, BO_{kl}) \cdot \lambda_{26} \cdot [1 + \cos^2(\omega_{ijkl} - 1) \cdot \sin(\theta_{ijk}) \cdot \sin(\theta_{jkl})]$$

where

$$\begin{aligned} f_{12}(BO_{ij}, BO_{jk}, BO_{kl}) \\ = \exp\left[-\lambda_{27} \cdot \left(BO_{ij} - \frac{1}{2}\right)^2\right] \cdot \exp\left[-\lambda_{27} \cdot \left(BO_{jk} - \frac{1}{2}\right)^2\right] \cdot \exp\left[-\lambda_{27} \cdot \left(BO_{kl} - \frac{1}{2}\right)^2\right] \end{aligned}$$

Besides these bonding interactions, ReaxFF also includes non-bonding interactions between the atoms in the system. This is described below.

2.1.5.6. Non-bonding van der Waals interactions

Apart from the valence interactions, which depend on the overlap of orbitals, also close-range repulsive interactions, based on the Pauli exclusion principle, and attractive interactions, caused by dispersion, exist and are included in the ReaxFF description. The van der Waals interactions are described by a distance corrected Morse potential:

$$E_{vdWaals} = D_{ij} \cdot \left\{ \exp\left[\alpha_{ij} \cdot \left(1 - \frac{f_{13}(r_{ij})}{r_{vdW}}\right)\right] - 2 \cdot \exp\left[\frac{1}{2} \cdot \alpha_{ij} \cdot \left(1 - \frac{f_{13}(r_{ij})}{r_{vdW}}\right)\right] \right\}$$

where

$$f_{13}(r_{ij}) = \left[r_{ij}^{\lambda_{29}} + \left(\frac{1}{\lambda_w} \right)^{\lambda_{28}} \right]^{\frac{1}{\lambda_{28}}}$$

The term $f_{13}(r_{ij})$ describes a screening interaction, which prevents extreme repulsion between bonded atoms (1-2 interactions) and between atoms that share a valence angle (1-3 interactions).

2.1.5.7. Coulomb interactions

In ReaxFF, Coulombic interactions are also taken into account for all atom pairs. A screened Coulomb potential is used to describe orbital overlap between the atoms at a short interatomic distance. The atomic charges are calculated at each iteration step with the Electronegativity Equilization Method (EEM)^{98,99}. Intra-atomic contributions to the energy are taken into account, to describe the energy cost to polarize the atoms in the system¹⁰⁰, which allows the force field to be used for ionic compounds. The Coulomb interactions are described by the following equation:

$$E_{coulomb} = C \cdot \frac{q_i \cdot q_j}{\left[r_{ij}^3 + \left(\frac{1}{\gamma_{ij}} \right)^3 \right]^{\frac{1}{3}}}$$

Where q_i and q_j are the charges on atoms i and j , respectively, and r_{ij} is the distance between these two atoms.

The ReaxFF potential contains 58 parameters in total, which are different for every combination of atoms. This means that the parameters for the valence angle energy E_{val} for the combination C-C-O is different to that of C-O-C, and so forth.

2.1.6. Force field development

In this dissertation a ReaxFF force field is developed for titanium dioxide with focus on the intrinsic point defects present in the structure. For the development of the parameter set, a training set is needed which includes experimental and quantum mechanical data.¹⁰¹ This training set should contain general data concerning the respective elements and data which is closely related to the desired processes and properties one wants to study. Thus, it is important to check for which system it is fitted. A validity check can be performed by comparing known data for the system of interest to their reproduction by the force field. If this is done one has a good indication that the results obtained by the force field are valid and not corrupt the obtained results. It is thus of the utmost importance that a force field is developed with care.

We performed the force field optimisation using an extensive experimental and theoretical data set, with an iterative optimisation scheme. In this scheme one minimizes the error of the force field, calculated as follows:

$$\text{Force field error} = \sum_{i=1}^n \left[\frac{x_{i,exp} - x_{i,calc}}{\sigma_i} \right]^2$$

The sum operator runs over all data included in the data set, where $x_{i,exp}$ is the experimental or quantum mechanical data and $x_{i,calc}$ is the same data but calculated with the current ReaxFF value. The partial errors are scaled with a value σ_i , which is used to set the weight of that data point in determining the total error. If the deviation between the “experimental” and ReaxFF value is larger than σ_i , the force field error will rapidly increase. Thus the desired force field accuracy can be tuned using σ_i .

To optimise the force field we used a sequential one-parameter optimisation procedure. A parabolic relationship between the value of the

force field error and a given parameter is assumed. This assumption is often correct for small intervals of the parameter that is optimized. Then, the optimal value for the given parameter is found by finding the minimum of the parabola. First the total force field error is calculated at three values of the given parameter within a small interval. Then this is used to determine the function for the parabola, from which the minimum is obtained. The corresponding parameter value of this minimum is then used to adjust the given parameter. The parameter is not just put on the minimal value but moved for a percentage of the difference between the original and minimal parameter value.

As most parameters in the force field are linked to other parameters, the optimisation of the force field has to be carried out iteratively. The linking means that the optimal value of one parameter can change if another parameter is adjusted, therefore the force field optimisation has to be done multiple times until the force field reaches the required accuracy.

2.2. Quantum chemistry

The correct description of atomic and molecular interactions is not possible within the framework of classical mechanics. Indeed, the energies involved have a discrete character instead of a continuous character as is assumed in classical mechanics. Therefore, atoms and molecules are best described within the framework of quantum mechanics.

Quantum mechanics is often used to gain a more fundamental understanding of chemical processes, as it is not always possible to extract detailed information from experiments. It is, for example, possible to calculate molecular geometries, dipole moments, energy differences between different conformers, differences in adsorption strengths at different adsorption sites, determine transition states in chemical reactions and their corresponding activation barriers, thermodynamic properties, et cetera.

In quantum chemistry, i.e., the application of quantum mechanics to chemical problems, most of the time one tries to solve the time-independent Schrödinger equation.¹⁰² However, there are only a discrete number of cases for which the Schrödinger equation can be solved in an exact manner. Therefore, approximations have to be introduced to find an approximation to the exact solution. This results in the development of a significant number of different methods such as Hartree-Fock, Density Functional Theory (DFT) and post-Hartree-Fock methods. As a basic source of information, the wavefunction, which contains all possible information about a system, is used for the Hartree-Fock and post-Hartree-Fock methods, while for DFT the electron density is used as the basic source of information for the atomic or the molecular system.

The major approximation within the Hartree-Fock method is that each electron experiences a mean field of the other electrons. This, however, is at variance with reality as the behavior of the different electrons is correlated, as there is an environment around each atom where the probability of finding a different electron is very small. This is called the Coulomb-hole. Within the post-Hartree-Fock methods one tries to overcome this shortcoming of the Hartree-Fock method. In Møller-Plesset perturbation theory, one includes the electron correlation as a perturbation. Another method that tries to overcome the absence of electron correlation is Configuration Interaction, which uses multiple Slater-determinants to describe the wavefunction. In Hartree-Fock only one determinant is used, which describes the electronic ground state. The extra determinants each describe one of the different excited states, such as one-particle excitations for CIS and two-particle excitations for CISD until all electronic states are described with Full CI. However, these post Hartree-Fock methods are computationally very expensive. With DFT one includes approximate electron correlation models, but at a computational cost similar to that of Hartree-Fock. This allows DFT to be applied to relatively large systems.

2.2.1. Many-body problem

One of the difficulties of quantum mechanics is that in most cases one wants to study a system containing more than one electron. The coupling of the electron interactions makes it impossible to find an analytic solution for these types of systems. In most cases where one tries to determine the properties of a quantum system, these properties can be obtained by solving the time-independent Schrödinger equation:

$$\hat{H} \Psi(\mathbf{r}_1, \mathbf{r}_2 \dots \mathbf{r}_N) = E \Psi(\mathbf{r}_1, \mathbf{r}_2 \dots \mathbf{r}_N)$$

For which \hat{H} is the Hamiltonian, E the total energy of the system and $\Psi(\mathbf{r}_1, \mathbf{r}_2 \dots \mathbf{r}_N)$ the wavefunction of the many-body system. The square of the wavefunction is the probability distribution of the particles in the molecule. The Hamiltonian \hat{H} is an operator that contains the sum of the different kinetic and potential energies. In a system consisting of n electrons and N nuclei, the Hamiltonian (in atomic units) can be written as:

$$\hat{H} = \hat{T}_e + \hat{T}_n + \hat{V}_{ne} + \hat{V}_{ee} + \hat{V}_{nn}$$

With the kinetic energy operator of the electrons i :

$$\hat{T}_e = - \sum_{i=1}^n \frac{1}{2} \nabla_i^2$$

the kinetic energy operator of the nuclei A :

$$\hat{T}_n = - \sum_{A=1}^N \frac{\nabla_A^2}{2M_A}$$

the Coulomb attraction between the nuclei and electrons:

$$\hat{V}_{ne} = - \sum_{i=1}^n \sum_{A=1}^N \frac{Z_A}{r_{iA}}$$

the repulsion between the electrons:

$$\hat{V}_{ee} = \sum_{i=1}^n \sum_{j>i}^n \frac{1}{r_{ij}}$$

and the repulsion between the nuclei:

$$\hat{V}_{nn} = \sum_{A=1}^N \sum_{B>A}^N \frac{Z_A Z_B}{R_{AB}}$$

For these operators r_{ij} , r_{iA} and R_{AB} are the distances between electron i and j , electron i and nuclei A , and nuclei A and B . ∇_i^2 and ∇_A^2 are the Laplace operators for the i^{th} electron and the A^{th} nucleus, that has a mass M_A and atomic number Z_A . As this form of the Hamiltonian cannot be solved analytically, approximations have to be made.

Since the nuclei are ~ 1800 times heavier than the electrons, they can be considered stationary compared to the electrons. The electrons will thus move within a fixed external potential due to the nuclei and the nuclei experience an average interaction with the surrounding electrons. This approximation, known as the Born-Oppenheimer (BO) approximation¹⁰³, allows decoupling the degrees of freedom of the electrons and nuclei. The full many-body Hamiltonian can be divided in two parts, the nuclear part:

$$\hat{H}_{nuc} = \hat{T}_n + \hat{V}_{nn}$$

and the electronic part:

$$\hat{H}_{el} = \hat{T}_e + \hat{V}_{ne} + \hat{V}_{ee}$$

Within the BO approximation the kinetic energy of the nuclei is neglected and the potential energy of the nuclei – nuclei repulsion is treated as a constant for a given inter-nuclear distance. Note that the nuclear coordinates in the \hat{V}_{ne} term are entered parametrically and are not treated as variables for solving the electronic Hamiltonian.

Also the wavefunction can be split into an electronic and nuclear part:

$$\Psi = \Psi_{el}(r^n, R^N) \cdot \Psi_{nuc}(R^N)$$

Again, R^N are included as parameters and not as variables.

Unfortunately, solving the electronic Schrödinger equation is still too complex for systems containing more than one electron, since the electronic wavefunction still contains $3n$ electrons for an n -electron system.

2.2.2. Hartree-Fock Theory

The variational theorem allows us to find an upper limit for the ground state energy. This theorem states that for a given system – whose Hamiltonian is time independent and for which the ground state energy (lowest energy eigenvalue) is E_0 – any given normalised, well-behaved function Ψ of the system's coordinates that satisfies the boundary conditions of the Hamiltonian, the following is true:

$$\int \Psi^* \hat{H} \Psi \geq E_0$$

The electron-electron repulsion terms make that the electronic Schrödinger equation is not separable for an atom containing many electrons. Hartree made the approximation to expand the many-electron wavefunction into a product of single electron wavefunctions, $\psi_i(\mathbf{r}_i s_i)$. The single electron wavefunctions consist of a spatial function $\varphi_i(\mathbf{r}_i)$, and an electron spin function $\sigma(s_i)$:

$$\psi_i(\mathbf{r}_i s_i) = \varphi_i(\mathbf{r}_i) \sigma_i(s_i)$$

The N electron wavefunction is then approximated by the product of the 1-electron spatial and spin functions:

$$\Psi(\mathbf{r}_1 s_1 \dots \mathbf{r}_N s_N) = \frac{1}{\sqrt{N}} \psi_1(\mathbf{r}_1 s_1) \dots \psi_N(\mathbf{r}_N s_N)$$

Now we only have to look for the functions $\psi_1, \psi_2, \dots, \psi_n$ that minimize the variational integral:

$$\frac{\int \Psi^* \hat{H} \Psi dv}{\int \Psi^* \Psi dv}$$

However, this representation does not follow the Pauli exclusion principle¹⁰⁴. For electrons the Pauli exclusion principle states that no two electrons can occupy the same spin-orbital. Mathematically this can be expressed by an antisymmetric wavefunction for the many-electron system. This means that the wavefunction has to change sign if the coordinates (both spatial and spin) are interchanged:

$$\Psi(\mathbf{r}_1 s_1, \dots, \mathbf{r}_i s_i, \dots, \mathbf{r}_j s_j, \dots, \mathbf{r}_N s_N) = -\Psi(\mathbf{r}_1 s_1, \dots, \mathbf{r}_j s_j, \dots, \mathbf{r}_i s_i, \dots, \mathbf{r}_N s_N)$$

This asymmetric wavefunction will disappear when two fermions with the same quantum numbers are present. This discrepancy with the Pauli exclusion principle of Hartree's approximation was solved by the Hartree-Fock approximation^{105,106}. The wavefunction is then written as an antisymmetrised linear combination of the following form:

$$\begin{aligned} \Psi_{HF} &= \Psi(\mathbf{r}_1 s_1 \dots \mathbf{r}_N s_N) \\ &= \frac{1}{\sqrt{N!}} [\psi_1(\mathbf{r}_1 s_1) \dots \psi_N(\mathbf{r}_N s_N) - \psi_1(\mathbf{r}_2 s_2) \psi_2(\mathbf{r}_1 s_1) \dots \psi_N(\mathbf{r}_N s_N) \\ &\quad - \dots + \psi_1(\mathbf{r}_3 s_3) \psi_2(\mathbf{r}_2 s_2) \psi_3(\mathbf{r}_1 s_1) \dots \psi_N(\mathbf{r}_N s_N) + \dots] \end{aligned}$$

Slater later determined that the approximation of the wavefunction according to the Hartree-Fock approximation could be represented as a determinant, the Slater determinant¹⁰⁷:

$$\Psi_{HF} = \frac{1}{\sqrt{N!}} \begin{vmatrix} \psi_1(\mathbf{r}_1 s_1) & \psi_2(\mathbf{r}_1 s_1) & \cdots & \psi_N(\mathbf{r}_1 s_1) \\ \psi_1(\mathbf{r}_2 s_2) & \psi_2(\mathbf{r}_2 s_2) & \cdots & \psi_N(\mathbf{r}_2 s_2) \\ \cdots & \cdots & \cdots & \cdots \\ \psi_1(\mathbf{r}_N s_N) & \psi_2(\mathbf{r}_N s_N) & \cdots & \psi_N(\mathbf{r}_N s_N) \end{vmatrix}$$

For which the orbitals are all orthonormal:

$$\int \psi_i^*(\mathbf{r})\psi_j(\mathbf{r}) = \langle \psi_i | \psi_j \rangle = \delta_{ij}$$

The expectation value of the Hamiltonian with the Slater determinant gives us the Hartree-Fock energy:

$$\begin{aligned} E_{HF} &= \langle \Psi_{HF} | \hat{H} | \Psi_{HF} \rangle \\ &= \sum_i^N \int \left(\frac{1}{2} |\nabla \psi_i(\mathbf{r})|^2 - \frac{Z}{r} |\psi_i(\mathbf{r})|^2 \right) d^3\mathbf{r} \\ &\quad + \frac{1}{2} \sum_{i,j,i \neq j}^N \iint |\psi_i(\mathbf{r})|^2 \frac{1}{|\mathbf{r} - \mathbf{r}'|} |\psi_j(\mathbf{r}')|^2 d^3\mathbf{r} d^3\mathbf{r}' \\ &\quad - \frac{1}{2} \sum_{i,j,i \neq j}^N \delta_{s_i s_j} \iint \psi_i^*(\mathbf{r}) \psi_j^*(\mathbf{r}') \frac{1}{|\mathbf{r} - \mathbf{r}'|} \psi_i(\mathbf{r}') \psi_j(\mathbf{r}) d^3\mathbf{r} d^3\mathbf{r}' \end{aligned}$$

In this equation the first term is the kinetic energy of the electrons, and the second and third terms are the electron-ion interactions and the electron-electron interactions. The fourth term is the exchange energy E_x , which disappears when $s_i \neq s_j$.

This last term ensures that, according to the Pauli exclusion principle, an electron repels nearby electrons with the same spin, and does not affect electrons with opposite spins as they do not have the same quantum

numbers. So around every electron there is a region that is depleted from electrons with the same spin quantum number. This region is called the exchange hole.

However, the motion of the electrons in the real system is more correlated than in the Hartree-Fock approximation. Apart from the exchange hole there also exists a Coulomb hole or the correlation hole. This is a consequence of electrostatic repulsion. This leads to an electron-depleted region that surrounds each electron.

2.2.3. Density Functional Theory

For a many-body system containing n electrons the electronic wave function depends on $4n$ variables, i.e., $3n$ spatial and n spin coordinates. As previously mentioned, the Hamiltonian operator for the system contains only one- and two-electron spatial terms, thus the molecular energy can be written in terms of integrals involving a maximum of 6 spatial coordinates. Thus one can say that the wavefunction contains more information than needed, and therefore it was interesting to search for methods that involve fewer variables than the wavefunction to calculate the energy and other properties.

2.2.3.1. Thomas-Fermi model

One model that was introduced shortly after the introduction of the Schrödinger equation by Llewellyn Thomas and Enrico Fermi to reduce the number of variables, uses the electron density $\rho(\mathbf{r})$.^{108,109} They used a functional of the density to express the total energy, $E_{TF}[\rho(\mathbf{r})]$. They expressed the kinetic energy of the electrons as the non-interacting electrons in a homogeneous electron gas, the electrostatic attraction between the nuclei and the electrons using an external potential $v_{ext}(\mathbf{r})$ as a

static Coulomb potential from the nuclei, and the repulsion between the electrons as a classical Coulomb repulsion:

$$E_{TF}[\rho(\mathbf{r})] = C_F \int \rho(\mathbf{r})^{5/3} d^3\mathbf{r} + \int \rho(\mathbf{r}) \left(- \sum_{A=1}^M \frac{Z_A}{|\mathbf{r} - \mathbf{r}'|} \right) d^3\mathbf{r} d\mathbf{r}' + \frac{1}{2} \iint \frac{\rho(\mathbf{r})\rho(\mathbf{r}')}{|\mathbf{r} - \mathbf{r}'|} d^3\mathbf{r} d\mathbf{r}'$$

The Thomas-Fermi model, however, is only correct in the limit of an infinite nuclear charge. The total energy of a molecule is higher than the sum of the atomic energies, meaning that molecular bonding can't be described. It also neglects the exchange and correlation in its description. Although the method thus has its shortcomings, it can be seen as the predecessor of the modern Density Functional Theory (DFT).

2.2.3.2. Modern Density Functional Theory

In 1964 Kohn and Hohenberg laid the foundation of the modern DFT methods.¹¹⁰ They proved a theorem that legitimizes the use of the electron density $\rho(\mathbf{r})$ as the basic variable to determine all properties for the ground state of the system. The theorem states that every observable (ground-state molecular energy, wave function, and all other molecular electronic properties) are uniquely determined by the ground-state electron density $\rho_0(\mathbf{r})$, which is only a function of three variables. This can be reformulated as: "Every observable can be written as a functional of the ground-state density, and therefore no information is lost between changing the basic source of information from the wave function to the electron density."

The ground state electronic energy E_0 can be written as a functional of the function $\rho_0(\mathbf{r})$:

$$E_0 = E[\rho_0(\mathbf{r})] = V_{ext}[\rho_0(\mathbf{r})] + T[\rho_0(\mathbf{r})] + V_{ee}[\rho_0(\mathbf{r})]$$

In this equation only the nuclear-electron attraction, $V_{ext}[\rho_0(\mathbf{r})]$, is known, while the electronic kinetic energy, $T[\rho_0(\mathbf{r})]$, is unknown and for the electron-electron interactions, $V_{ee}[\rho_0(\mathbf{r})]$, only the classical part, $\frac{1}{2} \int \frac{\rho(\mathbf{r})\rho(\mathbf{r}')}{|\mathbf{r}-\mathbf{r}'|} d\mathbf{r}d\mathbf{r}'$, is known.

$$E[\rho_0(\mathbf{r})] = V_{ext}[\rho_0(\mathbf{r})] + F_{HK}[\rho_0(\mathbf{r})] = \int \rho_0(\mathbf{r})V_{ext}(\mathbf{r})d\mathbf{r} + F_{HK}[\rho_0(\mathbf{r})]$$

The Hohenberg-Kohn functional F_{HK} is independent of the external potential and only dependent on the ground state density. This description does not provide a practical way to calculate the ground state energy from the ground state electron density, because the Hohenberg-Kohn functional F_{HK} is unknown.

The second Hohenberg-Kohn theorem and the approach developed by Kohn and Sham make Density Functional Theory a practical tool, instead of just a nice theory. The second theorem states: “There exists a universal functional of the electron density for the energy. The global minimum of this energy functional is the ground state energy and the density that minimizes the functional is the exact ground state density.”

This theorem has as consequence that in principle we can calculate the exact energy of the ground state and the corresponding ground state density by varying the density, since no density with the correct number of electrons N can result in a total energy lower than the true total energy. This only holds true for the universal energy functional, and the second Hohenberg-Kohn theorem only states there is such a functional, but doesn't give any information about its form or how to find it. It also doesn't tell how to find the ρ_0 without first finding the wavefunction. This approach is used in traditional quantum chemistry: first the wavefunction is found and then the wavefunction is integrated to find ρ_0 .

Kohn and Sham developed a practical method for finding ρ_0 and for finding E_0 from ρ_0 .¹¹¹ In principle their method could be exact; however, they introduce an unknown functional in the equations for which an approximation is needed, and therefore the Kohn-Sham formulation yields approximate results. Kohn and Sham introduced a fictitious reference system of non-interacting electrons that move in an effective potential $v_{eff}(\mathbf{r})$ due to all the other electrons. Since Hohenberg and Kohn proved that $\rho_0(\mathbf{r})$ determines the external potential, once we find the density of the reference system the external potential is uniquely determined. The electrons in the reference system do not interact with each other, so the Hamiltonian of the non-interacting system is

$$\hat{H}_s = \sum_{i=1}^n \left[-\frac{1}{2} \nabla_i^2 + v_{eff}(\mathbf{r}_i) \right]$$

The Kohn-Sham functional for a set of doubly occupied electronic states ψ_i^{KS} can be written as:

$$E[\rho_0(\mathbf{r})] = - \sum_{i=1}^n \left[\frac{1}{2} \langle \psi_i^{KS} | \nabla_i^2 | \psi_i^{KS} \rangle \right] + \int V_{ion}(\mathbf{r}) \rho(\mathbf{r}) d\mathbf{r} + \frac{1}{2} \int \frac{\rho(\mathbf{r}) \rho(\mathbf{r}')}{|\mathbf{r} - \mathbf{r}'|} d\mathbf{r} d\mathbf{r}' \\ + E_{xc}[\rho(\mathbf{r})] + E_{ion}[\mathbf{R}_n]$$

Where $E_{xc}[\rho(\mathbf{r})]$ is the exchange-correlation energy, $E_{ion}[\mathbf{R}_n]$ the Coulomb energy for the interactions between the nuclei for a certain configuration defined by the positions \mathbf{R}_n , and the electronic density given by $\rho(\mathbf{r}) = \sum_{i=1}^n |\psi_i^{KS}|^2$. The wavefunctions that minimize the Kohn-Sham functional satisfy the single-particle Kohn-Sham eigenvalue equations:

$$\left\{ -\frac{1}{2} \nabla^2 + V_{ion}(\mathbf{r}) + \int \frac{\rho(\mathbf{r}')}{|\mathbf{r} - \mathbf{r}'|} + V_{xc}(\mathbf{r}) \right\} \psi_i^{KS} = \varepsilon_i \psi_i^{KS}$$

For which ψ_i^{KS} is the wave function of the i -th Kohn-Sham orbital, ε_i the energy of the i^{th} Kohn-Sham orbital (i.e., the eigenvalue), and the exchange-correlation potential:

$$V_{xc}(\mathbf{r}) = \frac{\delta E_{xc}[\rho(\mathbf{r})]}{\delta \rho(\mathbf{r})}$$

As the wave functions determine the electronic density, the Kohn-Sham equations must be solved self-consistently. The summation of the single-particle Kohn-Sham eigenvalues does not result in the total electronic energy, as this would overcount the electron-electron interactions.

The exchange-correlation energy is difficult to evaluate accurately. However, it is a relatively small contribution to the total energy. To calculate the properties of a molecular system accurately, it is key to formulate a good approximation of the E_{xc} .

2.2.3.3. The exchange-correlation energy

The exchange-correlation energy E_{xc} contains different components, i.e., the exchange energy arising from the anti-symmetry requirements, the self-interaction correction arising from the $\frac{1}{2} \int \frac{\rho(\mathbf{r})\rho(\mathbf{r}')}{|\mathbf{r}-\mathbf{r}'|} d\mathbf{r}d\mathbf{r}'$ term in the Kohn-Sham functional ($\rho(\mathbf{r})$ can interact with $\rho(\mathbf{r}')$ even if parts of $\rho(\mathbf{r})$ and $\rho(\mathbf{r}')$ originate from the same electron), and the correlation energy which itself consists of two terms, i.e., the kinetic correlation energy, which is the difference between the kinetic energy of the electrons in a real system and the kinetic energy of the non-interacting particles, and the Coulombic correlation energy, associated with inter-electronic repulsions. In this section we will shortly describe the main approaches used in density functional theory.

2.2.3.4. Local Density Approximation (LDA)

A first simple approach is the Local Density Approximation (LDA). In this exchange-correlation functional one describes the exchange-correlation energy of the electronic system as that of a homogeneous electron gas. The exchange-correlation energy per electron at each point of space is approximated by the energy per electron of a uniform electron gas with the same density at that point of space \mathbf{r} .

$$E_{xc}^{LDA} = \int \varepsilon_{xc}^{hom}(\rho(\mathbf{r})) \rho(\mathbf{r}) d\mathbf{r}$$

for which $\varepsilon_{xc}^{hom}(\rho(\mathbf{r}))$ is the exchange-correlation energy per particle in a homogeneous electron gas with a density $\rho(\mathbf{r})$. This $\varepsilon_{xc}^{hom}(\rho(\mathbf{r}))$ can be accurately calculated for every density. It is also common to use separate exchange and correlation models in LDA. This method is very accurate for the homogeneous electron gas; however for molecular systems the method will only work well for a system where the spatial variations of the density are small.

Considering the inexact nature of the LDA method, we would expect very low applicability beyond the nearly uniform electron gas. However, accurate results have been obtained for atomic and molecular systems, which are far from homogeneous, i.e., the electron density does not vary slowly in function of the position. However, the method has its limitations, e.g. the LDA method overestimates of binding energies and the total energies of atoms are more accurately described in the Hartree-Fock approximation.

2.2.3.5. Generalized Gradient Approximation (GGA)

An improvement over the Local Density Approximation is the Generalized Gradient Approximation (GGA). Generally GGA's improve total energies, energy barriers, atomization energies and energy differences compared to the LDA method. The GGA method also takes the spatial variation of the density into account, in contrast to LDA.

$$E_{xc}^{GGA} = \int f(\rho(\mathbf{r}), \nabla\rho(\mathbf{r})) d\mathbf{r}$$

Often one splits up the exchange-correlation energy into an exchange and correlation part, which are modelled separately. As the exchange and correlation in the GGA's are modelled separately, one can combine any exchange functional with any correlation functional. Some of the functionals are derived solely from theoretical considerations such as the Perdew-Wang exchange functional PW86¹¹² or the Perdew-Burke-Ernzerhof exchange-correlation functional (PBE)¹¹³, while others make use of some empiricism, i.e., parameters are fitted so that known values of various molecular properties are reproduced, as is for example the case in the Becke exchange functional B88¹¹⁴:

$$E_x^{B88} = E_x^{LDA} - b \sum_{\sigma=\alpha,\beta} \int \frac{(\rho^\sigma)^{4/3} \chi_\sigma^2}{1 + 6b\chi_\sigma \ln[\chi_\sigma + (\chi_\sigma^2 + 1)^{1/2}]} d\mathbf{r}$$

For which b is an empirical parameter determined by fitting against known Hartree-Fock exchange energies of several atoms and is equal to 0.0042 a.u., and $\chi_\sigma = |\nabla\rho^\sigma|/(\rho^\sigma)^{4/3}$.

Further improvement to the GGA functionals is done in the so-called meta-GGA. Here one adds information beyond the first-order derivate of the

density, by adding a second order density gradient or by including the kinetic energy density.

2.2.3.6. Hybrid Functionals

Another successful group of exchange-correlation functionals are the hybrid functionals, which include a certain amount of the exact Hartree-Fock exchange term for the calculation of the exchange-correlation energy. A famous example of these types of functionals is the B3LYP exchange-correlation functional¹¹⁵:

$$E_x^{B3LYP} = (1 - a_0 - a_x)E_x^{LSDA} + a_0E_x^{HF} + a_xE_x^{b88} + (1 - a_c)E_c^{VWN} + a_cE_c^{LYP}$$

For which $a_0 = 0.20$, $a_x = 0.72$, and $a_c = 0.81$. Thus one mixes in 20% of the exact HF-exchange energy.

Chapter 3

Development of a ReaxFF reactive force field for intrinsic point defects in Titanium Dioxide

This chapter is based on the following publication: S. Huygh, A. Bogaerts, A.C.T. van Duin, E. Neyts, *Development of a ReaxFF reactive force field for intrinsic point defects in titanium dioxide*, *Computational materials science*, 95 (2014), 579 - 591

3.1. Introduction

Titanium dioxide (TiO_2) is the natural occurring oxide of titanium, which exists in various polymorphs. The three most stable polymorphs are rutile, anatase and brookite, in that order of abundance. Thanks to its high reactivity, anatase is widely applied in photocatalysis¹¹⁶ and solar energy conversion¹¹⁷. Especially the surface is critically important for these applications, and for this reason the interest in the chemical and physical properties of the surfaces has increased significantly in the past decades. The reader is referred to a review¹¹⁸ for a summary of the research on TiO_2 surfaces.

The higher catalytic activity of anatase with respect to rutile is due to the behaviour of its intrinsic point defects. It is indeed well known that point defects strongly affect the physical and chemical properties of metal oxides. In heterogeneous catalysis the defect sites act as an active site for adsorption of molecules and/or metal particles. In photocatalysis the defects influence the surface reactivity, either favourably or detrimentally. A favourable effect occurs when oxygen vacancies act as trap sites for photoexcited charge carriers such that these carriers are transported to the surface. A detrimental effect occurs when these oxygen vacancies act as recombination centers for these carriers which will lower the reactivity. Not only the “chemistry” is influenced significantly by these defects, but the diffusion of point defects also plays a key role in the mass transport between the surface and the bulk during surface preparation techniques such as annealing or sputtering.¹¹⁹

The location of the defect determines its role and its properties. Density functional theory (DFT) calculations demonstrated that for an anatase (101) surface, which is the lowest energy and most exposed surface,^{120,121} the subsurface oxygen vacancies are 0.5 eV more stable than surface

vacancies.¹²² The diffusion barriers of these defects from the surface region to the subsurface region are around 1 eV.¹²² This indicates that surface oxygen vacancies, once formed, diffuse relatively easily to the subsurface, which is consistent with the low density of surface defects found experimentally with scanning tunneling microscopy (STM)^{123,124} and the high density of O vacancies indicated by ultraviolet photoemission spectroscopy (UPS)¹²⁵ that also accesses the subsurface region. Therefore, the subsurface oxygen vacancies will play a more prominent role than the surface vacancies; this is in contrast with rutile where the opposite trend is observed, both theoretically¹¹⁹ as well as experimentally with STM^{123,124} and UPS¹²⁵. Because of the differences in these trends, anatase has a higher catalytic activity than rutile. The subsurface defects have a longer lifetime than surface defects, because the latter will be quenched by molecules in the environment.

Because of the accuracy and speed of modern quantum mechanical (QM) methods, they can be used to calculate the energy and the geometry of molecules and solid state systems. Ab initio MD has also been extensively used to model dynamical processes of relatively large molecules adsorbed on solid state substrates. However, to reach larger time and space scales, classical molecular dynamics simulations may be used as a complimentary technique. In this work, we developed a classical reactive force field for titanium dioxide for the ReaxFF method developed by van Duin and coworkers⁹⁰. The main focus of this force field is the correct description of intrinsic point defects, oxygen vacancies and titanium interstitials in anatase. The developed force field thus allows larger spatial scale and longer time scale simulations of the titanium dioxide system compared to DFT, with comparable accuracy. For instance, in the LAMMPS implementation of ReaxFF¹²⁶, it is possible to simulate systems with 10^6 atoms at nanosecond timescales.^{127–130} Within LAMMPS there is also

another variable-charge reactive force field implemented, namely the charge-optimized many-body potential (COMB) developed by Sinnott, Phillpot and coworkers.^{131–136} Also for COMB a parametrization for the titanium dioxide system has been developed.¹³⁷

3.2. Computational Methods

3.2.1. ReaxFF

The herein developed Ti-O force field has the same O atomic parameters and O/H pair parameters as the published ReaxFF descriptions for Zn/O/H¹³⁸, Fe/O/H¹³⁹, Si/O/H¹⁴⁰, proteins¹⁴¹ and Ti/O/H^{142–144}, making it straightforward to integrate these potentials. All mentioned force fields have the same O atomic parameters and O/H pair parameters. Only the Ti/H, Ti-O-H, O-Ti-O-H and Ti-O-O-H interactions thus need to be included in a further fitting to expand this force field to Ti/O/H. As best available initial guess for the development of a force field that describes the influence of intrinsic point defects on the chemistry of TiO₂, the Ti/O/H force field developed by Kim and co-workers¹⁴² was used.

3.2.2. Training set

In this work the force field parameters for the TiO₂-system have been re-evaluated, starting from the ReaxFF Ti/O parameters, as developed earlier by Kim and co-workers¹⁴², but refocusing the training on intrinsic point defects, which were previously not considered. The training set consists of a set of quantum mechanical (QM) and some experimental data. This data is taken from literature, the QM level and some of the computational details are given between parentheses after the description of the data points added to the training set. For the equations of state (EOS) of titanium dioxide, required for an adequate description of volume-energy

relations, approximately 10 data points for each of the 8 TiO₂ polymorphs (anatase, rutile, brookite, columbite, baddeleyite, pyrite, fluorite and cottunite), are added to the training set with an increment of about 2% increase or decrease in volume. (All polymorphs except brookite: LCAO-HF-TVAE*¹⁴⁵, brookite: DFT-B3LYP-6-31G¹³⁶) The QM results indicate that anatase is more stable than rutile while experiments indicate otherwise, and therefore the cohesive energy differences of anatase, rutile and brookite are taken from experiment¹⁴⁶. The five high energy polymorphs are not important for the final result, even though they are not very accurate. To match the corresponding geometry of each data point, the unit cell of each phase is expanded or contracted within the ReaxFF calculation.

For the three most abundant phases of titanium dioxide, i.e., rutile, anatase and brookite, the heats of formation were used. Also potential energy differences of 30 (TiO₂)_x-clusters (x=1-16) are added.^{142,147-149} (DFT-B3LYP, LACVP**)

For the anatase (101) surface, the formation energies of oxygen vacancies at the surface and in the subsurface^{150,151} (DFT-GGA PBE, Γ -point, spin restricted), the diffusion barriers of these vacancies^{150,151} (DFT-GGA PBE, 2x2x1 k-point mesh, spin restricted, NEB), the formation energies of interstitial titanium¹⁵⁰ (DFT-GGA PBE, Γ -point, spin restricted) and the oxygen adsorption energies at the reduced surface¹⁵² (DFT-GGA PBE, Γ -point, spin unrestricted) are added to the training set.

3.2.3. Force field fitting

The force field parameters were fitted to the training set containing all the data points mentioned in the previous section. The parameters that were adjusted are the Ti atomic parameters, the Ti-Ti, Ti-O and O-O bond

parameters and the O-Ti-O, Ti-O-Ti, Ti-O-Ti, Ti-O-O and Ti-Ti-O valence angle parameters.

To find the most optimal set of parameters a sequential one-parameter search¹⁴² has been used to minimize the sum-of-squares error function:

$$\text{Error} = \sum_i^n \left[\frac{(x_{i,QM} - x_{i,ReaxFF})}{\sigma_i} \right]^2$$

In this equation $x_{i,QM}$ is the QM value in the training set, $x_{i,ReaxFF}$ is the ReaxFF calculated value and σ_i is the weight assigned to data point i . In total around 270 data points were added and 240 corresponding structures were used in the force field fitting. The sequential one-parameter search method has been performed in multiple cycles of 88 adjusted parameters to account for parameter correlation⁹⁰. The result of the force field fitting and a comparison between the training set, reference QM data, and the ReaxFF calculated data are presented below.

3.3. Results and Discussion

In this section we will compare the ReaxFF calculated data, the data added to the training set and the data as calculated with other ReaxFF force fields^{142–144}. These data consist of the equations-of-state, relative phase stabilities, TiO₂-cluster stabilities, formation energies of interstitial titanium and oxygen vacancies, diffusion barriers of the oxygen vacancies and oxygen adsorption energies on a reduced anatase (101) surface. This comparison between the data as calculated with the currently developed force field, two other force fields and the data which was included in the training set is discussed below. Also the influence of defect concentration and compressing or expanding the anatase (101) surface on the oxygen vacancies diffusion barriers, and subsurface diffusion will be presented

after the evaluation of the developed force field; this subsection contains only data as obtained with the force field developed in this chapter.

In the further discussion the herein developed ReaxFF force field parameterization is simply indicated as “ReaxFF”. If Kim is mentioned, the ReaxFF force field as published in reference 142 is meant, and when Monti is mentioned, the ReaxFF force field as published in references 143 and 144 is meant.

3.3.1. Equations of state (EOS) and relative phase stability

Figure 2 shows the cohesive energy differences between the different titanium dioxide polymorphs relative to rutile. ReaxFF predicts that anatase is more stable than rutile, which is inconsistent with the experimental data where an energy difference is found of 0.62 kcal/mol.¹⁴⁶ The stability, however, is dependent on the surface area, and for larger surface areas, anatase becomes indeed more stable than rutile.¹⁵³ The value used by Levchenko et al.¹⁵⁴ and Smith et al.¹⁵⁵ is 0.4 ± 0.1 kcal/mol with rutile the most stable polymorph. For such a small difference it is not surprising that the ReaxFF force field does not reproduce the correct energy difference. Since phase transitions in solid phases lay far beyond the time scale typically attainable in MD simulations, this will, however, not cause problems. The cohesive energy differences for the four most stable phases (rutile, anatase, brookite and columbite) are correct within 1.6 kcal/mol. The four higher energy phases, which are not important for this force field, show discrepancies up to 8 kcal/mol, although the correct stability order is preserved.

The Kim and Monti force fields reproduce the cohesive energy differences of TiO₂ within 1.8 and 2.1 kcal/mol, respectively. In case of the Kim force field the order of the relative stabilities for the most stable phases is

correct. The Monti force field, on the other hand, predicts the anatase phase to be less stable than rutile, which is consistent with the experimental data, but more stable than brookite, which is inconsistent with the experimental data. This means that the trends in the other force fields are comparable to or slightly better than those in the current force field, but since phase transitions lay beyond the typical time scale of MD simulations, this will not cause problems during simulations.

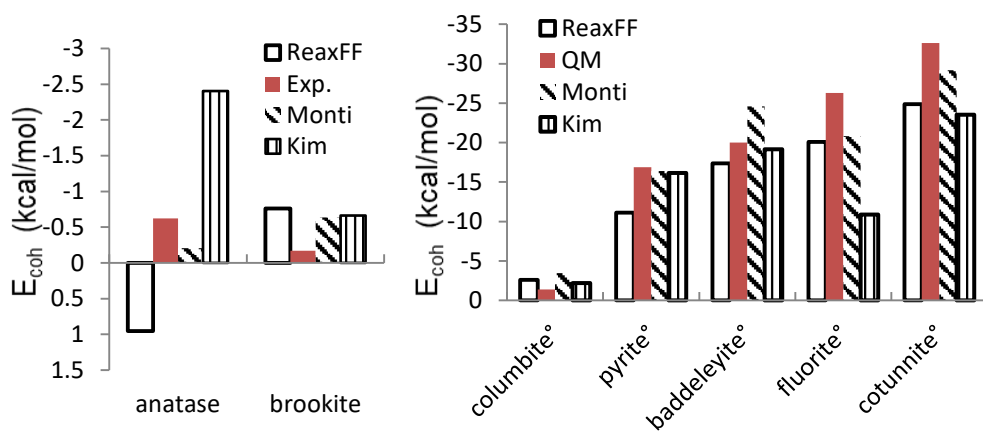


Figure 2: Energy differences between different TiO₂ polymorphs relative to rutile. The experimental data are from reference ¹⁴⁶ and the QM data from reference ¹⁴⁵.

Figure 3, Figure 4 and Figure 5 show the EOS of the three most abundant TiO₂ polymorphs, i.e., rutile, anatase and brookite, respectively.

The volume-energy relationship in ReaxFF describes the expansion of rutile very well, but when compressing the structure the error increases gradually up to 4.75 kcal/mol (28.6% error) when the volume is reduced with 15%. The three force fields reproduce similar equations of state. The Monti force field reproduces the compression in a better way, while the Kim force field performs worse when compression occurs.

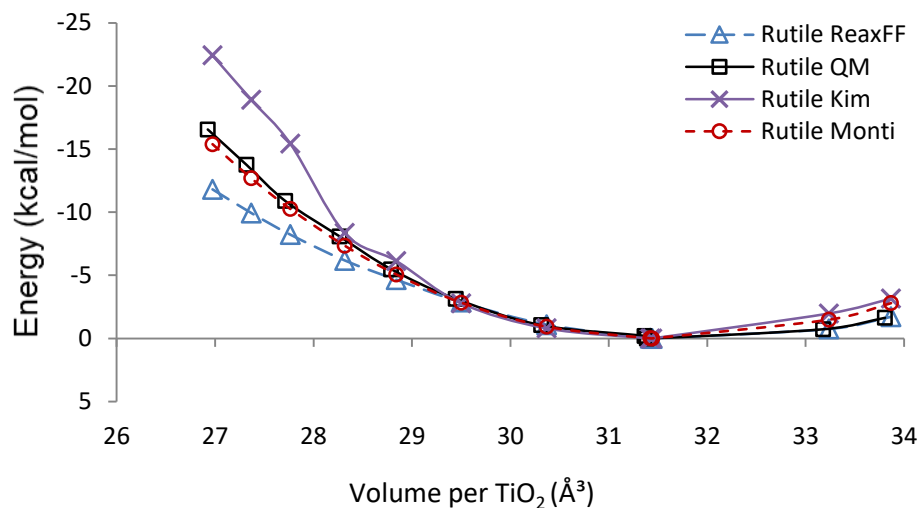


Figure 3: Comparison of the EOS of rutile calculated with ReaxFF, QM¹⁴⁵, Monti and Kim.

The volume-energy relationship of anatase is described very well overall, showing a maximum discrepancy of 0.81 kcal/mol (11.7% error) for a compression of 10%, while an error of only 0.65 kcal/mol (11.26% error) is found when the volume is expanded with 11%. This accurate description of the volume-energy relationship of anatase thus demonstrates the reliability of the force field with respect to a description of pressure effects on the chemistry of anatase. In the case of the Monti and Kim force fields the minimum is (incorrectly) shifted to lower volumes and the shape of the curve differs from the QM one. The Kim force field gives a curve which is a bit too narrow and Monti generates a curve which is too flat in the case of compression, corresponding to a force constant which is too high and too low, respectively. Overall, however, all three force fields are in decent agreement with the QM data.

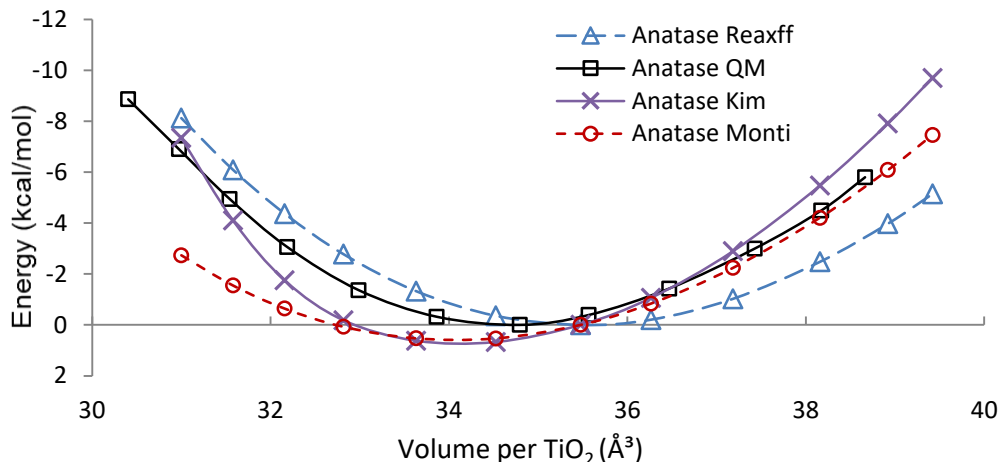


Figure 4: Comparison of the EOS of anatase calculated with ReaxFF, QM¹⁴⁵, Monti and Kim.

Finally, also the EOS of brookite is described well, with the error gradually increasing up to 3 kcal/mol (24.7% error) when the volume is reduced with 14%. The force fields of Kim and of Monti have errors within the same order of magnitude.

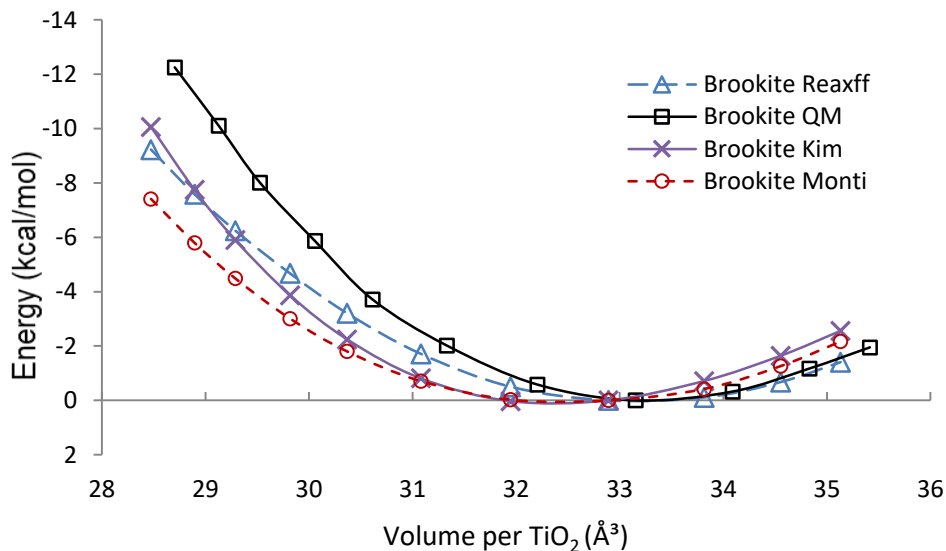


Figure 5: Comparison of the EOS of brookite calculated with ReaxFF, QM¹³⁶, Monti and Kim.

In Table 2 the lattice parameters as calculated with QM methods and ReaxFF are compared with the experimental values. As can be seen by the deviations, given in percentage, between the calculated and measured values, the currently developed force field overestimates the lattice parameters in all cases. The QM methods underestimate the a/b lattice value of rutile and anatase, and overestimate all other lattice parameters. The overestimation of the lattice parameters by ReaxFF is the same for all lattice parameters of the same polymorph of titanium dioxide. This means that the crystal structure is expanded equally in every direction in comparison with the experiments.

Table 2. Lattice parameters of rutile, anatase and brookite as calculated with QM methods and ReaxFF and as measured in the experiments, given in Å. The values between the parentheses are the deviations, given in percentage, in comparison with the experiment.

Method	a	b	c
Rutile			
HF-TVAE* ¹⁴⁵	4.575 (-0.26)		2.999 (1.52)
ReaxFF	4.605 (0.39)		2.966 (0.41)
Exp. ¹⁴⁵	4.587		2.954
Anatase			
HF-TVAE* ¹⁴⁵	3.781 (-0.03)		9.735 (2.45)
ReaxFF	3.837 (1.45)		9.639 (1.44)
Exp. ¹⁴⁵	3.782		9.502
Brookite			
B3LYP-6-31G ¹³⁶	9.276 (1.00)	5.502 (1.00)	5.197 (1.01)
ReaxFF	9.252 (0.74)	5.487 (0.73)	5.183 (0.74)
Exp. ¹⁵⁶	9.184	5.447	5.145

3.3.2. TiO₂ clusters

To ensure that the developed force field is able to describe the influence of structure and size on the potential energy per TiO₂ unit, 30 TiO₂ cluster structures of the type (TiO₂)_n with n equal to 1-16 were added to the training set for the force field fitting. Figure 6 shows the comparison of the results obtained with ReaxFF, DFT and the Monti and Kim force fields for the potential energy difference of 29 different (TiO₂)_n cluster configurations divided by n, the number of TiO₂ units, with the (TiO₂)₁₆ potential energy divided by 16 taken as reference point. The different structures are depicted in Figure 7. A reasonable agreement with the QM data^{142,147-149} is found for the smaller cluster sizes up to 4, and the error converges for the larger clusters. The data produced by Kim's force field is in very good agreement with the QM data, while Monti's force field gives results for which the agreement is in between the currently developed force field and the one from Kim. The discrepancy between ReaxFF and QM decreases with increasing cluster size. The larger discrepancies with ReaxFF between the relative stabilities for the smaller cluster sizes up to (TiO₂)₄ are caused by the oxygen atoms which are only bonded to one titanium atom; this type of oxygen atom is not found in the larger cluster sizes. The Ti-O bond lengths for this type of oxygen atom are found to be ~13.5% too short compared to the QM data, while the bond lengths for this type of oxygen are found to be too short; the other Ti-O bond lengths are almost identical in ReaxFF compared to DFT.

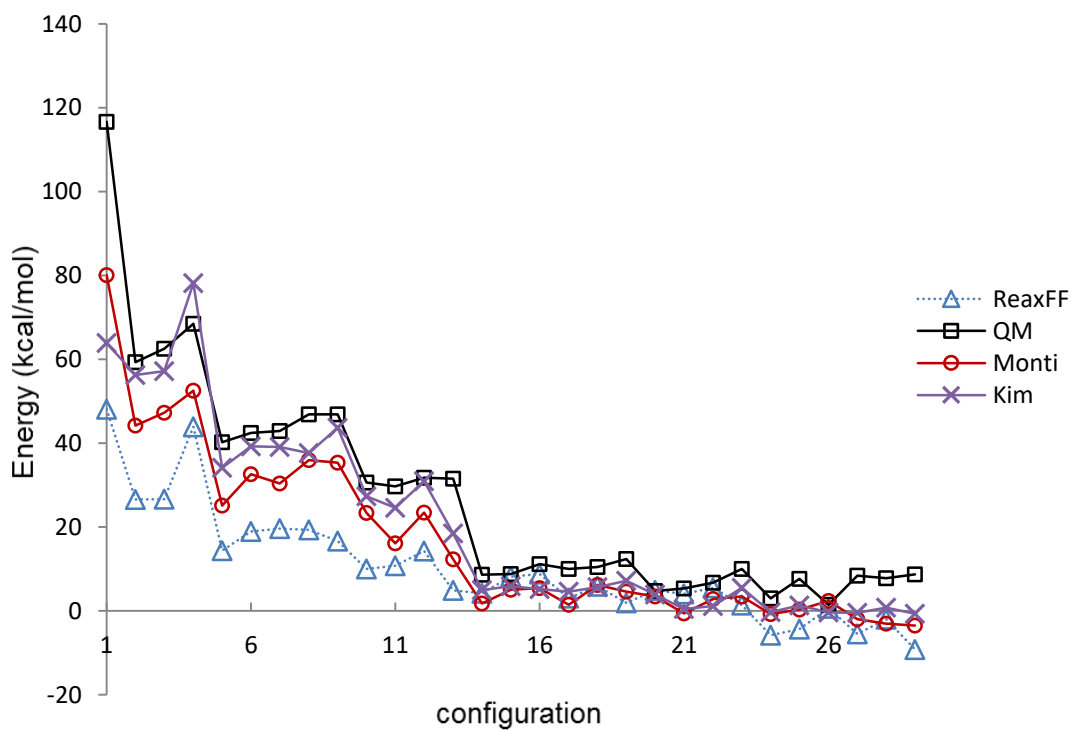
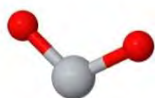
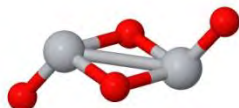
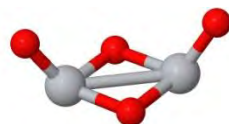
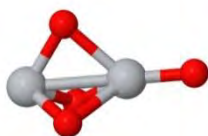
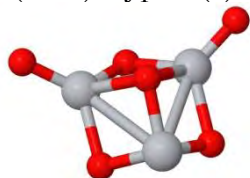
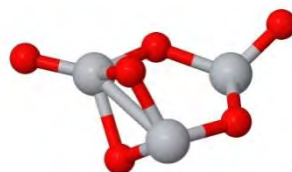
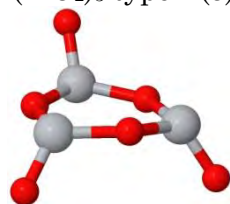
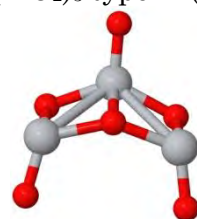
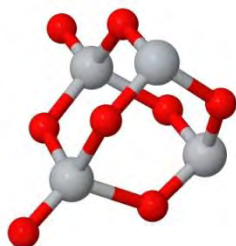
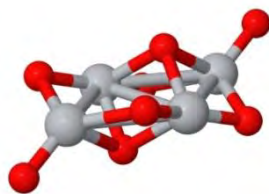
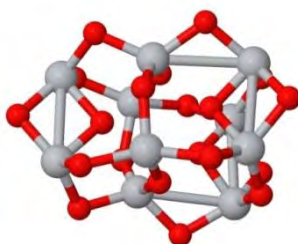
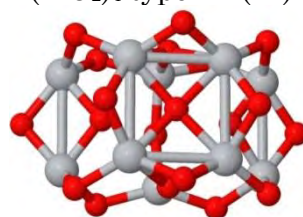
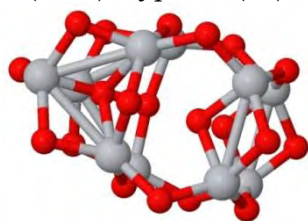
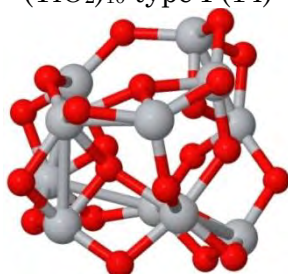
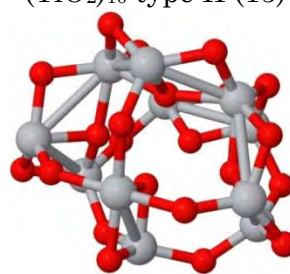


Figure 6: Potential energy difference divided by the the number of TiO_2 units between the different configurations (see Figure 7) and the reference structure (i.e., $(\text{TiO}_2)_{16}$)^{142,147–149}

TiO₂ (1)(TiO₂)₂ type I (2)(TiO₂)₂ type II (3)(TiO₂)₂ type III (4)(TiO₂)₃ type I (5)(TiO₂)₃ type II (6)(TiO₂)₃ type III (7)(TiO₂)₃ type IV (8)(TiO₂)₃ type V (9)(TiO₂)₄ type I (10)(TiO₂)₄ type II (11)(TiO₂)₄ type III (12)(TiO₂)₄ type IV (13)(TiO₂)₁₀ type I (14)(TiO₂)₁₀ type II (15)(TiO₂)₁₀ type III (16)(TiO₂)₁₁ type I (17)(TiO₂)₁₁ type II (18)

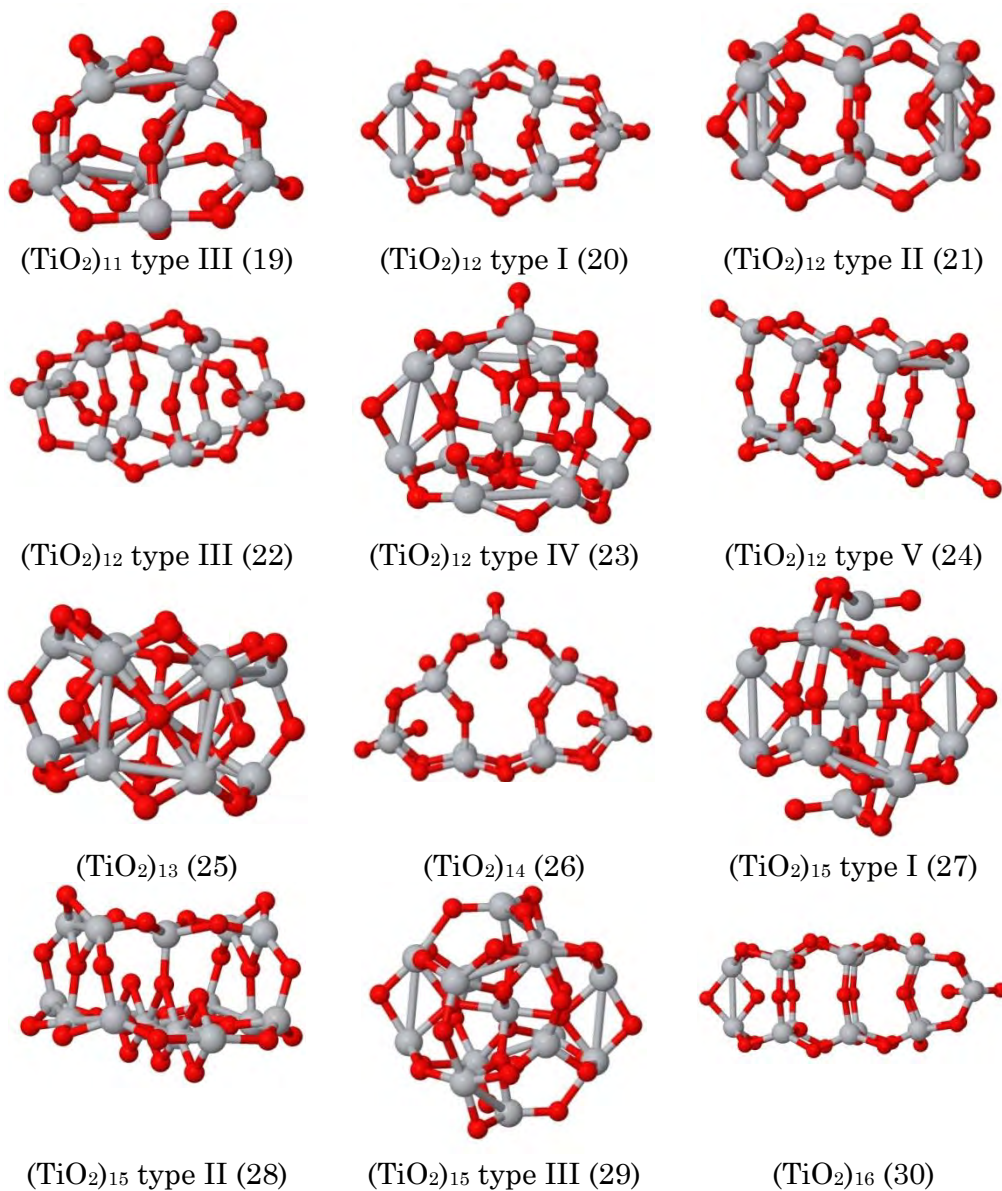


Figure 7: The DFT optimized configurations of the TiO₂ clusters
(Ti = gray, O = red)

3.3.3. Point defects

Point defects play an important role in the surface chemistry of metal oxides like titanium dioxide. They can act as centers where molecules can adsorb. For instance, molecular oxygen will not adsorb on a stoichiometric anatase (101) surface, but it will adsorb when an oxygen vacancy is present in the subsurface.¹⁵² An important feature of anatase (101) is the distribution of oxygen vacancies in the surface and the subsurface, as this distribution determines the catalytic superiority of anatase compared to rutile.¹⁵⁰ There are more subsurface vacancies present in anatase than surface vacancies because of the lower formation energy and thus higher stability and the low (around 1 eV) diffusion barriers. The opposite trend is found for rutile.^{150,151} Because of this clear importance of the point defects on the surface chemistry of anatase, data for these defects were added to the training set as well. These data consist of oxygen vacancy formation energies, diffusion barriers for oxygen vacancies, interstitial titanium formation energies and adsorption energies of molecular oxygen at a reduced anatase (101) surface.

3.3.3.1. Interstitial titanium

In Figure 8 the formation energies of interstitial titanium are shown, calculated with the new force field, with DFT¹⁵⁰ and with the force fields of Monti and Kim. T1-T6 represent the different locations where the interstitial titanium atom can occur in an anatase (101) surface composed of 72 atoms, corresponding to 3 atomic layers. The positions of T1-T6 are shown in Figure 9. The nomenclature is the same as in reference 150. T2 is not shown because this was found not to be stable during the minimization, which is consistent with the diffusion energy barrier from T2 to T1 to be 0 kcal/mol as calculated with DFT¹⁵⁰. ReaxFF underestimates all formation energies compared to the DFT result,

especially for T1, for which the formation energy calculated with ReaxFF lies 9.5% below the value calculated with DFT¹⁵⁰. This means that ReaxFF overestimates the significance of T1 in comparison with T3 and T4. More importantly, however, ReaxFF correctly predicts the T5 and T6 to be the most stable ones. This is specifically important for the defect distribution, since this distribution depends on the difference in formation energies between the different sites. The force fields of Kim and of Monti yield the same trends as found with the currently developed force field, but the formation energies as found with these force fields are about an order of magnitude off, such that the formation of interstitial titanium defects will occur too easily and therefore the concentration of these defects would be too high. The formation energies of interstitial titanium as calculated with DFT and ReaxFF are approximately twice the values of the formation energies of the oxygen vacancies, so they are of less importance for the surface chemistry. The higher formation energies of interstitial titanium compared to oxygen vacancies directly correlate with their lower stability, which might cause a higher reactivity of the surface. In a theoretical study¹⁵⁷ concerning the influence of subsurface defects on the water adsorption and dissociation of water on an anatase (101) stoichiometric and reduced surface, it is found that both interstitial titanium and oxygen vacancies increase the adsorption energy of adsorbed water in the vicinity of these defects. The energy barrier for the dissociation of water is decreased from 12.91 kcal/mol on the stoichiometric surface to 5.53 kcal/mol and 6.00 kcal/mol, for an anatase (101) surface with an interstitial titanium and a surface with an oxygen vacancy present, respectively. At one adsorption site in the case of an interstitial titanium present, the dissociation of water is found to be exothermic. In contrast, in all other cases the dissociation is found to be endothermic. Another theoretical study¹⁵⁸, which is focused on the adsorption and dissociation of CO₂ on an anatase (101) stoichiometric and reduced surface, indicates that

interstitial titanium and oxygen vacancies increase the adsorption energies of CO_2 in comparison with the stoichiometric anatase (101) surface. For the most stable CO_2 adsorption configurations the energy barriers of dissociation are 20.8 kcal/mol and 17.5 kcal/mol for surfaces with an oxygen vacancy and interstitial titanium present, respectively. Interstitial titanium seems to increase the adsorption energies and decrease the energy barriers for dissociation of water and CO_2 more than oxygen vacancies, but these differences are within a reasonable level. They do play a role, however, for the mass transport occurring between the surface and the bulk when the structure is annealed,¹¹⁹ due to their particularly low diffusion barriers (less than 0.5 eV).¹⁵⁰

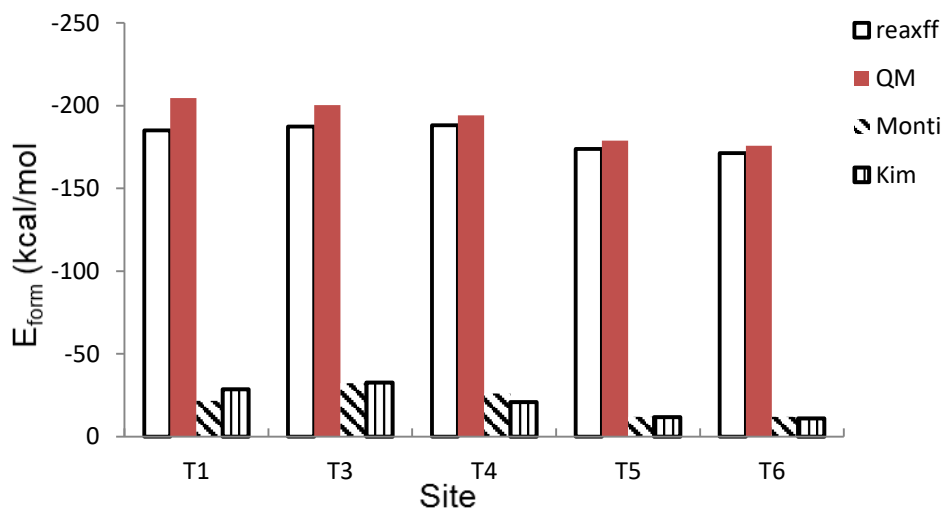


Figure 8: Formation energies calculated with ReaxFF, DFT¹⁵⁰, Monti and Kim for the different interstitial titanium sites located in the anatase (101) surface (see Figure 9)

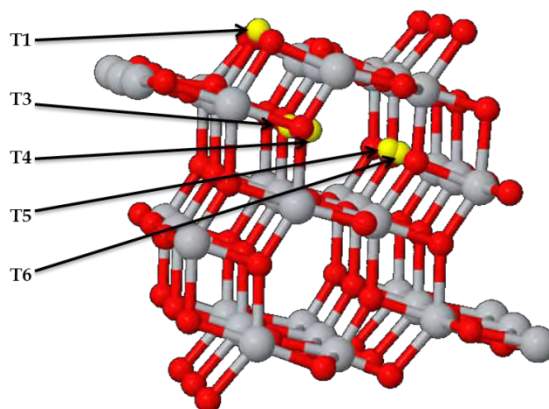


Figure 9: Different positions for interstitial titanium in the anatase (101) surface. (Ti = gray, $\text{Ti}_{\text{interstitial}}$ = yellow, O = red)

The diffusion pathways of the interstitial titanium¹⁵⁰ were not used during the fitting of the current force field. The comparison between the values calculated with ReaxFF and with DFT¹⁵⁰ are given in Table 3. The errors on the ReaxFF values are large, so it is advisable to not use the currently developed force field for reactions where the diffusion of the interstitial titanium might be important. In the case of migration from site T3 to T4 and T5 to T6 the discrepancies are reasonable so that the diffusion still might occur at room temperature. For reactions where the diffusion is not part of the reaction mechanism the force field will be able to reproduce the mechanism as long as the interstitial titanium defect was present at the desired site.

Table 3: Diffusion barriers for interstitial in anatase (101) as calculated with ReaxFF and DFT¹⁵⁰.

Pathway	Direct pathway		Reverse pathway	
	$E_{a, \text{ReaxFF}}$ (kcal/mol)	$E_{a, \text{QM}}$ (kcal/mol)	$E_{a, \text{ReaxFF}}$ (kcal/mol)	$E_{a, \text{QM}}$ (kcal/mol)
T1-T3	76.10	8.99	73.56	13.14
T3-T4	8.76	3.23	8.07	9.45
T4-T5	44.28	10.61	61.11	25.83
T5-T6	8.99	0.92	8.07	4.38

3.3.3.2. Oxygen vacancies

In Figure 10 the formation energies for oxygen vacancies in three different anatase (101) surfaces are shown, calculated with the new force field, with DFT^{150,151} and with the force fields of Monti and Kim. The structure containing 216 atoms (corresponding to the stoichiometric structure) consists of 6 atomic layers, while the structures containing 72 and 108 atoms consist of 3 atomic layers. These different structures are all used in the training set to account for the increasing stability of subsurface vacancies relative to the surface vacancies for increasing slab thickness¹⁵⁰. This is caused by the fact that the surface is more rigid than the subsurface, as indicated by the analysis of the structural relaxations around the vacancy sites, which shows larger atomic displacements in the subsurface region than at the surface.¹⁵⁰ If the structure size increases there will be more possibilities to relax if a vacancy is formed in the subsurface than when one is formed at the surface. Nomenclature can be found on Figure 11 and is the same as in reference ¹⁵⁰. V_{O1} , V_{O2} and V_{O3} are surface oxygen vacancies of which V_{O1} has the lowest formation energy and therefore will be the most abundant. V_{O4} and V_{O5} are subsurface vacancies which have a considerably lower formation energy, $\Delta E \approx 11.5$ kcal/mol, than that of V_{O1} , so they will play a more prominent role in the surface

chemistry of anatase. The relative probability of formation of a surface vacancy V_0 with respect to subsurface sites is $\sim 4 \times 10^{-9}$ and $\sim 1.6 \times 10^{-3}$ at $T = 300$ K and 900 K, respectively. The QM values for V_{O4} and V_{O5} are almost identical, i.e., 85.09 and 84.17 kcal/mol, respectively, and they are almost identical to the bulk V_0 formation energy, which is 85.09 kcal/mol (as calculated with only the Γ -point), so V_{O4} and V_{O5} can be considered “bulk-like”^{150,151}.

The values and the trends for the formation energies of V_0 are reproduced well for such an extensive data set that describes different influences on the formation energies. The root mean square error on the energy is 4.08 kcal/mol. A few rather large discrepancies, up to 9.4% for the least stable surface vacancies, V_{O2} , occur, while good agreement for V_{O1} and V_{O4} is obtained for which the root mean square error is 1.98 kcal/mol and 2.50 kcal/mol, respectively. The QM bulk oxygen vacancy formation energy is 101.70 kcal/mol ($2 \times 2 \times 2$ k-point mesh)¹⁵⁰ and 85.09 kcal/mol (Γ -point)¹⁵⁰, in comparison the ReaxFF value of 95.89 kcal/mol, which is close to the average between both QM values. For Kims and Monti’s force field the V_{O1} formation energy is lower than that of the subsurface vacancy sites. This is opposite to the trend shown by the DFT data. This fact, together with the fact that the errors for the oxygen vacancy formation energies of the two force fields are about one order of magnitude off, makes that these force fields are not capable of accurately describing the differences between the different oxygen vacancies. Because of these large discrepancies in absolute numbers and trends, the oxygen vacancy diffusion barriers were not calculated for these two force fields.

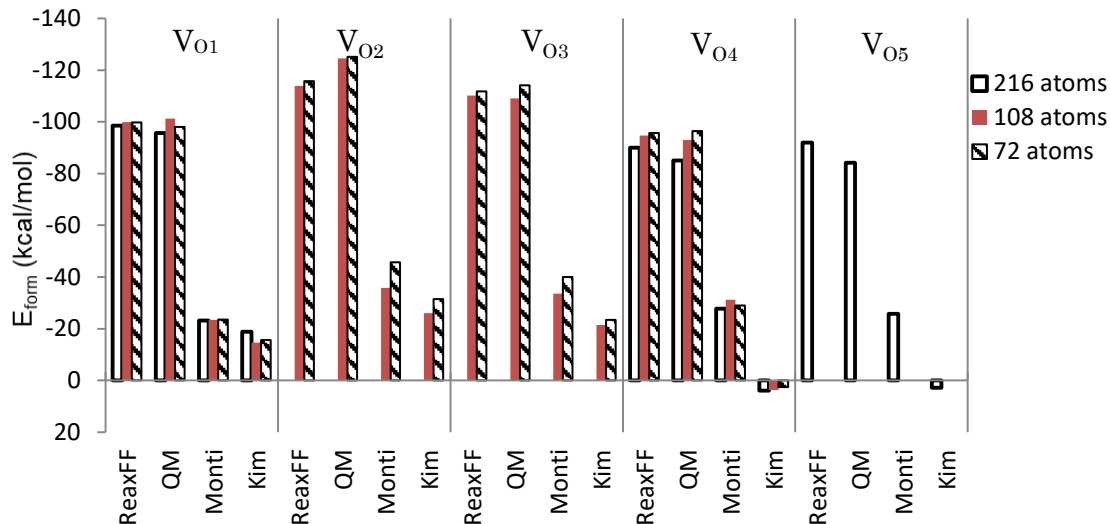


Figure 10: Oxygen vacancy formation energies calculated with ReaxFF, DFT^{150,151}, Monti and Kim for the different anatase (101) surfaces (216 atoms (6 atom layers), 108 and 72 atoms (3 atom layers))

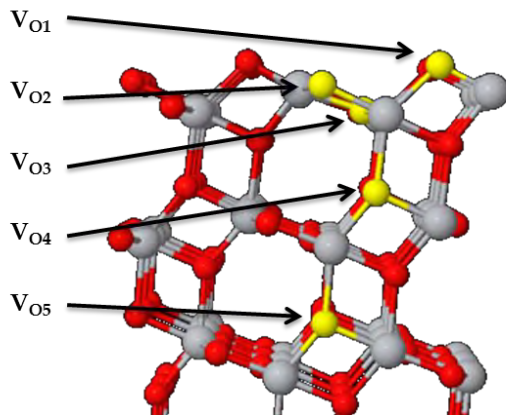


Figure 11: Different oxygen vacancy sites in anatase (101)

The diffusion barriers of the oxygen vacancies in anatase (101), as calculated with ReaxFF and with DFT^{150,151}, can be found in Table 4. The barriers were calculated using Nudged Elastic Band¹⁵⁹. These are the diffusion barriers for the anatase (101) surface consisting of 72 atoms and

3 atomic layers. Note that for the $V_{O1} \rightarrow V_{O4}$ pathway the diffusion barrier for the reverse pathway will be higher for a structure with for example 6 atomic layers. This is caused by the stabilisation of V_{O4} relative to V_{O1} because of the increasing possibilities to relax the perturbation. Only the unique and the lowest pathways were added to the training set. For example, the lowest energy pathway $V_{O1} \rightarrow V_{O2}$ consists of a combination of $V_{O1} \rightarrow V_{O3}$ and $V_{O3} \rightarrow V_{O2}$.

The barriers and the trends in the barriers are described quite well by our force field. Especially the most important pathway, $V_{O1} \rightarrow V_{O4}$, is described very well with a maximum error of 0.5 kcal/mol. Only the diffusion between V_{O2} and V_{O3} shows larger discrepancies which is caused by the larger error in the relative stability of V_{O2} . This, however, is of less importance because especially the distribution between the surface and subsurface vacancies will influence the surface chemistry and reactivity. The pathway of $V_{O1} \rightarrow V_{O4}$ is shown in Figure 12. This pathway consists of two atoms moving simultaneously. Vacancy diffusion on the surface is largely inhibited, particularly the $V_{O1} \rightarrow V_{O1'}$ diffusion along [010], which has a barrier of 61.12 kcal/mol as calculated with DFT¹⁵⁰. The $V_{O1} \rightarrow V_{O1'}$ diffusion pathway is shown in Figure 13.

Table 4: Diffusion barriers for oxygen vacancies in anatase (101) as calculated with ReaxFF and DFT^{150,151}.

Pathway	Direct pathway		Reverse pathway		Diffusion direction
	$E_{a, \text{ReaxFF}}$ (kcal/mol)	$E_{a, \text{QM}}$ (kcal/mol)	$E_{a, \text{ReaxFF}}$ (kcal/mol)	$E_{a, \text{QM}}$ (kcal/mol)	
$V_{O1} \rightarrow V_{O1'}$	79.6	61.12	79.6	61.12	[010]
$V_{O1} \rightarrow V_{O3}$	34.7	30.90	22.9	17.99	[66 $\bar{1}$]
$V_{O1} \rightarrow V_{O4}$	17.2	17.07	21.4	21.91	[301]+[30 $\bar{1}$]
$V_{O2} \rightarrow V_{O3}$	7.2	6.92	11.2	17.99	[031]
$V_{O3} \rightarrow V_{O4}$	20.2	17.99	36.3	35.98	[661]

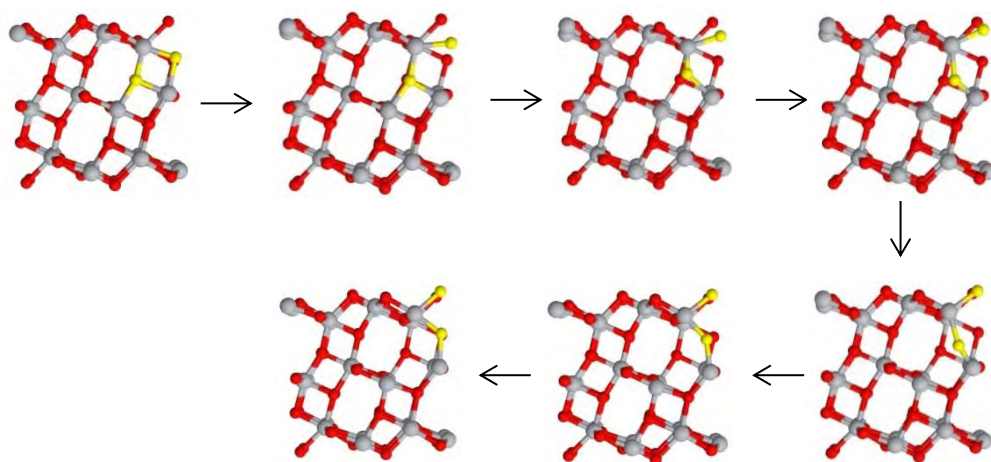


Figure 12: The ReaxFF optimized $V_{01} \rightarrow V_{04}$ pathway (Ti = gray, O = red, Moving O = yellow).

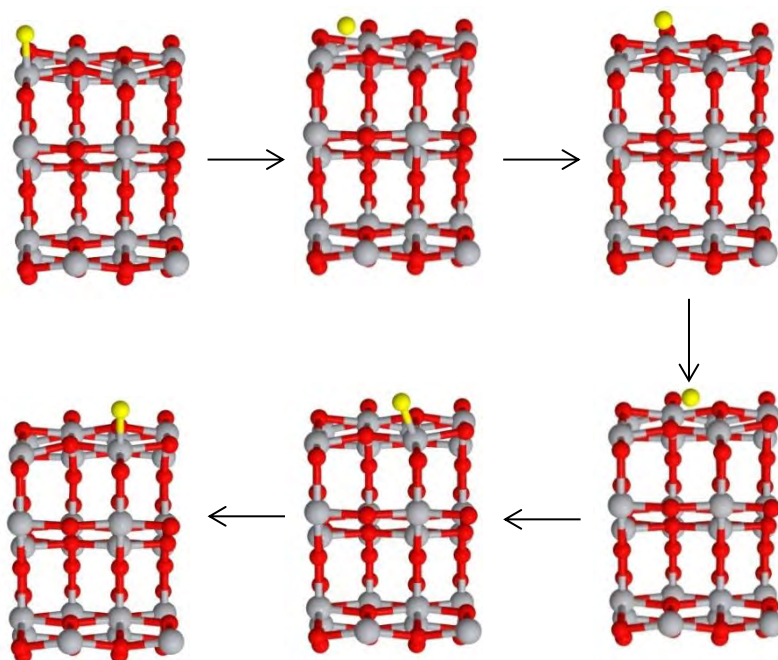


Figure 13: The ReaxFF optimized $V_{01} \rightarrow V_{0r}$ pathway (Ti = gray, O = red, Moving O = yellow).

3.3.4. Oxygen adsorption

Molecular oxygen (O_2) plays an important role in many of the TiO_2 -based catalytic processes. It is important to gather atomic scale information on the interaction of oxygen with reduced anatase surfaces to gain a better fundamental insight in which factors play an important role in the catalytic processes. The adsorption energies of two O_2 molecules on anatase (101) containing a V_{O4} -vacancy have been added to the training set.¹⁵² The behaviour of molecular adsorption is different for one O_2 molecule and for two O_2 molecules adsorbed at the surface. When only one O_2 molecule is adsorbed, it will behave as a peroxide, O_2^{2-} , whereas the adsorbed molecules behave as a superoxide, O_2^- , when two O_2 are adsorbed.¹⁵² Since ReaxFF is a classical force field, it cannot describe both situations, as both structures have a comparable geometry but a different electronic structure. However, the peroxide state will only play a role at very low coverages. Moreover, the superoxide state is also the state found in experimental studies^{160,161}. We therefore chose to add the superoxide data and not the peroxide data. It is also found theoretically that it is more favourable by 3.23 kcal/mol to have two O_2 molecules adsorbed than one O_2 adsorbed and one O_2 in the gas phase.¹⁵² This also indicates that the adsorbed O_2 molecule is more stable in its superoxide state than in its peroxide state. The different adsorption sites on an anatase (101) surface consisting of 3 atomic layers and 108 atoms (corresponding to the stoichiometric structure) are indicated in Figure 14 and correspond to the same sites as in reference 152. The ReaxFF, the DFT¹⁵², Monti and Kim data are represented in Figure 15. The site combination 1+5 is the most stable one in the ReaxFF and DFT calculations, due to the fact that in this combination the O_2 molecules are maximally separated and have one O_2 at the closest adsorption site relative to the V_{O4} oxygen vacancy (site 5). The stability of the adsorbed state increases when a molecule is adsorbed closer

to the defect. This trend is well reproduced by the force field. It should be noted, however, that the differences in adsorption energies between the most stable site combinations and the least stable are somewhat larger in ReaxFF than in DFT calculations¹⁵². This will cause a shift in distribution of the adsorbed states at thermodynamic equilibrium on the defected surface. At thermodynamic equilibrium at 300 K the relative probability of the adsorption configuration 1+5 is ~100% and ~96%, for ReaxFF and DFT, respectively. Since in MD we consider small surfaces with a high concentration of vacancies, the most stable configuration will have the main influence on the chemistry. Thermodynamic equilibrium is not reached during the “impact” and adsorption of O₂ on the surface, and therefore also the less stable configurations will be sampled and be accessible for further reactions. Because of the above reasons we consider that the currently developed force field will give a more than adequate description of reactions occurring at the reduced anatase surface.

It is clear that the force field of Monti and Kim cannot describe the trend and the absolute values. They both underestimate the adsorption energies, and the adsorption site combination of 1+2 is the most stable for Monti and 2+6 for Kim. In DFT both combinations are preceded by the combinations 1+5, 2+5 and 4+5. This will influence the adsorption rate and distribution in a significant manner, and therefore the force fields of Kim and Monti are not capable of describing the processes that will occur during the adsorption of O₂ on the reduced anatase surface.

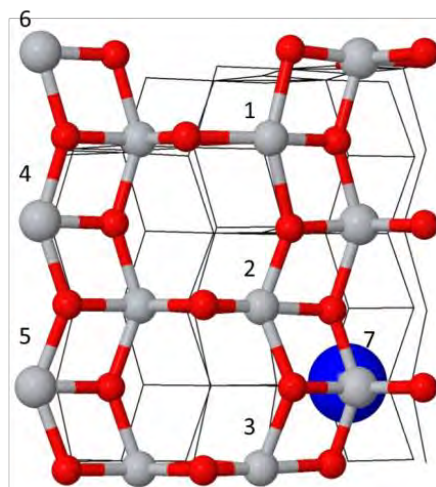


Figure 14: Different adsorption sites of molecular oxygen on a reduced anatase (101) surface containing a V_{O4} vacancy. (Ti = gray, O = red, V_{O4} vacancy = blue ball)

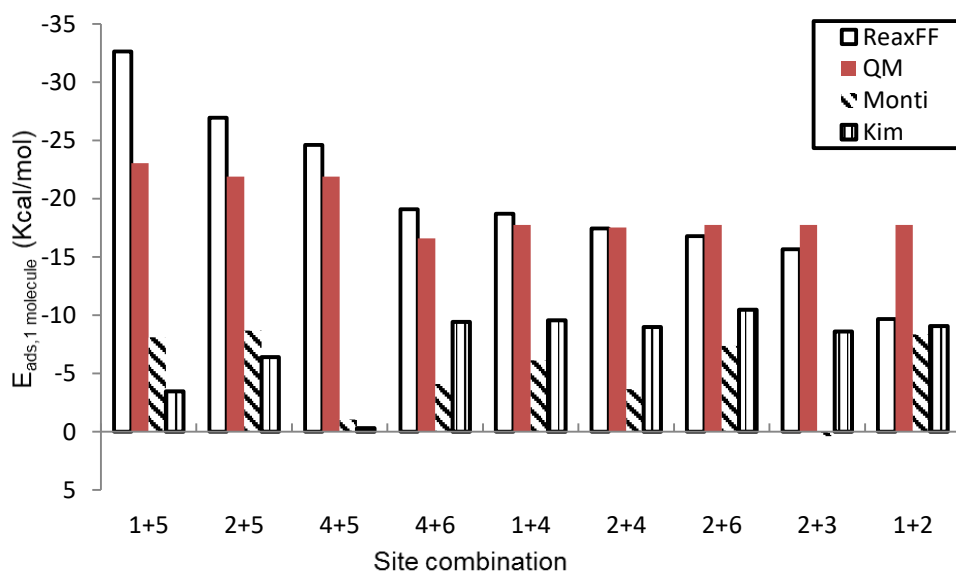


Figure 15: Oxygen adsorption energies per O_2 molecule in various configurations on a reduced anatase (101) surface.¹⁵²

3.3.5. Application to oxygen vacancy migration

We also applied the developed force field to study the influence of pressure and concentration on the diffusion of the oxygen vacancies on anatase (101) at the surface, $V_{O1} \rightarrow V_{O1'}$, and from the surface to the subsurface, $V_{O1} \rightarrow V_{O4}$. We did not find a significant vacancy concentration dependence on the diffusion barriers for $V_{O1} \rightarrow V_{O1'}$ and $V_{O1} \rightarrow V_{O4}$. A significant influence, on the other hand, was found when the structures were compressed or expanded.

The barrier for diffusion of a V_{O1} vacancy to another $V_{O1'}$ site along [010] at the surface does not decrease when expanding or compressing the structure, as can be seen in Figure 16. When the volume is increased the diffusion will be inhibited even stronger. This is caused by the increasing distance between the titanium atoms from the different V_{O1} sites, such that the bonding interaction at the transition state will be lower than in the unexpanded structure and therefore destabilizes the transition state. When compressing the structure, the diffusion barrier remains approximately the same up to a compression of 12%. Only after this point the barrier starts to increase.

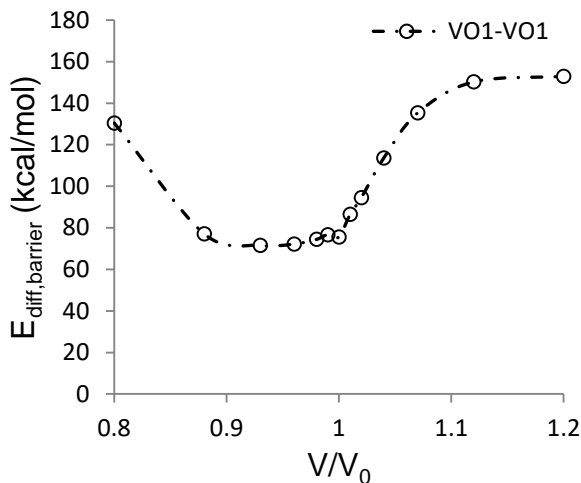


Figure 16: Diffusion energy barriers for the diffusion of a V_{O1} vacancy along the [010] direction on anatase (101) for compressing and expanding the surface.

Figure 17 shows the influence of compressing and expanding the structure on the diffusion barrier of oxygen vacancies from the surface to the subsurface in anatase (101). In this diffusion mechanism we can consider two barriers: one from the direct pathway and one from the reverse pathway. The two pathways correspond to surface-to-subsurface and subsurface-to-surface, respectively. The difference in height of the two barriers is directly related to the difference in stability. When the surface is expanded with about 10%, the barriers are approximately equal, and therefore also their stabilities are approximately equal. This indicates that in equilibrium there will be 50% V_{O1} vacancies and 50% V_{O4} vacancies. However, when compressing the structure, the barrier for the subsurface-to-surface pathway is much lower than for the surface-to-subsurface path. Since the barrier from the surface to the subsurface is quite low, equilibrium will be reached rather fast and most vacancies will occur in the subsurface. This will have a large influence on the surface reactivity, because of the different behaviour of subsurface sites compared to the

surface sites. When perturbing the structure more than 10-12% expansion or compression, the diffusion will be mainly inhibited.

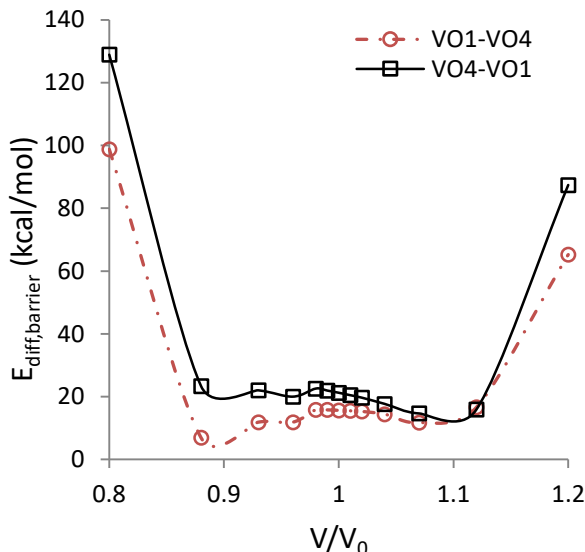


Figure 17: Diffusion energy barriers for the diffusion of a V_{O1} vacancy to a V_{O4} site and the reverse pathway in anatase (101) for compressing and expanding the surface.

Finally, we also studied the possibility of vacancy diffusion in the subsurface, since the diffusion at the surface is mainly inhibited (diffusion energy barrier of 61.12 kcal/mol for $V_{O1} \rightarrow V_{O1}$)^{150,151}. The minimal energy pathway for the diffusion between two V_{O4} subsurface sites is shown in Figure 18. The corresponding energy barrier is 27.7 kcal/mol, which is significantly lower than for the surface diffusion, $V_{O1} \rightarrow V_{O1}$ along [010]. The calculated barrier of 27.7 kcal/mol is in the range ~ 25 kcal/mol – 41 kcal/mol, as estimated for the lateral diffusion energies by Scheiber et al.¹⁶². It is clear that the lateral redistribution on the surface and in the subsurface will be dominated by diffusion in the subsurface, since also the barriers for diffusion from the surface to the subsurface and vice versa, 17.07 kcal/mol and 21.91 kcal/mol respectively^{150,151}, are significantly lower than for diffusion on the surface. This is in agreement with experimental

observations of a reduced anatase (101) surface, where surface defects disappear at one position and appear at another position at the same or neighboring rows¹⁶².

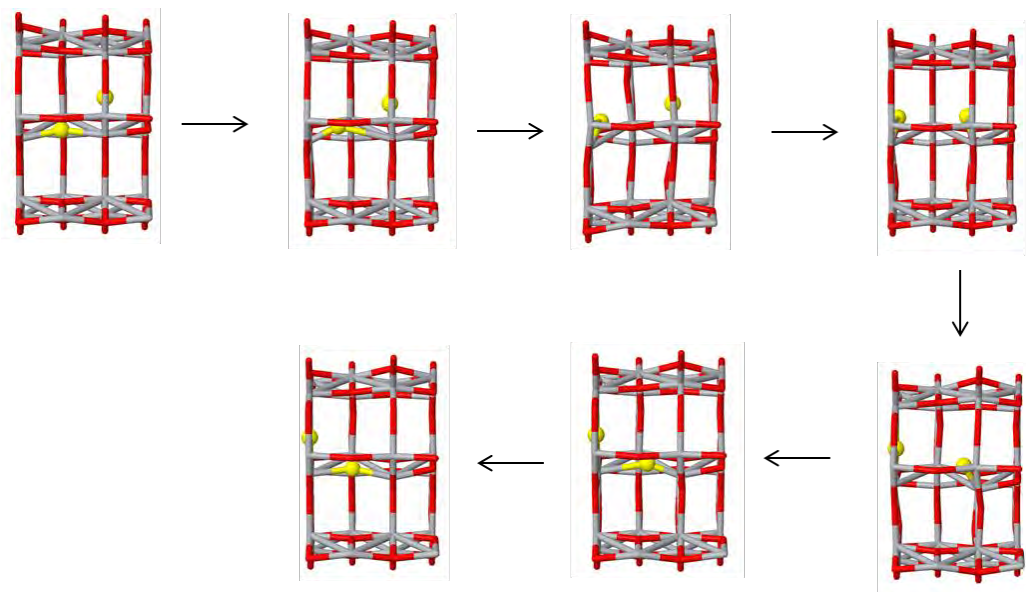


Figure 18: The ReaxFF optimized $V_{O4} \rightarrow V_{O4'}$ pathway (Ti = gray, O = red, Moving O = yellow)

3.4. Conclusions

We developed a ReaxFF reactive force field for studying the influence of intrinsic point defects on the chemistry of TiO₂ condensed-phases. The ReaxFF parameters were fitted against DFT and experimental data to reproduce the equations-of-state, TiO₂-cluster stabilities, defect formation energies, defect diffusion barriers and oxygen adsorption energies. All important data are reproduced in a satisfactory manner. In comparison with two other recently developed ReaxFF force fields for TiO₂, the current force field represents a significant improvement in the description of the chemistry related to intrinsic point defects. We should, however, emphasize that these two other force fields were not developed for this purpose and have already been used successfully in other studies relating to different topics. We have applied the developed force field to study the influence of concentration of oxygen vacancies and pressure on the diffusion energy barriers from the surface to the subsurface and on the surface and relative stabilities of the defects on an anatase (101) surface. No significant influence was found for varying the concentration. Compressing or expanding the structure, however, causes a significant redistribution of the surface and subsurface vacancy sites. Also the subsurface oxygen vacancy diffusion barrier was calculated and is found to be consistent with experimental data. The developed force field is able to describe a wide range of effects on the chemistry of the anatase titanium dioxide.

**Chapter 4 Adsorption
of C and CH_x radicals
on anatase (001) and
the influence of
oxygen vacancies**

4.1. Introduction

Considering all greenhouse gases, CO₂ and CH₄ contribute the most to the man-made greenhouse effect.³¹ The global warming potential of methane is even 21 times higher than that of CO₂.¹⁶³ Apart from being a greenhouse gas, CH₄ is also the main component (70-90%) of most natural gas resources.¹⁶⁴⁻¹⁶⁵ Natural gas can be used as fuel for heating and electrical power generation. However, this requires conversion of CH₄ to the greenhouse gas CO₂. Alternatively, methane may also be utilized for the production of valuable chemicals, such as methanol, formaldehyde, higher hydrocarbons, hydrogen gas, and syngas (CO/H₂).

For the conversion of methane to valuable chemicals there are two different synthesis routes, the indirect and the direct route. The indirect conversion of methane is a two-step process, in which methane is first converted to syngas, to be subsequently used for methanol synthesis or Fischer-Tropsch synthesis. Syngas can be produced by steam reforming, dry reforming or partial oxidation of methane.¹⁶⁶ These processes, however, require a high energy input and typically only give low overall yields.¹⁶⁷ Direct (thermal) conversion of methane does not require the energy intensive syngas synthesis. However, direct methane conversion is costly and technologically challenging, and only achieves the same low overall yields.¹⁶⁶ It would thus be interesting to find non-conventional synthesis routes. Plasma technology has already been used for the conversion of methane in useful chemicals.^{28,168-171} The main advantage of non-thermal plasmas is that the gas itself remains at room temperature, while being activated by electron impact excitation, ionization and dissociation reactions. Plasma processes, however, are mostly non-selective. Catalytic processes, on the other hand, can be very selective but often require a certain gas composition and high temperatures. Plasma-catalysis combines

the advantages of the high reactivity of plasmas and the high selectivity of catalysis¹³, by integrating the catalyst into the plasma. It is suggested that the catalyst can increase the retention time of the reacting species, thereby enhancing the conversion efficiency and selectivity, as well as the energy efficiency. Also the lifetime of short-lived active species can be extended by adsorption at the catalyst surface. To gain a more fundamental insight in the interaction of the plasma with the catalyst surface, we studied the adsorption of reactive CH_x radicals ($x = 0 - 3$), formed in the plasma^{170,171}, on an often-used catalyst, the anatase (001) titanium dioxide surface. We have chosen anatase as model system as it is the catalytically most active polymorph of titanium dioxide¹⁷² and is widely used in experimental plasma-catalysis studies¹⁷³. In thermal catalytic dry reforming of methane TiO_2 is not used as catalyst, but rather as support for catalytic metal particles and is reported to increase the coking-resistance of the catalyst.¹⁷⁴⁻¹⁷⁸ However, it is reported that the presence of TiO_2 is important for the catalytic activity of the catalyst, e.g. neither pure Pt nor pure TiO_2 shows appreciable conversions for dry reforming of methane.¹⁷⁴ The activity of the Pt/ TiO_2 catalyst is assigned to the activation and conversion of CO_2 on the TiO_2 support by adsorption on a Lewis base center, while the methane is activated on the metal surface¹⁷⁹ forming CH_x and H species. The combination of a plasma with TiO_2 allows the activation of methane in the plasma discharge, generating CH_x and H radicals which will adsorb and react on the TiO_2 surface.^{170,171} The results presented in this dissertation give insight in the reaction mechanisms of plasma-catalysis on TiO_2 . Furthermore, the results form an initial step for a study of the dry reforming of methane on a TiO_2 supported metal catalyst.

It is well known that intrinsic point defects, and specifically oxygen vacancies, affect the physical and chemical properties of titanium dioxide. Several studies already investigated the influence of defects in titanium dioxide anatase surfaces. Wang et al.¹⁸⁰ studied the adsorption of H₂O and O₂ on a (1x4) reconstructed anatase (001) surface and the influence of point defects on the adsorption using microscopic and spectroscopic techniques in combination with DFT. They found that on a stoichiometric surface H₂O has an adsorption energy of 10.38 kcal/mol and O₂ does not adsorb, while near a Ti³⁺ defect H₂O and O₂ molecules adsorb with a calculated adsorption energy of 22.14 kcal/mol and 41.51 kcal/mol, respectively. Aschauer et al.¹⁵⁷ studied H₂O adsorption on anatase (101) and the influence of subsurface defects on the adsorption using both scanning tunnelling microscopy (STM) experiments and DFT calculations. They found that H₂O preferentially adsorbs in the vicinity of subsurface defects. Both the STM and DFT results suggest an enhanced binding due to the defects. The adsorption of O₂ was also studied on the anatase (101) surface as well as the effect of subsurface defects on this adsorption. They found no O₂ adsorption on the stoichiometric surface. On the reduced surface with a subsurface oxygen vacancy they found a strong adsorption in the vicinity of the defect. Also studies of the adsorption of CO₂ on anatase (101) and rutile (110) surfaces have shown that surface defects significantly modify the adsorption of CO₂ on the reduced surface compared to the stoichiometric surface.^{158,181} The defect sites act as initiators for adsorption of molecules in heterogeneous catalysis. The role and properties of the defect are determined by its location on the reduced surface. It is therefore important to know the stability of the different oxygen vacancies in the anatase surface. Golberg-Oster et al.¹⁸² have shown that CH₃ radicals, and therefore probably also other alkyl radicals, react with the surface of TiO₂. They form long-lived transients with methyl σ -bonded to the surface of TiO₂ nanoparticles. The authors derived that the nanoparticle-CH₃ bond

strength should be greater than 16.7 kcal/mol¹⁸³, which is consistent with what we find in this study.

Since strong bonding is found for methyl radicals on TiO₂ nanoparticles¹⁸³ and since defects strongly influence the adsorption of species on TiO₂ surfaces¹⁸⁰, it is interesting to study how methyl radicals and other methane derived radicals adsorb on the perfect and defective anatase (001) surface. In total we performed 155 different calculations to determine the stability of different oxygen vacancies in the anatase (001) surface and the effects of these vacancies on the adsorption of CH_x radicals (x = 0 – 3) to gain a better insight in the adsorption of CH_x radicals (x = 0 – 3), relevant for plasma-catalysis^{170,171,184,185} on anatase and the influence of the reduction status of the surface on the adsorption.

4.2. Computational details

All calculations were carried out at the DFT-GGA level using the Vienna ab initio simulation package (VASP).^{186,187} For the treatment of the exchange and correlation, the Perdew-Burke-Ernzerhof (PBE) functional¹¹³ was used, using plane wave basis sets and the projector-augmented wave method¹⁸⁸ as implemented in VASP. We have not included zero-point energy corrections as these are found to not have a significant influence on the adsorption energies of CH_x species.¹⁸⁹ We used a (2x2) supercell containing 48 atoms for the clean stoichiometric anatase (001) surface and four TiO₂-layers. The bottom layer is kept fixed at the bulk positions. A vacuum layer of ~16 Å between the surface and the adjacent layers is used to prevent the influence of neighbouring slabs on the adsorption. Sampling of the Brillouin zone was performed using the Monkhorst-Pack scheme¹⁹⁰ with 6x6x1 k-points for the periodic structures and only the gamma-point for molecules. An energy cutoff for the plane wave basis set of 500 eV was used for the investigation of the oxygen vacancy formation in anatase (001)

and a cutoff of 440 eV for the study of the CH_x radical ($x = 0 - 3$) adsorption on the stoichiometric and reduced anatase (001) surface. The geometry optimization was stopped when the residual forces were below $0.03 \text{ eV} \cdot \text{\AA}^{-1}$. We performed spin-restricted calculations for the investigation of the oxygen vacancy formation in anatase (001) and spin-unrestricted calculations for the study of the CH_x radical ($x = 0 - 3$) adsorption on the stoichiometric and reduced anatase (001) surface, respectively.

The oxygen vacancy formation energies are calculated with the following expression:

$$E_{form} = E_{surf} - E_{VO} - \frac{1}{2}E_{O_2}$$

Where E_{surf} is the total energy of the stoichiometric surface, E_{VO} is the total energy of the reduced surface and E_{O_2} is the total energy of the optimized gas phase O_2 .

The adsorption energies of CH_x ($x=0-3$) on the stoichiometric and reduced surfaces are calculated as follows:

$$E_{ads} = E_{CHx} + E_{surf} - E_{(CHx+surf)}$$

where E_{CHx} is the energy of the optimized gas phase geometry of CH_x , E_{surf} is the total energy of the respective surface and $E_{(CHx + surf)}$ is the total energy of the slab with CH_x adsorbed. According to this definition, a more positive E_{ads} thus corresponds to a more stable configuration.

The extent of charge transfer from the CH_x ($x=0-3$) radical to the surface is calculated with the algorithm of Henkelman et al.^{191,192} using Bader charges¹⁹³.

The bond order (BO) for the C-O bond has been calculated as follows¹⁹⁴:

$$BO = a R^{-2} + b \quad (a = 5.75 \text{ \AA}^2; b = -1.85)$$

where R is the C-O bond length in \AA .

4.3. Oxygen vacancy formation energies

The calculated formation energies for different surface and subsurface oxygen vacancy defects (V_o) at the anatase (001) titanium dioxide surface are reported in Table 5. The labelling of the different sites is shown in Figure 19. At the surface, V_{O1} (formed by removing a twofold bridging oxygen in the [010] direction (O_{2c})) results in two fourfold coordinated Ti (Ti_{4c}). This is found to be the energetically most favourable oxygen vacancy. In anatase (101) and the (1x4) reconstructed (001) anatase surface, on the other hand, it is found that subsurface vacancies are energetically more favourable than surface vacancies.¹²² The higher stability of the subsurface vacancies relative to the surface vacancies in anatase (101) has been explained by the enhanced associated relaxation and greater atom displacement when subsurface vacancies are present, which is caused by the “rigidness” and stability of the anatase (101) surface.¹²² When comparing the average and maximal atom displacement for the different oxygen vacancies in the anatase (001) (see Table 5.), it is clear that the displacement of the atoms is much greater when the V_{O1} vacancy is formed than when the other vacancies are formed. This is caused by the fact that at the anatase (001) surface the bridging O_{2c} forms two asymmetric Ti-O bonds, having bond lengths of 1.75 \AA and 2.23 \AA . The Ti-O bonds of the neighbouring O_{2c} become symmetric with a bond length of 1.81 \AA , once the V_{O1} oxygen vacancy is formed. The better relaxation and the fact that fewer bonds have to be broken to form the vacancy, make V_{O1} the most stable vacancy. The relative probabilities of the different

vacancies at 300 K and 1000 K are also shown in Table 5. It is found that V_{O4} will not play a significant role in the adsorption of CH_x radicals ($x=0-3$) later discussed in this chapter. Our values and trends for the formation energies of the oxygen vacancies in anatase (001) are in good agreement with previously calculated formation energies.¹⁹⁵ For V_{O1} , V_{O2} , V_{O3} and V_{O4} formation energies in reference 195 were found to be -92.24 kcal/mol, -110.00 kcal/mol, -109.77 kcal/mol and -114.38 kcal/mol, respectively. The difference with our results can be explained by the different computational setup.

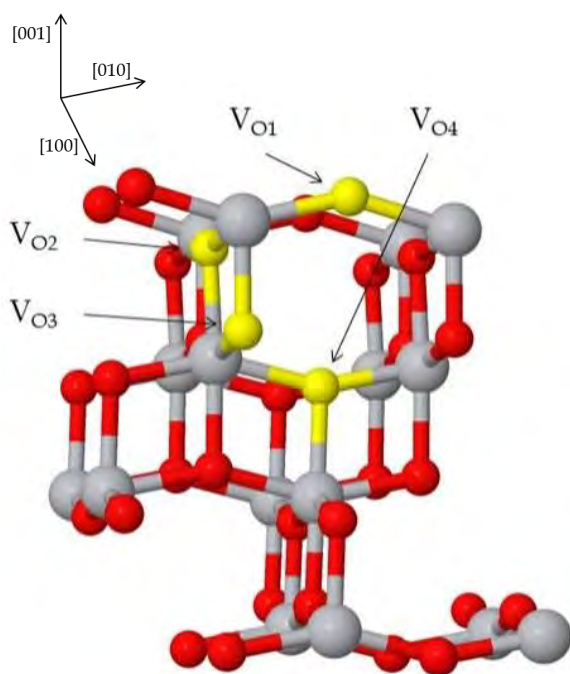


Figure 19. Different oxygen vacancies in an anatase (001) TiO₂ surface. (Ti = gray, O = red, Oxygen vacancy = yellow)

Table 5. Energy of formation for different oxygen vacancies in anatase (001) (E_{form}), the average and maximal atom displacement in the reduced surface relative to the stoichiometric surface (d_{av} and d_{max} , respectively) and the probability of finding each vacancy relative to the total concentration of the oxygen vacancies.

	E_{form} (kcal/mol)	d_{av} (Å)	d_{max} (Å)	Relative probability at 300 K (%)	Relative probability at 1000 K (%)
V _{O1}	-102.91	0.10	0.39	99.99	97.91
V _{O2}	-115.01	0.06	0.16	1.53E-07	0.22
V _{O3}	-110.78	0.06	0.15	1,87E-04	1.87
V _{O4}	-132.74	0.05	0.13	1.86E-20	2.96E-05

4.4. Adsorption of CH_x radicals (x = 0 – 3) on anatase (001)

Now we discuss the adsorption of radical species on anatase (001) and the influence of the different oxygen vacancies on this adsorption. The different adsorption configurations are indicated as A001-x-y-z (see Table 6)

Table 6. Explanation of A001-x-y-z naming

A001-x-y-z	
x	The adsorbed species (C, CH, CH ₂ and CH ₃)
y	The surface (S=stoichiometric surface, Vn=reduced surface with a V _{On} (n=1-3))
z	Index used for identifying specific adsorption configurations.

This index is consistently used for all different surfaces. z consists of a number and a letter (“a”-“d”) for the reduced surfaces. The lower the number of z, the higher the adsorption energy on the stoichiometric surface of that species. This number thus indicates the order of stability on the stoichiometric surface. The letter indicates the location of the oxygen

vacancy relative to the adsorbed species. The location will be indicated in the following paragraphs. A few examples are given:

- A001-C-S-1 corresponds to C (x=C) adsorbed in the most stable configuration (z=1) on the stoichiometric surface (y=S).
- A001-C-S-2 is the second (z=2) most stable configuration of C (x=C) on the stoichiometric surface (y=S).
- A001-C-V1-1b is C (x=C) adsorbed on the reduced surface with a V_{O1} vacancy (y=V1) at position b (z=1b) relative to the adsorbed C equivalent to the most stable adsorption configuration on the stoichiometric surface (z=1b). Note, however, that this does not necessarily mean that A001-C-V1-1b is also the most stable adsorption position on the reduced anatase (001) surface.

4.4.1. Adsorption of CH_x radicals (x = 0 - 3) on a stoichiometric anatase (001) surface.

4.4.1.1. Adsorption of C

For a C radical adsorbed on the stoichiometric anatase (001) surface we find three different adsorption configurations, which in order of stability are indicated as A001-C-S-1, A001-C-S-2 and A001-C-S-3 in Table 7 and Figure 20. A001-C-S-1 and A001-C-S-2 correspond to the adsorption of C at the O_{2c} site. This causes the spontaneous breaking of the bond between one Ti and O_{2c}, after which a Ti-C bond is formed. The difference between A001-C-S-1 and A001-C-S-2 is the relative position of the C with respect to the asymmetric Ti-O_{2c} bonds in the neighbouring [010] row. Only a small difference is found in the strength of the adsorption, corresponding to an adsorption energy of 153.71 kcal/mol and 153.40 kcal/mol for A001-C-S-1 and A001-C-S-2, respectively. The charge transfer from the C to the surface and also the Ti-C and C-O_{2c} bond lengths are found to be almost equal for A001-C-S-1 and A001-C-S-2. The third adsorption configuration,

A001-C-S-3, corresponds to C adsorbed on top of the surface O in the [100] row (hereafter denoted as O_{V02}). This is found to be 35.32 kcal/mol less stable than the most stable adsorption configuration of C on the stoichiometric surface, A001-C-S-1. The decrease in stability relative to A001-C-S-1 coincides with an increase in the Ti-C and C-O bond lengths, from 2.09 Å to 2.22 Å and 1.21 Å to 1.28 Å, respectively. This increase in C-O bond length corresponds to a decrease in double bond character, indicated by a decrease in bond order (BO) from BO = 2.08 in A001-C-S-1 and A001-C-S-2 to BO = 1.66 in A001-C-S-3. Also the charge transfer from C to the surface is lower than in the first two configurations.

4.4.1.2. Adsorption of CH

For the CH radical five different adsorption configurations are found. Just as is the case with C adsorbed on the surface, A001-CH-S-1 and A001-CH-S-2 correspond to the spontaneous breaking of a Ti-O_{2c} bond, and the formation of a Ti-C and C-O_{2c} bond. These two configurations differ by the relative position of the CH to the asymmetric Ti-O_{2c} bonds in the neighbouring [010] row. Again the difference between these two configurations is minimal: the adsorption energy is only 0.80 kcal/mol lower for A001-CH-S-2 relative to A001-CH-S-1. For the third configuration, A001-CH-S-3, the CH is bonded to a Ti and to both O_{2c} and O_{V02}. It is found to be 10.87 kcal/mol less stable than A001-CH-S-1, showing longer C-O bond lengths of 1.37 Å and 1.43 Å, to be compared to a C-O bond length of 1.29 Å in the A001-CH-S-1 configuration. The charge transfer to the surface is of the same order of magnitude as for A001-CH-S-1. In the fourth CH adsorption configuration, A001-CH-S-4, CH is bonded between two O_{2c} of neighbouring [010] rows. The adsorption of the CH radical in this configuration has a significantly larger charge transfer from the adsorbed species to the surface than for the other adsorption configurations. This configuration is 34.96 kcal/mol less stable than A001-

CH-S-1. For the fifth configuration the CH radical is adsorbed on top of a O_{VO2}. This configuration is exothermic by only 0.33 kcal/mol relative to the gas phase CH radical. This last configuration will therefore hardly contribute to the adsorption of CH on the stoichiometric anatase (001) surface, since all other adsorption configurations are much more strongly exothermic. In this configuration, no bond is present between carbon and oxygen.

4.4.1.3. Adsorption of CH₂

For the adsorption of the CH₂ radical on the anatase (001) surface, four adsorption configurations are found. Again the two most stable configurations, A001-CH₂-S-1 and A001-CH₂-S-2, are formed by the spontaneous bond breaking of a Ti-O_{2c} bond and the formation of a Ti-C and C-O_{2c} bond. The difference between the two configurations is the relative position of CH₂ with respect to the asymmetrical Ti-O_{2c} bonds in the neighbouring [010] row. In this case, however, the adsorption energy of these two configurations is found to be identical, 84.49 kcal/mol. The third most stable configuration, A001-CH₂-S-3, is 28.37 kcal/mol less stable than A001-CH₂-S-1 and A001-CH₂-S-2. In this case, the CH₂ is adsorbed on top of the O_{VO2} site. The two Ti-C bonds are asymmetrical, having bond lengths of 2.43 Å and 2.19 Å. The fourth adsorption configuration, A001-CH₂-S-4, has the C of the CH₂ bonded to two O_{2c} of neighbouring [010] rows. This configuration is equivalent to A001-CH-S-4 with CH adsorbed. The C-O_{2c} bond length in the case of CH₂ is 1.45 Å, which is significantly longer than the bond length in the case of CH adsorption, which is 1.33 Å. This increase in bond length corresponds to a sharp drop in bond order from 1.40 to 0.88. The difference in adsorption energy relative to A001-CH₂-S-1 is 29.72 kcal/mol. Just as in the case of A001-CH-S-4, a larger charge transfer occurs from the adsorbed species to the surface, relative to

the other adsorption configurations of that species, due to the C being bonded to two undercoordinated O_{2c} atoms.

4.4.1.4. Adsorption of CH₃

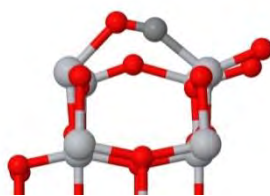
For CH₃ only two stable adsorption configurations are found. In the most stable configuration, A001-CH3-S-1, CH₃ is directly bonded to O_{2c}. In this case, the charge transfer occurs from the surface to the adsorbed CH₃. This configuration has an adsorption energy of 29.56 kcal/mol. In the second configuration, A001-CH3-S-2, CH₃ is bonded to O_{VO2}. In this configuration, one of the Ti-O_{VO2} bonds in the subsurface is broken spontaneously. A001-CH3-S-2 is found to be 21.76 kcal/mol less stable than A001-CH3-S-1, and shows a charge transfer from the adsorbate to the surface. As expected for both configurations, the C-O bond has a single bond character (BO_{C-O} ≈ 1). We also have performed calculations on the adsorption of CH₃ on a titanium atom; this led to spontaneous desorption of CH₃.

Table 7. The adsorption energy for the different adsorption configurations (E_{ads}), the bond lengths of the Ti-C bonds and C-O bonds ($BL_{\text{Ti-C}}$ and $BL_{\text{C-O}}$), the bond order of the C-O bond ($BO_{\text{C-O}}$) and the charge transfer from the CH_x-species to the surface ($\Delta q(\text{CH}_x)/|e|$, where a positive value corresponds to a charge transfer from the adsorbate to the surface)

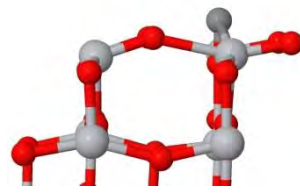
Adsorption configuration	E_{ads} (kcal/mol)	$BL_{\text{Ti-C}}$ (Å)	$BL_{\text{C-O}}$ (Å)	$BO_{\text{C-O}}$	$\Delta q(\text{CH}_x)/ e$
A001-C-S-1	153.71	2.09	1.21	2.08	1.341
A001-C-S-2	153.40	2.10	1.21	2.08	1.345
A001-C-S-3	118.39	2.22	1.28	1.66	0.771
A001-CH-S-1	118.07	2.11	1.29	1.61	0.369
A001-CH-S-2	117.27	2.12	1.29	1.61	0.388
A001-CH-S-3	107.20	2.08	1.37/1.43	1.21/0.96	0.393
A001-CH-S-4	83.11		1.33	1.40	1.570
A001-CH-S-5	0.33	2.10			0.754
A001-CH ₂ -S-1	84.49	2.18	1.41	1.04	0.726
A001-CH ₂ -S-2	84.49	2.18	1.40	1.08	0.864
A001-CH ₂ -S-3	56.12	2.43/2.19	1.42	1.00	0.808
A001-CH ₂ -S-4	54.77		1.45	0.88	1.275
A001-CH ₃ -S-1	29.56		1.43	0.96	-0.137
A001-CH ₃ -S-2	7.80		1.44	0.92	1.341



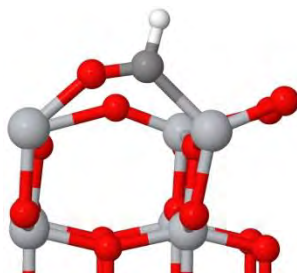
A001-C-S-1



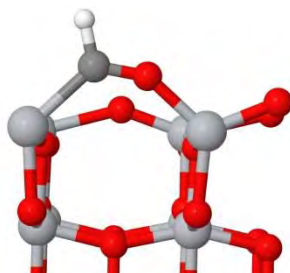
A001-C-S-2



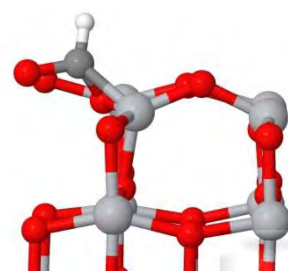
A001-C-S-3



A001-CH-S-1



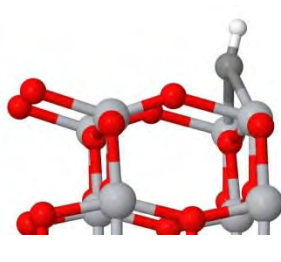
A001-CH-S-2



A001-CH-S-3



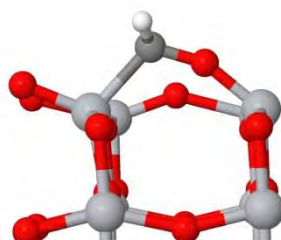
A001-CH-S-4



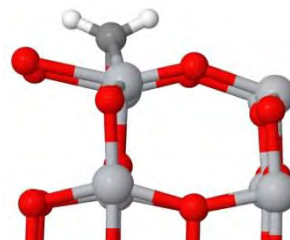
A001-CH-S-5



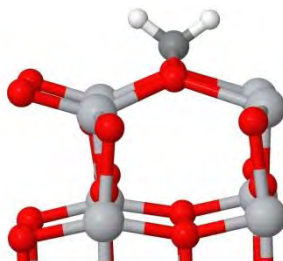
A001-CH2-S-1



A001-CH2-S-2



A001-CH2-S-3



A001-CH2-S-4

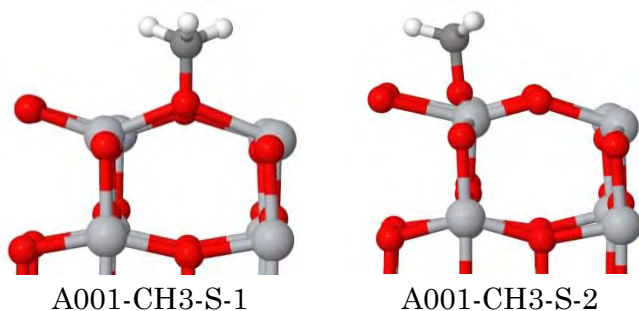


Figure 20: The different adsorption configurations of the CH_x (x=0-3) radicals on the stoichiometric anatase (001) surface. (Ti = light gray, O = red, C = dark gray, H = white)

4.4.2. Adsorption on a reduced anatase (001) surface

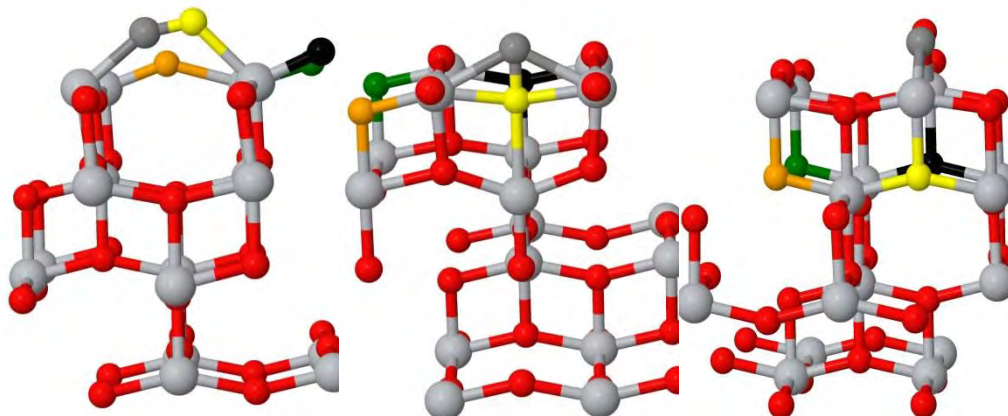


Figure 21. Locations of the oxygen vacancies. From left to right: V_{O1} (A001-C-S-1), V_{O2} (A001-C-S-3), V_{O3} (A001-C-S-1). (Ti = light gray, C = dark gray, O = red, Oxygen vacancy locations: “a” = yellow, “b” = black, “c” = orange, “d” = green). All oxygen vacancy locations (“a”-“d”) are relative to the adsorbed species, carbon in these examples.

In the section above, we investigated the formation energies of oxygen vacancies in the anatase (001) surface. Understanding the effect of these defects on the adsorption of species on the surface is essential for a more

fundamental understanding of the plasma-catalytic activity of this material. Therefore, here we study the influence of the three most stable vacancies V_{O1}, V_{O2} and V_{O3} on the adsorption of CH_x radicals. V_{O4} is not considered in this study, as its equilibrium concentration is negligible compared to the other vacancies (see Table 5). We have studied the influence of the vacancies and their position relative to the adsorbed species on the adsorption strength of the radical species in the different configurations.

4.4.2.1. Reduced anatase (001) surface containing a V_{O1} oxygen vacancy

The relative position of V_{O1} is indicated with the letters a-d, as indicated in Figure 21. Position “a” corresponds to the removal of the closest O_{2c} oxygen (V_{O1} oxygen) relative to the adsorbed C, position “b” to the removal of the O_{2c} in the same [010] row as “a”. Position “c” and “d” are equivalent to “a” and “b”, respectively, but in the neighbouring [010] row. The adsorption energies of the CH_x species on the reduced anatase (001) surface containing a V_{O1} vacancy are shown in Table 8.

4.4.2.1.1. Adsorption of C

For the C-radical adsorption we find three different adsorption configurations on the non-defective (stoichiometric) surface. In Figure 22 the difference in the adsorption energy of C on the stoichiometric surface and its adsorption energy on the reduced surface with a V_{O1} vacancy is shown. A negative ΔE_{ads} corresponds to a lower adsorption strength on the reduced surface, compared to adsorption on the stoichiometric surface. For A001-C-S-1 and A001-C-S-2, for which the adsorption interaction was almost identical on the stoichiometric surface, it is found that the influence of the presence of a V_{O1} vacancy is nearly identical. The presence of V_{O1} at

the “a” position leads to a new adsorption configuration, in which the Ti-C-O-Ti structure becomes Ti-C-Ti since the oxygen is removed. This new configuration is identical for A001-C-V1-1 and A001-C-V1-2. For all positions of the vacancy in configurations A001-C-V1-1 and A001-C-V1-2, the adsorption energy decreases relative to A001-C-S-1 and A001-C-S-2, respectively. The largest decrease is found for the “b” position of the vacancy. The influence of the vacancy in the [010] neighbouring row (position “c” and “d”) on the adsorption energy is found to be minimal ($|\Delta E_{\text{ads}}| < 5$ kcal/mol). For A001-C-V1-3 a small positive ΔE_{ads} relative to A001-C-S-3 is found for all positions of the oxygen vacancy.

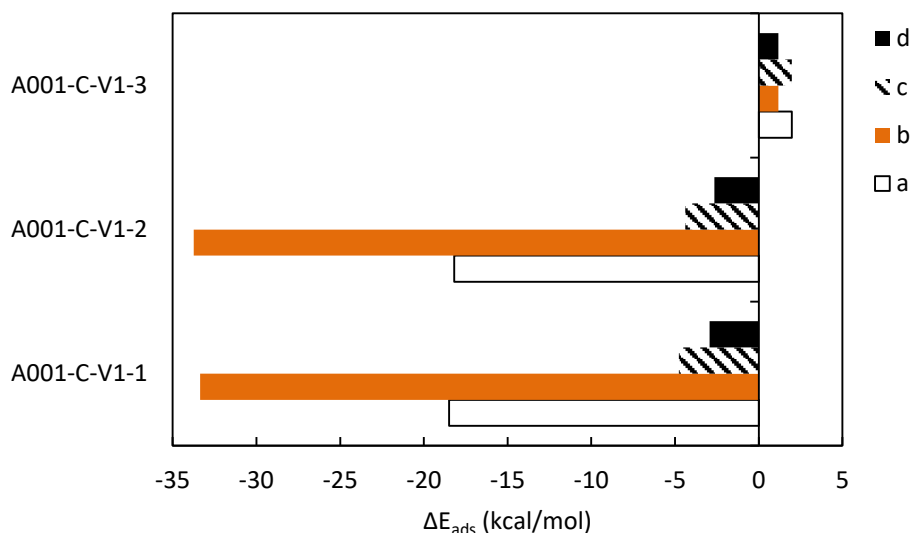


Figure 22. The difference in adsorption energy of the adsorption configurations of C on a reduced anatase (001) surface with a V_{O1} vacancy (location = “a”-“d”) relative to the A001-C-S-z (z=1-3) configurations.

4.4.2.1.2. Adsorption of CH

For the adsorption of CH on the stoichiometric surface, five different adsorption configurations were previously found. In Figure 23 the difference between the adsorption energy of CH on the stoichiometric surface and the adsorption energy on the reduced surface with a V_{O1} vacancy is shown. Also in this case the adsorption interaction was found to be almost identical for A001-CH-S-1 and A001-CH-S-2. This again leads to an influence of the oxygen vacancy that is almost identical for both configurations. Similar to C adsorption, the formation of the vacancy on position “a” leads to a new adsorption configuration. In this configuration, A001-CH-V1-1a (A001-CH-V1-2a is equivalent), the Ti-C-O-Ti structure is replaced by a Ti-C-Ti structure. This new adsorption configuration shows approximately the same adsorption energy for CH as the adsorption of CH in an A001-CH-S-1 or A001-CH-S-2 configuration on the stoichiometric surface. In the A001-CH-V1-1b and the A001-CH-V1-2b configuration the interaction of the adsorbed species is decreased significantly ($\Delta E_{\text{ads}} \approx -40$ kcal/mol), while for “c” and “d” the adsorption energy drops by less than 5 kcal/mol. A similar result is found for the adsorption configuration A001-CH-V1-3, i.e., a limited influence (although larger than for A001-CH-V1-1 and A001-CH-V1-2) is found for the positions “a”, “c” and “d”, and a significant decrease in adsorption strength is found for A001-CH-V1-3b. For A001-CH-V1-3a one of the C-O bonds, found in the stoichiometric surface adsorption configuration A001-CH-S-3, is replaced by an extra Ti-C bond with a bond length of 2.48 Å. For A001-CH-V1-4 only the vacancy positions “b” and “d” exist, as “a” and “c” cannot form a configuration that is equivalent to A001-CH-S-4 on the stoichiometric surface. The adsorption strength of the A001-CH-V1-4b and A001-CH-V1-4d configuration decreases significantly with respect to the A001-CH-S-4.

Recall that the A001-CH-S-5 configuration on the stoichiometric surface shows a very low adsorption energy. When a V_{O1} oxygen vacancy is introduced in this configuration, this configuration spontaneously converts in A001-CH-V1-1a.

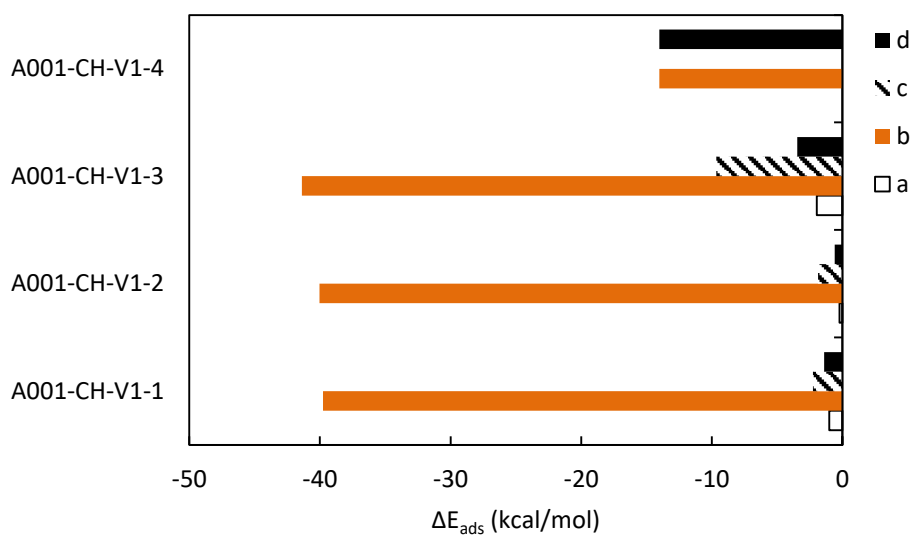


Figure 23. The difference in adsorption energy of the adsorption configurations of CH on a reduced anatase (001) surface with a V_{O1} vacancy (location = “a”-“d”) relative to the A001-CH-S-z (z=1-4) configurations.

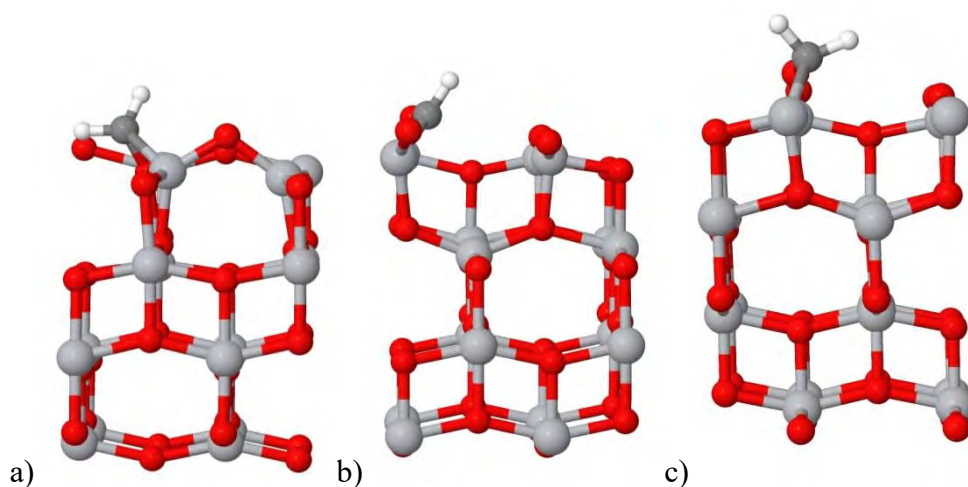


Figure 24. Adsorption Configurations: a) A001-CH₂-V1-3a, b) A001-CH₂-V2-1a, c) A001-CH₂-V2-1a (Ti = light gray, O = red, C = dark gray, H = white)

4.4.2.1.3. Adsorption of CH₂

As is the case for C and CH radical adsorption on the stoichiometric surface, the adsorption interactions of A001-CH₂-S-1 and A001-CH₂-S-2 are found to be nearly identical. In Figure 25 the difference between the adsorption energy of CH₂ on the stoichiometric surface and the adsorption energy of CH₂ on the reduced surface with a V_{O1} vacancy is shown. Again the influence of V_{O1} is very similar for both adsorption configurations. The A001-CH₂-V1-1b and A001-CH₂-V2-2b adsorption configurations show the greatest decrease in adsorption strength. The decrease in adsorption energy is found to be around 38 kcal/mol. A001-CH₂-V1-1a and A001-CH₂-V1-2a again correspond to a new adsorption configuration, where the Ti-C-O-Ti structure is replaced by a Ti-C-Ti structure. These new adsorption configurations are found to be the overall most stable adsorption configurations of CH₂, when a V_{O1} oxygen vacancy is present at the surface. When the vacancy is present in the neighbouring [010] row

(positions “c” and “d”), the adsorption interaction in configurations A001-CH₂-V1-1 and A001-CH₂-V1-2 only decreases by a small amount relative to A001-CH₂-S-1 and A001-CH₂-S-2, respectively. For A001-CH₂-V1-3 the interaction strength increases relative to A001-CH₂-S-3. The corresponding ΔE_{ads} is calculated to be around 7 kcal/mol. In these configurations on the reduced surface, one of the Ti-C bonds is broken, and CH rotates inwards in the direction of the V_{O1} vacancy (see Figure 24). For the last configuration, A001-CH₂-V1-4, only positions “b” and “d” are considered, because “a” and “c” do not lead to an adsorption configuration equivalent to A001-CH₂-V1-4 on the stoichiometric surface. The adsorption energies of A001-CH₂-V1-4b and A001-CH₂-V1-4d decrease by ~11 kcal/mol, relative to the adsorption on the stoichiometric surface.

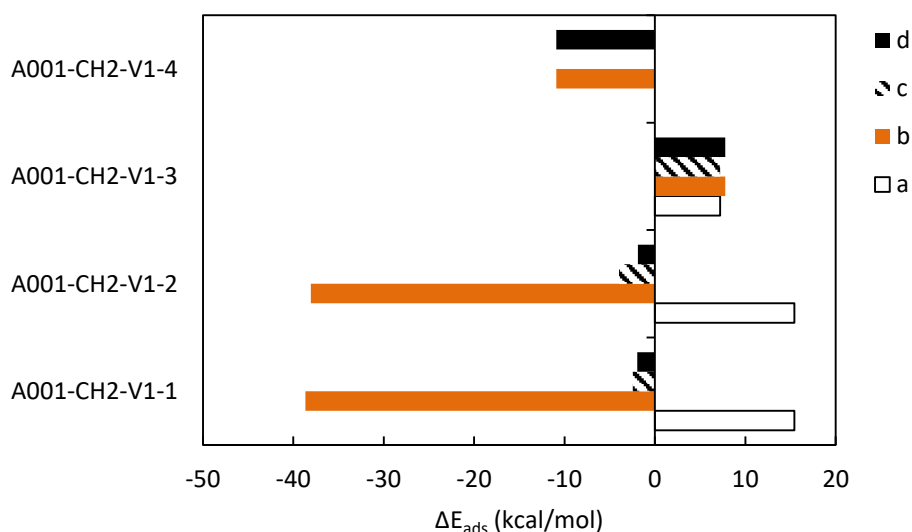


Figure 25. The difference in adsorption energy of the adsorption configurations of CH₂ on a reduced anatase (001) surface with a V_{O1} vacancy (location = “a”-“d”) relative to the A001-CH₂-S-z (z=1-4) configurations.

4.4.2.1.4. Adsorption of CH₃

We previously found two adsorption configurations for the CH₃ radical on the stoichiometric surface. In Figure 26 the difference between the adsorption energy of CH₃ on the stoichiometric surface and the adsorption energy on the reduced surface with a V_{O1} vacancy is shown. A001-CH3-V1-1 remains the most stable configuration for every location of the V_{O1} oxygen vacancy, but it is not possible to create A001-CH3-V1-1a because when V_{O1} is formed on location “a” the oxygen of the O-CH₃ bond would be removed. We find that for every position of the oxygen vacancy the adsorption strength is lower than on the stoichiometric surface. This effect is largest when the V_{O1} is located in the same [010] row as the adsorbed CH₃ (position “b”).

For A001-CH3-S-2 the effect of the vacancy is found to be minimal, and ΔE_{ads} ranges from -0.74 kcal/mol for A001-CH3-V1-2a and A001-CH3-V1-2c to +0.33 kcal/mol for A001-CH3-V1-b and A001-CH3-V1-d.

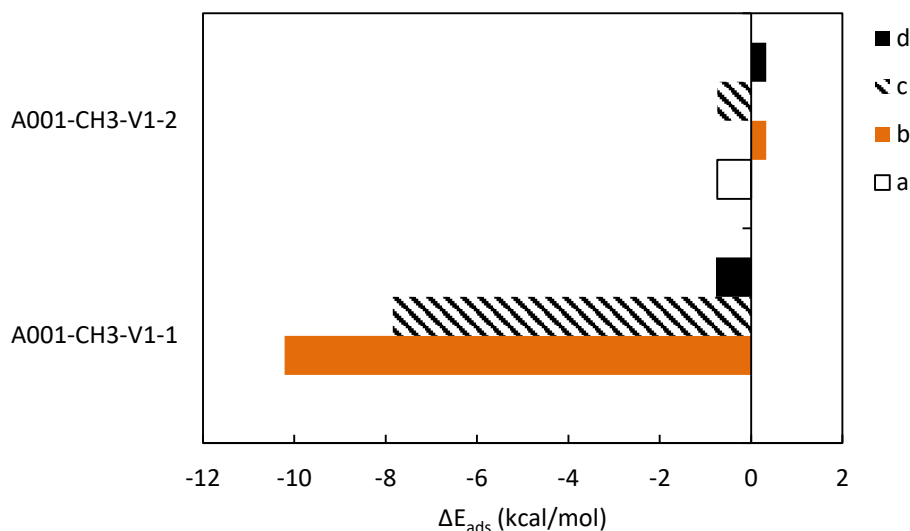


Figure 26. The difference in adsorption energy of the adsorption configurations of CH₃ on a reduced anatase (001) surface with a V_{O1} vacancy (location = “a”–“d”) relative to the A001-CH3-S-z (z=1-2) configurations.

Apart from the adsorption configurations on the reduced anatase (001) surface, which have an equivalent on the stoichiometric surface, a new adsorption configuration is found to be stable on the reduced surface, A001-CH3-V1-3x (x = “a”–“d”). The adsorption of CH₃ on Ti was found to be stable in the proximity of a V_{O1} oxygen vacancy. This was not the case for the stoichiometric surface, for which spontaneous desorption of CH₃ occurs. When CH₃ adsorbs on titanium in the same [010] row as V_{O1}, it folds inwards, as shown in Figure 27, stabilizing the structure through two C—H ... O_{V02} interactions. This corresponds to the configurations A001-CH3-V1-3a and A001-CH3-V1-3b. The adsorption energies corresponding to these adsorption configurations are 56.94 kcal/mol and 55.71 kcal/mol, respectively, which is significantly greater than 28.79 kcal/mol for the most stable adsorption configuration corresponding to one of the configurations on the stoichiometric surface, A001-CH3-V1-1d. For

adsorption occurring in the neighbouring [010] row, it is not possible for CH₃ to fold inwards. This corresponds to configurations A001-CH3-V1-3c and A001-CH3-V1-3d, for which we calculate the adsorption energies to be 31.13 kcal/mol and 28.24 kcal/mol, respectively. The presence of a V_{O1} vacancy thus stabilizes the adsorption of CH₃ on a titanium atom in the proximity of this vacancy.

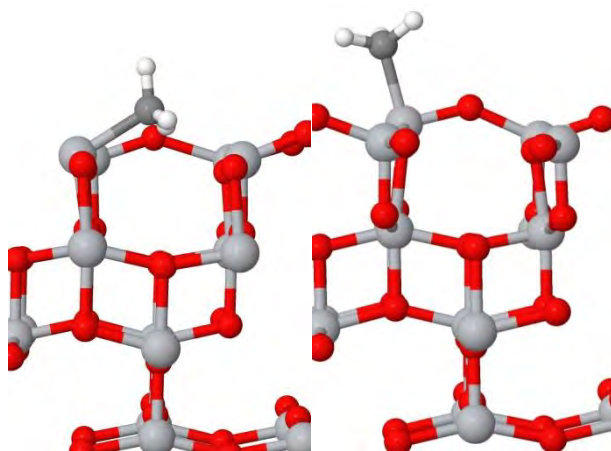


Figure 27. From left to right: A001-CH3-V1-3a and A001-CH3-V1-3c (Ti = light gray, O = red, C = dark gray, H = white)

4.4.2.1.5. Summary of CH_x adsorption on the reduced anatase (001) surface with a V_{O1} oxygen vacancy

The influence of the most stable oxygen vacancy, V_{O1}, on the adsorption of CH_x radicals (x = 0 - 3) on an anatase (001) surface was studied in this section. The adsorption energies of the CH_x species on the reduced anatase (001) surface containing a V_{O1} vacancy are shown in Table 8. For CH₂ and CH₃ we find an increased interaction energy relative to the most stable adsorption on the stoichiometric surface. For CH₂, A001-CH2-V1-1a and A001-CH2-V1-2a have an adsorption energy of 99.93 kcal/mol, thus showing a 18% increase from the 84.49 kcal/mol for the stoichiometric A001-CH2-S-1 and A001-CH2-S-2 configurations. For CH₃ a new stable adsorption configuration, A001-CH3-V1-3x (x = "a"-"d"), originates on the reduced anatase (001) surface. The configurations where x equals a, b and c have an adsorption energy of 56.94 kcal/mol, 55.71 kcal/mol and 31.13 kcal/mol, respectively, corresponding to a 93%, 88% and 5% increase relative to the 29.56 kcal/mol for the stoichiometric A001-CH3-S-1. The influence, however, of each adsorption configuration separately on the adsorption strength can be either negative or positive. We only found an increase in adsorption strength and energy for some cases where the species are adsorbed on top of O_{V02} and for the new adsorption configurations A001-CH2-V1-1a and A001-CH2-V1-2a. In all other cases the adsorption energy dropped compared to the configurations on the stoichiometric surface.

Table 8. The adsorption energy for the different adsorption configurations (E_{ads}), on the stoichiometric surface and on the reduced surface with a V_{O1} oxygen vacancy on the different locations “a”-“d”. (“X” marks configurations that were found unstable or could not be created, the configurations which are no longer equivalent to the configurations on the stoichiometric surface caused by the fact that certain bonds no longer can be formed are shown in boldface)

	Adsorption configuration	Stoichiometric	E_{ads} (kcal/mol)			
			a	b	c	d
C	A001-C-S-1	153.71	135.21	120.35	148.95	150.77
	A001-C-S-2	153.40	135.21	119.65	149.00	150.75
	A001-C-S-3	118.39	120.37	119.57	120.37	119.57
CH	A001-CH-S-1	118.07	117.05	78.29	115.82	116.67
	A001-CH-S-2	117.27	117.05	77.23	115.42	116.69
	A001-CH-S-3	107.20	105.23	65.82	97.55	103.75
	A001-CH-S-4	83.11	X	69.08	X	69.08
CH₂	A001-CH ₂ -S-1	84.49	99.93	45.81	82.05	82.52
	A001-CH ₂ -S-2	84.49	99.93	46.44	80.52	82.60
	A001-CH ₂ -S-3	56.12	63.36	63.89	63.36	63.89
	A001-CH ₂ -S-4	54.77	X	43.86	X	43.86
CH₃	A001-CH ₃ -S-1	29.56	X	19.35	21.72	28.79
	A001-CH ₃ -S-2	7.80	7.06	8.13	7.06	8.13
	A001-CH ₃ -V1-3	X	56.94	55.71	31.13	28.24

4.4.2.2. Reduced anatase (001) surface containing a V_{O2} oxygen vacancy

The relative position of the V_{O2} oxygen vacancy is indicated by the letters “a”-“d” as shown in Figure 21. Position “a” corresponds to the removal of the closest V_{O2} oxygen relative to the adsorbed C, position “b” is the removal of the V_{O2} oxygen in the same [010] row as “a”. Positions “c” and “d” are equivalent to “a” and “b”, respectively, but in the neighbouring [010] row. The adsorption energies of the CH_x species on the reduced anatase (001) surface containing a V_{O2} vacancy are shown in Table 9.

4.4.2.2.1. Adsorption of C

As discussed above, A001-C-S-1 and A001-C-S-2 show almost identical adsorption energies (C on the stoichiometric surface) because of their very similar structure. For these configurations, the influence of the V_{O2} vacancy on the adsorption energy is almost identical. In Figure 28 the difference in the adsorption energy of C on the stoichiometric surface and the adsorption energy on the reduced surface with a V_{O2} vacancy is shown. If the vacancy is present on the side of C, the adsorption strength is enhanced. If the vacancy is present on the side of O_{2c} of the Ti-C-O-Ti structure the adsorption strength is decreased. Both the increase and decrease in adsorption energy have an absolute value of ~5 kcal/mol.

For A001-C-S-3, which corresponds to adsorption on top of O_{V02}, we find a significant increase in adsorption energy for C in the A001-C-V2-3a configuration. In this configuration it is no longer possible to form a C-O bond, because the O_{V02} is removed, leading to a shortening of the Ti-C bonds from 2.22 Å in A001-C-S-3 to 2.19 Å in A001-C-V2-3a. Also an increase in adsorption strength is found for A001-C-V2-3b and A001-C-V2-3d, but a decrease is found for A001-C-V2-3c, relative to A001-C-S-3.

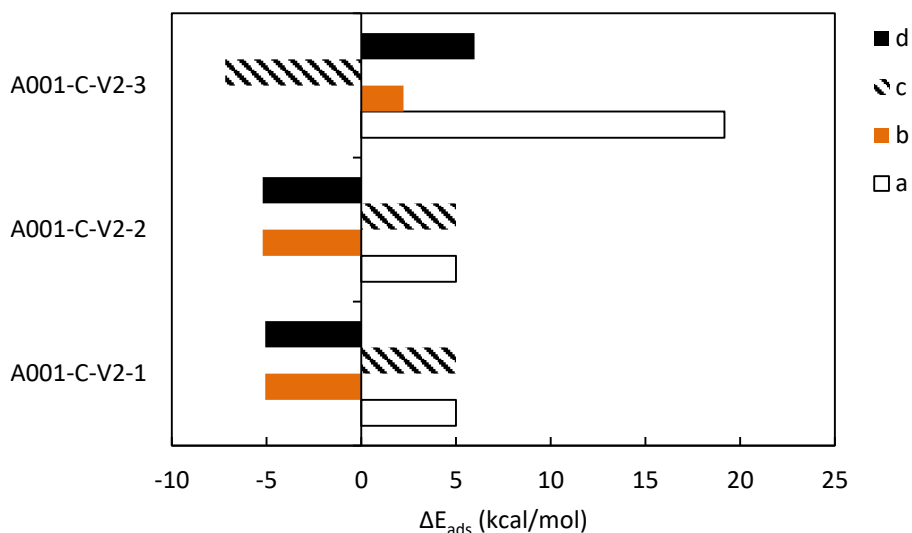


Figure 28. The difference in adsorption energy for the adsorption configurations of C on a reduced anatase (001) surface with a V_{O₂} vacancy (location = “a”-“d”) relative to the A001-C-S-z (z=1-3) configurations.

4.4.2.2.2. Adsorption of CH

In Figure 29 the difference between the adsorption energy of CH on the stoichiometric surface and the adsorption energy on the reduced surface with a V_{O₂} vacancy is shown. Five different adsorption configurations were found on the stoichiometric surface. A001-CH-S-1 and A001-CH-S-2, which were found to be almost identical on the stoichiometric surface, again are similarly influenced by the presence of an oxygen vacancy. As is the case for the C adsorption in the A001-C-V2-1 and A001-C-V2-2 configurations, it is found that CH adsorption is enhanced when V_{O₂} is located on the side of the C of the adsorbent (positions “a” and “c”), and the strength of adsorption is decreased when V_{O₂} is located on the side of the O_{2c} of the Ti-C-O-Ti structure (positions “b” and “d” of V_{O₂}). The presence of V_{O₂} on positions “b” and “d” leads to a shortening of the Ti-C bond from 2.11 Å on

the stoichiometric surface to 2.00 Å. When V_{O2} is located in positions “a” and “c” the CH folds inwards in the direction of the V_{O2} vacancy, with a Ti-Ti-C angle of 60.4°, where the two Ti atoms are those in the same [100] row (see Figure 24). For A001-CH-V2-3 the position of V_{O2} on position “a” leads to configuration A001-CH-V2-1a, and so is not calculated separately. The adsorption energy of A001-CH-V2-3b increases by ~4 kcal/mol relative to A001-CH-S-3. The adsorption energy for A001-CH-V2-3c drops significantly by 18.62 kcal/mol and the adsorption energy of A001-CH-V2-3d drops by ~4 kcal/mol.

While CH is bonded to two O_{2c} in the A001-CH-S-4 configuration, it is bonded to two O_{2c} and the two Ti, between the removed oxygen, in the A001-CH-V2-4a and A001-CH-V2-4b configurations. The O_{2c}-C bond lengths are increased from 1.33 Å (BO = 1.40) to 1.42 Å (BO = 1) in A001-CH-S-4. The adsorption energy increases significantly ($\Delta E_{\text{ads}} \approx 32$ kcal/mol). A001-CH-V2-4c on the other hand leads to the breaking of a Ti-O_{2c} bond on each side of the adsorbed CH, which causes the O_{2c}-C bonds to shorten to 1.28 Å. This leads to a decrease in adsorption strength ($\Delta E_{\text{ads}} \approx 18$ kcal/mol). For A001-CH-V2-4d the adsorption strength drops significantly ($\Delta E_{\text{ads}} \approx -14$ kcal/mol).

On the stoichiometric surface A001-CH-S-5 was found to be only slightly exothermic relative to the gas phase CH (0.33 kcal/mol), and was not stable in the A001-CH-V1-5 configurations. However, in the A001-CH-V2-5 configurations, there is a strong stabilization with ΔE_{ads} ranging from 52.2 kcal/mol to 106.6 kcal/mol. The largest stabilization is found for the V_{O2} locations “a” and “c”, corresponding to V_{O2} located in the same [100] row as the adsorbed CH. In the configuration A001-CH-V2-5a the O_{2c}-Ti-C-H dihedral angle changes from 100° in A001-CH-S-5 to 37° in the A001-CH-V2-5a configuration. In A001-CH-V2-5c O_{V03} migrates spontaneously to the location between where O_{V02} and O_{V03} were.

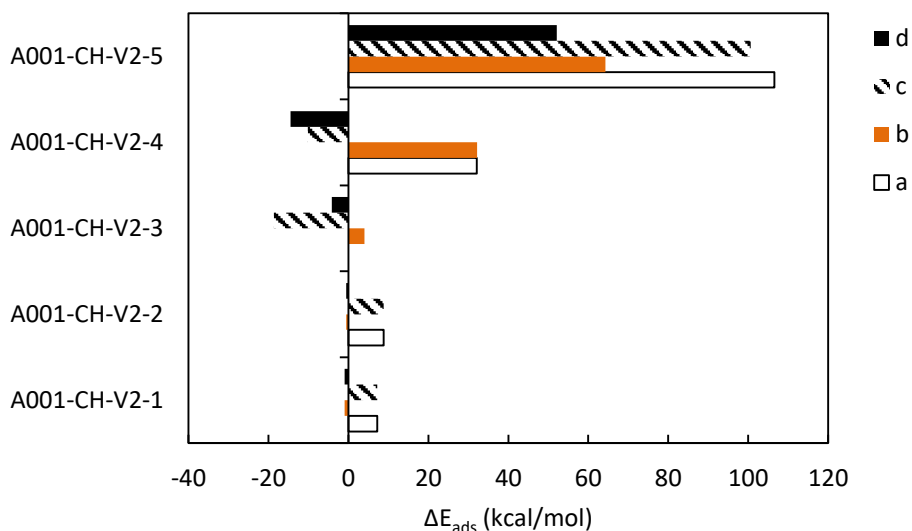


Figure 29. The difference in adsorption energy of the adsorption configurations of CH on a reduced anatase (001) surface with a V_{O2} vacancy (location = “a”-“d”) relative to the A001-CH-S-z (z=1-5) configurations.

4.4.2.2.3. Adsorption of CH₂

In Figure 30 the difference between the adsorption energy of CH₂ on the stoichiometric surface and the adsorption energy on the reduced surface with a V_{O2} vacancy is shown. Similar to our previous observations it is found that for A001-CH₂-S-1 and A001-CH₂-S-2 the influence of the V_{O2} vacancy is almost identical. For positions “a” and “c”, for which the vacancy is located closest to the C-atom, a positive influence on the adsorption strength is found. However, the increase in adsorption energy is only ~2 kcal/mol, while for the CH adsorption in the A001-CH-V2-1a configuration an increase of ~7 kcal/mol was found. Again the C atom is tilted inwards in the A001-CH₂-V2-1 and A001-CH₂-V2-2 configurations, if the vacancy is located on the “a” or “c” location. In this case, the Ti-Ti-C angle is 75.1°, compared to 60.4° for A001-CH-V2-1a and 91.2° for A001-CH₂-S-1 (see

Figure 24). For locations “b” and “d”, for which the vacancy is located closest to the O_{2c}-atom bonded to the C-atom, a small negative influence is found on the adsorption strength ($\Delta E_{\text{ads}} \approx -2.5$ kcal/mol).

In the case of the A001-CH₂-V2-3 configuration, it is found that A001-CH₂-V2-3a shows a significant boost in adsorption strength, making it the most stable adsorption configuration of CH₂ on the reduced surface. E_{ads} is calculated to be 92.97 kcal/mol, which is an increase of 36.85 kcal/mol compared to A001-CH₂-S-3 on the stoichiometric surface. In this configuration the Ti-C bond lengths are shortened from 2.43 Å and 2.19 Å on the stoichiometric surface to 2.07 Å.

For A001-CH₂-V2-4 the position of V_{O₂} in locations “a”, “b” and “c” causes two Ti-O_{2c} bonds to break. This has a positive influence on the adsorption strength when this occurs for A001-CH₂-V2-4a and A001-CH₂-V2-4c, and a negative influence for A001-CH₂-V2-4b. For A001-CH₂-V2-4d no bond breaking occurs, and the adsorption energy decreases by ~14 kcal/mol relative to A001-CH₂-S-4.

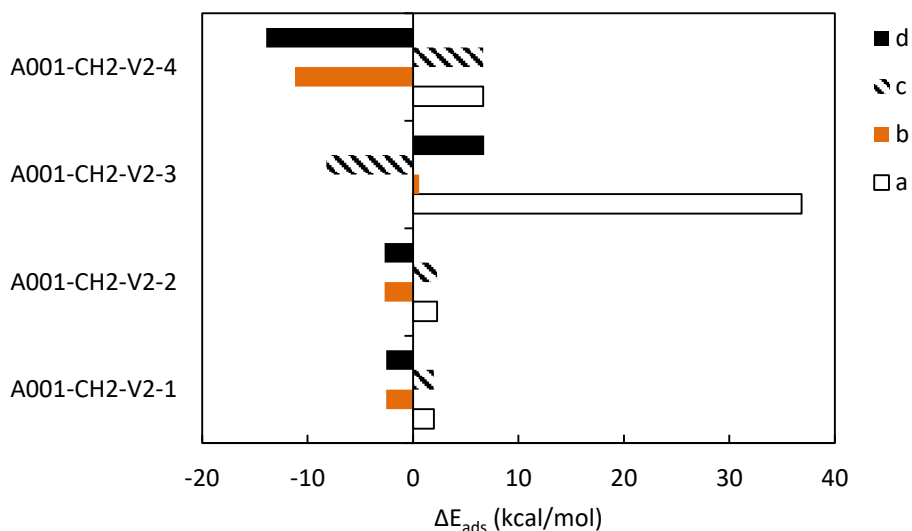


Figure 30. The difference in adsorption energy of the CH₂ adsorption configurations on a reduced anatase (001) surface with a V_{O2} vacancy (location = “a”-“d”) relative to the A001-CH2-S-z (z=1-4) configurations.

4.4.2.2.4. Adsorption of CH₃

In Figure 31 the difference between the adsorption energy of CH₃ on the stoichiometric surface and the adsorption energy on the reduced surface with a V_{O2} vacancy is shown. For all 4 locations of V_{O2} in the A001-CH3-V2-1 configuration, a negative influence on the adsorption strength is found. For A001-CH3-V3-2 it is not possible to have this configuration with the vacancy located on position “a”. The other positions of the vacancy strengthen the adsorption on the reduced surface.

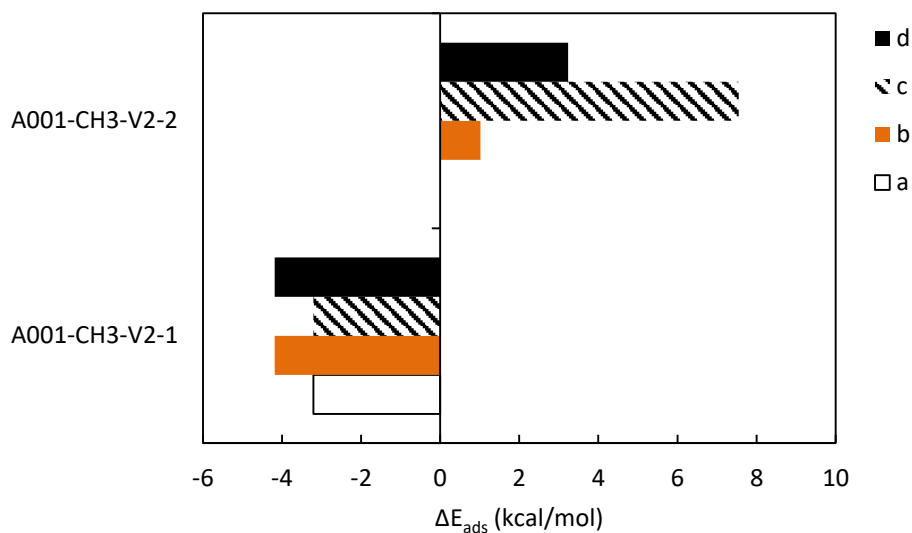


Figure 31. The difference in adsorption energy of the adsorption configurations of CH₃ on a reduced anatase (001) surface with a V_{O2} vacancy (location = “a”-“d”) relative to the A001-CH3-S-z (z=1-2) configurations.

Apart from the adsorption configurations on the reduced anatase (001) surface which have an equivalent on the stoichiometric surface, a new adsorption configuration is found to be stable on the reduced surface, A001-CH3-V2-3x (x = “a”-“b”). The adsorption of CH₃ on Ti was found to be stable in the close proximity of a V_{O2} oxygen vacancy. This was not the case for the stoichiometric surface, for which spontaneous desorption of CH₃ occurs. Only A001-CH3-V2-3a and A001-CH3-V2-3b were found to be stable. These configurations correspond to CH₃ being adsorbed on top of one of titanium atoms which are located in the same [100] row as the V_{O2} vacancy. They have an adsorption energy of 33.99 kcal/mol, which is greater than 26.35 kcal/mol for A001-CH3-V2-1a. Adsorption of CH₃ in the [100] row neighbouring the one containing the V_{O2} oxygen vacancy results in spontaneous migration of the V_{O2} oxygen vacancy to a V_{O1} vacancy. The

presence of a V_{O2} vacancy stabilizes the adsorption of CH₃ on a titanium atom in close proximity of the vacancy.

4.4.2.2.5. Summary of CH_x adsorption on the reduced anatase (001) surface with a V_{O2} oxygen vacancy

The influence of the presence of a V_{O2} vacancy on the adsorption of CH_x radicals (x = 0 – 3) on the anatase (001) surface has been studied in this section. The adsorption energies of the CH_x species on the reduced anatase (001) surface containing a V_{O2} vacancy are shown in Table 9. For V_{O1} we find that in the case of CH₂ and CH₃, the maximal adsorption energy increases. In the case of V_{O2} the maximal adsorption energy increases for all CH_x (x = 0 – 3). The configurations with the maximal adsorption energy for each adsorbed species are A001-C-V2-1a, A001-CH-V2-2a, A001-CH₂-V1-3a, and A001-CH₃-V2-3x (x = “a”–“b”). The influence on each adsorption configuration can be positive or negative, not only depending on the considered configuration itself, but also on the position of the oxygen vacancy relative to the adsorbent. The different influence of V_{O2} on the different adsorption configurations also results in a shift of the relative stabilities of the different configurations and therefore on their distribution on the surface.

Table 9. The adsorption energy for the different adsorption configurations (E_{ads}), on the stoichiometric surface and on the reduced surface with a V_{O_2} oxygen vacancy on the different locations “a”-“d”. (X marks configurations that were found unstable or could not be created, the configurations which are no longer equivalent to the configurations on the stoichiometric surface caused by the fact that certain bonds no longer can be formed are shown in boldface)

	Adsorption configuration	Stoichiometric	E_{ads} (kcal/mol)			
			a	b	c	d
C	A001-C-S-1	153.71	158.71	148.64	158.71	148.64
	A001-C-S-2	153.40	158.39	148.20	158.39	148.20
	A001-C-S-3	118.39	137.56	120.61	111.20	124.37
CH	A001-CH-S-1	118.07	125.31	117.10	125.31	117.10
	A001-CH-S-2	117.27	126.12	116.68	126.12	116.68
	A001-CH-S-3	107.20	X	111.23	88.57	103.02
	A001-CH-S-4	83.11	115.23	115.30	72.92	68.61
	A001-CH-S-5	0.33	106.89	64.65	100.93	52.49
CH₂	A001-CH ₂ -S-1	84.49	86.46	81.96	86.46	81.96
	A001-CH ₂ -S-2	84.49	86.77	81.79	86.77	81.79
	A001-CH ₂ -S-3	56.12	92.97	56.72	47.91	62.88
	A001-CH ₂ -S-4	54.77	61.42	43.60	61.43	40.86
CH₃	A001-CH ₃ -S-1	29.56	26.35	25.37	26.35	25.37
	A001-CH ₃ -S-2	7.80	X	8.81	15.35	11.03
	A001-CH ₃ -V ₂ -3	X	33.99	33.99	X	X

4.4.2.3. Reduced anatase (001) surface containing a V_{O3} oxygen vacancy

The relative position of V_{O3} is indicated with the letters “a”-“d”, as indicated in Figure 21. Position “a” is the removal of the V_{O3} oxygen closest to the adsorbed C, position “b” is the removal of the V_{O3} oxygen in the same [010] row as “a”. Positions “c” and “d” are equivalent to positions “a” and “b”, respectively, but in the neighbouring [010] row. The adsorption energies of the CH_x species on the reduced anatase (001) surface containing a V_{O3} vacancy are shown in Table 10.

4.4.2.3.1. Adsorption of C

In Figure 32 the difference in adsorption energy of C on the stoichiometric surface and on the reduced surface with a V_{O3} vacancy is shown. The influence of V_{O3} on A001-C-S-1 and A001-C-S-2 is found to be almost identical. The adsorption is influenced the most for positions “a” and “d” of V_{O3}, with $\Delta E_{\text{ads}} \approx -3.8$ kcal/mol. It is found that for A001-C-V3-3a and A001-C-V3-3c the adsorption strength is not influenced significantly ($\Delta E_{\text{ads}} \approx -0.9$ kcal/mol). For A001-C-V3-3b, on the other hand, the adsorption strength drops by ~ 7 kcal/mol.

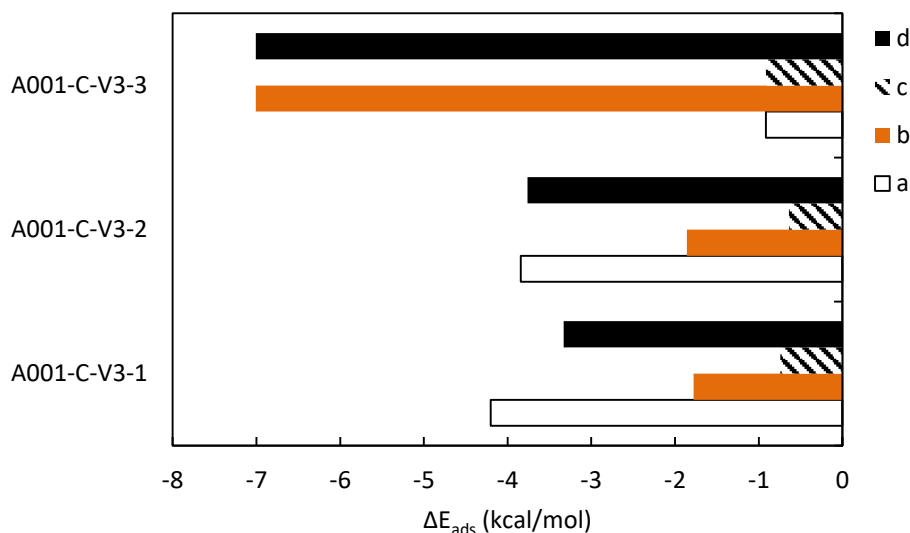


Figure 32. The difference in adsorption energy of the adsorption configurations of C on a reduced anatase (001) surface with a V_{O3} vacancy (location = “a”-“d”) relative to the A001-C-S-z (z=1-3) configurations.

4.4.2.3.2. Adsorption of CH

In Figure 33 the difference in adsorption energy of CH on the stoichiometric surface and on the reduced surface with a V_{O3} vacancy is shown. We find that V_{O3} influences the adsorption in the A001-CH-V3-1 and A001-CH-V3-2 configurations in a similar way. The adsorption energy decreases by ~ 2.2 kcal/mol for A001-CH-V3-1a and A001-CH-V3-1b, and with ~ 1.8 kcal/mol for A001-CH-V3-2a and A001-CH-V3-2b. The influence of V_{O3} on positions “c” and “d” is weaker. For A001-CH-V3-3 the influence of the vacancy is found to be the greatest if it is located in the same [100] row as the adsorbed CH. ($\Delta E_{\text{ads}} \approx -10$ kcal/mol for A001-CH-V3-3a and $\Delta E_{\text{ads}} \approx -9$ kcal/mol for A001-CH-V3-3b). For all positions of V_{O3} we find a positive influence on the adsorption energy in the A001-CH-V3-4 configuration. For these configurations one of the Ti-O_{2c} bonds is broken on

each side of the adsorbed CH. The C-O_{2c} bond lengths decrease from 1.33 Å in the A001-CH-S-4 configuration to 1.28 Å in the A001-CH-V3-4 configuration.

The O_{V02} in A001-CH-V3-5a and A001-CH-V3-5c closest to V_{O3} undergoes spontaneous migration to the middle of the location of O_{V02} and O_{V03} in the stoichiometric surface. The adsorption energy increases by ~56 kcal/mol. If V_{O3} is located at positions “b” or “d” then one Ti-C bond breaks spontaneously, and the CH points upwards on top of Ti. The adsorption energy increases with ~96 kcal/mol.

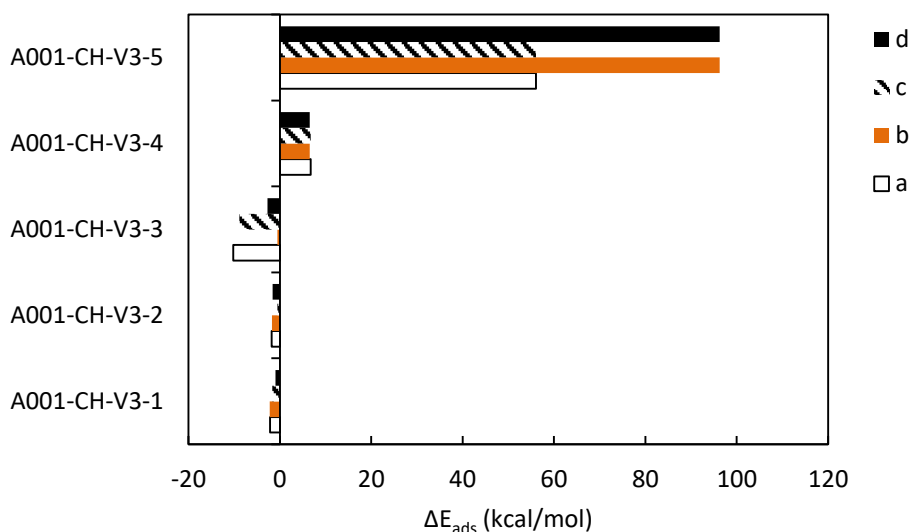


Figure 33. The difference in adsorption energy of the adsorption configurations of CH on a reduced anatase (001) surface with a V_{O3} vacancy (location = “a”-“d”) relative to the A001-CH-S-z (z=1-5) configurations.

4.4.2.3.3. Adsorption of CH₂

In Figure 34 the difference in adsorption energy of CH₂ on the stoichiometric surface and on the reduced surface with a V_{O3} vacancy is shown. For A001-CH2-V3-1 and A001-CH2-V3-2 the influence of V_{O3} is found to be almost identical. The drop in adsorption energy ranges from ~-0.21 kcal/mol for A001-CH2-V3-1a to ~-2.48 kcal/mol for A001-CH2-V3-1c relative to the adsorption on the stoichiometric surface. For A001-CH2-V3-3a and A001-CH2-V3-3c the adsorption energy goes down by 4.66 kcal/mol, while a decrease of only 0.39 kcal/mol is found if the oxygen vacancy is present in the neighbouring [100] row. For A001-CH2-V3-4b and A001-CH2-V3-4d one Ti-O_{2c} bonds breaks on each side of the adsorbed CH₂. The adsorption strength increases in this configuration relative to the A001-CH2-S-4 configuration. A001-CH2-V3-4a and A001-CH2-V3-4c show a small drop in adsorption strength ($\Delta E_{\text{ads}} = 0.22$ kcal/mol). In this configuration none of the Ti-O_{2c} bonds are broken.

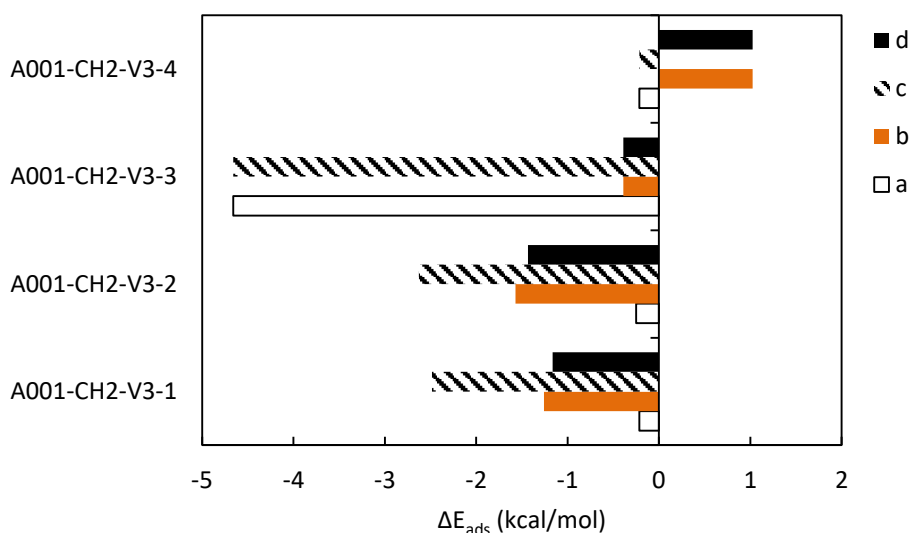


Figure 34. The difference in adsorption energy for the adsorption configurations of CH₂ on a reduced anatase (001) surface containing a V_{O3} vacancy (location = “a”-“d”) relative to the A001-CH2-S-z (z=1-4) configurations.

4.4.2.3.4. Adsorption of CH₃

In Figure 35 the difference in adsorption energy of CH₃ on the stoichiometric surface and on the reduced surface with a V_{O3} vacancy is shown. The adsorption of CH₃ in configuration A001-CH3-V3-1 is not influenced significantly: The change in adsorption energy ranges from -0.88 kcal/mol for A001-CH3-V3-1d to 1.22 kcal/mol for A001-CH3-V3-1b.

For A001-CH3-V3-2 it is found that the presence of the oxygen vacancy decreases the CH₃ adsorption energy for all vacancy positions. For A001-CH3-V3-2a and A001-CH3-V3-2c the adsorption becomes unstable with respect to the gas phase CH₃ radical. A001-CH3-V3-2b and A001-CH3-V3-2d, on the other hand, remain stable.

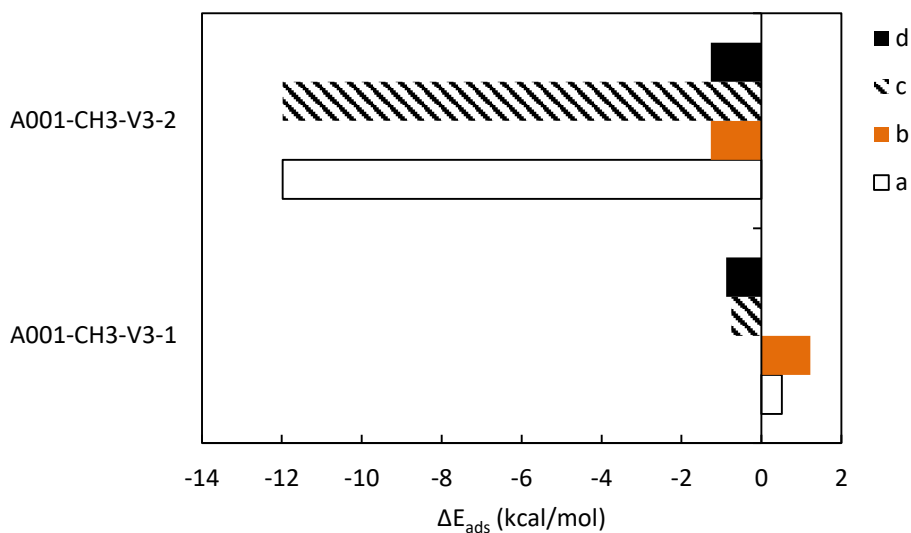


Figure 35. The difference in adsorption energy for the adsorption configurations of CH₃ on a reduced anatase (001) surface with a V_{O3} vacancy (location = “a”–“d”) relative to the A001-CH3-S-z (z=1-2) configurations.

Apart from the adsorption configurations on the reduced anatase (001) surface which have an equivalent on the stoichiometric surface, a new adsorption configuration is found to be stable on the reduced surface, A001-CH3-V3-3x (x = “a”–“d”). A001-CH3-V3-3a and A001-CH3-V3-3b correspond to CH₃ being adsorbed on top of titanium in the same [010] row as the V_{O3} vacancy. They have an adsorption energy of 37.04 kcal/mol and 21.57 kcal/mol, respectively. This means that A001-CH3-V3-3a is more stable than A001-CH3-V3-1b, which has an adsorption energy of 30.78 kcal/mol. In the neighbouring [010] row the adsorption of CH₃ on top of a titanium atom results in the adsorption configurations A001-CH3-V3-3c and A001-CH3-V3-3d, with an adsorption energy 24.77 kcal/mol and 27.10 kcal/mol, respectively.

4.4.2.3.5. Summary of CH_x adsorption on the reduced anatase (001) surface with a V_{O3} oxygen vacancy

The influence on the adsorption of CH_x radicals (x=0-3) of V_{O3} in an anatase (001) surface has been studied in this section. The V_{O3} vacancy increases the maximal adsorption strength only for the CH₃ radical. The adsorption configuration of CH₃ with the new maximal adsorption energy is A001-CH3-V3-3a. The adsorption energy corresponding with this configuration is 37.04 kcal/mol, which is an increase of 25% relative to A001-CH3-S-1. As is the case for the other vacancies, the influence on each adsorption configuration can be positive or negative, thereby changing the relative distribution of the adsorbent on the surface.

Table 10. The adsorption energy for the different adsorption configurations (E_{ads}), on the stoichiometric surface and on the reduced surface with a V_{O_3} oxygen vacancy on the different locations “a”-“d”. (X marks configurations that were found unstable or could not be created, the configurations which are no longer equivalent to the configurations on the stoichiometric surface caused by the fact that certain bonds no longer can be formed are shown in boldface)

	Adsorption configuration	Stoichiometric	E_{ads} (kcal/mol)			
			a	b	c	d
C	A001-C-S-1	153.71	149.51	151.94	152.97	150.38
	A001-C-S-2	153.40	149.55	151.54	152.76	149.64
	A001-C-S-3	118.39	117.47	111.38	117.47	111.38
<hr/>						
CH	A001-CH-S-1	118.07	115.89	115.84	116.42	117.11
	A001-CH-S-2	117.27	115.43	115.55	116.70	115.67
	A001-CH-S-3	107.20	96.95	106.67	98.34	104.51
	A001-CH-S-4	83.11	89.81	89.60	89.81	89.60
	A001-CH-S-5	0.33	56.40	96.56	56.40	96.56
<hr/>						
CH₂	A001-CH ₂ -S-1	84.49	84.27	83.23	82.00	83.32
	A001-CH ₂ -S-2	84.49	84.24	82.91	81.86	83.05
	A001-CH ₂ -S-3	56.12	51.46	55.73	51.46	55.73
	A001-CH ₂ -S-4	54.77	54.56	55.80	54.56	55.80
<hr/>						
CH₃	A001-CH ₃ -S-1	29.56	30.07	30.78	28.81	28.68
	A001-CH ₃ -S-2	7.80	-4.18	6.53	-4.18	6.53
	A001-CH ₃ -V3-3	X	37.04	21.57	24.77	27.10

4.4.3. Effect of oxygen vacancy defects on the distribution of adsorbed CH_x (x = 0 – 3) radicals

We have shown in section 4.4.2 that the presence of oxygen vacancy defects in an anatase (001) surface influences the adsorption of C and CH_x (x=1-3) radicals at the surface. In this section we will determine the relative probability of finding an adsorbed particle in a certain adsorption configuration either on a stoichiometric part of the surface or at or near an oxygen vacancy at equilibrium conditions. We determine the relative probability by using the Frenkel equation¹⁹⁶:

$$\tau_{config} = \frac{1}{\nu_0} * \exp\left(\frac{E_{ads}}{k_B * T}\right)$$

Where τ_{config} is the mean lifetime of the particle in a certain adsorption configuration, and ν_0 the vibrational frequency of the adsorbed particle. We calculated ν_0 for a number of different adsorption configurations and found that ν_0 varies with a factor between 0.66 and 3.61. However, we found for adsorption configurations, for which ν_0 varies strongly from the ν_0 of the most stable configuration, that the exponential part of the Frenkel equation varies with at least 11 orders of magnitude. These findings allow us to assume ν_0 to be constant, since the influence of ν_0 on the mean lifetime will be insignificant compared to the influence of the exponential part of the Frenkel equation. This allows us to calculate the relative probability (see equation below) of a configuration i by multiplying the average lifetime, $\tau_{config,i}$, by the percentage, n_i , of adsorption sites for which this configuration exists divided by the sum of the product of the average lifetime and percentage of adsorption sites for each configuration j, assuming ν_0 to be a constant:

$$P_i = \frac{n_i * \tau_{config,i}}{\sum_j n_j * \tau_{config,j}} = \frac{n_i * \exp\left(\frac{E_{ads,i}}{k_B * T}\right)}{\sum_j n_j * \exp\left(\frac{E_{ads,j}}{k_B * T}\right)}$$

We divided the surface into four regions, *viz.* a stoichiometric region, where no oxygen vacancies are present near the adsorbed particle, and one region for each vacancy, to determine the influence of the oxygen vacancies on the adsorption. We also give a weight to each oxygen vacancy based on their equilibrium distribution in the surface at 400 K. As can be seen in Table 11 to Table 14, V_{O1} will have by far the greatest influence on the adsorption distribution, caused by the much greater abundance of V_{O1} in the surface with respect to V_{O2} and V_{O3}. The oxygen vacancy regions we defined consist of nine adsorption sites per oxygen vacancy, one for the oxygen vacancy and eight for the direct surroundings of this vacancy. We have studied the adsorption at different concentrations of oxygen vacancies showing the importance of reduced states in the surface.

In Table 11 the relative probability of finding the adsorbed carbon in a certain region of the anatase (001) surface at equilibrium conditions is shown. At low defect concentrations almost all carbon will be present in the stoichiometric region of the surface. At an oxygen vacancy concentration of 11.11 % the concentration of C on the stoichiometric region drops to 0.00 %, since at this concentration no more stoichiometric region is left for C to adsorb. However, the probability of finding carbon adsorbed in the adsorption configurations A001-C-V1-1d or A001-C-V1-2d is 94.6 % for an 11.11% oxygen vacancy concentration, indicating that C preferentially will stay as far away as possible from the oxygen vacancy. At an oxygen vacancy concentration of 25% we find that the probability of finding C adsorbed in the adsorption configurations A001-C-V1-1d or A001-C-V1-2d decreases with about 5%. A large part of this decrease is caused by an increase in probability of finding C in the adsorption configurations A001-C-V1-1c or A001-C-V1-2c.

Table 11. The relative probability of finding an adsorbed C particle in a certain region of the surface.

% oxygen vacancies	0.00	2.50	5.00	10.00	11.11	16.67	25.00
Surface region	Relative probability (%)						
stoichiometric	100.00	99.60	98.89	89.03	0.00	0.00	0.00
V_{O1}	0.00	0.39	1.10	10.93	99.64	99.42	99.11
V_{O2}	0.00	0.00	0.00	0.04	0.32	0.52	0.81
V_{O3}	0.00	0.00	0.00	0.00	0.04	0.06	0.08
V_O (total)	0.00	0.40	1.11	10.97	100.00	100.00	100.00

In Table 12 the relative probability of finding the adsorbed CH radical in a certain region of the anatase (001) surface at equilibrium conditions is shown. The influence of oxygen vacancies on the adsorption of CH is larger than for C. For a vacancy concentration between 5 and 10 % we find that the probability of finding the CH near an oxygen vacancy becomes larger than 50%. At 10 % defect concentration we find 8.5% of the adsorbed CH at the V_{O1} oxygen vacancy in the A001-CH-V1-1a configuration. This means that a fraction of CH would be adsorbed close to the vacancy, where the influence of the vacancy on possible reactions will be the greatest. However, 48.7 % is found in a [010] row neighbouring the V_{O1} oxygen vacancy. The probability of finding CH in the A001-CH-V1-1a configuration increases to 14.7 %, 24.4 %, and 37.6 % for an oxygen vacancy concentration of 11.11 %, 16.67 % and 25 %, respectively.

Table 12. The relative probability of finding an adsorbed CH particle in a certain region of the surface.

% oxygen vacancies	0.00	2.50	5.00	10.00	11.11	16.67	25.00
Surface region	Relative probability (%)						
stoichiometric	100.00	95.74	88.86	42.03	0.00	0.00	0.00
V_{O1}	0.00	4.20	10.99	57.20	98.67	98.16	97.73
V_{O2}	0.00	0.06	0.15	0.77	1.33	1.83	2.26
V_{O3}	0.00	0.00	0.00	0.00	0.01	0.01	0.01
V_O (total)	0.00	4.26	11.14	57.97	100.00	100.00	100.00

In Table 13 the relative probability of finding the adsorbed CH₂ radical in a certain region of the anatase (001) surface at equilibrium conditions is shown. The probability of finding CH₂ in the A001-CH₂-V1-1a at equilibrium conditions is almost 100% at all oxygen vacancy concentrations, while on the stoichiometric surface CH₂ is distributed equally between the A001-CH₂-S-1 and A001-CH₂-S-2 configurations.

Table 13. The relative probability of finding an adsorbed CH₂ particle in a certain region of the surface.

% oxygen vacancies	0.00	2.50	5.00	10.00	11.11	16.67	25.00
Surface region	Relative probability (%)						
stoichiometric	100.00	0.00	0.00	0.00	0.00	0.00	0.00
V_{O1}	0.00	100.00	100.00	100.00	100.00	100.00	100.00
V_{O2}	0.00	0.00	0.00	0.00	0.00	0.00	0.00
V_{O3}	0.00	0.00	0.00	0.00	0.00	0.00	0.00
V_O (total)	0.00	100.00	100.00	100.00	100.00	100.00	100.00

In Table 14 the relative probability of finding the adsorbed CH₃ radical in a certain region of the anatase (001) surface at equilibrium conditions is shown. For CH₃ we find that almost all adsorbed CH₃ can be found in either the A001-CH₃-V1-3a or the A001-CH₃-V1-3b adsorption configuration at all oxygen vacancy concentrations.

Table 14. The relative probability of finding an adsorbed CH₃ particle in a certain region of the surface.

% oxygen vacancies	0.00	2.50	5.00	10.00	11.11	16.67	25.00
Surface region	Relative probability (%)						
stoichiometric	100.00	0.00	0.00	0.00	0.00	0.00	0.00
V_{O1}	0.00	100.00	100.00	100.00	100.00	100.00	100.00
V_{O2}	0.00	0.00	0.00	0.00	0.00	0.00	0.00
V_{O3}	0.00	0.00	0.00	0.00	0.00	0.00	0.00
V_O (total)	0.00	100.00	100.00	100.00	100.00	100.00	100.00

From the results in this section it becomes clear that oxygen vacancies significantly influence the distribution of the adsorbed particles at the surface and create new possible adsorption configurations. This in turn will have an effect on which reaction pathways will be accessible for the adsorbed particles, apart from the possible changes to reaction barriers, which can be either a positive or a negative effect. It can therefore be concluded that oxygen vacancies are expected to have a profound effect on the possible reaction products that can be formed during plasma-catalytic conversion of methane to useful chemicals.

4.5. Conclusions

Detailed DFT calculations at the PBE level were carried out to elucidate the adsorption configurations and energies of CH_x -radicals ($x = 0 - 3$) on stoichiometric and reduced anatase (001) surfaces in the presence of oxygen vacancies. For the oxygen vacancies in anatase (001) we found that a surface oxygen vacancy is the most stable vacancy, in contrast to oxygen vacancies in anatase (101) and (1x4)-reconstructed anatase (001) surfaces, which are found to be the most stable in the subsurface.¹²²

On the stoichiometric anatase (001) surface we find that the maximal adsorption energies for C, CH, CH_2 and CH_3 are 153.71 kcal/mol, 118.07 kcal/mol, 84.49 kcal/mol and 29.56 kcal/mol, respectively. The presence of oxygen vacancies in and at the surface influences the maximal adsorption energy. For the adsorption of the C-radical, the adsorption energy dropped from 153.71 kcal/mol on the stoichiometric surface to 150.77 kcal/mol (-1.9%) and 152.97 kcal/mol (-0.5%) for $\text{V}_{\text{O}1}$ and $\text{V}_{\text{O}3}$, respectively, and increases to 158.71 kcal/mol (+3.3%) for $\text{V}_{\text{O}2}$. Also for CH-radical adsorption the maximal adsorption energy drops from 118.07 kcal/mol on the stoichiometric surface to 117.05 kcal/mol (-0.9%) and 115.89 kcal/mol (-1.8%) for $\text{V}_{\text{O}1}$ and $\text{V}_{\text{O}3}$, respectively, and increased to 126.12 kcal/mol (+6.8%) for $\text{V}_{\text{O}2}$. For CH_2 we found an increase in maximal adsorption energy from 84.49 kcal/mol on the stoichiometric surface to 99.93 kcal/mol (+18.3%) and 92.97 kcal/mol (+10.0%) for $\text{V}_{\text{O}1}$ and $\text{V}_{\text{O}2}$, respectively, and a drop to 84.27 kcal/mol (-0.3%) for $\text{V}_{\text{O}3}$. For CH_3 , however, we find an increase in the maximal adsorption energy from 29.56 kcal/mol on the stoichiometric surface to 56.94 kcal/mol (+92.6%) in the presence of $\text{V}_{\text{O}1}$, to 33.99 kcal/mol (+15.0%) for $\text{V}_{\text{O}2}$ and 37.04 kcal/mol (+25.3%).

Apart from influencing the maximal adsorption strength, oxygen vacancies are also found to influence the stability of the various adsorption configurations differently, which results in a different probability of each adsorption configuration. We have studied the distribution of the adsorbed particles on the anatase (001) surface at different oxygen vacancy concentrations. We find that C preferentially adsorbs far away from the oxygen vacancy, while CH₂ and CH₃ adsorb preferentially at the oxygen vacancy site. CH partially adsorbs preferentially further away from the vacancy and partially at the oxygen vacancy. The oxygen vacancies significantly influence the distribution of adsorbed CH_x particles, which will in turn influence the accessible (new) reaction pathways for the adsorbed species. Based on these results, future computational quantum mechanical and classical studies targeting the reaction pathways themselves may be envisaged, taking into account the influence of oxygen vacancies on the pathways and the dynamics of adsorption and co-adsorption, in order to gain a more fundamental insight in plasma-catalytic conversion of greenhouse gases.

**Chapter 5 How Oxygen
Vacancies Activate
CO₂ Dissociation on
TiO₂ Anatase (001)**

5.1. Introduction

To achieve a strong reduction in the global CO₂ concentration, the reduction of the CO₂ emission could be combined with the conversion to added-value chemicals. Amongst other techniques, including e.g. plasma conversion⁷⁻¹⁴, heterogeneous catalysis on reactive metal and metal oxide surfaces is a viable route¹⁵. Indeed, this approach combines a mitigation of the greenhouse effect with the chemical conversion of CO₂ to useful chemicals.

In 1979 Inoue and co-workers reported that the aqueous suspension of a semiconductor (TiO₂, ZnO, CdS, etc.) can photoreduce CO₂ to form formic acid, formaldehyde, methanol and methane.¹⁹⁷ Among the various catalysts reported in that paper, TiO₂ is often used as a model system for the catalytic properties of metal oxides.

To improve the performance of catalytic processes on TiO₂ it is important to get a better fundamental insight in the adsorption and activation of CO₂ on TiO₂ surfaces. In this chapter we study the interaction of CO₂ with anatase (001), and more specifically the influence of oxygen vacancies on the adsorption and activation of CO₂. Yu et al. found that the photocatalytic reduction of CO₂ on anatase is strongly influenced by the ratio of (101) and (001) facets in the crystal.¹⁹⁸ They found that the sample with 58% (001) facet has the highest reactivity for the photocatalytic reduction of CO₂. Also, a higher methane production was reported for samples consisting of mostly the (001) facet than the samples consisting of mostly the (101) facet. For other small molecules it is suggested that the (001) facet has a higher reactivity compared to the most stable (101) facet.^{199,200} Mino et al. performed combined FTIR and DFT studies of the adsorption of CO and CO₂ on TiO₂ anatase surfaces and found that the surface Ti sites present at the (001) facet have a lower Lewis acidity than

the Ti sites at the (101) facet, and the surface oxygen sites exhibit a stronger Lewis basicity on anatase (001) than on the anatase (101) surface.^{201,202} This strongly influences the adsorption of CO₂ on anatase. CO₂ is mainly adsorbed in linear form on the anatase (101) surface with an adsorption energy of -11.1 kcal/mol, as the carbonate-like adsorption configuration has an adsorption energy of only -3.7 kcal/mol,¹⁵⁸ while on the anatase (001) surface CO₂ adsorbs mostly in a carbonate like structure with an adsorption energy of -30.1 kcal/mol and the linear configuration only has an adsorption energy of -5.3 kcal/mol.²⁰²

Apart from the inherent difference in Lewis acidity and basicity of the surfaces, it is possible to increase the Lewis basicity of the surface by introduction of oxygen vacancies.²⁰³ Sorescu et al. found that oxygen vacancies significantly influence the adsorption properties of CO₂ on rutile (110) and anatase (101) surfaces, and they anticipated that these defects play an important role in the complex surface chemistry of CO₂ catalysis.^{158,181} Previous studies have also shown a significant influence of the presence of oxygen vacancies on the adsorption properties of H₂O, O₂, and methane derived radicals.^{152,157,180,204} Barzan et al. have shown the unprecedented potential of TiO₂ samples reduced in a H₂ atmosphere in the conversion of ethylene to high density polyethylene under mild conditions and without any activator.²⁰⁵ It is shown that reduced TiO₂ always has a higher catalytic activity for the reduction of CO₂ as the presence of point defects provide more active sites.²⁰⁶ The presence of Ti³⁺ generated by the presence of oxygen vacancies is suggested to facilitate CO₂ reduction.²⁰⁷ The intrinsic defects can act as active sites for heterogeneous catalysis. Understanding the influence of oxygen vacancies on the adsorption and reactions of CO₂ on TiO₂ is thus key for a fundamental understanding of the catalytic activity of TiO₂. As the position of the defects determines the surface chemistry, we here study the

adsorption and dissociation of CO₂ on anatase (001) surfaces containing one of the three most stable oxygen vacancies.²⁰⁴ For anatase (101) it has been shown experimentally¹⁶² and suggested by simulations^{151,208} that oxygen vacancies diffuse easily even at room temperature, therefore we expect that the same is true for anatase (001). This means that the different oxygen vacancies will all be accessible for reactions and adsorption.

5.2. Computational details

The calculations were performed using the Vienna ab initio simulation package (VASP).^{186,187} For the treatment of the exchange and correlation, the Perdew-Burke-ernzerhof (PBE) functional was applied,¹¹³ using plane wave basis sets and the projector-augmented wave method¹⁸⁸ as implemented in VASP. It has been shown by Sorescu et al. that long-range dispersion interactions play an important role in the interactions of CO₂ with TiO₂.¹⁵⁸ Therefore, we have corrected the PBE functional with long-range dispersion interactions by applying the Tkatchenko and Scheffler method²⁰⁹ as implemented in VASP.²¹⁰

The stoichiometric anatase (001) surface was modelled using a (2x2) supercell containing 48 atoms corresponding to four TiO₂ layers. We fixed the bottom layer of the surface at the bulk positions and expanded the simulation box to create a vacuum layer of ~ 16 Å between adjacent surfaces to prevent influence of neighbouring slabs on the adsorption properties. An energy cutoff of 440 eV was used, and the sampling of the Brillouin zone was performed using 6x6x1 k-points for the surface models and only the gamma-point for the CO₂ and CO molecules. Geometry optimizations were performed with endpoint criterion of the residual forces to be below 0.03 eV.Å⁻¹. Spin polarization was applied for all calculations.

The vibrational analysis was performed with the finite difference method implemented in VASP. Two sets of calculations were performed for the vibrational analysis. In the first set of calculations that were performed, the finite difference displacements were only applied to the CO₂ molecule. The resulting frequencies were reported as the vibrational frequencies of the adsorbed molecule. The second set of calculations included the displacements to both the CO₂ molecule and the top layer of the TiO₂ surface. These results were used for the thermodynamical analysis as performed with the TAMKIN tool.²¹¹

The adsorption energy of CO₂ on the stoichiometric and reduced surfaces is calculated as follows:

$$E_{ads} = E_{CO_2+surface} - E_{CO_2} - E_{surface}$$

where E_{CO_2} is the total energy of the optimized gas phase CO₂ molecule with zero-point energy corrections included, $E_{surface}$ is the total energy of the respective surface with zero-point energy corrections and $E_{CO_2+surface}$ is the total energy of the respective surface with CO₂ adsorbed with zero-point energy corrections.

The extent of charge transfer from the surface to the adsorbed CO₂ molecule was calculated using Hirshfeld charges.²¹² To study the adsorption mechanism and the effect of the oxygen vacancies on the activation barrier of CO₂ reduction, we calculated the corresponding minimum energy barriers with Nudged Elastic Band (NEB)^{159,213–217} as implemented in the VASP code.

5.3. Results and discussion

5.3.1. CO₂ adsorption on the oxidized (non-defective) anatase (001) surface

We identified different binding configurations of CO₂ on the stoichiometric surface, of which a pictorial view is shown in Figure 36. The relevant bond lengths, bond angles, adsorption energies, vibrational frequencies and charge transfer are given in Table 15. The first and most stable configuration is a monodentate carbonate-like structure, B(I). In this configuration, CO₂ binds with its oxygen atoms to two 5-fold coordinated Ti(5f) centers in the same [010] row, and with its carbon atom to the two-fold coordinated oxygen (O(2f)) center of the Ti-O(2f)-Ti bridge. The O-C-O bond angle is 129.9°. This configuration has a strong exothermic adsorption energy of -32.8 kcal/mol, despite the energy cost of bending the CO₂ from its linear gas phase configuration to the bent configuration and the significant deformation of the anatase surface. The O(2f), participating in the monodentated carbonate-like structure, is displaced inward by 0.8 Å, and the Ti-O(2f)-Ti angle changes from 155.2° to 179.2°. This structure has previously been reported by Mino, Indrakanti and Pipornpong, with adsorption energies ranging from -30.1 to -26.2 kcal/mol.^{202,218,219} However, they did not include zero point energy corrections, nor long-range dispersion corrections.

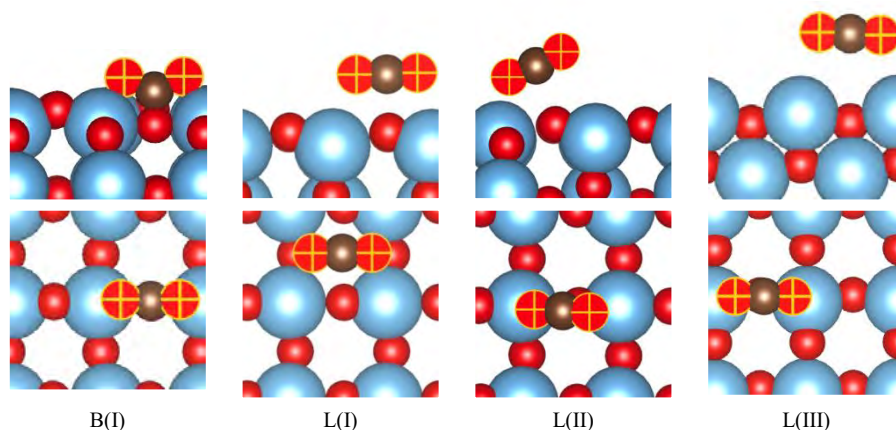


Figure 36. The different adsorption configurations of CO_2 on the stoichiometric anatase (001) surface, in side view and top view (upper and lower panels, respectively). Ti = blue, O_{TiO_2} = red, O_{CO_2} = red with yellow plus sign, C = brown. B(I) is a strong chemisorbed monodentate carbonate configuration, while L(I), L(II) and L(III) are physisorbed configurations.

Mino et al. reported IR frequencies for the monodentated carbonate configuration of 1587 and 1316 cm^{-1} for spectra taken at room temperature of CO_2 adsorbed on TiO_2 anatase nanopowder outgassed at 823 K to remove residual co-adsorbed water and fully oxidized by exposure to O_2 at 723 K.²⁰² These values correspond well with the values obtained in our calculation, *viz.* 1558 and 1313 cm^{-1} , respectively. The increasing C-O bond length (from 1.18 Å in gas phase to 1.28 Å in the B(I) configuration), the strong red-shift of the asymmetric stretch (from 2365 cm^{-1} to 1558 cm^{-1}), and the significant charge transfer to CO_2 (-0.214 a.u.) as resulting from the adsorption, all suggest an activation of CO_2 for the reduction of CO_2 . However, as shown by Pipornpong et al., dissociative adsorption of CO_2 on a fully oxidized anatase (001) surface has an unfavourable adsorption energy of 76.2 kcal/mol.²¹⁹ In comparison, we find a similar dissociative adsorption energy of 67.4 kcal/mol and a dissociation energy barrier of

113.6 kcal/mol, as will be shown later. It is thus clear that CO₂ dissociation on the fully oxidized surface will not occur without the help of co-adsorbates that stabilize the transition state and the reaction products, i.e., CO and atomic oxygen adsorbed on the fully oxidized surface.

Apart from the strong chemisorbed monodentate carbonate configuration, there exist several physisorbed configurations, which form shallow metastable intermediates upon adsorption of CO₂ from the gas phase (see configurations L(I), L(II) and L(III) in Figure 1). In particular, when CO₂ undergoes physisorption, it will subsequently convert to the B(I) configurations over low energy barrier pathways. These barriers range from 0.2 kcal/mol to 0.8 kcal/mol, and hence the conversion from any of the physisorbed configurations to the B(I) chemisorbed configuration will easily occur, even at room temperature. However, diffusion from one chemisorbed configuration to a neighbouring adsorption site requires crossing an energy barrier of 30.4 kcal/mol, which is not easily accessible at low temperatures. As this barrier is comparable to the desorption energy of 32.8 kcal/mol, desorption and diffusion will be competitive at elevated temperatures.

Table 15. Adsorption properties of CO₂ on a stoichiometric TiO₂ anatase (001), for the gas phase, chemisorbed (B(I)) and several physisorbed (L(I), L(II), L(III)) configurations; The bond lengths between Ti and O of CO₂, $r(\text{Ti-O}_{\text{CO}_2})$, between the surface O and C, $r(\text{O}_{\text{surf-C}}$, and between C and O of CO₂, $r(\text{C-O}_{\text{CO}_2})$, the bond angle of CO₂, $\alpha(\text{OCO})$, the adsorption energy, vibrational frequencies $\nu(\text{CO}_2)$, the charge transfer from the surface to CO₂, $\Delta q(\text{CO}_2)$ and the activation energy for diffusion to a B(I) adsorption configuration E_a .

Configuration	$r(\text{Ti-O}_{\text{CO}_2})$ (Å)	$r(\text{O}_{\text{surf-C}}$ (Å)	$r(\text{C-O}_{\text{CO}_2})$ (Å)	$\alpha(\text{OCO})$ (deg.)	E_{ads} (kcal/mol)	E_a (kcal/mol)
Gas phase			1.177, 1.177	180.0		
B(I)	2.073, 2.088	1.323	1.284, 1.280	129.9	-32.82	30.42
L(I)		2.956, 2.924	1.177, 1.177	177.7	-7.31	0.80
L(II)	2.460	2.514	1.187, 1.170	173.5	-6.19	0.20
L(III)	3.089, 3.249		1.177, 1.176	179.7	-4.34	0.26
			$\nu(\text{CO}_2)$ (cm ⁻¹)		$\Delta q(\text{CO}_2)$ (a.u.)	
Gas phase		1316	632	631		
B(I)		1558	1313	844	751	-0.214
L(I)		2356	1315	615	613	0.066
L(II)		2344	1304	622	566	0.104
L(III)		2358	1317	634	620	0.098

5.3.2. CO₂ adsorption on a reduced (defective) anatase (001) surface

As mentioned in the introduction of this chapter, the behaviour of reactive species under the influence of oxygen vacancies present in TiO₂ is a key factor in its catalytic activity. We determined the formation energy of different oxygen vacancies in anatase (001) in section 4.3. The position of the different oxygen vacancies is shown in Figure 37. The formation energies for V_{O1}, V_{O2}, V_{O3}, and V_{O4} are 102.9, 115.0, 110.8, and 132.7 kcal/mol, respectively.²⁰⁴ We will only investigate the influence of V_{O1}, V_{O2} and V_{O3}, as V_{O4} is too unstable to have a significant influence on the adsorption of CO₂.

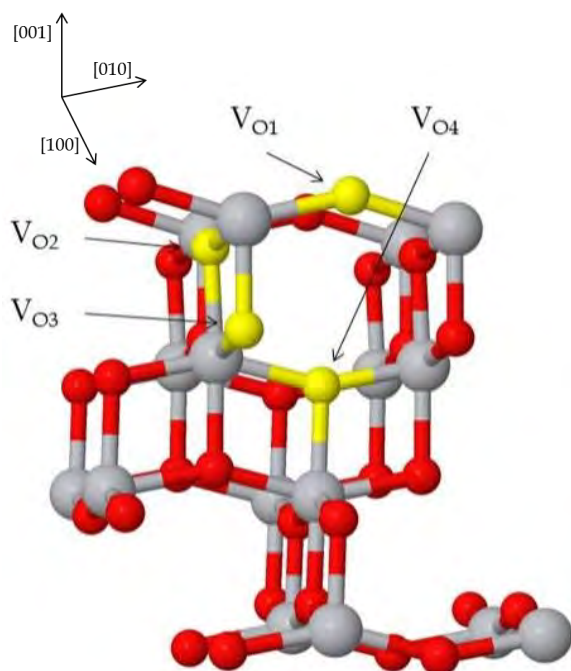


Figure 37. Different oxygen vacancies in an anatase (001) TiO₂ surface. (Ti = gray, O = red, oxygen vacancy = yellow)

5.3.2.1. CO₂ adsorption near an oxygen vacancy

In this section, we investigate the influence of the presence of different oxygen vacancies on the adsorption properties of the stable adsorption configurations found on the fully oxidized surface. The adsorption energies of CO₂ on the oxygen vacancy containing surface as well as the original adsorption strengths (i.e., on the fully oxidized surface) are shown in Figure 38. In panel a, site 0 corresponds to the stoichiometric configuration (i.e., without an oxygen vacancy present in the surface). Sites 1 and 2 correspond to an oxygen vacancy present closest to the adsorbed CO₂, and the vacancy present on the position of the neighbouring O(2f) in the same [010] row (see Figure 37) of the stoichiometric surface, respectively. Sites 3

and 4 are equivalent to sites 1 and 2, respectively, but in the neighbouring [010] row.

In panel b, site 0 corresponds to the configuration on the stoichiometric surface and site 1 corresponds to the oxygen vacancy present closest to the adsorbed CO₂ molecule. For B(I), site 2 is equivalent to site 1 as the removal of any of the V_{O2} oxygen atoms will result in the same adsorption configuration due to symmetry. For L(I), the oxygen vacancy is located in the parallel [010] row, and for L(II) and L(III) the oxygen vacancy is located in the parallel [100] row.

In panel c, site 0 corresponds to the configuration on the stoichiometric surface. Sites 1 and 2 correspond to the V_{O3} oxygen vacancy present closest to the adsorbed CO₂ and the vacancy present in the same [010] row of the neighbouring [100] row, respectively. Sites 3 and 4 are equivalent to sites 1 and 2, respectively, but in the neighbouring [010] row.

In general, the influence of the oxygen vacancy stays limited compared to the influence found on different TiO₂-surfaces. The adsorption energy does not change more than 5 kcal/mol for the bent configuration, and changes by about 2 kcal/mol for the physisorbed configurations. Also, the presence of the vacancy does not lead to additional charge transfer, and the bond length and red shift also stay very similar. In contrast, on the anatase (101) surface, it was found in literature that for the bent configuration the adsorption energy changes by up to 13 kcal/mol and for the physisorbed configuration up to 4.5 kcal/mol.¹⁵⁸

Only for the V_{O1} vacancy, a strong influence is found for the B(I) configuration, and this only occurs when the oxygen vacancy is present in the same [010] row and neighbouring the Ti-O(2f)-Ti bridge at which CO₂ is adsorbed. In this case a strong destabilisation of the binding configuration is found. The adsorption energy increases from -32.8 kcal/mol on the fully oxidized surface to 1.1 kcal/mol on the reduced

anatase (001) facet. The destabilization originates from both electronic and structural causes. The electronic destabilisation occurs due to the binding of the Lewis base centers of CO₂, i.e., the oxygen atoms, directly to the Lewis base centers of the surface (i.e., Ti³⁺), which are generated upon the introduction of an oxygen vacancy. Moreover, the carbon, the Lewis acid center, is not directly bonded to the Ti³⁺ centers, thus not leading to any stabilisation of the adsorbed configurations.

Apart from this first electronic contribution, we expect the largest part of the destabilization to originate from the relaxation of the surface, which occurs after the formation of the V_{O1} oxygen vacancy, and which is counteracted by the adsorbed CO₂ molecule. The Ti-O(2f)-Ti angle is 145.6° for the stoichiometric surface and becomes 102.8° upon reduction for the Ti-O(2f)-Ti moiety located in the same [010] row as the oxygen vacancy. Once CO₂ adsorbs, this angle increases to 167.1° for B(I) located above the Ti-O(2f)-Ti bridge neighbouring the oxygen vacancy, thus introducing stress on the surface and thereby destabilizing the adsorption configuration.

The generally small influence of the reduction of the surface on the adsorption configurations of the stoichiometric surface compared to the generally larger influence as found on the anatase (101) surface by Sorescu et al.¹⁵⁸ can be explained by the inherent difference in Lewis acidity and basicity of both surfaces. As mentioned above, Mino et al.^{201,202} performed combined FTIR and DFT studies on the adsorption of CO and CO₂ on anatase (001) and (101) facets. They concluded that on the (001) facet the Lewis acidity of the Ti-centers is lower compared to the (101) facet, as indicated by the strong bonding of the Ti-cations with the O(2f) anions, resulting in a more screened electrostatic potential. The Lewis basicity of the surface oxygen sites, on the other hand, is higher on the (001) facet, as

indicated by the up-shift of the valence band characterized by the O 2sp states with the main contribution coming from the O(2f) sites.

In the study of Sorescu, it is found that on the stoichiometric anatase (101) surface CO₂ preferentially adsorbs in a nearly gas phase structure, Sorescu-L(I) ($E_{\text{ads}} = -11.1$ kcal/mol), while the bent configurations, Sorescu-B(I) ($E_{\text{ads}} = -3.7$ kcal/mol) and Sorescu-B(II) ($E_{\text{ads}} = -0.3$ kcal/mol), are unfavourable, as a result of the lower Lewis basicity of the surface oxygens compared to anatase (001).¹⁵⁸ If then an oxygen vacancy is introduced in the surface, new Lewis base centers are introduced causing a significant stabilization of the Sorescu-B(II) configuration ($E_{\text{ads}} = -16$ kcal/mol), which has a comparable structure as the B(I) configuration on the anatase (001) surface. However, on the anatase (001) surface the monodentated carbonate like structure B(I) is very stable ($E_{\text{ads}} = -32.8$ kcal/mol). This stronger interaction is due to the stronger Lewis basicity of the O(2f) surface oxygens, as also indicated by the greater charge transfer of -0.214 a.u. from the surface to CO₂ for B(I) compared to a charge transfer of -0.146 a.u. for Sorescu-B(II). In reality, this difference in charge transfer is likely to be larger, since the charge transfer for Sorescu-B(II) was calculated with the Bader method, while we employ the Hirshfeld method, and the Bader method tends to give larger charges compared to the Hirshfeld method.²²⁰ The smaller influence of the presence of oxygen vacancies in anatase (001) is thus due to the already large inherent Lewis basicity of anatase (001), and further increasing the Lewis basicity does not lead to significant change in interaction.

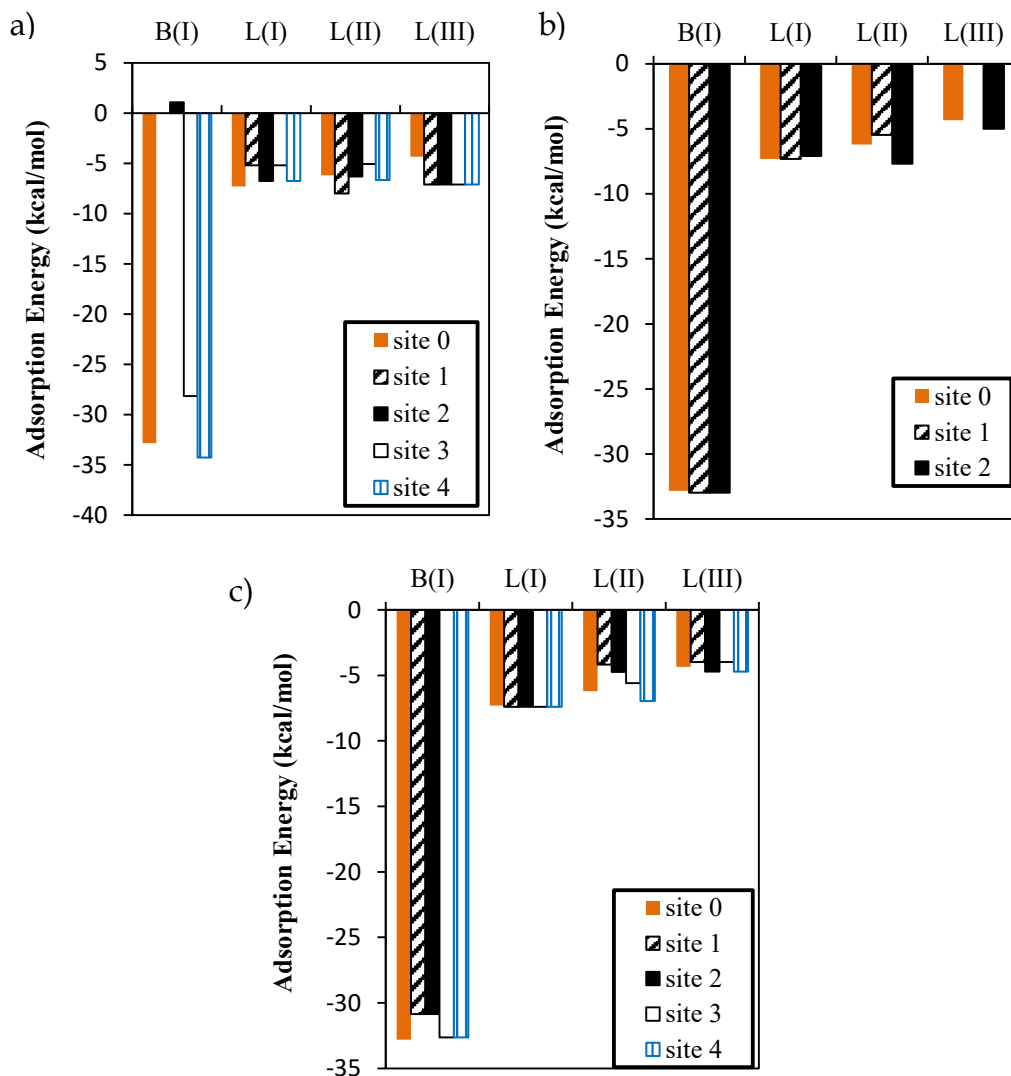


Figure 38. The adsorption energy of the adsorption configurations of CO₂ on a reduced anatase (001) surface with a a) V₀₁ vacancy b) V₀₂ vacancy c) V₀₃ vacancy.

Apart from the possible influence of the reduction of the TiO₂ surface on the original adsorption configurations, new adsorption possibilities arise on the reduced surfaces. A pictorial view of the newly formed adsorption configurations is shown in Figure 39, and the relevant bond lengths, bond

angles, adsorption energies, vibrational frequencies and charge transfer are given in Table 16.

5.3.2.2. CO₂ adsorption at an oxygen vacancy

5.3.2.2.1. At the surface bridging oxygen vacancy, V_{O1}

Three new adsorption configurations, D_VO1(I) to D_VO1(III), are found on the reduced surface containing a V_{O1} vacancy (see Figure 39). D_VO1(I) and D_VO1(II) are configurations which arise when an oxygen atom is removed from the surface. D_VO1(I) has an adsorption energy of -48.65 kcal/mol (see Table 16) and has a structure similar to the monodentated carbonate configuration B(I), which had an adsorption energy of -32.8 kcal/mol. However, opposed to the latter configuration, the carbon is no longer bonded to the surface Lewis base center, O(2f), as this is no longer available, but now binds to the newly formed Lewis base centers, the Ti³⁺ atoms. The strong stabilization is thus caused by the strong interaction of carbon with the metallic centers, and not due to interactions of the CO₂ oxygen atoms with the titanium atoms. A larger charge transfer from the surface to the CO₂ molecule is found for D_VO1(I) than for B(I), i.e., -0.338 a.u. vs. -0.214 a.u., respectively. Almost all this charge is transferred to the carbon atom: we calculate a charge of -0.247 a.u. to be transferred to the carbon compared to the charge located on the carbon atom in the gas phase geometry, while the charge on the oxygen atoms only changes by -0.039 a.u. and -0.052 a.u. The greater charge transfer to CO₂ and the stronger red-shift of the CO₂ vibrations in D_VO1(I) compared to B(I) indicates a better activation of the CO₂ molecule for CO₂ splitting. However, the C-O bond lengths do not change significantly (cf. Table 15 and Table 16). Pipornpong et al. reported a similar structure on the reduced anatase (001) surface, denoted as CO₂/[TiO₂+V_O]-C' in their publication.²¹⁹ They found

an adsorption energy of -93.74 kcal/mol for their adsorption configuration, which is much larger than the -48.65 kcal/mol reported in this work. We suspect that this significant difference might be caused by their use of frozen clusters. These frozen clusters do not allow relaxation of the surface when the oxygen vacancy is created, which causes a structure that is significantly less stable and therefore increases the adsorption energy as the adsorption of CO₂ will release a significant part of the stress in the structure.

The D_VO1(II) configuration (see Figure 39) is an adsorption configuration in which CO₂ is bent and one oxygen is located on the position where a surface oxygen atom was removed to create the vacancy. The adsorption energy is -25.25 kcal/mol (see Table 16). A strong charge transfer is noticeable to the carbon atom, caused by the weakened interaction with the oxygen located at the oxygen vacancy site, as this oxygen now fills the oxygen vacancy. The C-O bond length is increased from 1.177 Å in the gas phase to 1.346 Å for the oxygen located at the oxygen vacancy site and to 1.289 Å for the oxygen located above the Ti³⁺ site. The total charge transfer to CO₂ is -0.422 a.u., which is larger than for any previously discussed adsorption configuration. Most of this transferred charge is located on the carbon atom with a change of -0.286 a.u. compared to the gas phase structure. In this configuration, a strong red shift is again found, from 2365 cm⁻¹ to 1207 cm⁻¹. The longer C-O bonds, strong red shift and the significant charge transfer indicate the strongest activation of CO₂ reduction to CO thus far.

The last configuration that was found to be stable on the anatase (001) surface containing a surface oxygen vacancy is D_VO1(III) (see Figure 39). We have also tried obtaining this configuration on the stoichiometric surface. However, we find it spontaneously converts to B(I). Only when located near the surface oxygen vacancy, this configuration is found to be

stable. The adsorption configuration is -1.64 kcal/mol (see Table 16). As this configuration is only slightly stable, we expect it to either convert to B(I) or D_VO1(I), or else desorption will occur and not contribute significantly to the reactivity of anatase (001) with respect to reduction of CO₂. The C-O bonds are less activated than in the other obtained configurations. In particular, we find a smaller red shift of the asymmetric stretch, shorter C-O bonds, and a smaller charge transfer compared to the other chemisorbed configurations.

We have tried to reproduce the structure CO₂/[TiO₂+V_o]-C of Pipornpong et al.²¹⁹ In this non-dissociative adsorption configuration the oxygen vacancy is filled with one of the oxygen atoms of CO₂, and CO₂ is oriented in a similar manner as D_VO1(III). However, we found that this configuration is not stable and spontaneously converts to D_VO1(I). Possibly, Pipornpong et al. found this structure to be stable as the result of their frozen cluster approach, which can erroneously create an energy barrier between these two configurations.

5.3.2.2.2. At the first subsurface oxygen vacancy, V_{O2}

One new adsorption configuration, D_VO2(I), is found on the reduced surface containing a V_{O2} oxygen vacancy. In this configuration, CO₂ takes on a bent configuration and is very comparable to the D_VO1(I) configuration (see Figure 39). However, the CO₂ in this case is bonded to two Ti³⁺ atoms located in the same [100] row as opposed to the same [010] row. The adsorption energy for the D_VO2(I) configuration is -25.50 kcal/mol (see Table 16), which is significantly lower than the -32.96 kcal/mol found for the monodentated carbonate-like structure B(I) if a V_{O2} vacancy is present in the vicinity of the adsorbed CO₂ molecule. However, just as is the case for the D_VO1(I) configuration, a larger charge transfer

to CO₂ is found compared to the B(I) configurations. In view of this larger charge transfer and the comparable red-shift of the CO₂ vibrations (see Table 17), we expect a greater activation of CO₂ in this bonding configuration.

5.3.2.2.3. At the second subsurface oxygen vacancy, V_{O3}

When a V_{O3} oxygen vacancy is present, we find two new monodentated carbonate configurations on the anatase (001) surface. The only difference between the two configurations is their orientation relative to the oxygen vacancy. In the D_VO3(I) configuration, the oxygen atom of CO₂ that is bonded to the surface, is located above the titanium atom located at the oxygen vacancy site, while in the D_VO3(II) configuration this oxygen is located above the titanium atom in the same [010] row and neighbouring [100] row. As mentioned before we have tried to create similar configurations on the stoichiometric surface but found these to spontaneously convert to the B(I) configuration, also when V_{O3} is located in the neighbouring [010] row. The lower stability of D_VO3(I) and D_VO3(II) compared to the B(I) configuration and the similarity between the three configurations, indicates that the D_VO3(I) and D_VO3(II) will easily convert to B(I). Thus we do not expect a strong activation of the CO₂ molecule for CO₂ dissociation in these configurations. We rather expect that first a conversion of D_VO3(I) and D_VO3(II) to a B(I) configuration or diffusion of the oxygen vacancy creating a V_{O1} or V_{O2} oxygen vacancy takes place, after which further reactions can occur.

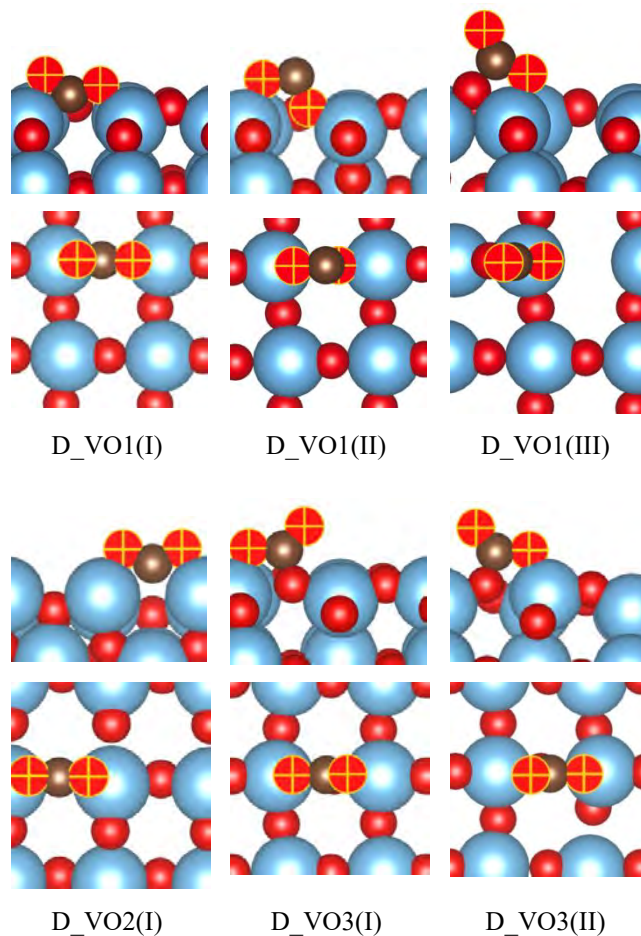


Figure 39. The new adsorption configurations of CO_2 on a reduced anatase (001) surface with different oxygen vacancies, in side view and top view (upper and lower panels, respectively). See text for explanation. (Ti = blue, O_{TiO_2} = red, O_{CO_2} = red and yellow plus sign, C = brown)

Table 16. Adsorption properties of CO₂ on the reduced TiO₂ anatase (001) surfaces with different oxygen vacancies: The bond lengths between Ti and O of CO₂, $r(\text{Ti-O}_{\text{CO}_2})$, between the surface O and C, $r(\text{Os-C})$, and between C and O of carbon, $r(\text{C-O})$, the bond angle of CO₂, $\alpha(\text{OCO})$, the adsorption energy, vibrational frequencies $\nu(\text{CO}_2)$, and the charge transfer from the surface to CO₂, $\Delta q(\text{CO}_2)/|e|$.

Configuration	$r(\text{Ti-O})$ (Å)	$r(\text{Os-C})$ (Å)	$r(\text{C-O})$ (Å)	$\alpha(\text{OCO})$ (deg.)	E_{ads} (kcal/mol)
Gas phase			1.177, 1.177	180.0	
D_VO1(I)	2.075, 1.973		1.272, 1.286	125.1	-48.65
D_VO1(II)	1.971, 2.642, 1.880		1.289, 1.346	108.9	-25.25
D_VO1(III)	2.016	1.472	1.200, 1.300	134.7	-1.64
D_VO2(I)	2.008, 1.994		1.265, 1.270	126.1	-25.50
D_VO3(I)	1.932	1.365	1.218, 1.335	128.6	-24.12
D_VO3(II)	1.905	1.366	1.213, 1.347	126.9	-23.56
			$\nu(\text{CO}_2)$ (cm ⁻¹)		$\Delta q(\text{CO}_2)$ (a.u.)
Gas phase	2365	1316	632	631	
D_VO1(I)	1503	1256	767	455	-0.338
D_VO1(II)	1207	928	728	363	-0.422
D_VO1(III)	1852	1113	740	714	-0.228
D_VO2(I)	1577	1235	757	469	-0.314
D_VO3(I)	1734	1128	824	739	-0.256
D_VO3(II)	1754	1082	825	729	-0.252

5.3.3. CO₂ adsorption at 300 K on anatase (001)

At non-zero temperature we find that the CO₂ adsorption is destabilized, reducing the adsorption strength of the chemisorbed configuration from -32.8 kcal/mol at 0 K to -22.9 kcal/mol at 300 K on the fully oxidized surface. The physisorbed configurations become metastable and the adsorption becomes endergonic with an adsorption energy ranging from 1.4 to 4.2 kcal/mol, maintaining the same order in stability as at absolute zero. The diffusion barriers from the physisorbed configurations to the bent carbonate configuration decrease for the L(I) configuration from 0.8 kcal/mol at 0 K to 0.7 kcal/mol at 300 K, and increase for L(II) and L(III) with a maximal barrier of 1.8 kcal/mol at 400 K for L(III). The rate constants for the conversion of the physisorbed configuration to the chemisorbed configuration are in the order of $10^{11} - 10^{12} \text{ s}^{-1}$. However, diffusion between adsorption sites for B(I) is unlikely to occur at these temperatures as the reaction rate equals $8.1 \times 10^{-11} \text{ s}^{-1}$ at 300 K. The influence of oxygen vacancies on the adsorption stays similar at elevated temperatures compared to their influence at absolute zero. All adsorption energies at absolute zero, 300 K and 400 K are given in Table 17.

Table 17. The adsorption energies on the stoichiometric and reduced surfaces at absolute zero, 300 K and 400 K in kcal/mol. The endothermic and endergonic adsorption configurations are given in red.

	Absolute zero					300 K					
	site 0	site 1	site 2	site 3	site 4	site 0	site 1	site 2	site 3	site 4	
	V _{O1}					V _{O1}					
B(I)	-32.82		1.08	-28.16	-34.27	-22.88		11.62	-17.06	-23.18	
L(I)	-7.31	-5.19	-6.75	-5.19	-6.75	1.43	3.84	1.36	3.84	1.36	
L(II)	-6.19	-8.01	-6.30	-5.06	-6.67	3.65	0.72	3.58	2.98	3.25	
L(III)	-4.34	-7.09	-7.09	-7.09	-7.09	4.24	2.74	2.74	2.74	2.74	
	V _{O2}					V _{O2}					
B(I)	-32.82	-32.96	32.96			-22.88	-22.70	-22.70			
L(I)	-7.31	-7.30	7.10			1.43	2.27	1.39			
C L(II)	-6.19	-5.46	7.69			3.65	4.24	2.30			
L(III)	-4.34		5.00			4.24		4.09			
	V _{O3}					V _{O3}					
B(I)	-32.82	-30.85	-30.85	-32.64	-32.64	-22.88	-19.86	-19.86	-23.83	-23.83	
L(I)	-7.31	-7.39	-7.39	-7.39	-7.39	1.43	0.33	0.33	0.33	0.33	
L(II)	-6.19	-4.19	-4.73	-5.60	-6.96	3.65	3.09	4.92	4.04	2.88	
L(III)	-4.34	-3.98	-4.72	-3.98	-4.72	4.24	2.99	4.09	2.99	4.09	
	400 K					0 K 300 K 400 K					
	site 0	site 1	site 2	site 3	site 4						
	V _{O1}					D_VO1(I)	-48.65	-37.54	-33.63		
B(I)	-19.46	0.00	15.36	-13.01	-19.14	D_VO1(II)	-25.25	-14.98	-11.42		
L(I)	4.15	6.85	3.86	6.85	3.86	D_VO1(III)	-1.64	8.51	11.98		
L(II)	6.98	3.47	6.92	5.49	6.61						
L(III)	7.07	6.06	6.06	6.06	6.06	D_VO2(I)	-25.50	-14.14	-10.10		
	V _{O2}										
B(I)	-19.46	-19.11	-19.11			D_VO3(I)	-24.12	-13.58	-9.84		
L(I)	4.15	5.48	4.02			D_VO3(II)	-23.56	-12.78	-8.87		
L(II)	6.98	7.51	5.69								
L(III)	7.07	0.00	7.09								
	V _{O3}										
B(I)	-19.46	-15.87	-15.87	-20.87	-20.87						
L(I)	4.15	2.70	2.70	2.70	2.70						
L(II)	6.98	5.29	8.18	7.29	6.20						
L(III)	7.07	5.04	7.00	5.04	7.00						

5.3.4. CO₂ dissociation on anatase (001)

5.3.4.1. Stoichiometric anatase (001) surface

As previously mentioned, the dissociation of CO₂ on the fully oxidized anatase (001) surface is unlikely to occur without the help of co-adsorbates to stabilize the transition state and the reaction products. We find a dissociative adsorption energy of 67.4 kcal/mol. In the dissociation mechanism, as determined using NEB and shown in Figure 40, we start from the B(I) configuration, as this configuration showed to be the most promising for CO₂ activation as inferred from the calculated charge transfer to CO₂, the significant elongation of the C-O bonds and the red shift in the vibrations. However, we find that B(I) first converts to L(II), which is not activated compared to the gas phase CO₂. The reaction proceeds further through the rotation of the CO₂ molecule, resulting in a transition state with the carbon atom being bonded to Ti and one of the oxygen atoms bonded to O(2f), while maintaining a bent configuration. Subsequently, the C-O bond of the corresponding atoms breaks and CO and O remain adsorbed on the TiO₂ surface. The corresponding energy barrier corrected for the ZPE is 113.6 kcal/mol, and the reaction enthalpy of the dissociation is equal to 98.9 kcal/mol. The corresponding dissociation rate at 300 K is $4.4 \times 10^{-71} \text{ s}^{-1}$. Therefore, this reaction is highly unlikely to occur on the fully oxidized surface, even at elevated temperatures. However, in the previous sections we found that the presence of oxygen vacancies yields newly available adsorption configurations with an apparent higher activation than B(I) and the possibility to stabilize the reaction products by the healing of the vacancy. We shall now discuss the CO₂ dissociation for these new adsorption configurations on the reduced surface.

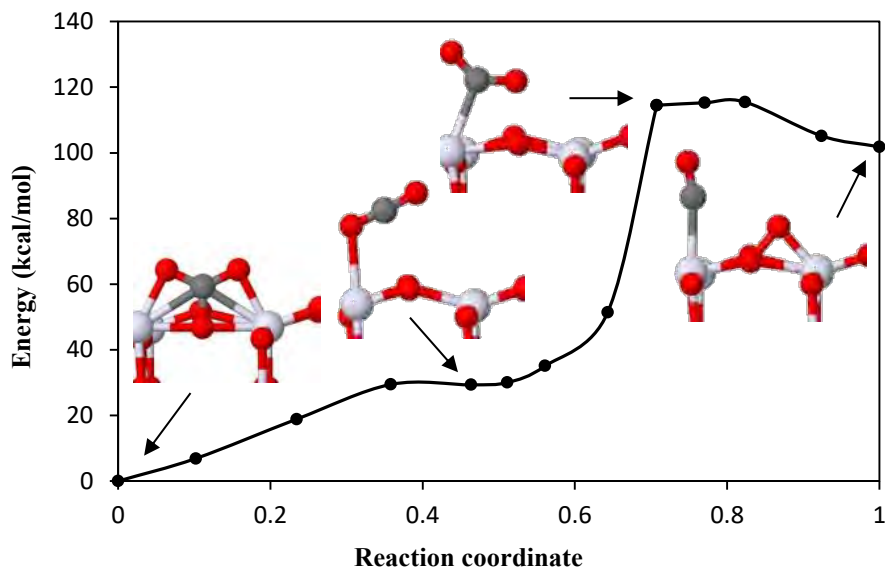


Figure 40. The CO₂ dissociation minimal energy pathway starting from B(I) on the stoichiometric anatase (001) surface. No zero-point energy corrections are included in the minimal energy pathway shown.

5.3.4.2. Reduced anatase (001) surface

We here discuss the reaction possibilities and rates for CO₂ dissociation in the presence of the different oxygen vacancies. We exclude the V_{O3} vacancy as we found that the dissociation reaction would be endothermic by around 50 kcal/mol, and would hence not yield a feasible dissociation possibility. We rather expect that the V_{O3} vacancy will be healed by the diffusion of a surface or subsurface oxygen to the V_{O3} site, thereby creating a V_{O1} or V_{O2} vacancy, respectively.

As starting points for the activation of the dissociation reaction on the reduced anatase (001) surface with a V_{O1} oxygen vacancy, we used three different adsorption configurations, i.e., D_VO1(I), D_VO1(II), and D_VO1(III), for which the minimal energy pathways are shown in Figure

41, Figure 42 and Figure 43, respectively. The reactions all resulted in the oxygen vacancy being healed, similar to the reaction mechanism for CO₂ dissociation on the reduced rutile (110)²²¹, and the reduced anatase (101)¹⁵⁸. CO is adsorbed on the now fully oxidized surface, with an adsorption energy of -8.3 kcal/mol at absolute zero and -0.06 kcal/mol at 300 K, relative to the gas phase CO and the fully oxidized surface.

For D_VO1(I) (see Figure 41) the minimal energy pathway first crosses a small energy barrier of 1.3 kcal/mol, to yield a minimum which is 0.05 kcal/mol less stable than D_VO1(I). In this minimum, the CO₂ molecule is bonded with its carbon atom to one Ti³⁺ atom and with one of its oxygen atoms to the other Ti³⁺. The reaction subsequently continues over an energy barrier of 18.1 kcal/mol. At the transition state, we find that CO₂ is already dissociated. The overall reaction is endothermic with a corresponding reaction enthalpy (corrected for the ZPE) of 14.9 kcal/mol. As the barrier for the backward reaction in which CO₂ and the oxygen vacancy are recreated is 3.2 kcal/mol and the desorption energy of CO₂ is 0.06 kcal/mol at 300 K, these reactions will be competitive. The reaction rate for dissociation at 300 K is 1.08 s⁻¹.

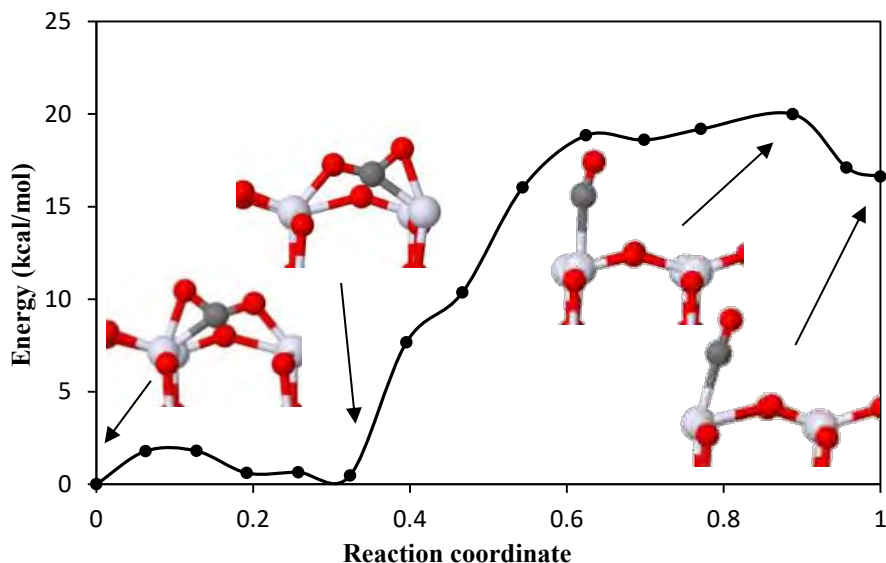


Figure 41. The CO₂ dissociation minimal energy pathway starting from D_VO1(I) on the reduced anatase (001) surface. No zero-point energy corrections are included in the minimal energy pathway shown.

For D_VO1(II) we find a barrier of 7.3 kcal/mol (see Figure 42). At the transition state, the C-O bond length has increased from 1.35 Å to 1.83 Å, after which it will convert to an adsorbed CO on the fully oxidized surface. The reaction is exothermic with a reaction enthalpy of -6.4 kcal/mol. The equilibrium constant at 300 K is equal to 1.0×10^5 , with a dissociation rate of $5.44 \times 10^6 \text{ s}^{-1}$.

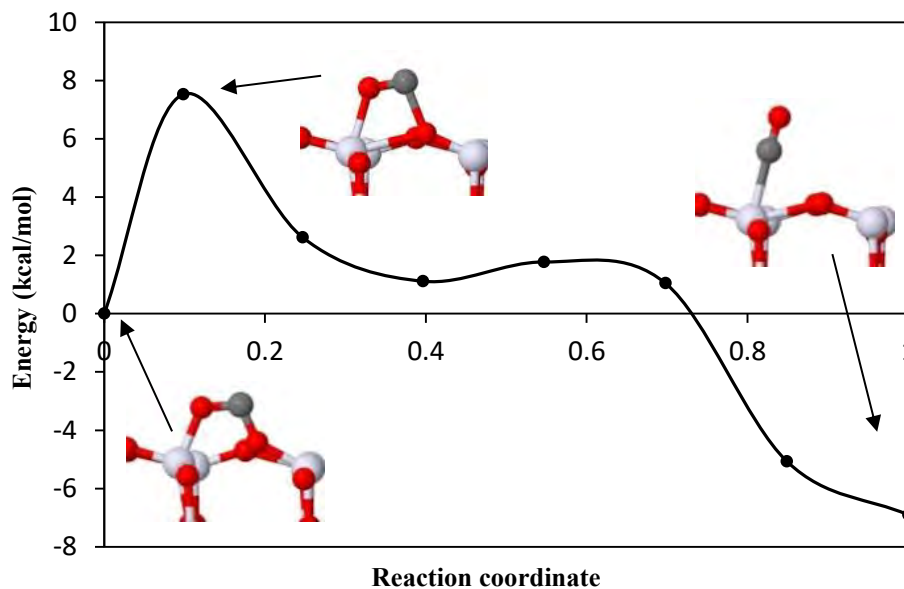


Figure 42. The CO₂ dissociation minimal energy pathway starting from D_VO1(II) on the reduced anatase (001) surface. No zero-point energy corrections are included in the minimal energy pathway shown.

We also performed a nudged elastic band calculation for the dissociation pathway of the D_VO1(III) configuration. This configuration had an adsorption energy of only -1.6 kcal/mol at absolute zero and 8.5 kcal/mol at 300 K, so it will not significantly contribute to the overall dissociation of CO₂. This configuration first converts to the L(II) configuration with no barrier, after which the CO₂ in the L(II) configuration crosses a barrier of 6.5 kcal/mol. The overall reaction enthalpy is equal to -32.0 kcal/mol, so if a reaction occurs it is unlikely that the reformation of D_VO1(III) will occur, as the equilibrium constant for dissociation is 6.54×10^{18} . This pathway also shows that once CO₂ is adsorbed in the L(II) configuration, it only has to cross a barrier of 6.5 kcal/mol to dissociate, resulting in a dissociation reaction rate of $9.2 \times 10^5 \text{ s}^{-1}$ at 300 K. This reaction is competitive to the conversion of L(II) to B(I), which had a barrier of 0.2 kcal/mol.

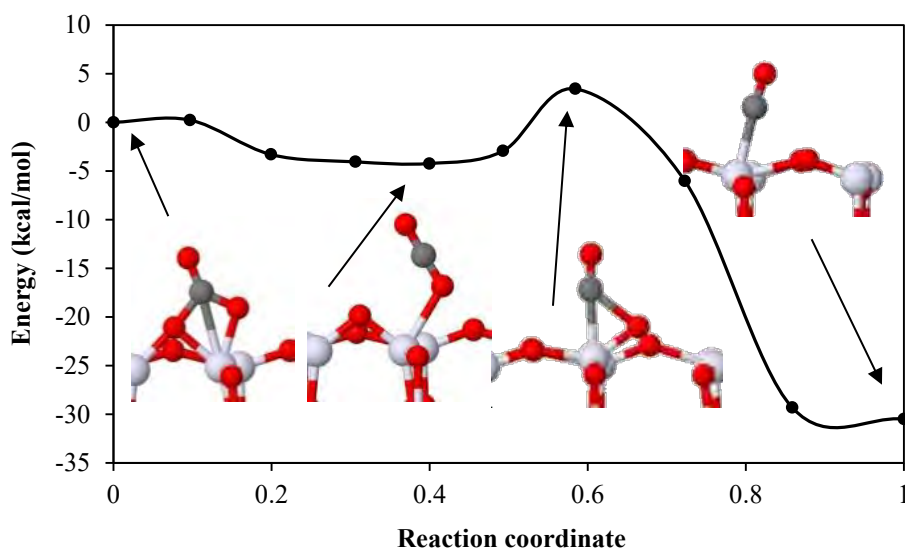


Figure 43. The CO₂ dissociation minimal energy pathway starting from D_VO1(III) on the reduced anatase (001) surface. No zero-point energy corrections are included in the minimal energy pathway shown.

As starting points for the activation of the dissociation reaction on the reduced anatase (001) surface with a V_{O2} oxygen vacancy, we used two different adsorption configurations, i.e., D_VO2(I) and B(I) adsorbed with one of the oxygen atoms of CO₂ bonded to one of the Ti³⁺ centers. The corresponding reaction mechanisms are shown in Figure 44 and Figure 45, respectively. Both reactions result in the oxygen vacancy being healed, and CO being adsorbed on the now fully oxidized surface with an adsorption energy of -8.3 kcal/mol at absolute zero and -0.06 kcal/mol at 300 K, relative to the gas phase CO and the fully oxidized surface.

For D_VO2(I) an exothermic dissociation is found. The dissociation of CO₂ follows a rotation of CO₂ crossing a barrier of 22.2 kcal/mol. In the dissociation process, one of the oxygen atoms heals the vacancy and CO stays adsorbed on the resulting stoichiometric surface. The total reaction

enthalpy equals -26.3 kcal/mol. For this reaction to occur at a sufficient rate, elevated temperatures are needed. We find the reaction rate to increase from $1.1 \times 10^{-3} \text{ s}^{-1}$ to 17 s^{-1} upon increasing the temperature from 300 K to 400 K. When this reaction takes place, the backward reaction is not likely to occur as the reaction barrier is 49.5 kcal/mol at 300 K.

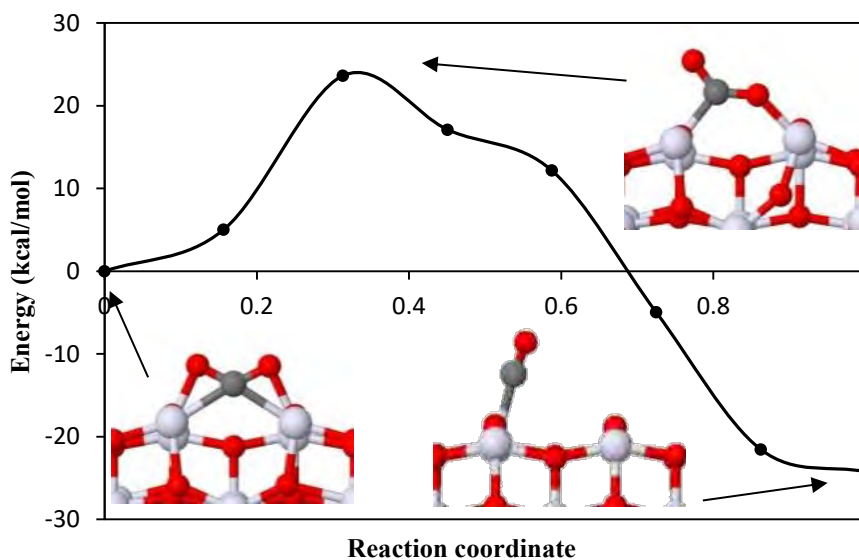


Figure 44. The CO₂ dissociation minimal energy pathway starting from D_VO2(I) on the reduced anatase (001) surface. No zero-point energy corrections are included in the minimal energy pathway shown.

The CO₂ in the B(I) configuration on the reduced anatase surface containing a V_{O2} vacancy will first undergo a rotation out of the [010] plane, into the direction of the oxygen vacancy. The first barrier, corresponding to this rotation, is 3.4 kcal/mol, resulting in the formation of an intermediate structure. In this structure, one of the oxygen atoms of CO₂ heals the vacancy, and the resulting Ti-O_{CO2} bond lengths are 2.07 Å and 2.18 Å. The carbon atom stays bonded to all of the three original oxygen atoms of the B(I) configuration. The reaction pathway continues by

the elongation of the C-O bond from the oxygen that is filling the V_{O2} oxygen vacancy. The bond elongates from 1.38 Å in the intermediate structure to 1.74 Å in the transition state. In this process, a barrier of 18.2 kcal/mol needs to be overcome. After healing the oxygen vacancy, the $D_VO1(I)$ configuration is formed, and the dissociation of CO_2 will then occur through the pathway of $D_VO1(I)$. The overall reaction is exothermic and the reaction enthalpy is equal to -18.9 kcal/mol. The rate limiting step in this reaction mechanism is the elongation of the C-O bond from the oxygen that is filling the V_{O2} oxygen vacancy, causing the reaction rate to drop to 0.28 s^{-1} at 300 K, which increases to $7.7 \times 10^2\text{ s}^{-1}$ at 400 K.

All energy barriers at absolute zero, 300 K and 400 K and all rate constants for diffusion and dissociation at 300 K and 400 K are given in Table 18.

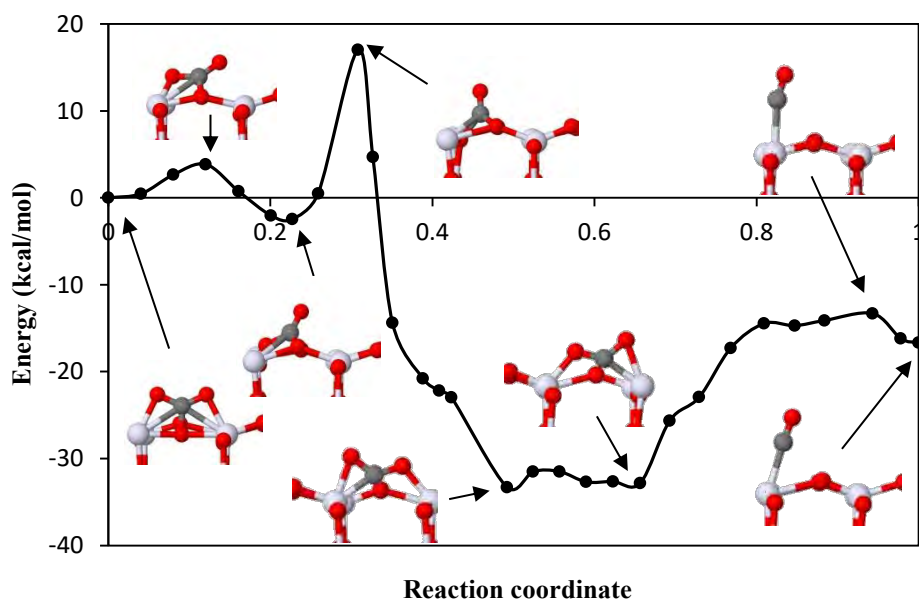


Figure 45. The CO_2 dissociation minimal energy pathway starting from $B(I)$ on the reduced anatase (001) surface containing a V_{O2} oxygen vacancy. No zero-point energy corrections are included in the minimal energy pathway shown.

Table 18. The energy barriers at absolute zero, 300 K and 400 K and rate constants for diffusion and dissociation at 300 K and 400 K. The cells for conversion of the physisorbed states to the chemisorbed B(I) configuration are shown in grey, and the backward reaction in orange. For the dissociation, the cells corresponding to the reaction from the dissociated state to the adsorbed CO₂ configurations are given in grey, and the dissociation is given in orange. The rates below 1 s⁻¹ are given in red. In this table Int. is the contraction of intermediate.

	Start	End	R _{e,300K} (s ⁻¹)	R _{e,400K} (s ⁻¹)	ΔG _{300K}	ΔG _{400K}	ΔE _{elect+zpe}
Diffusion	L(I)	B(I)	2.02x10 ¹²	3.69x10 ¹²	0.7	0.6	0.8
	B(I)	L(I)	3.94x10⁻⁶	4.61x10⁻¹	25.0	24.3	26.3
	L(II)	B(I)	1.02x10 ¹²	1.14x10 ¹²	1.1	1.6	0.2
	B(I)	L(II)	4.75x10⁻⁸	4.07x10⁻³	27.6	28.0	26.8
	L(III)	B(I)	2.98x10 ¹¹	3.32x10 ¹¹	1.8	2.6	0.3
	B(I)	L(III)	5.16x10⁻⁹	1.06x10⁻³	28.9	29.1	28.7
	B(I)	B(I)	8.06x10⁻¹¹	2.59x10⁻⁵	31.4	32.0	30.4
Dissociation	Dissociated	B(I)	19.7	9.17 x10 ³	15.8	16.4	14.7
	B(I)	Dissociated	4.39x10⁻⁷¹	2.71x10⁻⁵⁰	114.1	114.4	113.6
V _{O1}	Dissociated	Int. D_VO1(I)	8.04x10 ⁹	3.19x10 ¹⁰	4.0	4.4	3.2
	Int. D_VO1(I)	D_VO1(I)	2.64x10 ¹²	6.56x10 ¹²	0.5	0.2	1.2
	Total		8.01x10 ⁹	3.18x10 ¹⁰			
	D_VO1(I)	Int. D_VO1(I)	2.34x10 ¹²	5.95x10 ¹²	0.6	0.3	1.3
	Int. D_VO1(I)	Dissociated	1.08	3.37x10 ³	17.5	17.2	18.1
	Total		1.08	3.37x10 ³			
	Dissociated	D_VO1(II)	52.3	1.34x10 ⁴	15.2	16.1	13.7
	D_VO1(II)	Dissociated	5.44x10 ⁶	1.33x10 ⁸	8.3	8.8	7.3
	Dissociated	Int. D_VO1(III)	1.41x10⁻¹³	1.34x10⁻⁷	35.2	36.2	33.6
	Int. D_VO1(III)	D_VO1(III)	1.06x10 ⁸	6.43x10 ⁸	6.6	7.5	4.3
Total		1.41x10⁻¹³	1.34x10⁻⁷				
	D_VO1(III)	Int. D_VO1(III)	5.54x10 ¹²	4.69x10 ¹²	0.1	0.5	-0.6
	Int. D_VO1(III)	Dissociated	9.21x10 ⁵	1.25x10 ⁷	7.7	10.7	6.5
Total			9.21x10 ⁵	1.25x10 ⁷			
V _{O2}	Dissociated	D_VO2(I)	5.06x10⁻²⁴	3.10 x10⁻¹⁵	49.5	50.2	48.5
	D_VO2(I)	Dissociated	1.10x10⁻³	17.2	21.6	21.4	22.2
	Dissociated	Int. D_VO1(I)	8.04x10 ⁹	3.19x10 ¹⁰	4.0	4.4	3.2
	Int. D_VO1(I)	D_VO1(I)	2.64x10 ¹²	6.56x10 ¹²	0.5	0.2	1.2
	D_VO1(I)	Int. B(I)	2.24x10⁻²⁴	2.00x10⁻¹⁵	50.0	50.6	49.3
	Int. B(I)	B(I)	1.01x10 ⁸	1.43x10 ⁹	6.6	6.9	6.1
	Total		2.24x10⁻²⁴	2.00x10⁻¹⁵			
	B(I)	Int. B(I)	4.2 x10 ⁹	1.85x10 ¹⁰	4.3	4.9	3.4
	Int. B(I)	D_VO1(I)	3.77x10⁻¹	9.93x10 ²	18.1	18.2	18.2
	D_VO1(I)	Int. D_VO1(I)	2.34x10 ¹²	5.95x10 ¹²	0.6	0.3	1.3
	Int. D_VO1(I)	Dissociated	1.08	3.37x10 ³	17.5	17.2	18.1
	Total		2.79x10⁻¹	7.67x10 ²			

5.4. Conclusion

We have studied the adsorption of CO_2 and the activation for CO_2 dissociation on the fully oxidized and reduced anatase (001) surfaces using DFT calculations with long range dispersion energy corrections. On the fully oxidized surface we identified four different adsorption configurations for CO_2 : One strongly chemisorbed bent configuration, B(I), and three linear physisorbed configurations, L(I)-L(III), which almost retain their gas phase properties. We also studied the influence of the introduction of different oxygen vacancies on the aforementioned adsorption configurations. The influence of the different vacancies on the adsorption configurations found on the stoichiometric surface stays limited, except when the CO_2 is adsorbed in the B(I) configuration on top of the Ti-O(2f)-Ti moiety neighbouring a $\text{V}_{\text{O}1}$ oxygen vacancy in the same [010] row. This configuration is strongly destabilized through the counteraction of the relaxation of the surface after formation of the vacancy, and the interaction of Lewis base centers. New adsorption configurations originate from the presence of oxygen vacancies in the anatase (001) surface. For the different oxygen vacancies we found a total of six new bent adsorption configurations. Just as with the B(I) configuration, significant charge transfer to CO_2 , large vibrational red shifts, and sizeable elongations of the C-O bonds indicate a substantial bond weakening for these newly formed adsorption configurations. For D_VO1(III), D_VO3(I), and D_VO3(II) we found a smaller red shift than for B(I). CO_2 dissociation on a fully oxidized anatase (001) surface starting from the B(I) adsorption configuration is unlikely to occur, as the corresponding barrier equals 113.6 kcal/mol. In the presence of the $\text{V}_{\text{O}3}$ vacancy, we found that the reaction is endothermic with at least 45 kcal/mol, and hence also unlikely to happen. However, we found significantly lower reaction barriers in the presence of the other oxygen vacancies, as these vacancies provide a means of stabilizing the end

products, by using one of the oxygen atoms of the CO₂ molecule to heal the oxygen vacancy. As D_VO1(III) converts to L(II) without a barrier and the barrier for dissociation starting from the physisorbed configuration is 6.54 kcal/mol, direct dissociation after physisorption is competitive with the conversion of the physisorbed configuration to the bent monodentated carbonate-like structure B(I). All dissociations starting from different adsorption configurations, except for the D_VO1(I) configuration, on the reduced surfaces are exothermic. The end product for all these reaction pathways is a CO molecule being adsorbed on the fully oxidized surface with an adsorption energy of -8.3 kcal/mol with respect to the gas phase CO and the fully oxidized surface. The results of this study show that oxygen vacancies play a significant role in the dissociation of CO₂ on the anatase (001) surface, and thus we anticipate they will play an important role in complex problems, such as the conversion of CO₂ to value-added chemicals.

**Chapter 6 Insight in
the surface reactions
of the plasma-
catalytic dry
reforming of methane
on anatase (001)**

6.1. Introduction

As mentioned in Chapter 1, the dry reforming of methane is a highly attractive process from an environmental point of view as one uses waste gases to form chemical feedstock. The combination of CO₂ and CH₄ allows the use of low-grade natural gas that is obtained as by-product at oil platforms, which is otherwise flared, and one can use biogas as a renewable feedstock for the chemical industry. During dry reforming of methane, CO₂ is used to oxidize methane to syngas, i.e., a mixture of CO and H₂:



Syngas can then be utilized for the chemical synthesis of fuels, e.g. through the Fischer-Tropsch synthesis to make liquid fuels²². Furthermore, oxygenated products such as methanol, ethanol and aldehydes can be synthesized through syngas.²²² Other uses of syngas are the direct combustion of syngas²²³, and the use of the water gas shift reaction to increase the H₂ content and use the hydrogen in the Haber-Bosch process to generate ammonia. However, it would also be beneficial to directly form value-added chemicals, apart from syngas, through dry reforming of methane.

Due to the high endothermicity of dry reforming, high temperatures and a catalyst are required to obtain significant conversions of methane and CO₂ at an acceptable rate. Other challenges than the high energy requirement relate to the state of the catalyst, including sintering, sulphur poisoning, coke formation and maintaining a sufficiently high activity.²⁴ It is therefore opportune to pursue alternative technologies. A combination of a non-thermal atmospheric plasma with a catalyst, i.e., plasma-catalysis, is a promising technique, since the plasma will activate the gas mixture

inducing reactions at lower temperatures, while the catalyst can reduce the activation barriers and increase selectivity.

Due to the high complexity of the plasma-catalytic system, the exact mechanisms are far from understood.^{13,25,26} The production of oxygen vacancies within the titanium dioxide surface is highly important for its catalytic activity. Sorescu et al. found that these defects play an important role in the catalytic dissociation of CO₂ on the rutile (110) and anatase (101) surfaces.^{158,181,221} We have found that dissociation of CO₂ on the defect-free anatase (001) surface is impossible, and oxygen vacancies will significantly reduce the activation barriers and cause the reaction to become exothermic.²²⁴ Previous studies have also indicated the significance of oxygen vacancies in the adsorption of H₂O, O₂ and methane derived radicals^{152,157,180,204} and on reaction mechanisms of H₂O dissociation^{225,226} and NO removal²²⁷.

As the dissociation of CO₂ leads to the healing of the oxygen vacancy, a regeneration mechanism is needed. Plasma-catalytic dry reforming of methane could provide this mechanism, as the methane derived radicals, formed in the plasma,^{170,171} act as a reductant. As the first step in obtaining a molecular understanding of the reduction of the surface by these radicals, we have studied the dehydrogenation reactions of the adsorbed CH_x radicals (x = 0 – 3) to determine which of these radicals will be readily available to reduce the surface. In Chapter 4 we have determined the stable adsorption configurations of the CH_x radicals on the stoichiometric anatase (001) surface, which we have used as starting points for the dehydrogenation reactions of those radicals.²⁰⁴ After the possible dehydrogenation, the surface will be reduced by the desorption of oxygenated reaction products, leaving behind the most stable oxygen vacancy, i.e., the surface oxygen vacancy.²⁰⁴ Further, we study the

formation and desorption of value-added chemicals during the surface reactions in the plasma-catalytic dry reforming of methane.

6.2. Computational details

We performed DFT calculations using VASP.^{186,187} For the treatment of the exchange and correlation, the Perdew-Burke-Ernzerhof (PBE) functional was applied,¹¹³ using plane wave basis sets and the projector-augmented wave method¹⁸⁸ as implemented in VASP. We have corrected the PBE functional with long-range dispersion interactions by applying the Tkatchenko and Scheffler method²⁰⁹ as implemented in VASP.²¹⁰ The stoichiometric anatase (001) surface was modelled using a (2x2) supercell containing 48 atoms corresponding to four TiO₂ layers. We fixed the bottom layer of the surface at the bulk positions and the simulation box was created to maintain a vacuum layer of ~ 16 Å between adjacent surfaces to prevent influence of neighbouring slabs on the calculated energies and reactions. The sampling of the Brillouin zone was performed using a 6x6x1 k-points grid for the surface models whereas only the gamma-point was taken into account for the molecules. An energy cutoff of 440 eV was used. Geometry optimizations were performed with the conjugate gradient method, with the endpoint criterion for the residual forces set to $0.03 \text{ eV}\cdot\text{Å}^{-1}$. Spin polarization was applied for all calculations.

The vibrational analysis was performed with the finite difference method implemented in VASP. The calculations included the displacements to both the adsorbed molecules and the top layer of the TiO₂ surface. These results were used for the thermodynamical analysis, as performed with the TAMKIN tool.²¹¹ All reported energies are corrected for the zero-point energy. TAMKIN was used for the determination of the Gibbs Free Energy and reaction rate constants applying Transition State Theory. To determine the readily available radicals, we calculated the corresponding

dehydrogenation minimal energy pathways (MEP) with Nudged Elastic Band (NEB)^{159,213–217}. We have also used NEB to study the relevant MEP for the formation of the end products of the plasma-catalytic dry reforming of methane.

The colour code for the different elements of the configurations shown in the figures below is as follows: Ti = light gray, O = red, H = white, C = dark gray. In all reported energy values, negative values for ΔH and ΔG indicate exothermic and exergonic processes, respectively, and positive values for ΔH and ΔG indicate endothermic and endergonic processes, respectively. If the anatase (001) surface is reduced we consider the oxygen to be removed to be the 2-coordinated O, i.e., O_{2c} as shown in Figure 46. This results in the formation of the most stable oxygen vacancy, i.e., the surface oxygen vacancy V_{O1} , as reported in our previous work.²⁰⁴ Below, we report the half-lives of the calculated reactions; the conversion from the half-lives, $t_{1/2}$, to the reaction rate constants, k , can be done as follows:

$$k_i = \frac{\ln 2}{t_{\frac{1}{2},i}}$$

In the case of non-activated adsorption, we have calculated the rate constant using kinetic gas theory. The rate constant of adsorption is then calculated as follows:

$$k_{ads} = \sqrt{\frac{k_b T}{2\pi M}}$$

where M is the mass of the gas-phase species.

For non-activated desorption, the rate constant is calculated using the following equation²²⁸:

$$k_{des} = \frac{k_b * T}{h} * \exp\left(-\left(\frac{G_{gas} + G_{surf} - G_{ads} + S_{1D-trans} * T}{R * T}\right)\right)$$

where G_{gas} , G_{surf} , G_{ads} , and $S_{1D-trans}$ correspond to the Gibbs Free Energy of the gas-phase species, the surface left behind after desorption, and the adsorbed configuration, and the entropy contribution of the translational degree of freedom perpendicular to the surface. Thus the transition state corresponds to the system in the state where the desorbed molecule is far away from the surface, i.e., when the molecule no longer interacts with the surface. The entropy of this transition state is identical to that of the gas-phase molecule, except for the entropy contribution of the translational degree of freedom perpendicular to the surface that is removed.

6.3. Results and discussion

6.3.1. CH_x (x = 1 – 3) dehydrogenation

As starting geometries for the dehydrogenation reactions of the different CH_x radicals (x = 1-3), we took the most stable adsorption configurations as reported in our previous work.²⁰⁴ The configurations and reaction products after dehydrogenation are shown in Figure 46. After dehydrogenation of CH₃ and CH₂ the hydrogen is either bonded to the 2-coordinated oxygen, O_{2c}, or the first subsurface 3-coordinated oxygen, O_{3c} (see Figure 46). For the CH dehydrogenation only the O_{3c} configuration is found to be stable. The reaction enthalpy is corrected for the zero-point energy. All reactions are found to be endothermic.

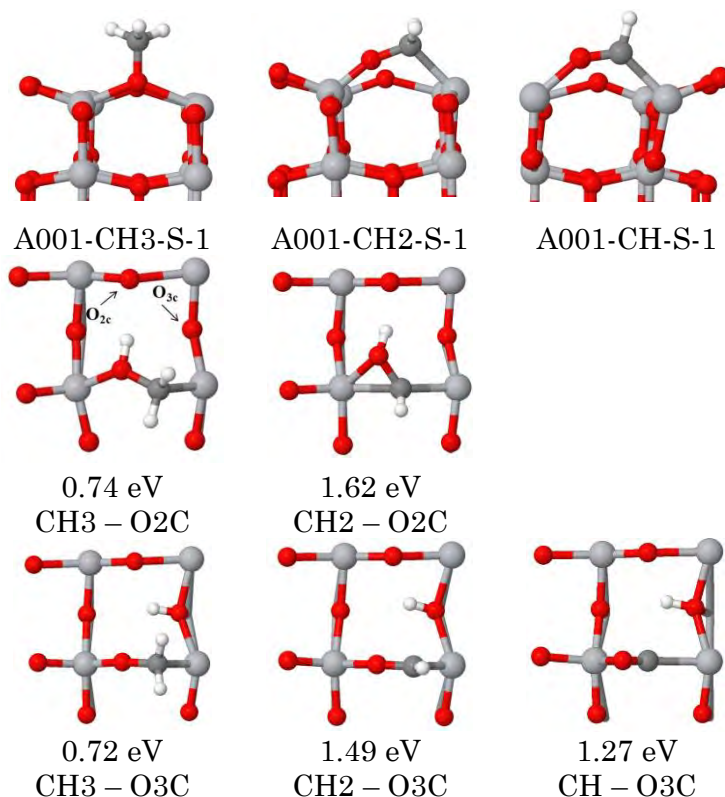


Figure 46. A side view of the most stable adsorption configurations of the CH_x radicals ($x = 1 - 3$) (top-row), and a top-view is given of the reaction products after dehydrogenation. The second row corresponds to reaction products where H is bonded to O_{2c}, while the third row corresponds to H bonded to the O_{3c}. The reaction enthalpies are given below each configuration. In the first structure of the second row we indicate a two-coordinated oxygen O_{2c}, and a three-coordinated O_{3c}.

In Figure 47 we give the Gibbs free energy of reaction for the different dehydrogenation reactions at temperatures ranging from absolute zero to 1000 K. All reactions are found to be endergonic at all considered temperatures, and thus the equilibrium will lie towards the hydrogenated reactants. The temperature only exerts a small influence on the relative

stabilities between the reactants and reaction products, with a maximum difference of -0.1 eV between absolute zero and 1000 K for $\text{CH}_3 - \text{O}_2\text{X}$.

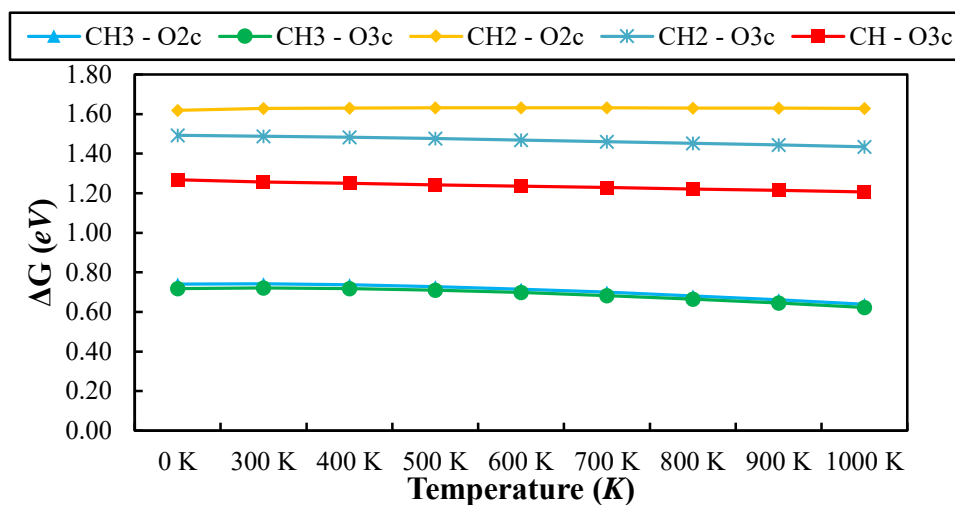


Figure 47. The Gibbs free energy of reaction for dehydrogenation of the CH_x radicals ($x = 1-3$) with hydrogen either adsorbed at the O_{2c} atom bonded to the CH_{x-1} radical or to the O_{3c} site neighbouring the reaction site. (see Figure 46)

However, if the reaction products, i.e. CH_{x-1} and H, further separate and move to their individually preferred sites through hydrogen diffusion, the relative stability of the dehydrogenated radical increases compared to the radical, as is shown in Figure 48. In this case there is no distinction between the binding site of H, as it will be bonded in its most stable configuration, i.e., bonded to the O_{2c} atom. The relative stability of the O_{2c} and O_{3c} binding sites for the H atom is -0.67 eV, the same value was found by Hussain et al.²²⁹ The increased stability of the end products results in an exergonic reaction for the CH_3 dehydrogenation. The exergonicity of this reaction corresponds to -0.10 eV at absolute zero and increases up to -0.29 eV at 1000 K. CH_2 and CH dehydrogenation remain endergonic, even when the reaction products are separated.

The stability of the reaction products can also be increased by the desorption of hydrogen gas (the reaction will be discussed in section 6.3.4.5). As is the case for the separation of the reaction products to their preferred binding sites, the dehydrogenation of CH_2 and CH remain endergonic over the considered temperature range (see Figure 48). On the other hand, for the dehydrogenation the reaction becomes exergonic between 500 and 600 K. Thus both the desorption, and the product separation results in a shift of the equilibrium towards CH_2 . (see Figure 48)

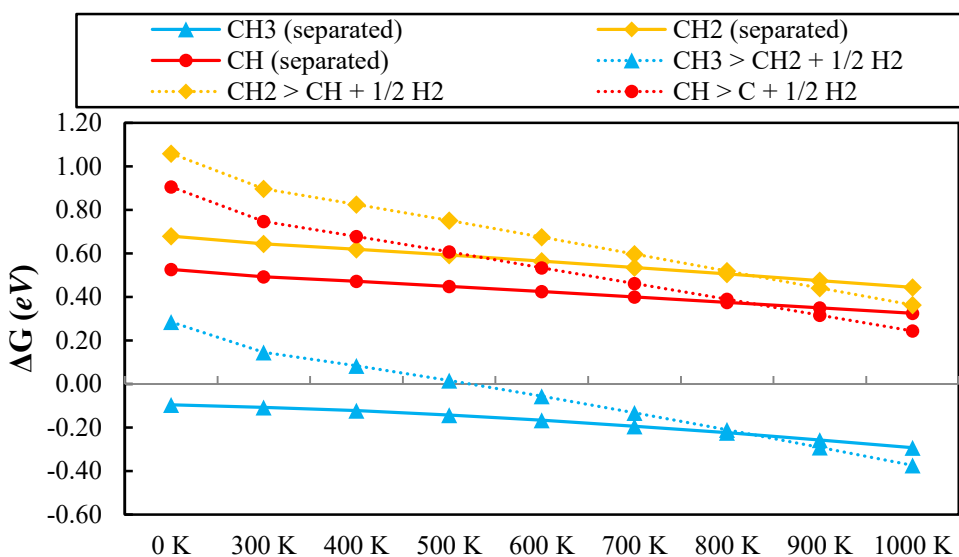


Figure 48. The relative stability of the CH_x radical with his dehydrogenated counterpart $\text{CH}_{x-1} + \text{H}$ after product separation (solid lines) and with his dehydrogenated counterpart $\text{CH}_{x-1} + \text{Hydrogen gas}$ (dotted lines).

6.3.2. Hydrogen diffusion

We have determined the minimal energy pathway for the hydrogen diffusion, between the O_{2c} binding site and the O_{3c} binding site, which is given in Figure 49. The full diffusion between the most stable sites will consist of a consecutive diffusion from O_{2c} to O_{3c} followed by the diffusion from O_{3c} to O_{2c} . Both these reaction steps are taken into account for the half-lives given in Figure 49. At elevated temperatures, hydrogen diffusion occurs rapidly. For instance, at 600 K the half-life equals 4.5 μ s. As the hydrogen can diffuse rapidly over the surface, it is possible to have both CH_3 and CH_2 radicals to be present on the surface, as the equilibrium of the dehydrogenation reaction of CH_3 can be pushed to CH_2 by the removal of the resulting H-atom, either by diffusion or by desorption with one of the reaction products considered in the next sections. However, CH_2 , CH , and C adsorbed from the gas-phase can easily be converted to CH_3 by reaction with adsorbed H-atoms that diffuse towards the adsorbed radical. Snoeckx et al. calculated the species densities in a 1:1 CH_4/CO_2 Dielectric Barrier Discharge, using a 0D-kinetic model.¹⁷¹ They found for a Specific Energy Input (SEI) of 18 J/cm^3 that the concentrations of the CH_3 , CH_2 , CH , and C radicals are $3.0 \cdot 10^{14} \text{ cm}^{-3}$, $4.5 \cdot 10^{13} \text{ cm}^{-3}$, $1.5 \cdot 10^{12} \text{ cm}^{-3}$ and $3.7 \cdot 10^{11} \text{ cm}^{-3}$, respectively, and for an SEI equal to 36 J/cm^3 , the concentrations are equal to $9.0 \cdot 10^{14} \text{ cm}^{-3}$, $2.0 \cdot 10^{14} \text{ cm}^{-3}$, $4.0 \cdot 10^{12} \text{ cm}^{-3}$, and $9.0 \cdot 10^{11} \text{ cm}^{-3}$, respectively. Thus, in the plasma gas-phase, the concentrations of CH_3 and CH_2 are significantly higher than those of CH and C . Because of the higher gas-phase concentrations of CH_3 and CH_2 , and due to the thermodynamics, i.e., the higher relative stability of CH_3 and CH_2 versus CH and C , both the CH_3 and CH_2 radicals will be readily available on the surface for other reactions to occur, while CH and C will become hydrogenated and will not play a significant role in the reactions. In the next section we will show that also the kinetics of the process corroborates this conclusion.

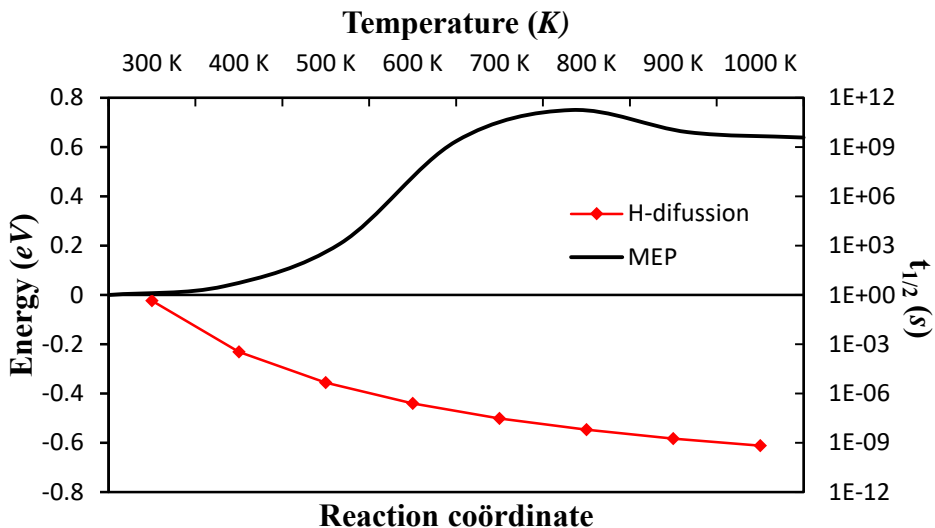


Figure 49. The minimal energy pathway (MEP) for H-diffusion and the half-life for the H-diffusion to occur. The MEP is given on the bottom and left axis, while the half-life of reaction is given on the top and right axis.

6.3.3. CH_x ($x = 1 - 3$) dehydrogenation reactions

6.3.3.1. CH_3 dehydrogenation

In Figure 50 the minimal energy pathways and half-lives for the dehydrogenation of CH_3 and the hydrogenation of CH_2 is given with the abstracted H bonded to O_{2c} and O_{3c} . The energy barrier for the dehydrogenation is significantly lower when the abstracted hydrogen is bonded to the O_{3c} compared to when it is bonded to the O_{2c} . The barriers for dehydrogenation are 1.26 eV and 2.94 eV, respectively. The high barrier for the O_{2c} route will prevent the dehydrogenation from occurring at an appreciable rate even at 1000 K, where the half-life for the reaction is equal to 0.47 s, through this route, while the O_{3c} route will go through at elevated temperatures. The hydrogenation is always faster than the

dehydrogenation, but this will be partially counteracted by the diffusion of hydrogen away from the reaction site. The energy gain by the diffusion of hydrogen results in the end product of dehydrogenation to be more stable than the CH_3 radical.

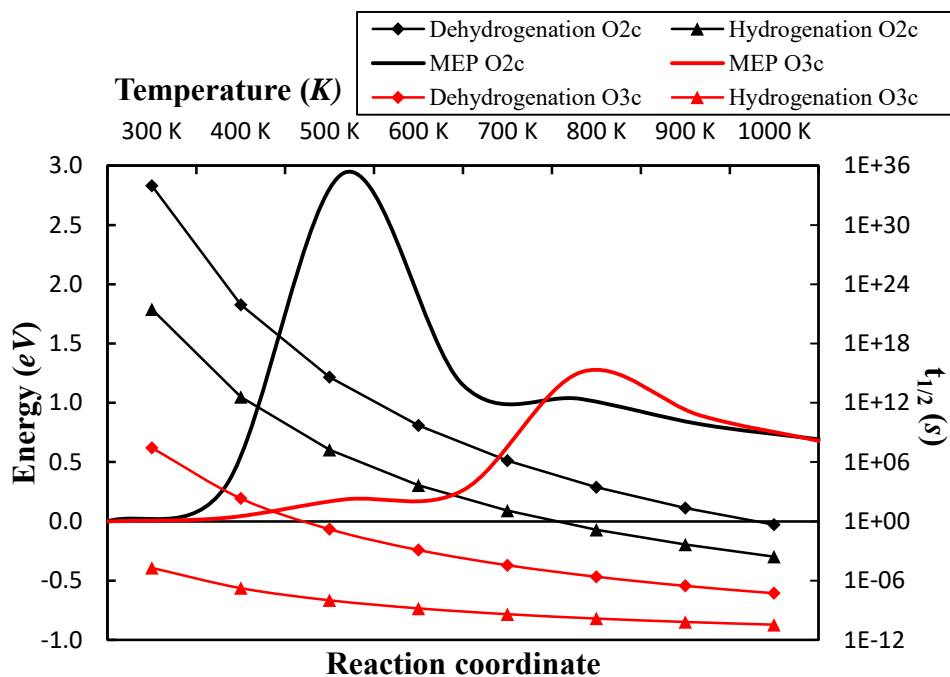


Figure 50. The minimal energy pathway (MEP) as calculated with NEB for the dehydrogenation of CH_3 , and the half-life for the hydrogenation of CH_2 and the dehydrogenation CH_3 . The MEP is given on the bottom and left axis, while the half-life of reaction is given on the top and right axis.

6.3.3.2. CH_2 dehydrogenation

In Figure 51 the minimal energy pathways and half-lives for the dehydrogenation of CH_2 and the hydrogenation of CH is given with the abstracted H bonded to O_{2c} and O_{3c} . Also in the case of CH_2 we find that the O_{3c} route is the more viable route compared to the O_{2c} route. However,

the reaction rate for the dehydrogenation of CH_2 , even at elevated temperatures, is significantly lower than for the dehydrogenation of CH_3 , e.g. at 600 K the half-life is $4 \cdot 10^4$ times greater than for the CH_2 dehydrogenation, and at 1000 K it is 700 times greater. Similar to CH_3 , the hydrogenation reaction is significantly faster than the dehydrogenation. When hydrogen diffuses away from the reaction site to stabilize the reaction products, we find that CH_2 stays significantly more stable than the dehydrogenated products, thus indicating that the dehydrogenation reaction will halt at the CH_2 radical.

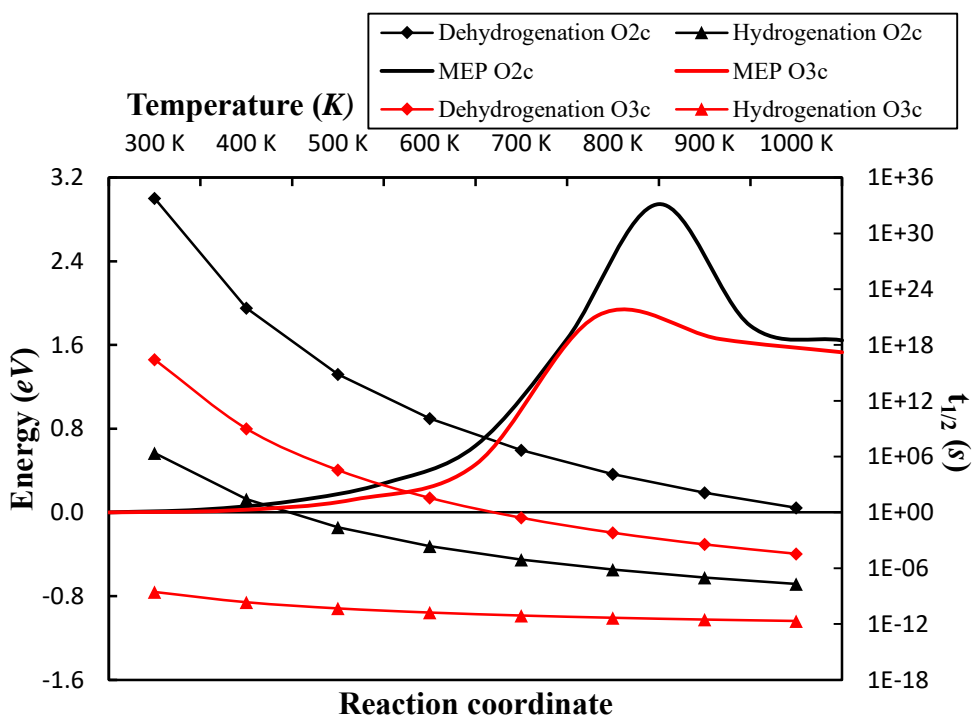


Figure 51. The minimal energy pathway (MEP) as calculated with NEB for the dehydrogenation of CH_2 , and the half-life for the hydrogenation and dehydrogenation reactions. The MEP is given on the bottom and left axis, while the half-life of reaction is given on the top and right axis.

6.3.3.3. CH dehydrogenation

In Figure 52 the minimal energy pathways and half-lives for the dehydrogenation of CH and the hydrogenation of C is given. For CH the dehydrogenation can only result in the abstracted hydrogen to end up at O_{3c} , as the configuration with H bonded to O_{2c} is found to be unstable. The reaction rate of the dehydrogenation and hydrogenation of CH is very similar to that of CH_2 . Also in this case we find that the hydrogenation is significantly faster than the dehydrogenation reaction. As for CH_2 dehydrogenation, the diffusion of H to a more stable adsorption site will not result in a higher stability of the reaction products, i.e., C and H, compared to the CH radical. If a C radical is adsorbed at the surface, it will most likely become hydrogenated to CH, which will subsequently be hydrogenated to CH_2 . It is also possible to desorb C as CO, leaving behind an oxygen vacancy, as will be discussed below.

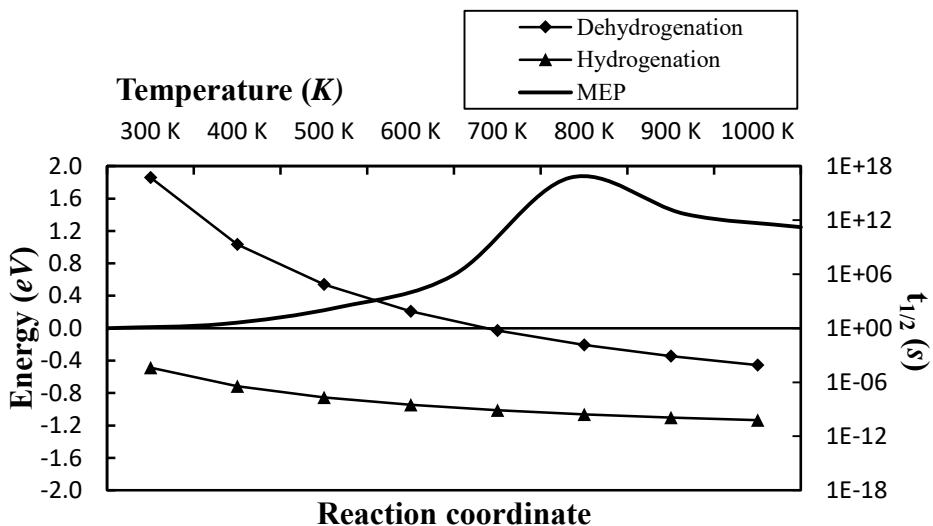


Figure 52. The minimal energy pathway (MEP) as calculated with NEB for the dehydrogenation of CH with hydrogen bonded to O_{3c} , and the half-life for the hydrogenation and dehydrogenation reactions. The MEP is given on the bottom and left axis, while the half-life of reaction is given on the top and right axis.

In Figure 53 we give the average waiting time for the adsorption of CH_x ($x = 0 - 3$) and H per unit cell, based on the average densities of these species as calculated by Snoeckx et al.¹⁷¹, and the average waiting time for desorption of these species on both the hydrogenated as the clean surface, all in a temperature range of 300 – 1000 K. We only show the cases for which the half-life of reaction is lower than 1000 s. Thus, the C and CH desorption are not shown, as the half-life of desorption in the considered temperature range is always larger than 1000 s. The rate of adsorption is calculated by multiplying the rate constant with the surface area per unit cell and the densities of the gas-phase species as calculated by Snoeckx et al.¹⁷¹. The influence of the temperature on the rate of adsorption, and thus the half-life of adsorption, is negligible compared to the temperature influence on desorption, as k_{ads} depends on the square root of the

temperature, while k_{des} depends on the temperature as follows $\sim T \cdot \exp(-1/T)$. This causes the desorption of CH_3 on both the clean as the hydrogenated surface to become faster than the adsorption above 500 K, and the desorption of CH_2 on the hydrogenated surface will only be observed significantly above 800 K. Hydrogen desorption as a radical will occur through the adsorption configuration with the hydrogen on the O_{3c} site, as the combination of hydrogen diffusion with desorption is faster than the direct desorption of H from the O_{2c} site. At 700 K, the average waiting time of desorption will be around the ms range, and it becomes faster than adsorption above 800 K. As can be seen from the average waiting time for the different species to adsorb on a unit cell, the adsorption of C and CH are slower than 10^{-2} s, while the adsorption of CH_2 , CH_3 , and H are faster than 0.1 ms. Thus these latter species will be readily available on the surface. Especially CH_3 and H will be present all over the surface, and can diffuse easily starting from 500 K and 400 K (see Figure 49), respectively. We approximate the diffusion of CH_3 by assuming desorption and readsorption on the surface.

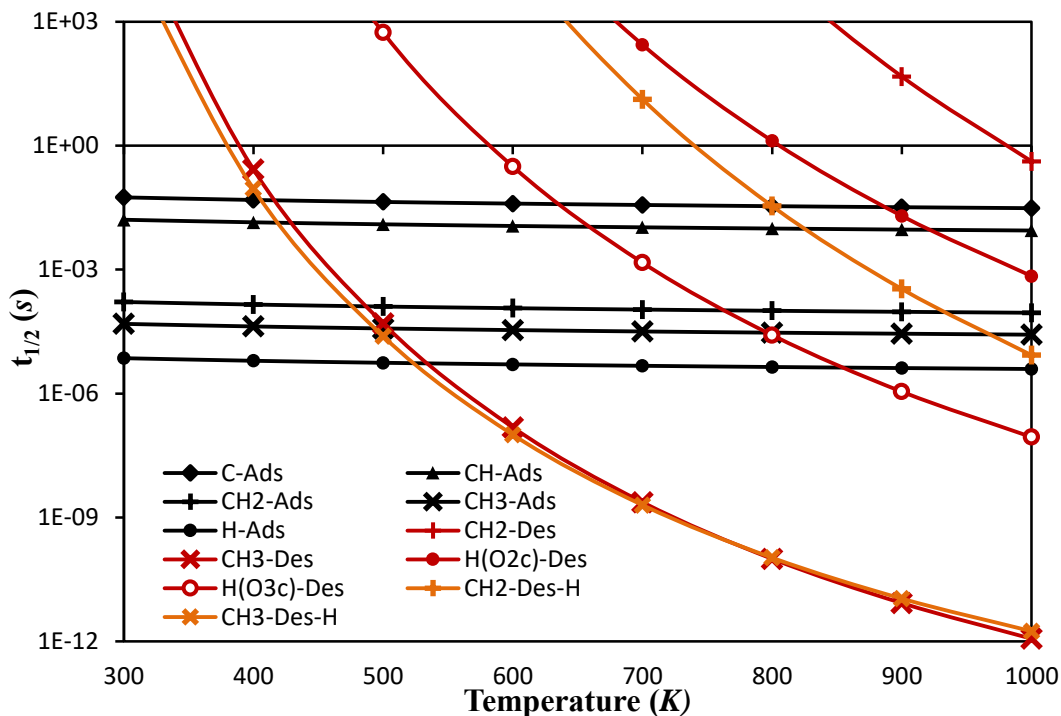


Figure 53. The half-lives of adsorption (X-Ads, black), and desorption on the clean (X-Des, red) and hydrogenated (X-Des-H, orange) surface for CH₃, CH₂, CH, C and H.

As shown by the results discussed above, the readily available methane derived radicals will be CH₃ and CH₂, which allow the possible formation of formaldehyde, methanol, ethane, and ethene. The readily available hydrogen radicals allow the formation of water and hydrogen gas, and the adsorbed CO₂ will be reduced to CO. These formation reactions and desorption of these chemicals will be discussed below.

6.3.4. Formation and desorption of value-added chemicals

6.3.4.1. Formaldehyde

In Figure 54 the Gibbs free energy of adsorption of formaldehyde in the configuration A001-CH₂-S-1 (see Figure 46) on the reduced anatase (001), containing a surface oxygen vacancy, is given. At all considered temperatures, the adsorption of formaldehyde is found to be exergonic. Liu et al. found that formaldehyde adsorbs preferentially in a dioxymethylene structure, with an adsorption enthalpy of 1.91 eV.²³⁰ The adsorption of formaldehyde in a surface oxygen vacancy is found to be 1.14 eV more exothermic than on the stoichiometric surface. In Figure 55 the half-lives of adsorption and desorption of CH₂O are given. The half-life of adsorption is calculated per unit cell based on the average density of CH₂O in the gas-phase, as calculated by Snoeckx et al.¹⁷¹. Starting from 700 K the half-life of desorption falls in the ms region, and will further drop with increasing temperatures. The hydrogenation of CH₂ in this temperature range is much faster, but will be limited by the slower hydrogen diffusion. However, the hydrogen diffusion, and thus the hydrogenation of CH₂, is $\sim 10^5$ times faster than the desorption of CH₂O at 700 K. This difference drops to a factor 4 at 1000 K. Due to the need of significant temperatures before desorption of CH₂O from a reduced surface can be observed, and the competition with the hydrogenation to CH₃ and possible ethene formation (see below), it is very likely that the catalytic component of the plasma-catalytic setup will not contribute significantly to the formation of formaldehyde in the end products. It might even be that the interaction of the plasma-formed formaldehyde with the catalyst can convert formaldehyde to other products.

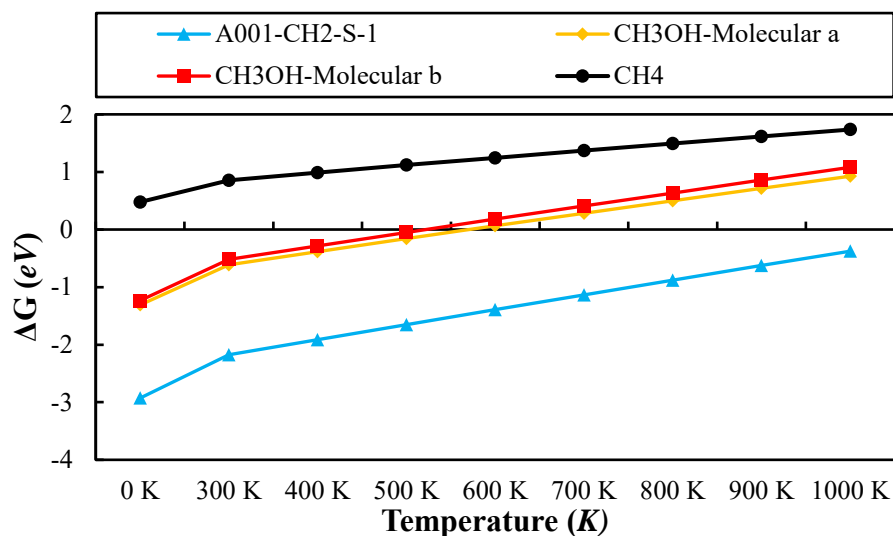


Figure 54. The Gibbs free energy of adsorption of CH_2O (A001-CH2-S-1) and CH_3OH (CH_3OH – Molecular a and b) on the reduced anatase (001) surface, and of the dissociative adsorption of methane on the stoichiometric surface.

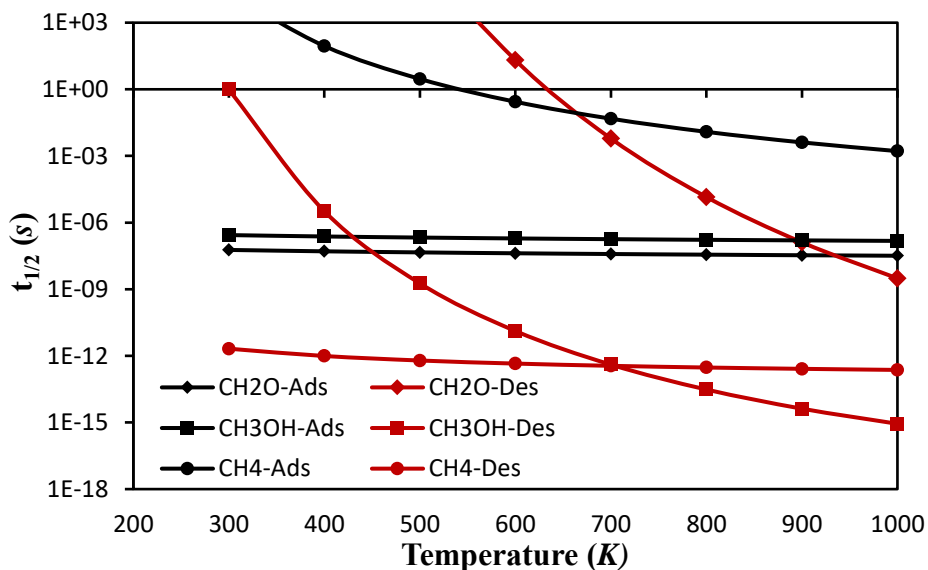


Figure 55. The half-lives of adsorption (X-Ads, black), and desorption (X-Des, red) for CH_2O , CH_3OH and CH_4 .

6.3.4.2. Methanol

In Figure 57 we show the different adsorption configurations of CH_3OH on the reduced anatase (001) surface, with their corresponding adsorption energies. Methanol will preferentially adsorb in a dissociative manner. However, to allow desorption, we start from the molecular adsorbed configurations, which are significantly less stable. The most stable dissociative adsorption configuration, CH_3OH -Dissociative a, has an adsorption energy of -2.62 eV, while the most stable molecular adsorption configuration, CH_3OH -Molecular a, only has an adsorption energy equal to -1.31 eV. In Figure 54 the Gibbs free energy of adsorption of methanol in the molecular adsorbed configurations CH_3OH -Molecular a and CH_3OH -Molecular b on the reduced anatase (001), containing a surface oxygen vacancy, is given. Starting from 600 K, desorption becomes exergonic. The Gibbs free energy of adsorption for CH_3OH -Molecular a ranges from 0.06 eV at 600 K to 0.93 eV at 1000 K, and for CH_3OH -Molecular b the range goes from 0.18 eV at 600 K to 1.08 eV at 1000 K. In Figure 55 the half-lives of adsorption per unit cell, based on the average density of methanol in the gas-phase as calculated by Snoeckx et al.¹⁷¹, and of desorption are given. The average waiting time before methanol will desorb from the CH_3OH -Molecular a configuration is in the μs region at 400 K, and drops to $\sim 10^{-11}$ s at 600 K, and to $\sim 10^{-15}$ s at 1000 K. However, this desorption first requires the formation of the molecular adsorbed configuration, which will be the rate limiting step. The calculated reaction pathway to form CH_3OH -Molecular a from the CH_3OH -Dissociative a adsorption configuration is given in Figure 56, together with the corresponding half-lives. As can be seen in the figure, the half-life for methanol formation drops below 1s at 600 K, ranging from $5 \cdot 10^{-2}$ s at 600 K to $3 \cdot 10^{-7}$ s at 1000 K, while the dissociation only has a half-life of $\sim 10^{-12}$ s in this temperature range. However, as the desorption of the molecular adsorbed methanol only has a

half-life of $\sim 10^{-11}$ s at 600 K, methanol will be one of the reaction products of plasma-catalytic dry reforming on the anatase (001) surface, as the reaction is pulled to the formation of methanol by its desorption. The average time before methanol reaches a unit cell is $\sim 0.1 \mu\text{s}^1$, and is thus significantly slower than the desorption in a temperature range of 500 – 1000 K. The desorption of methanol results in the formation of surface oxygen vacancies, which are necessary for the reduction of CO_2 ²²⁴.

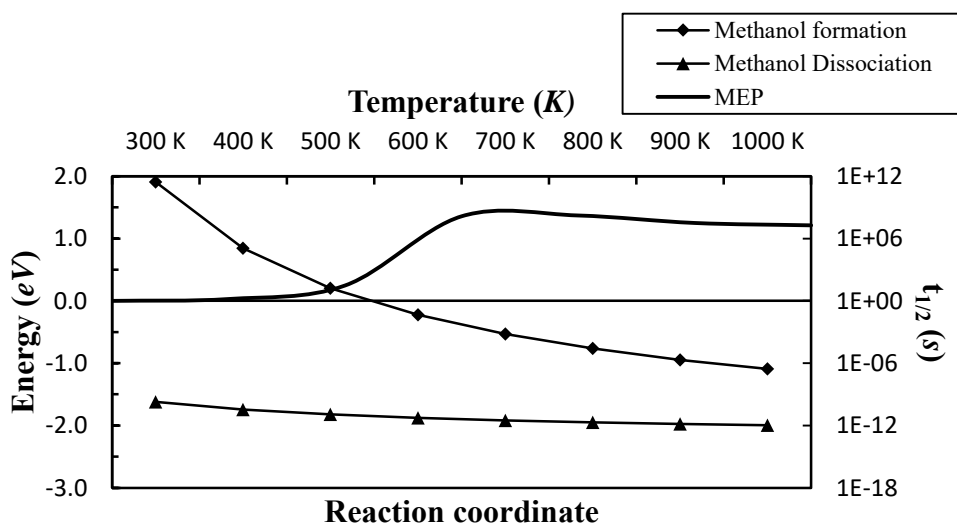


Figure 56. The minimal energy pathway (MEP) as calculated with NEB for the methanol formation on a reduced anatase (001) surface, containing a surface oxygen vacancy, and the half-life for methanol formation and dissociation. The MEP is given on the bottom and left axis, while the half-life of reaction is given on the top and right axis.

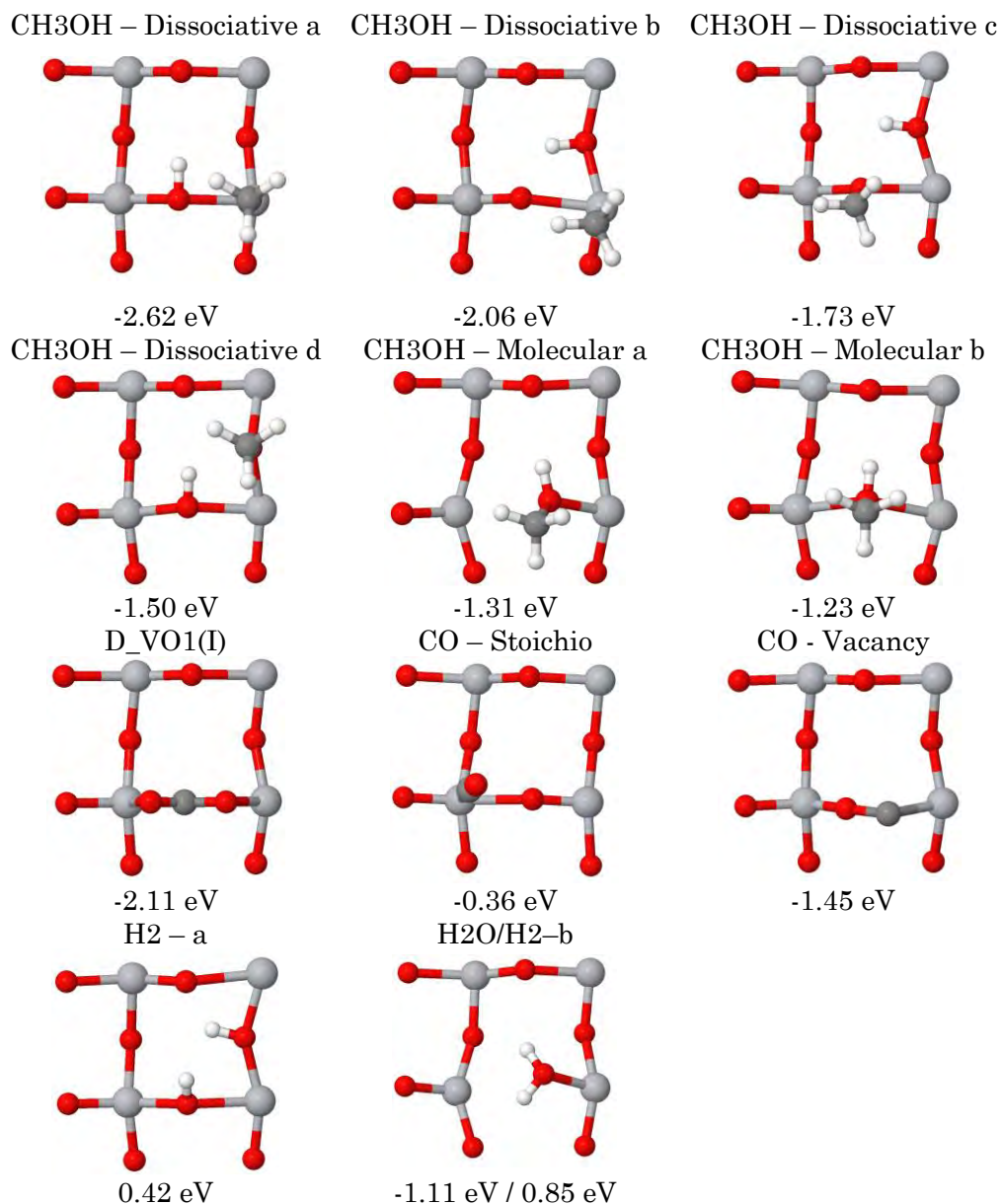


Figure 57. Methanol, H₂O and CO₂ adsorption configurations on a reduced anatase (001) surface, and CO and H₂ adsorption configurations on the stoichiometric anatase (001) surface, together with their corresponding adsorption energies.

6.3.4.3. Methane

Instead of desorption of methanol from the reduced anatase (001) surface, it is also possible to form and desorb methane from the stoichiometric surface, which is not desirable as this regenerates one of the reactants of the plasma-catalytic dry reforming of methane. The Gibbs free energy of adsorption of methane in a temperature range of 300 K – 1000 K and at absolute zero is given in Figure 54. The adsorption energy is relative to the adsorption configuration CH₃OH – Dissociative a given in Figure 57. In Figure 55 the half-lives of adsorption per unit cell, based on the average density of methane in the gas-phase as calculated by Snoeckx et al.¹⁷¹, and desorption are given. In the entire temperature range, 300 – 1000 K, the half-life of desorption is always faster than the half-life of adsorption. Above 700 K the desorption of methanol becomes faster than that of methane, which is beneficial as methane formation is counterproductive towards the plasma-catalytic dry reforming of methane to value-added chemicals. Once methane is desorbed, it can either re-adsorb through dissociative adsorption or be converted to CH_{4-x} + x H in the plasma. As can be seen in Figure 53, the temperature must exceed 900 K before the half life of dissociative adsorption of methane drops below 1 ms, while this is not the case for the adsorption of CH₃ and H. The half lives of adsorption for CH₃ and H at 300 K are equal to 48.5 μs and 7.2 μs, respectively. Thus, the hybridization of a plasma discharge with a TiO₂ catalyst surface significantly reduces the temperature threshold for dry reforming of methane. In a plasma-catalytic setup the overall reaction is no longer limited by the dissociative adsorption of methane, as this is circumvented by the dissociation of methane in the plasma discharge.

6.3.4.4. Water

Water can be formed on the surface by adsorbing two hydrogens to an O_{2c} atom, causing one Ti-O bond to break (see Figure 57) and forming two hydrogen bonds with neighbouring O_{3c} atoms. However, we found that the formed H_2O is 1.61 eV less stable at absolute zero than two hydrogens adsorbed separately on the surface; this increases to 1.65 eV at 1000 K. In comparison, the molecular adsorbed methanol, i.e., CH_3OH – Molecular a, is 1.35 eV less stable than the separated CH_3 and H, and the dissociative adsorption of H_2 on the O_{2c} and O_{3c} adsorption sites, i.e., H_2 – a, is 1.19 eV less stable than the separated hydrogens, all at absolute zero. After its formation, water could desorb from the surface and create an oxygen vacancy. In Figure 58 the Gibbs free energy of adsorption is given for H_2O at the reduced anatase (001) surface, containing a surface oxygen vacancy. The adsorption configuration of H_2O on the reduced surface is the same as the adsorption of H_2 on the stoichiometric surface (see Figure 57, H_2O/H_2 –b). In Figure 59 the half-lives of adsorption per unit cell, based on the average density of methane in the gas-phase as calculated by Snoeckx et al.¹⁷¹, and desorption of H_2O and H_2 are given. From 400 K onwards, the desorption of H_2O , and thus formation of oxygen vacancies, can occur, and the half-life of adsorption and desorption become equal at 600 K. Above this temperature, the half-life of desorption becomes shorter than the time required for water to adsorb onto the adsorption site. From the H_2O/H_2 –b configuration, there is also the possibility to desorb H_2 , which is faster than H_2O desorption up to 500 K. Above this temperature, more H_2O and oxygen vacancies will be formed than H_2 from the H_2O/H_2 –b configuration. If H_2 desorbs, it is more likely to readsorb in the H_2 – a configuration than H_2O/H_2 –b configuration. Furthermore, the readsorption of the formed H_2 is significantly slower than the readsorption

of the formed H_2O . Thus, we expect that the formation of H_2 will be much more prominent than the formation of H_2O .

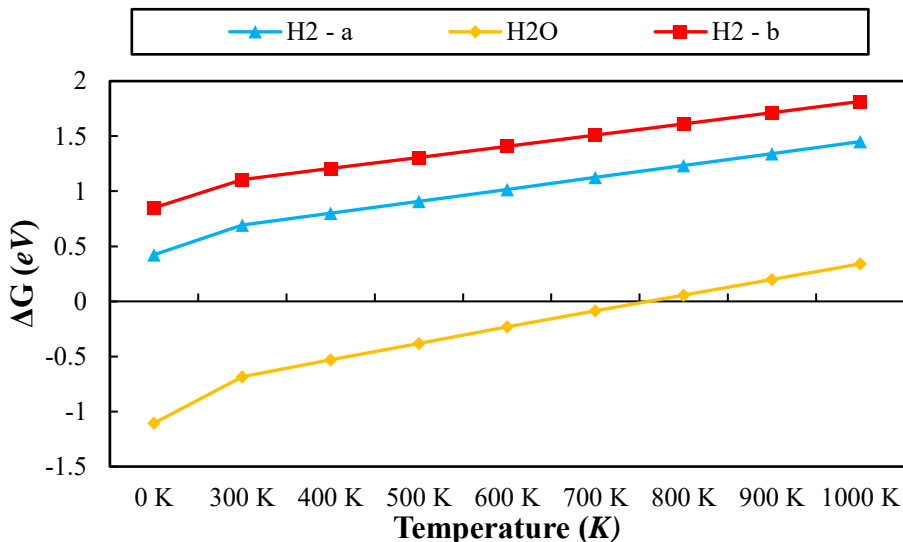


Figure 58. The Gibbs free energy of adsorption of H_2O on the reduced anatase (001) surface and of H_2 (dissociative $\text{H}_2 - \text{a}$, and molecular $\text{H}_2 - \text{b}$) on the stoichiometric anatase (001) surface.

6.3.4.5. Hydrogen gas

From the Gibbs free energy of adsorption of H_2 on the stoichiometric surface, given in Figure 58, it is seen that the desorption of H_2 is exergonic both for the dissociative adsorption channel, i.e., $\text{H}_2 - \text{a}$, as for the molecular channel, i.e., $\text{H}_2 - \text{b}$, in the entire temperature range of 300 K – 1000 K. The configurations of $\text{H}_2 - \text{a}$ and $\text{H}_2 - \text{b}$ are given in Figure 57. Due to the increased stability of $\text{H}_2 - \text{a}$ compared to $\text{H}_2 - \text{b}$, e.g. the energy difference at absolute zero is equal to -0.43 eV, and the comparable rates of H_2 formation through both channels, especially at 500 K and above (see Figure 59), more H_2 will be formed through the $\text{H}_2 - \text{a}$ configuration than

through the H2 – b configuration. As mentioned above, the readsorption of H₂ is significantly slower than its formation, e.g., $\sim 10^5$ times slower at 500 K, possibly resulting in a large fraction of the end products consisting of hydrogen gas.

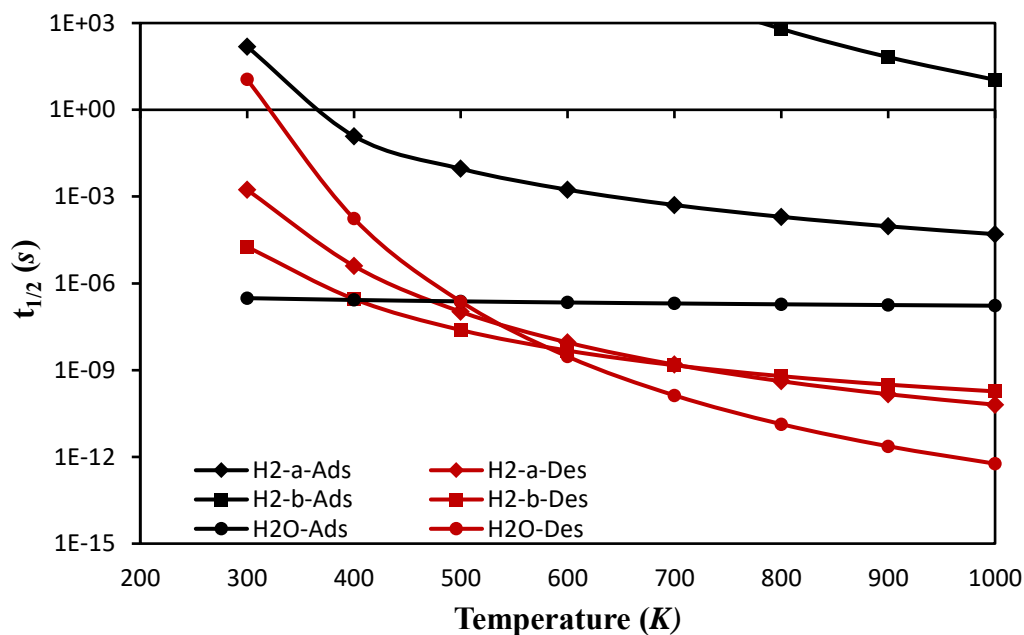


Figure 59. The half-lives of adsorption (X-Ads) and desorption (X-Des) for H₂O and H₂ on the anatase (001) surface.

6.3.4.6. Carbon monoxide

We have shown in our previous work that the reduction of CO₂ on the anatase (001) surface requires the presence of oxygen vacancies.²²⁴ These are intrinsically present in the surface, but will be depleted after the reduction of CO₂, as an oxygen of CO₂ heals the oxygen vacancy and results in a stoichiometric surface with CO adsorbed. In Figure 63 the Gibbs free energy of adsorption of CO on the stoichiometric anatase (001) surface, and of CO₂ in the most stable adsorption configuration on the reduced surface, i.e., D_VO1(I) (see Figure 57),²²⁴ is given in a temperature

range of 300 K – 1000 K. The Gibbs free energy of adsorption of CO is equal to 0.02 eV at 300 K, increasing to 0.39 eV at 600K and up to 0.85 eV at 1000 K, while the adsorption of CO₂ in the D_VO1(I) configuration remains exergonic within the entire considered temperature range. In Figure 64 the half-lives of adsorption are given per unit cell, based on the average density of CO and CO₂ in the gas-phase as calculated by Snoeckx et al.,¹⁷¹ as well as the desorption of CO and CO₂ on the reduced and stoichiometric anatase (001) surface. Once CO is formed, it will desorb easily at all considered temperatures. The average time it takes for the formed CO to desorb at 300 K is 0.015 ns, dropping to 1.7 fs at 1000 K. Thus, the rate limiting step in the formation of CO will be the reduction of CO₂ on the surface. The minimal energy pathway of CO₂ in the D_VO1(I) configuration, as we recently reported,²²⁴ is shown in Figure 60, together with the half-lives in the temperature range of 300 K – 1000 K. While CO₂ dissociation will only occur sporadically at room temperature, it will significantly increase at elevated temperatures and the equilibrium will shift towards the formed CO, e.g. the half-life for dissociation decreases from 0.6 s at room temperature to $6 \cdot 10^{-8}$ s ($8 \cdot 10^{-11}$ s) at 600 K (1000 K) and the equilibrium constant changes from $1.50 \cdot 10^{-10}$ to $8.33 \cdot 10^{-5}$ ($2.5 \cdot 10^{-2}$) at 600 K (1000 K). Taking into account the significant reaction rate of CO formation and that the desorption of CO is faster than the reformation of CO₂, cf. Figure 60 and Figure 62, it is clear that CO will form a significant part of the reaction products, provided that sufficient oxygen vacancies can be supplied by the reduction of the surface to form other reaction products, i.e., methanol, formaldehyde and H₂O.

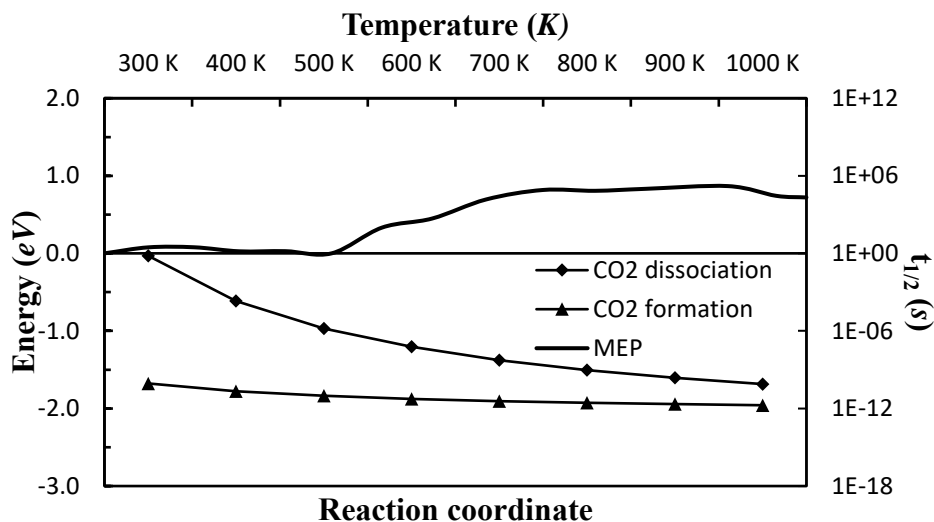


Figure 60. The minimal energy pathway (MEP) as calculated with NEB for the CO_2 reduction on the reduced anatase (001) surface, and the half-life for the CO_2 dissociation and formation. The MEP is given on the bottom and left axis, while the half-life of reaction is given on the top and right axis.

If CO_2 is adsorbed on a stoichiometric region of the anatase (001) surface, in order to reduce CO_2 to CO, it will need to diffuse over the surface to adsorb in an oxygen vacancy site, or a nearby O_{2c} has to be removed by the formation of either methanol, formaldehyde, CO from an adsorbed C radical or water. Else CO_2 will act as a “spectator” and will block activate sites until it is desorbed. In Figure 61 we show the minimal energy pathway for the diffusion of CO_2 over the stoichiometric surface, and the corresponding half-life at a temperature range of 300 K – 1000 K. In order for sufficiently fast diffusion to occur over the surface elevated temperatures are required. At 600 K the half-life drops to 90 ms, decreasing to 6 μs at 1000 K. However, it is also possible for the CO_2 to desorb from the stoichiometric region and re-adsorb in an oxygen vacancy. At 600 K the average time for a CO_2 molecule to desorb from the surface is

equal to $0.7 \mu\text{s}$, which is significantly faster than the calculated diffusion. Thus CO_2 is more likely to desorb, than it will diffuse to an oxygen vacancy.

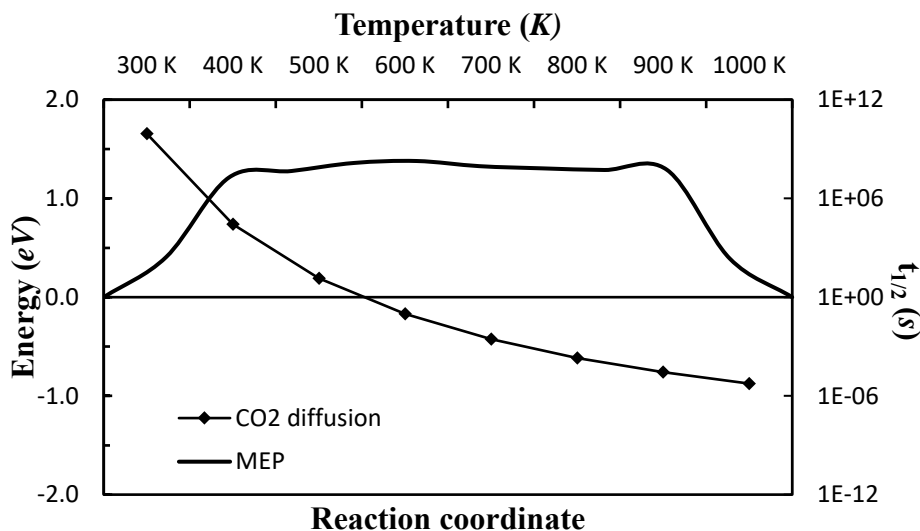


Figure 61. The minimal energy pathway (MEP) as calculated with NEB for the CO_2 diffusion on the stoichiometric anatase (001) surface, and the half-life for diffusion. The MEP is given on the bottom and left axis, while the half-life of reaction is given on the top and right axis.

Should the C radical be available on the surface, either through the unfavoured dehydrogenation reactions or through adsorption from the gas-phase, it would be possible to desorb CO and create an oxygen vacancy upon doing so. The Gibbs free energy of adsorption for CO being adsorbed on a reduced surface is given in Figure 63. This adsorption configuration is equivalent to the adsorption of C on the stoichiometric surface, and is shown in Figure 57 as CO – Vacancy. The desorption of CO leaving behind an oxygen vacancy, is slower than the hydrogenation of C, however this latter reaction will be limited by the presence of H in the proximity of the

C. The hydrogen can be provided through either H diffusion, H adsorption or dissociative adsorption of H_2 . The relevant data for the comparison between the rate of each of these reactions is given in Figure 49, Figure 53, Figure 59, and Figure 62. Starting from 500 K, the desorption of CO will become faster than the hydrogenation of C, as the hydrogenation of C is limited by the H supply. Thus, above 500 K, the formation of CO through the oxidation of C will contribute to the formation of oxygen vacancies, and increase the concentration of CO in the end products.

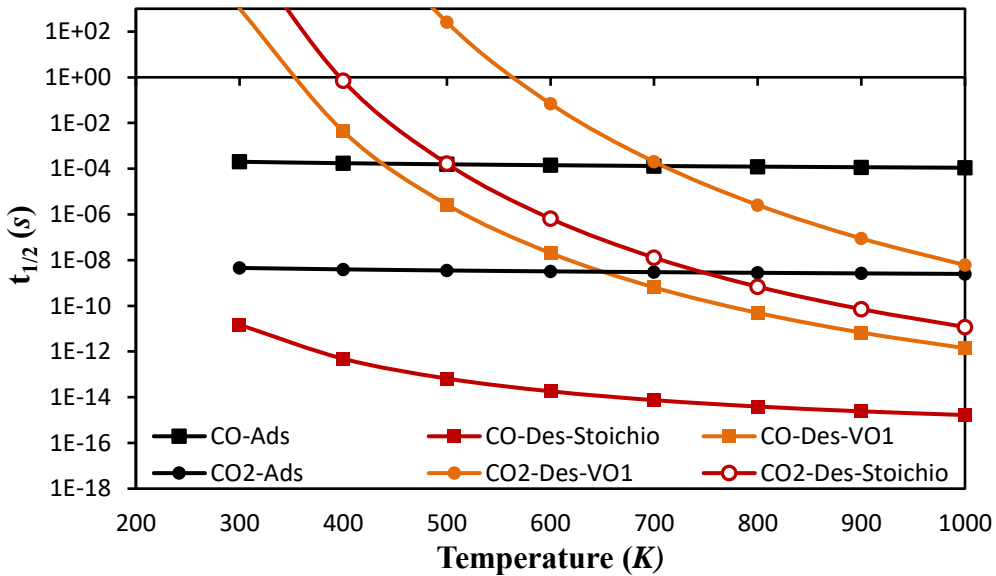


Figure 62. The half-lives of adsorption (X-Ads, black), desorption (X-Des-stoichio, red) of the stoichiometric anatase (001) surface, and desorption (X-Des-VO1, orange) of the reduced surface for CO and CO₂.

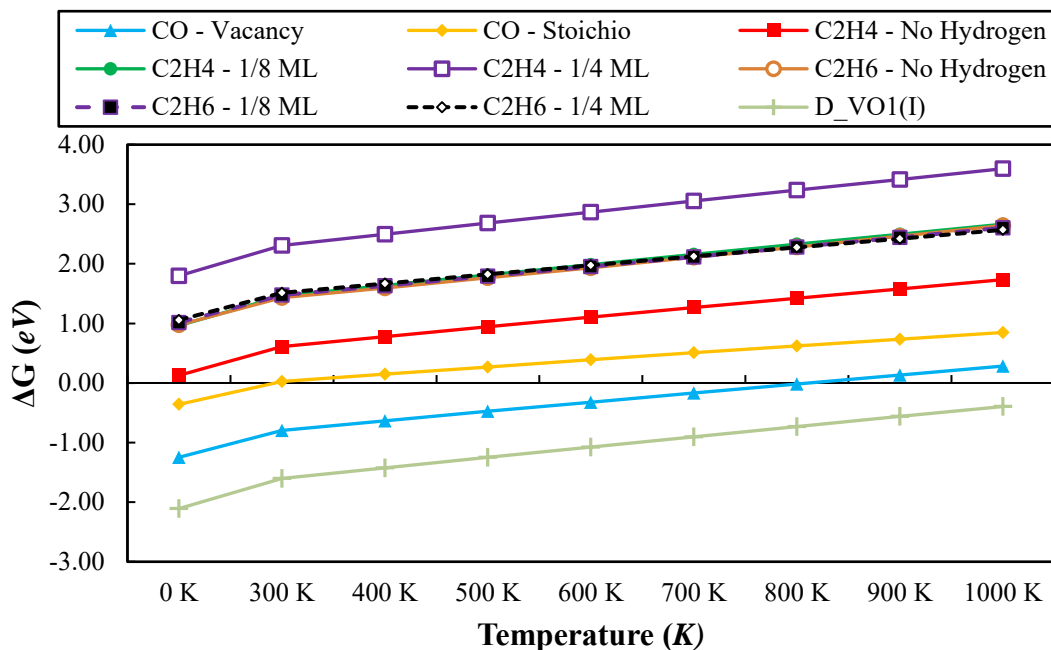


Figure 63. The Gibbs free energy of adsorption of ethane and ethene on the stoichiometric anatase (001) surface with different degrees of hydrogenation of the surface (no hydrogenation, 1/4 ML and 1/8 ML of Hydrogen), of CO on the stoichiometric surface, and of CO and CO₂ (D_VO1(I)) on the reduced surface .

6.3.4.1. Ethane and Ethene

The hydrogen radicals are removed from the surface as methanol, formaldehyde, water and hydrogen gas, thus depleting the hydrogen present on the surface, which could react with the adsorbed methane derived radicals. This could lead to poisoning of the surface by the adsorbed CH_x radicals. This can be resolved by the desorption of CO, ethane and ethene, which will be formed by the C, CH₃ and CH₂ radicals, respectively. The Gibbs free energy of adsorption of ethane and ethene is given in Figure 63. The desorption of both ethane and ethene is found to

be exergonic at all temperatures. The half-lives of adsorption per unit cell, based on the average density of ethane and ethene in the gas-phase as calculated by Snoeckx et al.¹⁷¹, and the half lives of desorption, formation and dissociation of ethane and ethane are given in Figure 64. Only the half-lives faster than 1000 s are given, causing the half-life of the dissociative adsorption of ethane to not appear on the graph. For ethene molecular adsorption is preferred. The enthalpy of dissociation is equal to 2.15 eV, causing the equilibrium to lie towards the formation of ethene. Its desorption is significantly faster than the adsorption on the surface. Also the formation and desorption of ethane will be high. The half-lives of ethane and ethene formation range from 1.3 ns to 18 ps for ethane and from 0.5 μ s to 3.5 ps for ethene in the temperature range of 300 – 1000 K. Once ethane is formed and desorbs from the surface, no re-adsorption will occur. However, ethane can dissociate in the plasma, and thus re-adsorb as CH_3 radicals.

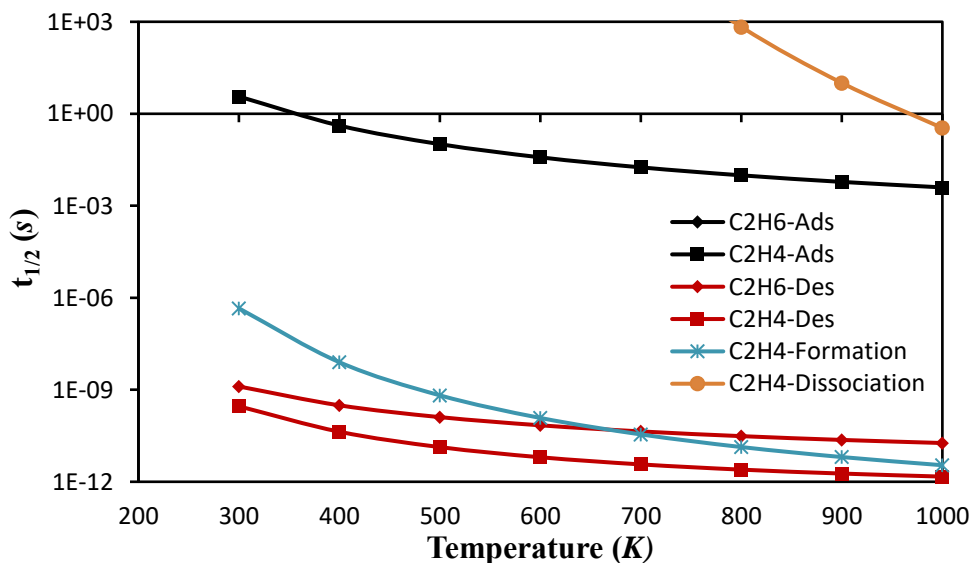


Figure 64. The half-lives of adsorption (X-Ads, black) and desorption (X-Des, red) of the anatase (001) surface for C_2H_6 and C_2H_4 .

6.4. Conclusion

We have studied the plasma-surface interactions of the plasma-catalytic dry reforming of methane into value-added chemicals on an anatase (001) surface using DFT calculations with the PBE exchange-correlation functional with long range dispersion energy corrections of Tkatchenko and Scheffler²⁰⁹. The methane derived radicals will act as a reducing agent, to provide a consistent formation of oxygen vacancies in the surface required for the reduction of CO₂. The readily available methane derived radicals are CH₃, CH₂, and H, since further dehydrogenation is thermodynamically and kinetically limited. Moreover, the adsorption of CH and C from the plasma gas-phase will be significantly lower than of CH₃, CH₂, and H, due to their low concentrations.

We have studied the formation of formaldehyde, methanol, methane, water, H₂, CO, ethane and ethene on the surface in a temperature range of 300 – 1000 K. The contribution of the catalytic component of the plasma-catalytic setup to the formation of formaldehyde will be negligible, due to the slow desorption kinetics of formaldehyde, and the depletion of CH₂ radicals due to the significantly faster hydrogenation rate to CH₃ and formation rate of ethene. Despite the fact that methanol will preferentially adsorb dissociatively, significant formation of methanol can be achieved at 600 K and above. The desorption of methanol is a two-step process, starting with the association of CH₃ and OH and subsequently the molecular desorption of methanol, which creates an oxygen vacancy. The rate limiting step is the association of CH₃ and OH, which requires 600 K to proceed at a significant rate. It is also possible to form methane from the same adsorption configurations as the methanol formation. The formation of methane is a rapid reaction, and will counter-act its reforming to value-added chemicals. We found that the formation of water is possible, leaving

behind an oxygen vacancy after desorption. However, the formation of H_2 will be much more prominent than that of water. H_2 will form a significant fraction of the end products. We studied the dissociation of CO_2 in an oxygen vacancy, as its reduction was previously found not to be possible on the stoichiometric surface. Once CO is formed, it will desorb almost instantaneously from the surface. Thus, the reaction will be limited by the CO_2 reduction, which starts to occur significantly from 400 K. The diffusion of CO_2 from a stoichiometric region to the oxygen vacancy would require temperatures of at least 600 – 700 K. However, the desorption from the stoichiometric region of the surface and readsorption in an oxygen vacancy of CO_2 will occur easily at 500 K and above. CO can also be formed by the desorption of a C radical with a surface oxygen to form CO and an oxygen vacancy. The rate of this process will be faster than the hydrogenation of C starting from 500 K. However, this will be limited by the supply of C radicals, which are not readily available. The formation and desorption of ethane and ethene will occur very rapidly at all considered temperatures, and once formed these species will not dissociate on the surface. However, they can be dissociated in a plasma-discharge. The combination of a plasma with a catalytic TiO_2 surface results in a synergistic effect. To observe a significant rate of the dry reforming of methane in thermal catalysis a temperature of 900 K is required due to the slow kinetics of the dissociative adsorption of methane. In plasma-catalytic dry reforming of methane this temperature threshold is lowered, as methane will dissociate in the gas phase and adsorb as CH_3 and H.

The rich variety of surface reactions occurring in the plasma-catalytic dry reforming of methane, their different behaviour as a function of temperature, and their dependency on the availability of the different plasma-species make it possible to tune the end products and their selectivities based on the plasma properties. The plasma will activate the

source gas by electron impact reactions, and by changing the plasma conditions the formation of specific plasma species can be controlled. This will influence their densities and fluxes towards the catalyst surface, which changes the plasma-surface interactions and thus the formation of the end products.

Critical assessment

In this part, I critically assess a number of aspects of my thesis and topics closely related to my thesis, based on the results obtained during my Ph.D. research.

In Chapter 6 it was concluded that the presence of methane-derived radicals in the plasma-catalytic dry reforming of methane (PC-DRM) results in the lowering of the temperature threshold of the reforming reaction compared to thermal reforming. However, for the PC-DRM using DBD reactors, typical energy efficiencies are reported between 6 and 23%^{34,35,50,58}, which is significantly lower than the theoretical energy efficiency of classical DRM at 973 K, i.e. 58%.¹⁷¹ Thus, to be competitive in terms of energy efficiency with classical DRM, the energy efficiency of PC-DRM still needs to increase significantly.

However, the lower operating temperature of PC-DRM reduces, or can even completely remove, the necessity of external heating. In plasma-catalysis electricity is used as the energy source for the conversion rather than external heating. This enables the use of renewable energy sources, such as wind and solar energy. Furthermore, the production of electricity through these renewable energy sources is highly variable. This results in an energy deficit and surplus, when the demand does not match the supply. The surplus provides a carbon neutral electricity source, which can be utilized for the PC-DRM to store this excess energy in a chemical form. The variable energy supply is not much of a problem for PC-DRM, as the plasma can be turned on and off very quickly. For these reasons, it is not a major problem that the current energy efficiency of the PC-DRM lies significantly below the theoretical maximum energy efficiency of thermal

Critical assessment

DRM. Nevertheless, the search for a more efficient process and highly active catalysts should still be continued.

In this dissertation the DRM on a TiO₂ anatase (001) surface was studied. In Chapter 4 and Chapter 6 the interaction with the surface and the oxidation reactions on the catalyst surface of methane-derived radicals were reported. In Chapter 5 the CO₂ adsorption and reduction were reported. At the end of Chapter 6 the link between the chemistry of CO₂ and CH₄ was reported. The overall dry reforming reaction on anatase (001) can be summarized as a Mars-van Krevelen mechanism. The intrinsically present oxygen vacancies in the TiO₂ surface heal during the reduction of CO₂, and thus the surface will become oxidized. Subsequently, the surface is reduced, i.e., new oxygen vacancies are formed, by the reaction of methane-derived radicals on the surface, forming oxygenated products. The rate limiting step is the formation of oxygen vacancies, as the reduction of CO₂ is a rapid reaction (see Chapter 5). The most important route for oxygen vacancy formation will need to be determined in future modelling attempts on the mesoscale level, using for example kinetic Monte Carlo or microkinetic models. These models can be built based on the results obtained during this Ph.D. research.

The strength of mesoscale models depends on whether or not the considered reaction list is exhaustive. The combination of DFT with the Nudged Elastic Band (NEB) method, used in this research, does not allow to assess whether all the important surface reactions and reaction mechanisms are considered. This is due to the fact that NEB depends in part on the chemical intuition of the user. One has to provide both the initial and final configuration of the reaction. Currently, several reactions necessary for the construction of a mesoscale model are still missing, such as the diffusion of the different CH_x radicals over the surface, the formation of C₃-chemicals, e.g., the reaction between CH₃ and CH₂ results

in an adsorbed C_2H_5 radical, which can further react to for example propane and propene, but also ethanol could be formed. To reduce the risk of missing important surface reactions, the sampling of the possible pathways can be extended by for example the use of the DIMER method²³¹ or by accelerated MD methods, such as CVHD²³². These methods can be used as an explorative tool, as only the initial geometries need to be supplied. However, even for these methods, there is still the risk that not all (important) reactions are found.

In my research I employed a (2x2) supercell of the anatase (001) surface. Even the introduction of a single oxygen vacancy in this model results in an overestimation of the defect concentration, i.e., 0.25 ML in comparison with 0.08 – 0.15 ML found under ultra-high-vacuum conditions^{233,234}. The calculated formation energy for the different oxygen vacancies is increased, due to the repulsive interactions between the defects.²³⁵ However, the order of stability remains the same. The lower stability of the reduced surface might result in an underestimation of the energy barriers of reactions consuming oxygen vacancies and an overestimation of the energy barriers of reactions that generated oxygen vacancies.

LDA and GGA-DFT functionals typically fail to describe the electronic structure of defect states in metal-oxides.^{150,236} This originates from the self-interaction error in these functionals, resulting in a bias towards delocalization of the excess electrons in the structure.²³⁷ These errors can be mitigated by applying hybrid functionals or DFT+U methods.^{237,238} Due to the high computational cost of hybrid functionals in comparison with GGA functionals²³⁹, one often applies DFT+U. However, the exact value of U tends to be very susceptible to the considered physical property.²³⁶ For the reduction of TiO_2 to Ti_2O_3 Lutfalla et al.²³⁶ report an optimal value of $U = 2.3$ eV based on the enthalpy of reduction, which is significantly different from the value of $U = 4.2$ eV proposed by Morgan and Watson based on the

Critical assessment

location of the defect states in the band gap²⁴⁰. Further, Cheng and Selloni report an optimal value in the range of $U = 3 - 3.5 \text{ eV}$ ¹⁵⁰ to obtain a reasonable description of the energy levels of the defect states. These authors also found that at the reported values the stability between surface and subsurface oxygen vacancies in anatase (101) becomes equal, which is inconsistent with the significantly higher stability of subsurface oxygen vacancies reported based on experimental observations.¹⁵⁰ The value of U depends significantly on the considered properties, and it is not clear whether applying the Hubbard correction will introduce errors in the calculated adsorption energies, energy barriers, etc. I therefore have chosen to not apply Hubbard $+U$ corrections in my calculations.

The results and the conclusions obtained in this dissertation form the basis of a more profound molecular understanding of the plasma-surface interactions for the plasma-catalytic dry reforming of methane. The herein presented research will form a starting point to further unravel the mechanisms of plasma-catalysis. The next steps will be to complete the list of relevant surface reactions, so that mesoscale models can be built, to include the effect of the presence of excess electrons due to the plasma in the surface and to include the effect of the electric field. The comparison between the different effects, the presence of plasma species, electric field and surface charging will provide insight in possible synergistic effects. Furthermore, it would be valuable to study the role of metal particles dispersed on TiO_2 and to evaluate the importance of the catalytic activity of the TiO_2 support on the overall reaction.

Summary

The continuously increasing anthropogenic emission of greenhouse gasses has introduced substantial changes in the magnitude of the greenhouse effect. This has already resulted in changes in the global climate, e.g. an increase of the average surface temperature, the rise in sea level, the acidification of the oceans, more extreme weather conditions and so forth. To fight the global climate change, proper actions need to be taken. The decrease of the greenhouse gas emissions and concentrations is required to prevent further changes to our climate.

Conventional conversion methods of greenhouse gases have their disadvantages, such as a high energy requirement, and sintering, coke formation and sulphur poisoning of the employed catalysts. It has been suggested that plasma-catalysis is a promising alternative to the conventional reforming processes. In plasma-catalysis one combines the catalyst with plasma technology. The plasma will activate the feed gas by electron impact reactions, while the catalyst will lower the energy barrier for surface reactions. The plasma and catalyst will influence each other, which can lead to synergism. The plasma will change the gas composition to a highly reactive and complex mixture of reactive species in the proximity of the catalyst, and might change the physicochemical properties of the catalyst. Vice versa, the catalyst will change the gas composition as well. Furthermore, there will be changes in the structural and electronic properties of the catalyst, and the retention time of the plasma species increases. Due to the high complexity of the plasma-catalytic system, there is still a lack of fundamental knowledge on the plasma-surface interactions. Experimentally it is difficult to study these interactions without disturbing the plasma properties. To gain a fundamental

Summary

understanding of the plasma-catalytic system, computational studies can form a complementary tool to experiments.

In this dissertation, I have used both classical MD simulations and DFT calculations to gain insight in the catalytic activity of a titanium dioxide catalyst, and more specifically to gain insight in the interactions of plasma species with the catalyst surface in plasma-catalytic dry reforming of methane.

In Chapter 3, a classical reactive force field was developed for the study of intrinsic point defects in titanium dioxide. The ReaxFF force field parameters were fitted against DFT and experimental data to reproduce the structural and energetic properties of TiO_2 , the formation and diffusion of oxygen vacancies and interstitial titanium, and the influence of defects on the adsorption of oxygen. This force field was applied to study oxygen vacancy diffusion. We found that surface oxygen vacancy diffusion occurs through the subsequent diffusion into the subsurface, subsurface diffusion and subsequently the diffusion from the subsurface to the surface, rather than through surface diffusion.

The adsorption of plasma generated CH_x radicals on an anatase (001) surface is reported in Chapter 4. The influence of oxygen vacancies on the adsorption was studied. In contrast with anatase (101), the most stable oxygen vacancy is located at the surface, rather than in the subsurface. The presence of oxygen vacancies will influence the stability of the various adsorption configurations and result in new adsorption configurations. One observation is the strongly increased adsorption of CH_3 on the reduced surface. CH_3 can adsorb strongly on a titanium atom on the reduced surface, which was not possible on the oxidized surface. Because of this new adsorption configuration, CH_3 preferentially adsorbs in the proximity of an oxygen vacancy. This is also seen for CH_2 , while C adsorbs

preferentially in a stoichiometric region, and CH has no preferential adsorption region.

Chapter 5 focusses on the influence of oxygen vacancies on the dissociation of CO₂ on anatase (001). The increased Lewis basicity of the surface due to the introduction of oxygen vacancies does not significantly influence the adsorption strength. However, new adsorption configurations were found, which also showed increased activation of the C-O bonds compared to the gas-phase. The dissociation of CO₂ on the stoichiometric surface was found to have a barrier of ~5 eV, and is thus unlikely to occur. However, significantly lower barriers were found on the reduced surface, as the oxygen vacancy provides a means to stabilize the end product. For the most stable adsorption configuration on the reduced surface we found a barrier of ~0.8 eV, thus it only requires slightly elevated temperatures to occur (cf. Chapter 6). Hence, the oxygen vacancies play a significant role in the catalytic activity of anatase (001), and of titanium dioxide in general. As the CO₂ dissociation on the reduced surface heals the oxygen vacancy, a regeneration mechanism is required. In the plasma-catalytic dry reforming of methane this would be possible by the use of methane derived radicals as reductant.

The surface reactions of the plasma-catalytic dry reforming of methane on anatase (001) are reported in Chapter 6. A CO₂/CH₄ mixture is introduced in a plasma discharge, where the electron impact reactions activate the gas molecules. In Chapter 5, it is shown that CO₂ can be reduced to CO on the catalyst surface, if oxygen vacancies are present in the surface. The reaction itself is not catalytic, but stoichiometric, since one of the oxygens of CO₂ heals the oxygen vacancy upon reduction. However, when methane is introduced in the feed gas, it is possible to reduce the surface by the methane derived species in the plasma. The focus is on the most prominent plasma species, C, CH, CH₂, CH₃ and H. Once the CH_x radicals adsorb on

Summary

the surface, they can hydrogenate and dehydrogenate. Together with the higher concentrations of CH_3 and CH_2 compared to C and CH in the plasma discharge, this makes CH_3 and CH_2 the readily available radicals adsorbed on the surface, together with H. The formation reactions of formaldehyde, methanol, methane, water, H_2 , CO, ethane and ethene were reported in a temperature range of 300 – 1000 K. Based on the reaction rates, the most prominent reaction products will be methanol, H_2 , CO, ethane, and ethene. Elevated temperatures will be required to form these products at acceptable rates. However, the temperature threshold to observe acceptable rates for plasma-catalytic dry reforming of methane is significantly lower than for thermal reforming, i.e., 500 K for the plasma-catalytic reforming and 900 K for the thermal reforming.

Based on the results reported in this chapter, it is expected that the selectivities to specific end products of the plasma-catalytic dry reforming of methane can be tuned based on the properties of the plasma-catalytic system. The surface reactions exhibit a different dependency on the temperature, and will depend on the concentration of adsorbed plasma species, and thus on their rate of adsorption and desorption. The rate of adsorption in turn depends on the density of the different species in the plasma gas-phase. This will be determined by the formation reactions, which depend on the plasma properties. The results of this chapter are the first step to find the missing links required to control and steer the plasma-catalytic dry reforming of methane.

I envision a number of important steps to further elucidate the plasma-catalytic surface interactions in the future. In this dissertation I have studied the surface reactions on a quantum mechanical level, which results in information on the atomic level. However, to be able to couple these insights to the macroscopic world, and reach realistic time scales, it would be opportune to build a mesoscale model that allows to study longer

time and larger length scales. With the results obtained in this dissertation it would be possible to build a kinetic Monte Carlo model, that allows to study the effect of varying the plasma species densities on the formation reactions and thus the end products. This can further be combined with a study of the influence of the temperature on the end products. A schematic overview of this strategy is given in Figure 65.

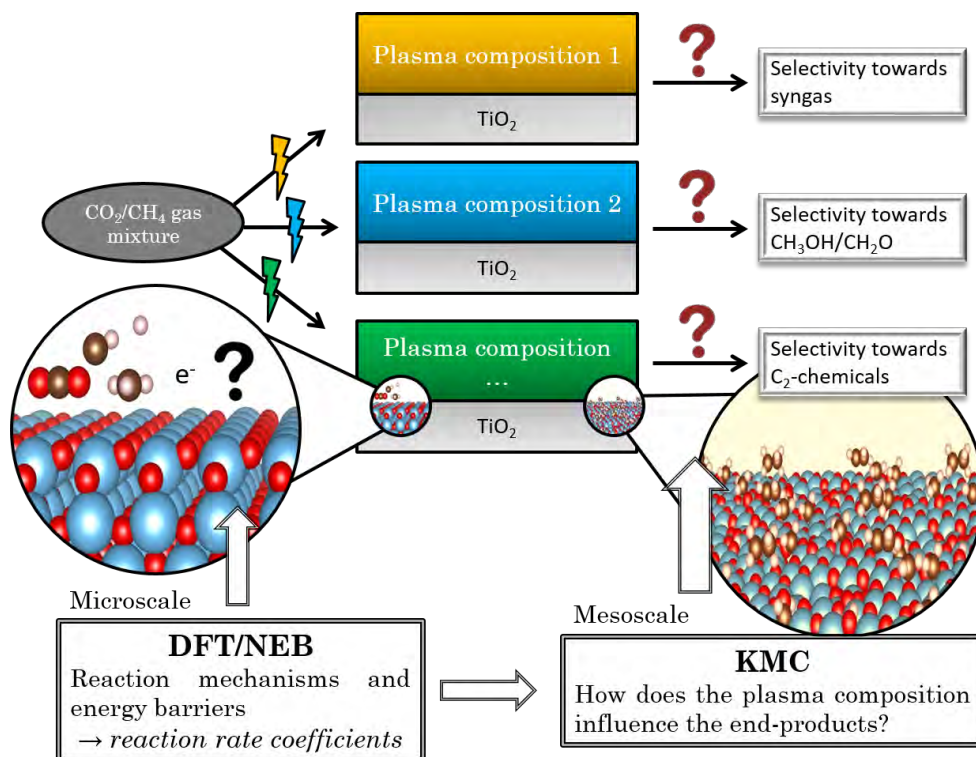


Figure 65. Schematic overview of the future outlooks.

A next step could be to study the effects of the electric field and surface charging, which typically occurs at a surface exposed to a plasma discharge, on the adsorption-desorption equilibrium and surface reactions, using quantum mechanical modelling. These results can again be implemented in a mesoscale model. The combination of the results of both mesoscale models will allow insight in the origin of possible synergism,

Summary

and which parameters are important to steer the plasma-catalytic process towards a desired composition of the output gas stream.

Samenvatting

De antropogene uitstoot van broeikasgassen heeft aanzienlijke veranderingen in de omvang van het broeikaseffect geïntroduceerd. Dit heeft geleid tot veranderingen in het mondiale klimaat, bijvoorbeeld een stijging in de gemiddelde oppervlaktetemperatuur, een stijging van de zeespiegel, de acidificatie van de oceanen, meer extreme weersomstandigheden, enzovoort. Om de globale klimaatveranderingen te bestrijden, dienen er dringend maatregelen genomen te worden. De daling van de uitstoot van broeikasgassen en de daling van hun concentraties is noodzakelijk om verdere veranderingen in ons klimaat te voorkomen.

De conventionele conversiemethoden voor broeikasgassen kampen met een aantal problemen, zoals een hoge energieconsumptie, sintering, zwavelvergiftiging van de katalysator, en cokesafzetting. Plasmakatalyse wordt voorgesteld als een veelbelovend alternatief voor de conventionele methoden. Binnen plasmakatalyse combineert men plasmatechnologie met een katalysator. Het plasma zal de gasfase activeren met behulp van elektron impact reacties, terwijl de katalysator de energiebarrière voor de oppervlaktereacties zal verlagen. De aanwezigheid van de katalysator in het plasma zorgt voor een wederzijdse invloed van de katalysator en het plasma op elkaar. Het plasma zal de gassamenstelling veranderen in de nabijheid van de katalysator naar een reactief en complex mengsel van reactieve deeltjes, en kan de fysico-chemische eigenschappen van de katalysator veranderen. Omgekeerd zal de katalysator de gassamenstelling ook veranderen, en bovendien zal de katalysator invloed hebben op de elektronische eigenschappen van het plasma en de retentietijd van de plasma species beïnvloeden. Vanwege de grote complexiteit van het plasmakatalytisch systeem is er een gebrek aan fundamentele kennis over de plasma-katalysator interacties.

Samenvatting

Experimenteel wordt het bestuderen van deze interacties bemoeilijkt doordat elke invasieve techniek de plasma-eigenschappen zal beïnvloeden. Daarom is het opportuun om computationele simulaties uit te voeren die complementair zijn aan experimenten.

In dit proefschrift heb ik zowel klassieke Moleculaire Dynamica simulaties als DichtheidsFunctionaal Theorie berekeningen gebruikt om inzicht te verwerven in de katalytische activiteit van een titanium dioxide katalysator, en in het bijzonder in de interacties van plasma species met het katalysatoroppervlak voor de plasmakatalytische *dry reforming* van methaan.

In hoofdstuk 3 werd een klassiek reactief krachtveld ontwikkeld om de intrinsieke puntdefecten in titanium dioxide te bestuderen. De ReaxFF krachtveld parameters werden gefit tegen DFT en experimentele data van structurele en energetische parameters van TiO_2 , de vorming en diffusie van zuurstofvacatures en interstitieel titanium, en de invloed van deze defecten op de adsorptie van zuurstof. Dit krachtveld werd toegepast om zuurstofvacature diffusie te bestuderen. De oppervlak zuurstofvacature diffusie treedt op via de opeenvolgende diffusie in het suboppervlak, suboppervlak diffusie en vervolgens diffusie vanuit het suboppervlak naar het oppervlak, in plaats van rechtstreeks oppervlakdiffusie.

De adsorptie van plasma gegenereerde CH_x radicalen op een anataas (001) oppervlak wordt beschreven in hoofdstuk 4. De invloed van zuurstofvacatures op de adsorptie werd onderzocht. In tegenstelling tot anataas (101) is de meest stabiele zuurstofvacature degene aan het oppervlak, in plaats van in het suboppervlak. De aanwezigheid van zuurstofvacatures beïnvloedt de stabiliteit van de verschillende adsorptieconfiguraties en leidt tot nieuwe adsorptie configuraties. Eén van de vaststellingen is de sterk toegenomen adsorptie van CH_3 op het

gereduceerde oppervlak. CH_3 kan op het gereduceerde oppervlak adsorberen boven een titanium atoom, wat niet mogelijk is op het stoichiometrische oppervlak. Vanwege deze nieuwe adsorptieconfiguratie zal CH_3 preferentieel adsorberen in de nabijheid van een zuurstofvacature. Dit is ook zo voor CH_2 , terwijl C liefst zal adsorberen in een stoichiometrische regio van het oppervlak, en CH geen voorkeur vertoont.

Hoofdstuk 5 richt zich op de invloed van zuurstofvacatures op de dissociatie van CO_2 op anataas (001). De toegenomen Lewis basiciteit van het oppervlak door de aanwezigheid van zuurstofvacatures heeft geen significante invloed op de adsorptiesterkte. Er ontstaan echter nieuwe adsorptieconfiguraties, die eveneens een verhoogde activering van de C-O bindingen vertonen ten opzichte van de gasfase. De dissociatie van CO_2 op het stoichiometrische oppervlak bleek een barrière te hebben van ~ 5 eV, en is dus zeer traag. Echter, significant lagere barrières werden gevonden op het gereduceerde oppervlak, omdat de aanwezigheid van zuurstofvacatures het eindproduct stabiliseert. Voor de meest stabiele adsorptieconfiguratie van het gereduceerde oppervlak vonden we een barrière van $\sim 0,8$ eV, hetgeen slechts een kleine verhoging in temperatuur vereist om te kunnen doorgaan (zie hoofdstuk 6). Zuurstofvacatures spelen dus een belangrijke rol bij de katalytische activiteit van anataas (001) en titaniumdioxide in het algemeen. Aangezien de CO_2 dissociatie op het gereduceerde oppervlak een zuurstofvacature opvult, is er een regeneratiemechanisme vereist. In het plasmakatalytische *dry reforming* van methaan is dat mogelijk door het gebruik van methaan afgeleide radicalen als reductant.

De oppervlakreacties van de plasmakatalytische *dry reforming* van methaan op anataas (001) worden beschreven in hoofdstuk 6. Een CO_2/CH_4 gasmengesel wordt geactiveerd in een plasma-ontlading door elektron impact reacties. In hoofdstuk 5 werd aangetoond dat CO_2 kan gereduceerd

Samenvatting

worden tot CO op het katalysatoroppervlak, indien er zuurstofvacatures aanwezig zijn in het oppervlak. De reactie op zichzelf is niet katalytisch, maar stoichiometrisch, aangezien één van de zuurstofatomen van CO₂ de zuurstofvacature opvult bij reductie. Echter, wanneer methaan toegevoegd wordt aan het brongas, wordt het mogelijk om het oppervlak te reduceren door methaan afgeleide species in het plasma. De meest prominente plasma species, CH₃, CH₂, CH, C en H, worden gebruikt om de oppervlakreacties te bestuderen. Wanneer de CH_x radicalen geadsorbeerd zijn op het oppervlak, kunnen hydrogenatie en dehydrogenatie reacties optreden. Samen met de hogere gasfase concentraties van CH₃ en CH₂, vergeleken met C en CH in de plasma ontlading, maakt dat CH₃ en CH₂ de meest prominent aanwezige radicalen zijn op het oppervlak, samen met H. De vormingsreacties van formaldehyde, methanol, methaan, water, H₂, CO, ethaan en etheen werden bestudeerd binnen een temperatuursgebied van 300 – 1000 K. Op basis van de reactiesnelheden zullen de belangrijkste producten methanol, H₂, CO, ethaan en etheen zijn. Verhoogde temperaturen zijn nodig om voldoende vorming te krijgen van deze producten. Echter, de minimum temperatuur die vereist is om voldoende omzetting te verkrijgen voor de plasma-katalytische omzetting van methaan is significant lager dan voor de thermische omzetting. Deze minimum temperatuur bedraagt 500 K voor de plasma-katalytische omzetting ten opzichte van 900 K voor de thermische omzetting van methaan.

Op basis van de resultaten in dit hoofdstuk verwachten we dat de selectiviteiten voor specifieke eindproducten van de plasmakatalytische *dry reforming* van methaan kunnen worden gestuurd op basis van de eigenschappen van het plasmakatalytische systeem. De verschillende oppervlakreacties vertonen een andere afhankelijkheid in functie van de temperatuur. Eveneens is er een afhankelijkheid van de vormingsreacties

in functie van de concentratie van geadsorbeerde plasma species, die op hun beurt afhangen van de adsorptiesnelheid. De adsorptiesnelheid hangt dan weer af van de gasfase dichtheid van de plasma species. Dit wordt bepaald door de vormingsreacties in het plasma, welke afhangen van de plasma eigenschappen. De resultaten uit dit hoofdstuk vormen de eerste stap om de ontbrekende schakels te vinden die nodig zijn om de plasmakatalytische *dry reforming* van methaan te kunnen sturen en controleren zodat een specifieke gassamenstelling kan bereikt worden.

Voor de toekomst heb ik een aantal belangrijke stappen voor ogen die nodig zijn om de plasmakatalytische oppervlakinteracties verder te ontrafelen. In deze dissertatie heb ik de oppervlakreacties bestudeerd op kwantummechanisch niveau, waardoor inzicht is vergaard op atomair niveau. Echter, om deze inzichten te koppelen aan de macroscopische wereld, zou het opportuun zijn om een mesoschaal model te ontwikkelen dat toelaat om grotere tijd- en lengteschalen te bestuderen. De resultaten uit dit proefschrift kunnen geïncorporeerd worden in een kinetisch Monte Carlo model. Dit model kan dan gebruikt worden om het effect te bestuderen van de verandering in de dichtheden van de verschillende plasma species op de oppervlakreacties, en hoe deze de eindproducten beïnvloeden. Dit model kan eveneens gebruikt worden om de invloed van de temperatuur op de eindproducten te bestuderen. Een schematisch overzicht van deze strategie is weergegeven in figuur 65.

De volgende stap kan dan zijn om het effect van het elektrisch veld en oppervlakte lading, welke typisch aanwezig is op een oppervlak dat blootgesteld wordt aan een plasma, te bestuderen op het adsorptie-desorptie evenwicht en de oppervlakreacties, met kwantummechanische simulaties. De resultaten van deze simulaties kunnen opnieuw geïncorporeerd worden in een mesoschaal model. De combinatie van de resultaten van beide mesoschaal modellen laat toe om de oorsprong van

Samenvatting

mogelijke synergie te vinden, en te ontrafelen welke parameters belangrijk zijn om de plasmakatalytisch processen te sturen naar een gewenste gassamenstelling.

List of publications

Publications related to this Ph.D. dissertation

- 1) **S. Huygh**, A. Bogaerts, A.C.T. van Duin, E.C. Neyts, “Development of a ReaxFF reactive force field for intrinsic point defects in titanium dioxide”, *Computational Materials Science* 95 (2014), 579-591
- 2) **S. Huygh**, E.C. Neyts, “Adsorption of C and CH_x Radicals on Anatase (001) and the Influence of Oxygen Vacancies”, *The Journal of Physical Chemistry C* 119 (2015), 4908-4921
- 3) **S. Huygh**, A. Bogaerts, E.C. Neyts, “How Oxygen Vacancies Activate CO₂ Dissociation on TiO₂ Anatase (001)”, *The Journal of Physical Chemistry C* 120 (2016), 21659-21669

Publications not related to this Ph.D. dissertation

- 1) M. Yusupov, A. Bogaerts, **S. Huygh**, R. Snoeckx, A.C.T. van Duin, E.C. Neyts, “Plasma-induced destruction of bacterial cell wall components: a reactive molecular dynamics simulation”, *The Journal of Physical Chemistry C* 117 (2013), 5993-5998
- 2) U. Khalilov, G. Pourtois, **S. Huygh**, A.C.T. van Duin, E.C. Neyts, A. Bogaerts, “New mechanism for oxidation of native silicon oxide”, *The Journal of Physical Chemistry C* 117 (2013), 9819-9825
- 3) W. Somers, A. Bogaerts, A.C.T. Van Duin, **S. Huygh**, K.M. Bal, E.C. Neyts, “Temperature influence on the reactivity of plasma species on a nickel catalyst surface: An atomic scale study”, *Catalysis today* 211 (2013), 131-136

List of publications

- 4) N. Khosravian, A. Bogaerts, **S. Huygh**, M. Yusupov, E.C. Neyts, “How do plasma-generated OH radicals react with biofilm components? Insights from atomic scale simulations”, *Biointerphases* 10 (2015), 029501

List of conference contributions

- 1) **S. Huygh**, A. Bogaerts, E.C. Neyts, "Adsorption of C and CH_x radicals on anatase (001) and the influence of oxygen vacancies.", **poster presentation** at Computational tools for materials science, April 13th 2015, University of Ghent (Belgium)
- 2) **S. Huygh**, A. Bogaerts, E.C. Neyts, "The surface chemistry of plasma-generated radicals on reduced titanium dioxide.", **poster presentation** at VSC Users Day, November 30th 2015, University of Antwerp (Belgium)
- 3) **S. Huygh**, A. Bogaerts, E.C. Neyts, "The activation and dissociation of CO₂ on anatase (001) surfaces of titanium dioxide and the role of oxygen vacancies.", **oral presentation** at ChemCys, March 16-18, 2016, Blankenberge (Belgium)
- 4) **S. Huygh**, A. Bogaerts, E.C. Neyts, "Activation of CO₂ for dissociation on TiO₂ Anatase (001): Defects!", **poster presentation** at Chemical Research in Flanders, October 24-26, 2016, Blankenberge (Belgium)
- 5) **S. Huygh**, A. Bogaerts, E.C. Neyts, "How oxygen vacancies activate CO₂ dissociation on TiO₂ anatase (001)", **poster presentation** at Computational Chemistry for pollutants mitigation, March 13-14 2017, Rueil-Malmaison (France)

List of conference contributions

- 6) **S. Huygh**, A. Bogaerts, E.C. Neyts, "The surface chemistry of methane derived radicals on anatase (001) and the influence of oxygen vacancies", **poster presentation** at Computational Chemistry for pollutants mitigation, March 13-14 2017, Rueil-Malmaison (France)

References

- (1) IPCC. *Climate Change 2014: Synthesis Report*; 2014.
- (2) Global Temperature. <http://climate.nasa.gov/vital-signs/global-temperature/> (accessed May 31, 2016).
- (3) Sea Level Rise. <http://climate.nasa.gov/vital-signs/sea-level/> (accessed May 31, 2016)
- (4) IPCC. *Climate Change 2007: Synthesis Report*; 2007.
- (5) Oreskes, N. The Scientific Consensus on Climate Change. *Science*. **2005**, *306*, 2004–2005.
- (6) Bowman, J. The Greenhouse Effect. *Land use policy* **1990**, *7*, 101–108.
- (7) Snoeckx, R.; Heijckers, S.; Van Wesenbeeck, K.; Lenaerts, S.; Bogaerts, A. CO₂ Conversion in a Dielectric Barrier Discharge Plasma: N₂ in the Mix as a Helping Hand or Problematic Impurity? *Energy Environ. Sci.* **2016**, *9* (3), 999–1011.
- (8) Bogaerts, A.; Kozak, T.; van Laer, K.; Snoeckx, R. Plasma-Based Conversion of CO₂: Current Status and Future Challenges. *Faraday Discuss.* **2015**, *183*, 217–232.
- (9) Ramakers, M.; Michielsen, I.; Aerts, R.; Meynen, V.; Bogaerts, A. Effect of Argon or Helium on the CO₂ Conversion in a Dielectric Barrier Discharge. *Plasma Process. Polym.* **2015**, *12* (8), 755–763.
- (10) Aerts, R.; Martens, T.; Bogaerts, A. Influence of Vibrational States on CO₂ Splitting by Dielectric Barrier Discharges. *J. Phys. Chem. C* **2012**, *116* (44), 23257–23273.

- (11) Aerts, R.; Somers, W.; Bogaerts, A. Carbon Dioxide Splitting in a Dielectric Barrier Discharge Plasma: A Combined Experimental and Computational Study. *ChemSusChem* **2015**, *8* (4), 702–716.
- (12) Paulussen, S.; Verheyde, B.; Tu, X.; Bie, C. De; Martens, T.; Petrovic, D.; Bogaerts, A.; Sels, B. Conversion of Carbon Dioxide to Value-Added Chemicals in Atmospheric Pressure Dielectric Barrier Discharges. *Plasma Sources Sci. Technol.* **2010**, *19* (3), 034015 1--6.
- (13) Neyts, E. C.; Bogaerts, A. Understanding Plasma Catalysis through Modelling and Simulation - a Review. *J. Phys. D. Appl. Phys.* **2014**, *47* (22), 224010.
- (14) Neyts, E. C.; Ostrikov, K.; Sunkara, M. K.; Bogaerts, A. Plasma Catalysis: Synergistic Effects at the Nanoscale. *Chem. Rev.* **2015**, *115* (24), 13408–13446.
- (15) D'Alessandro, D. M.; Smit, B.; Long, J. R. Carbon Dioxide Capture: Prospects for New Materials. *Angew. Chem. Int. Ed. Engl.* **2010**, *49*, 6058–6082.
- (16) Oh, Y. S.; Roh, H. S.; Jun, K. W.; Baek, Y. S. A Highly Active Catalyst, Ni/Ce-ZrO₂/γ-Al₂O₃, for on-Site H₂ Generation by Steam Methane Reforming: Pretreatment Effect. *Int. J. Hydrogen Energy* **2003**, *28* (12), 1387–1392.
- (17) Kalamaras, C. M.; Efstathiou, A. M. Hydrogen Production Technologies: Current State and Future Developments. *Conf. Pap. Energy* **2013**, *2013*, 9.
- (18) Iulianelli, A.; Liguori, S.; Wilcox, J.; Basile, A. Advances on Methane Steam Reforming to Produce Hydrogen through Membrane Reactors Technology: A Review. *Catal. Rev.* **2016**, *58* (1), 1–35.

- (19) Ogden, J. M.; Steinbugler, M. M.; Kreutz, T. G. Comparison of Hydrogen, Methanol and Gasoline as Fuels for Fuel Cell Vehicles: Implications for Vehicle Design and Infrastructure Development. *J. Power Sources* **1999**, *79* (2), 143–168.
- (20) Adris, A. M.; Pruden, B. B.; Lim, C. J.; Grace, J. R. On the Reported Attempts to Radically Improve the Performance of the Steam Methane Reforming Reactor. *Canadian Journal of Chemical Engineering*. 1996, *74* (2), 177–186.
- (21) Rostrup-Nielsen, J. Hydrogen Generation by Catalysis. *Encycl. Catal.* **2003**.
- (22) Dry, M. E. The Fischer-Tropsch Process: 1950-2000. *Catalysis Today*, **2002**, *71*, 227–241.
- (23) Fan, M.-S.; Abdullah, A. Z.; Bhatia, S. Catalytic Technology for Carbon Dioxide Reforming of Methane to Synthesis Gas. *ChemCatChem* **2009**, *1* (2), 192–208.
- (24) Sehested, J. Four Challenges for Nickel Steam-Reforming Catalysts. *Catalysis Today*, **2006**, *111*, 103–110.
- (25) Whitehead, J. C. Plasma–catalysis: The Known Knowns, the Known Unknowns and the Unknown Unknowns. *J. Phys. D. Appl. Phys.* **2016**, *49* (24), 243001.
- (26) Bruggeman, P. J.; Czarnetzki, U. Retrospective on “The 2012 Plasma Roadmap.” *J. Phys. D. Appl. Phys.* **2016**, *49* (43), 431001.
- (27) Zhang, Y. P.; Li, Y.; Wang, Y.; Liu, C. J.; Eliasson, B. Plasma Methane Conversion in the Presence of Carbon Dioxide Using Dielectric-Barrier Discharges. *Fuel Process. Technol.* **2003**, *83* (1–3 SPEC.), 101–109.

- (28) Tao, X.; Bai, M.; Li, X.; Long, H.; Shang, S.; Yin, Y.; Dai, X. CH₄-CO₂ Reforming by Plasma - Challenges and Opportunities. *Progress in Energy and Combustion Science*. **2011**, 113–124.
- (29) Jiang, T.; Li, Y.; Liu, C. J.; Xu, G. H.; Eliasson, B.; Xue, B. Plasma Methane Conversion Using Dielectric-Barrier Discharges with Zeolite A. In *Catalysis Today*; 2002; Vol. 72, pp 229–235.
- (30) Indarto, A.; Coowanitwong, N.; Choi, J. W.; Lee, H.; Song, H. K. Kinetic Modeling of Plasma Methane Conversion in a Dielectric Barrier Discharge. *Fuel Process. Technol.* **2008**, 89 (2), 214–219.
- (31) Indarto, A.; Choi, J. W.; Lee, H.; Song, H. K. Decomposition of Greenhouse Gases by Plasma. *Environmental Chemistry Letters*. 2008, 215–222.
- (32) Aghamir, F. M.; Matin, N. S.; Jalili, A. H.; Esfarayeni, M. H.; Khodagholi, M. A.; Ahmadi, R. Conversion of Methane to Methanol in an Ac Dielectric Barrier Discharge. *Plasma Sources Sci. Technol.* **2004**, 13, 707–711.
- (33) Havran, V.; Duduković, M. P.; Lo, C. S. Conversion of Methane and Carbon Dioxide to Higher Value Products. *Ind. Eng. Chem. Res.* **2011**, 50 (12), 7089–7100.
- (34) Tu, X.; Whitehead, J. C. Plasma-Catalytic Dry Reforming of Methane in an Atmospheric Dielectric Barrier Discharge: Understanding the Synergistic Effect at Low Temperature. *Appl. Catal. B Environ.* **2012**, 125, 439–448.
- (35) Wang, Q.; Cheng, Y.; Jin, Y. Dry Reforming of Methane in an Atmospheric Pressure Plasma Fluidized Bed with Ni/γ-Al₂O₃ Catalyst. *Catal. Today* **2009**, 148 (3–4), 275–282.

- (36) Sentek, J.; Krawczyk, K.; Młotek, M.; Kalczyńska, M.; Kroker, T.; Kolb, T.; Schenk, A.; Gericke, K. H.; Schmidt-Szałowski, K. Plasma-Catalytic Methane Conversion with Carbon Dioxide in Dielectric Barrier Discharges. *Appl. Catal. B Environ.* **2010**, *94* (1–2), 19–26.
- (37) Mei, D.; Zhu, X.; Wu, C.; Ashford, B.; Williams, P. T.; Tu, X. Plasma-Photocatalytic Conversion of CO₂ at Low Temperatures: Understanding the Synergistic Effect of Plasma-Catalysis. *Appl. Catal. B Environ.* **2016**, *182*, 525–532.
- (38) Bravo-Suárez, J. J.; Chaudhari, R. V.; Subramaniam, B. Design of Heterogeneous Catalysts for Fuels and Chemicals Processing: An Overview. In *ACS Symposium Series*, **2013**, *1132*, 3–68.
- (39) IUPAC Compendium of Chemical Terminology, <http://goldbook.iupac.org/C00876.html> (accessed November 11, 2016).
- (40) Quoc An, H. T.; Pham Huu, T.; Le Van, T.; Cormier, J. M.; Khacef, A. Application of Atmospheric Non Thermal Plasma-Catalysis Hybrid System for Air Pollution Control: Toluene Removal. In *Catalysis Today*; 2011; *176*, 474–477.
- (41) Van Durme, J.; Dewulf, J.; Leys, C.; Van Langenhove, H. Combining Non-Thermal Plasma with Heterogeneous Catalysis in Waste Gas Treatment: A Review. *Applied Catalysis B: Environmental.* **2008**, 324–333.
- (42) Van Durme, J.; Dewulf, J.; Sysmans, W.; Leys, C.; Van Langenhove, H. Efficient Toluene Abatement in Indoor Air by a Plasma Catalytic Hybrid System. *Appl. Catal. B Environ.* **2007**, *74* (1–2), 161–169.
- (43) Kim, H. H.; Lee, Y. H.; Ogata, A.; Futamura, S. Plasma-Driven Catalyst Processing Packed with Photocatalyst for Gas-Phase Benzene Decomposition. *Catal. Commun.* **2003**, *4* (7), 347–351.

- (44) Huang, H.; Ye, D.; Leung, D. Y. C.; Feng, F.; Guan, X. Byproducts and Pathways of Toluene Destruction via Plasma-Catalysis. *J. Mol. Catal. A Chem.* **2011**, *336* (1–2), 87–93.
- (45) Huang, H. B.; Ye, D. Q.; Leung, D. Y. C. Removal of Toluene Using UV-Irradiated and Nonthermal Plasma-Driven Photocatalyst System. *Journal of Environmental Engineering.* **2010**, 1231–1236.
- (46) Tang, X.; Feng, F.; Ye, L.; Zhang, X.; Huang, Y.; Liu, Z.; Yan, K. Removal of Dilute VOCs in Air by Post-Plasma Catalysis over Ag-Based Composite Oxide Catalysts. *Catal. Today* **2013**, *211*, 39–43.
- (47) Nozaki, T.; Okazaki, K. Non-Thermal Plasma Catalysis of Methane: Principles, Energy Efficiency, and Applications. *Catal. Today* **2013**, *211*, 29–38.
- (48) Nozaki, T.; Muto, N.; Kado, S.; Okazaki, K. Dissociation of Vibrationally Excited Methane on Ni Catalyst: Part 1. Application to Methane Steam Reforming. *Catalysis Today*, **2004**, *89*, 57–65.
- (49) Nozaki, T.; Muto, N.; Kadio, S.; Okazaki, K.; Kado, S.; Okazaki, K. Dissociation of Vibrationally Excited Methane on Ni Catalyst: Part 2. Process Diagnostics by Emission Spectroscopy. *Catalysis Today*, **2004**, *89*, 67–74.
- (50) Zeng, Y.; Zhu, X.; Mei, D.; Ashford, B.; Tu, X. Plasma-Catalytic Dry Reforming of Methane over γ -Al₂O₃ Supported Metal Catalysts. *Catal. Today* **2015**, *256* (P1), 80–87.
- (51) Kraus, M.; Eliasson, B.; Kogelschatz, U.; Wokaun, A. CO₂ Reforming of Methane by the Combination of Dielectric-Barrier Discharges and Catalysis. *Phys. Chem. Chem. Phys.* **2001**, *3* (3), 294–300.

- (52) Kraus, M.; Egli, W.; Haffner, K.; Eliasson, B.; Kogelschatz, U.; Wokaun, A. Investigation of Mechanistic Aspects of the Catalytic CO₂ Reforming of Methane in a Dielectric-Barrier Discharge Using Optical Emission Spectroscopy and Kinetic Modeling. *Phys. Chem. Chem. Phys.* **2002**, *4* (4), 668–675.
- (53) Long, H.; Shang, S.; Tao, X.; Yin, Y.; Dai, X. CO₂ Reforming of CH₄ by Combination of Cold Plasma Jet and Ni/γ-Al₂O₃ Catalyst. *Int. J. Hydrogen Energy* **2008**, *33* (20), 5510–5515.
- (54) Tao, X.; Qi, F.; Yin, Y.; Dai, X. CO₂ Reforming of CH₄ by Combination of Thermal Plasma and Catalyst. *Int. J. Hydrogen Energy* **2008**, *33* (4), 1262–1265.
- (55) Xu, Y.; Wei, Q.; Long, H.; Zhang, X.; Shang, S.; Dai, X.; Yin, Y. CO₂ Reforming of CH₄ by Synergies of Binode Thermal Plasma and Catalysts. *Int. J. Hydrogen Energy* **2013**, *38* (3), 1384–1390.
- (56) Schmidt-Szałowski, K.; Krawczyk, K.; Sentek, J.; Ulejczyk, B.; Górska, A.; Młotek, M. Hybrid Plasma-Catalytic Systems for Converting Substances of High Stability, Greenhouse Gases and VOC. *Chem. Eng. Res. Des.* **2011**, *89* (12), 2643–2651.
- (57) Wang, Y. F.; Tsai, C. H.; Chang, W. Y.; Kuo, Y. M. Methane Steam Reforming for Producing Hydrogen in an Atmospheric-Pressure Microwave Plasma Reactor. *Int. J. Hydrogen Energy* **2010**, *35* (1), 135–140.
- (58) Tu, X.; Gallon, H. J.; Twigg, M. V; Gorrry, P. a; Whitehead, J. C. Dry Reforming of Methane over a Ni/Al₂O₃ Catalyst in a Coaxial Dielectric Barrier Discharge Reactor. *J. Phys. D. Appl. Phys.* **2011**, *44* (27), 274007.

- (59) Song, H. K.; Choi, J.-W.; Yue, S. H.; Lee, H.; Na, B.-K. Synthesis Gas Production via Dielectric Barrier Discharge over Ni/ γ -Al₂O₃ Catalyst. *Catal. Today* **2004**, *89* (1–2), 27–33.
- (60) Gallon, H. J.; Tu, X.; Whitehead, J. C. Effects of Reactor Packing Materials on H₂ Production by CO₂ Reforming of CH₄ in a Dielectric Barrier Discharge. *Plasma Process. Polym.* **2012**, *9* (1), 90–97.
- (61) Samukawa, S.; Hori, M.; Rauf, S.; Tachibana, K.; Bruggeman, P.; Kroesen, G.; Whitehead, J. C.; Murphy, A. B.; Gutsol, A. F.; Starikovskaia, S.; et al. The 2012 Plasma Roadmap. *J. Phys. D Appl. Phys.* **2012**, *45* (45), 253001.
- (62) Mei, D.; Zhu, X.; He, Y.-L.; Yan, J. D.; Tu, X. Plasma-Assisted Conversion of CO₂ in a Dielectric Barrier Discharge Reactor: Understanding the Effect of Packing Materials. *Plasma Sources Sci. Technol.* **2015**, *24* (1), 15011–15021.
- (63) Malik, M. A.; Minamitani, Y.; Schoenbach, K. H. Comparison of Catalytic Activity of Aluminum Oxide and Silica Gel for Decomposition of Volatile Organic Compounds (VOCs) in a Plasmacatalytic Reactor. *IEEE Trans. Plasma Sci.* **2005**, *33* (1 I), 50–56.
- (64) Hensel, K.; Katsura, S.; Mizuno, A. DC Microdischarges inside Porous Ceramics. *IEEE Trans. Plasma Sci.* **2005**, *33* (2 I), 574–575.
- (65) Zhang, Y.-R.; Neyts, E. C.; Bogaerts, A. Influence of the Material Dielectric Constant on Plasma Generation inside Catalyst Pores. *J. Phys. Chem. C* **2016**, acs.jpcc.6b09038.
- (66) Zhang, Y. R.; Van Laer, K.; Neyts, E. C.; Bogaerts, A. Can Plasma Be Formed in Catalyst Pores? A Modeling Investigation. *Appl. Catal. B Environ.* **2016**, *185*, 56–67.

- (67) Kim, H.-H.; Teramoto, Y.; Negishi, N.; Ogata, A. A Multidisciplinary Approach to Understand the Interactions of Nonthermal Plasma and Catalyst: A Review. *Catal. Today* **2015**, *256*, Part 1, 13–22.
- (68) Holzer, F.; Kopinke, F. D.; Roland, U. Influence of Ferroelectric Materials and Catalysts on the Performance of Non-Thermal Plasma (NTP) for the Removal of Air Pollutants. *Plasma Chem. Plasma Process.* **2005**, *25* (6), 595–611.
- (69) Van Laer, K.; Bogaerts, A. Improving the Conversion and Energy Efficiency of Carbon Dioxide Splitting in a Zirconia-Packed Dielectric Barrier Discharge Reactor. *Energy Technol.* **2015**, *3* (10), 1038–1044.
- (70) van Laer, K.; Bogaerts, A. Fluid Modelling of a Packed Bed Dielectric Barrier Discharge Plasma Reactor. *Plasma Sources Sci. Technol.* **2016**, *25* (1), 15002.
- (71) Tu, X.; Gallon, H. J.; Whitehead, J. C. Electrical and Spectroscopic Diagnostics of a Single-Stage Plasma-Catalysis System: Effect of Packing with TiO₂. *J. Phys. D. Appl. Phys.* **2011**, *44*, 482003.
- (72) Kang, W. S.; Park, J. M.; Kim, Y.; Hong, S. H.; Woo Seok, K.; Jin Myung, P.; Yongho, K.; Sang Hee, H. Numerical Study on Influences of Barrier Arrangements on Dielectric Barrier Discharge Characteristics. *IEEE Trans. Plasma Sci.* **2003**, *31* (4), 504–510.
- (73) Blin-Simiand, N.; Tardiveau, P.; Risacher, A.; Jorand, F.; Pasquiers, S. Removal of 2-Heptanone by Dielectric Barrier Discharges - The Effect of a Catalyst Support. *Plasma Process. Polym.* **2005**, *2* (3), 256–262.
- (74) Hong, J.; Chu, W.; Chernavskii, P. A.; Khodakov, A. Y. Cobalt Species and Cobalt-Support Interaction in Glow Discharge Plasma-Assisted Fischer-Tropsch Catalysts. *J. Catal.* **2010**, *273* (1), 9–17.

- (75) Liu, C.-J.; Zou, J.; Yu, K.; Cheng, D.; Han, Y.; Zhan, J.; Ratanatawanate, C.; Jang, B. W.-L. Plasma Application for More Environmentally Friendly Catalyst Preparation. *Pure Appl. Chem.* **2006**, *78* (6), 1227–1238.
- (76) Shang, S.; Liu, G.; Chai, X.; Tao, X.; Li, X.; Bai, M.; Chu, W.; Dai, X.; Zhao, Y.; Yin, Y. Research on Ni/ γ -Al₂O₃ Catalyst for CO₂ Reforming of CH₄ Prepared by Atmospheric Pressure Glow Discharge Plasma Jet. *Catal. Today* **2009**, *148* (3–4), 268–274.
- (77) Martínez, R.; Romero, E.; Guimon, C.; Bilbao, R. CO₂ Reforming of Methane over Coprecipitated Ni-Al Catalysts Modified with Lanthanum. *Appl. Catal. A Gen.* **2004**, *274* (1–2), 139–149.
- (78) Tu, X.; Gallon, H. J.; Whitehead, J. C. Plasma-Assisted Reduction of a NiO/Al₂O₃ Catalyst in Atmospheric Pressure H₂/Ar Dielectric Barrier Discharge. *Catal. Today* **2013**, *211*, 120–125.
- (79) Demidyuk, V.; Whitehead, J. C. Influence of Temperature on Gas-Phase Toluene Decomposition in Plasma-Catalytic System. *Plasma Chem. Plasma Process.* **2007**, *27* (1), 85–94.
- (80) Guo, Y. F.; Ye, D. Q.; Chen, K. F.; He, J. C.; Chen, W. L. Toluene Decomposition Using a Wire-Plate Dielectric Barrier Discharge Reactor with Manganese Oxide Catalyst in Situ. *J. Mol. Catal. A Chem.* **2006**, *245* (1–2), 93–100.
- (81) Sun, M. Y.; Jin-Oh, J.; Heon-Ju, L. Dielectric Barrier Discharge Plasma-Induced Photocatalysis and Ozonation for the Treatment of Wastewater. *PLASMA Sci. & Technol.* **2008**, *10* (1), 100–105.
- (82) Kang, M.; Kim, B. J.; Cho, S. M.; Chung, C. H.; Kim, B. W.; Han, G. Y.; Yoon, K. J. Decomposition of Toluene Using an Atmospheric Pressure plasma/TiO₂ Catalytic System. *J. Mol. Catal. A Chem.* **2002**, *180* (1–2), 125–132.

- (83) Whitehead, J. C. Plasma Catalysis: A Solution for Environmental Problems. *Pure Appl. Chem.* **2010**, *82* (6), 1329–1336.
- (84) Assadi, A. A.; Bouzaza, A.; Vallet, C.; Wolbert, D. Use of DBD Plasma, Photocatalysis, and Combined DBD Plasma/photocatalysis in a Continuous Annular Reactor for Isovaleraldehyde Elimination - Synergetic Effect and Byproducts Identification. *Chem. Eng. J.* **2014**, *254*, 124–132.
- (85) Wallis, A. E.; Whitehead, J. C.; Zhang, K. Plasma-Assisted Catalysis for the Destruction of CFC-12 in Atmospheric Pressure Gas Streams Using TiO₂. *Catal. Letters* **2007**, *113* (1–2), 29–33.
- (86) Frenkel, D.; Smit, B. *Understanding Molecular Simulation*; **2002**, 139-163.
- (87) Morse, P. Diatomic Molecules According to the Wave Mechanics. II. Vibrational Levels. *Phys. Rev.* **1929**, *34* (1), 57–64.
- (88) Jones, J. E. On the Determination of Molecular Fields. I. From the Variation of the Viscosity of a Gas with Temperature. *Proc. R. Soc. A Math. Phys. Eng. Sci.* **1924**, *106* (738), 441–462.
- (89) Burdett, J. K.; Hughbanks, T.; Miller, G. J.; Richardson, J. W.; Smith, J. V. Structural-Electronic Relationships in Inorganic Solids: Powder Neutron Diffraction Studies of the Rutile and Anatase Polymorphs of Titanium Dioxide at 15 and 295 K. *J. Am. Chem. Soc.* **1987**, *109* (12), 3639–3646.
- (90) Van Duin, A. C. T.; Dasgupta, S.; Lorant, F.; Goddard, W. A. ReaxFF: A Reactive Force Field for Hydrocarbons. *J. Phys. Chem. A* **2001**, *105* (41), 9396–9409.

- (91) Allinger, N. L.; Yuh, Y. H.; Lii, J. H. Molecular Mechanics. The MM3 Force Field for Hydrocarbons. 1. *J. Am. Chem. Soc.* **1989**, *111* (23), 8551–8566.
- (92) Allinger, N. L.; Li, F.; Yan, L. Molecular Mechanics. The MM3 Force Field for Alkenes. *J. Comput. Chem.* **1990**, *11* (7), 848–867.
- (93) Allinger, N. L.; Li, F.; Yan, L.; Tai, J. C. Molecular Mechanics (MM3) Calculations on Conjugated Hydrocarbons. *J. Comput. Chem.* **1990**, *11* (7), 868–895.
- (94) Mayo, S. L.; Olafson, B. D.; Goddard, W. A. DREIDING: A Generic Force Field for Molecular Simulations. *J. Phys. Chem.* **1990**, *94* (26), 8897–8909.
- (95) Rappe, a. K.; Casewit, C. J.; Colwell, K. S.; Goddard, W. a.; Skiff, W. M. UFF, a Full Periodic Table Force Field for Molecular Mechanics and Molecular Dynamics Simulations. *J. Am. Chem. Soc.* **1992**, *114* (25), 10024–10035.
- (96) Brenner, D. Empirical Potential for Hydrocarbons for Use in Simulating the Chemical Vapor Deposition of Diamond Films. *Phys. Rev. B* **1990**, *42* (15), 9458–9471.
- (97) Pauling, L. Atomic Radii and Interatomic Distances in Metals. *J. Am. Chem. Soc.* **1947**, *69* (3), 542–553.
- (98) Mortier, W. J.; Ghosh, S. K.; Shankar, S. Electronegativity-Equalization Method for the Calculation of Atomic Charges in Molecules. *J. Am. Chem. Soc.* **1986**, *108* (15), 4315–4320.
- (99) Janssens, G. O. A.; Baekelandt, B. G.; Toufar, H.; Mortier, W. J.; Schoonheydt, R. A. Comparison of Cluster and Infinite Crystal Calculations on Zeolites with the Electronegativity Equalization Method (EEM). *J. Phys. Chem.* **1995**, *99* (10), 3251–3258.

- (100) Smirnov, K. S.; van de Graaf, B. Consistent Implementation of the Electronegativity Equalization Method in Molecular Mechanics and Molecular Dynamics. *J. Chem. Soc. Faraday Trans.* **1996**, *92* (13), 2469.
- (101) van Duin, A. C. T.; Baas, J. M. a.; van de Graaf, B. Delft Molecular Mechanics A New Approach to Hydrocarbon Force Fields. *J. Chem. Soc. Faraday Trans.* **1994**, *90* (19), 2881.
- (102) Schrödinger, E. Quantisierung Als Eigenwertproblem. *Ann. Phys.* **1926**, *384* (4), 361–376.
- (103) Born, M.; Oppenheimer, J. R. Born-Oppenheimer Approximation. *Ann. Phys.* **1927**, *84*, 457.
- (104) Pauli, W. Über Den Zusammenhang Des Abschlusses Der Elektronengruppen Im Atom Mit Der Komplexstruktur Der Spektren. *Zeitschrift für Phys.* **1925**, *31* (1), 765–783.
- (105) Hartree, D. R. The Wave Mechanics of an Atom with a Non-Coulomb Central Field. Part I. Theory and Methods. *Math. Proc. Cambridge Philos. Soc.* **1928**, *24* (1), 89–110.
- (106) Fock, V. Näherungsmethode Zur Lösung Des Quantenmechanischen Mehrkörperproblems. *Zeitschrift für Phys.* **1930**, *61* (1–2), 126–148.
- (107) Slater, J. C. A Simplification of the Hartree-Fock Method. *Phys. Rev.* **1951**, *81* (3), 385–390.
- (108) Fermi, E. Statistical Method to Determine Some Properties of Atoms. *Rend. Accad. Naz. Lincei* **1927**, *6*, 602–607.
- (109) Thomas, L. H. The Calculation of Atomic Fields. *Math. Proc. Cambridge Philos. Soc.* **1927**, *23* (5), 542.
- (110) Hohenberg, P.; Kohn, W. The Inhomogeneous Electron Gas. *Phys. Rev.* **1964**, *136* (3B), B864.

- (111) Kohn, W.; Sham, L. J. Self-Consistent Equations Including Exchange and Correlation Effects. *Phys. Rev.* **1965**, *140* (4A).
- (112) Perdew, J. P.; Yue, W. Accurate and Simple Density Functional for the Electronic Exchange Energy: Generalized Gradient Approximation. *Phys. Rev. B* **1986**, *33* (12), 8800–8802.
- (113) Perdew, J.; Burke, K.; Ernzerhof, M. Generalized Gradient Approximation Made Simple. *Phys. Rev. Lett.* **1996**, *77*, 3865–3868.
- (114) Becke, A. D. Density-Functional Exchange-Energy Approximation with Correct Asymptotic Behavior. *Phys. Rev. A* **1988**, *38* (6), 3098–3100.
- (115) Becke, A. D. Density-Functional Thermochemistry. III. The Role of Exact Exchange. *J. Chem. Phys.* **1993**, *98* (7), 5648.
- (116) Linsebigler, A. L.; Linsebigler, A. L.; Yates Jr, J. T.; Lu, G.; Lu, G.; Yates, J. T. Photocatalysis on TiO₂ Surfaces: Principles, Mechanisms, and Selected Results. *Chem. Rev.* **1995**, *95* (3), 735–758.
- (117) Grätzel, M. Photoelectrochemical Cells. *Nature* **2001**, *414* (6861), 338–344.
- (118) Diebold, U. The Surface Science of Titanium Dioxide. *Surf. Sci. Reports* **2003**, *48* (5), 53–229.
- (119) Henderson, M. a. A Surface Perspective on Self-Diffusion in Rutile TiO₂. *Surf. Sci.* **1999**, *419* (2–3), 174–187.
- (120) Lazzeri, M.; Vittadini, A.; Selloni, A. Structure and Energetics of Stoichiometric TiO₂ Anatase Surfaces. *Phys. Rev. B - Condens. Matter Mater. Phys.* **2001**, *63* (15), 1554091–1554099.

- (121) Diebold, U.; Ruzycki, N.; Herman, G. S.; Selloni, A. One Step towards Bridging the Materials Gap: Surface Studies of TiO₂ Anatase. *Catalysis Today*. 2003, pp 93–100.
- (122) Cheng, H.; Selloni, A. Surface and Subsurface Oxygen Vacancies in Anatase TiO₂ and Differences with Rutile. *Phys. Rev. B* **2009**, *79* (9), 92101.
- (123) Hebenstreit, W.; Ruzycki, N.; Herman, G. S.; Gao, Y.; Diebold, U. Scanning Tunneling Microscopy Investigation of the TiO₂ Anatase (101) Surface. *Phys. Rev. B* **2000**, *62* (24), R16334–R16336.
- (124) He, Y.; Dulub, O.; Cheng, H.; Selloni, A.; Diebold, U. Evidence for the Predominance of Subsurface Defects on Reduced Anatase TiO₂(101). *Phys. Rev. Lett.* **2009**, *102* (10).
- (125) Thomas, A. G.; Flavell, W. R.; Mallick, A. K.; Kumarasinghe, A. R.; Tsoutsou, D.; Khan, N.; Chatwin, C.; Rayner, S.; Smith, G. C.; Stockbauer, R. L.; et al. Comparison of the Electronic Structure of Anatase and Rutile TiO₂ Single-Crystal Surfaces Using Resonant Photoemission and X-Ray Absorption Spectroscopy. *Phys. Rev. B* **2007**, *75*, 1–12.
- (126) Plimpton, S. Fast Parallel Algorithms for Short-Range Molecular Dynamics. *Journal of Computational Physics*. 1995, pp 1–19.
- (127) Nakano, A.; Kalia, R. K.; Ichi Nomura, K.; Sharma, A.; Vashishta, P.; Shimojo, F.; van Duin, A. C. T.; Goddard, W. A.; Biswas, R.; Srivastava, D. A Divide-and-Conquer/cellular-Decomposition Framework for Million-to-Billion Atom Simulations of Chemical Reactions. *Comput. Mater. Sci.* **2007**, *38* (4), 642–652.

- (128) Nomura, K. I.; Kalia, R. K.; Nakano, A.; Vashishta, P.; Van Duin, A. C. T.; Goddard, W. A. Dynamic Transition in the Structure of an Energetic Crystal during Chemical Reactions at Shock Front prior to Detonation. *Phys. Rev. Lett.* **2007**, *99* (14).
- (129) Chen, H. P.; Kalia, R. K.; Kaxiras, E.; Lu, G.; Nakano, A.; Nomura, K. I.; Van Duin, A. C. T.; Vashishta, P.; Yuan, Z. Embrittlement of Metal by Solute Segregation-Induced Amorphization. *Phys. Rev. Lett.* **2010**, *104* (15).
- (130) Zybin, S. V.; Goddard, W. A.; Xu, P.; Van Duin, A. C. T.; Thompson, A. P. Physical Mechanism of Anisotropic Sensitivity in Pentaerythritol Tetranitrate from Compressive-Shear Reaction Dynamics Simulations. *Appl. Phys. Lett.* **2010**, *96* (8).
- (131) Liang, T.; Devine, B.; Phillpot, S. R.; Sinnott, S. B. Variable Charge Reactive Potential for Hydrocarbons to Simulate Organic-Copper Interactions. *J. Phys. Chem. A* **2012**, *116* (30), 7976–7991.
- (132) Devine, B.; Shan, T. R.; Cheng, Y. T.; McGaughey, A. J. H.; Lee, M.; Phillpot, S. R.; Sinnott, S. B. Atomistic Simulations of Copper Oxidation and Cu/Cu₂O Interfaces Using Charge-Optimized Many-Body Potentials. *Phys. Rev. B - Condens. Matter Mater. Phys.* **2011**, *84* (12).
- (133) Cheng, Y. T.; Shan, T. R.; Devine, B.; Lee, D.; Liang, T.; Hinojosa, B. B.; Phillpot, S. R.; Asthagiri, A.; Sinnott, S. B. Atomistic Simulations of the Adsorption and Migration Barriers of Cu Adatoms on ZnO Surfaces Using COMB Potentials. *Surf. Sci.* **2012**, *606* (15–16), 1280–1288.

- (134) Shan, T.-R.; Devine, B. D.; Hawkins, J. M.; Asthagiri, A.; Phillpot, S. R.; Sinnott, S. B. Second-Generation Charge-Optimized Many-Body Potential for Si/SiO₂ and Amorphous Silica. *Phys. Rev. B* **2010**, *82* (23), 235302.
- (135) Yu, J.; Sinnott, S. B.; Phillpot, S. R. Charge Optimized Many-Body Potential for the Si/SiO₂ System. *Phys. Rev. B - Condens. Matter Mater. Phys.* **2007**, *75* (8).
- (136) Li, Y.; Shan, T.-R.; Liang, T.; Sinnott, S. B.; Phillpot, S. R. Classical Interatomic Potential for Orthorhombic Uranium. *J. Phys. Condens. Matter* **2012**, *24* (23), 235403.
- (137) Liang, T.; Shin, Y. K.; Cheng, Y.-T.; Yilmaz, D. E.; Vishnu, K. G.; Verners, O.; Zou, C.; Phillpot, S. R.; Sinnott, S. B.; van Duin, A. C. T. Reactive Potentials for Advanced Atomistic Simulations. *Annu. Rev. Mater. Res.* **2013**, *43* (1), 109–129.
- (138) Raymand, D.; van Duin, A. C. T.; Spångberg, D.; Goddard, W. A.; Hermansson, K. Water Adsorption on Stepped ZnO Surfaces from MD Simulation. *Surf. Sci.* **2010**, *604* (9–10), 741–752.
- (139) Aryanpour, M.; Van Duin, A. C. T.; Kubicki, J. D. Development of a Reactive Force Field for Iron-Oxyhydroxide Systems. *J. Phys. Chem. A* **2010**, *114* (21), 6298–6307.
- (140) Fogarty, J. C.; Aktulga, H. M.; Grama, A. Y.; van Duin, A. C. T.; Pandit, S. a. A Reactive Molecular Dynamics Simulation of the Silica-Water Interface. *J. Chem. Phys.* **2010**, *132* (17), 174704.
- (141) Rahaman, O.; Van Duin, A. C. T.; Goddard, W. A.; Doren, D. J. Development of a ReaxFF Reactive Force Field for Glycine and Application to Solvent Effect and Tautomerization. *J. Phys. Chem. B* **2011**, *115* (2), 249–261.

- (142) Kim, S. Y.; Kumar, N.; Persson, P.; Sofu, J.; Van Duin, A. C. T.; Kubicki, J. D. Development of a ReaxFF Reactive Force Field for Titanium Dioxide/water Systems. *Langmuir* **2013**, *29* (25), 7838–7846.
- (143) Monti, S.; van Duin, A. C. T.; Kim, S.-Y.; Barone, V. Exploration of the Conformational and Reactive Dynamics of Glycine and Diglycine on TiO₂: Computational Investigations in the Gas Phase and in Solution. *J. Phys. Chem. C* **2012**, *116* (8), 5141–5150.
- (144) Kim, S. Y.; van Duin, A. C. T.; Kubicki, J. D. Molecular Dynamics Simulations of the Interactions between TiO₂ Nanoparticles and Water with Na⁺ and Cl⁻, Methanol, and Formic Acid Using a Reactive Force Field. *J. Mater. Res.* **2013**, *28* (3), 513–520.
- (145) Muscat, J.; Swamy, V.; Harrison, N. M. First-Principles Calculations of the Phase Stability of TiO₂. *Phys. Rev. B - Condens. Matter Mater. Phys.* **2002**, *65* (22), 2241121–22411215.
- (146) Ranade, M. R.; Navrotsky, A.; Zhang, H. Z.; Banfield, J. F.; Elder, S. H.; Zaban, A.; Borse, P. H.; Kulkarni, S. K.; Doran, G. S.; Whitfield, H. J. Energetics of Nanocrystalline TiO₂. *Proc. Natl. Acad. Sci. U. S. A.* **2002**, *99*, 6476–6481.
- (147) Albaret, T.; Finocchi, F.; Noguera, C. Density Functional Study of Stoichiometric and O-Rich Titanium Oxygen Clusters. *J. Chem. Phys.* **2000**, *113* (6), 2238–2249.
- (148) Jeong, K. S.; Chang, C.; Sedlmayr, E.; Sulzle, D. Electronic Structure Investigation of Neutral Titanium Oxide Molecules Ti_xO_y. *J. Phys. B At., Mol. Opt. Phys.* **2000**, *33*, 3417–3430.

- (149) Lundqvist, M. J.; Nilsing, M.; Persson, P.; Lunell, S. DFT Study of Bare and Dye-Sensitized TiO₂ Clusters and Nanocrystals. In *International Journal of Quantum Chemistry*; 2006; Vol. 106, pp 3214–3234.
- (150) Cheng, H.; Selloni, A. Energetics and Diffusion of Intrinsic Surface and Subsurface Defects on Anatase TiO₂ (101). *J. Chem. Phys.* **2009**, *131* (5).
- (151) Cheng, H.; Selloni, A. Surface and Subsurface Oxygen Vacancies in Anatase TiO₂ and Differences with Rutile. *Phys. Rev. B* **2009**, *79*, 2–5.
- (152) Aschauer, U.; Chen, J.; Selloni, A. Peroxide and Superoxide States of Adsorbed O₂ on Anatase TiO₂ (101) with Subsurface Defects. *Phys. Chem. Chem. Phys.* **2010**, *12* (40), 12956–12960.
- (153) Zhu, K. R.; Zhang, M. S.; Hong, J. M.; Yin, Z. Size Effect on Phase Transition Sequence of TiO₂ Nanocrystal. *Mater. Sci. Eng. A* **2005**, *403* (1–2), 87–93.
- (154) Levchenko, A. A.; Li, G.; Boerio-Goates, J.; Woodfield, B. F.; Navrotsky, A. TiO₂ Stability Landscape: Polymorphism, Surface Energy, and Bound Water Energetics. *Chem. Mater.* **2006**, *18* (26), 6324–6332.
- (155) Smith, S. J.; Stevens, R.; Liu, S.; Li, G.; Navrotsky, A.; Boerio-Goates, J.; Woodfield, B. F. Heat Capacities and Thermodynamic Functions of TiO₂ Anatase and Rutile: Analysis of Phase Stability. *Am. Mineral.* **2009**, *94* (2–3), 236–243.
- (156) Beltrán, A.; Gracia, L.; Andrés, J. Density Functional Theory Study of the Brookite Surfaces and Phase Transitions between Natural Titania Polymorphs. *J. Phys. Chem. B* **2006**, *110* (46), 23417–23423.

- (157) Aschauer, U.; He, Y.; Cheng, H.; Li, S. C.; Diebold, U.; Selloni, A. Influence of Subsurface Defects on the Surface Reactivity of TiO₂: Water on Anatase (101). *J. Phys. Chem. C* **2010**, *114*, 1278–1284.
- (158) Sorescu, D. C.; Al-Saidi, W. A.; Jordan, K. D. CO₂ Adsorption on TiO₂(101) Anatase: A Dispersion-Corrected Density Functional Theory Study. *J. Chem. Phys.* **2011**, *135*, 124701.
- (159) Henkelman, G.; Uberuaga, B. P.; Jónsson, H. Climbing Image Nudged Elastic Band Method for Finding Saddle Points and Minimum Energy Paths. *J. Chem. Phys.* **2000**, *113* (22), 9901–9904.
- (160) Berger, T.; Sterrer, M.; Diwald, O.; Knözinger, E.; Panayotov, D.; Thompson, T. L.; Yates, J. T. Light-Induced Charge Separation in Anatase TiO₂ Particles. *J. Phys. Chem. B* **2005**, *109* (13), 6061–6068.
- (161) Carter, E.; Carley, A. F.; Murphy, D. M. Evidence for O₂- Radical Stabilization at Surface Oxygen Vacancies on Polycrystalline TiO₂. *J. Phys. Chem. C* **2007**, *111* (28), 10630–10638.
- (162) Scheiber, P.; Fidler, M.; Dulub, O.; Schmid, M.; Diebold, U.; Hou, W.; Aschauer, U.; Selloni, A. (Sub)Surface Mobility of Oxygen Vacancies at the TiO₂ Anatase (101) Surface. *Phys. Rev. Lett.* **2012**, *109* (13), 136103 (1-5).
- (163) Solomon, S., D.; Qin, M.; Manning, Z.; Chen, M.; Marquis, K. B.; Averyt, M. T.; Miller HL; Solomon, S.; Qin, D.; Manning, M.; et al. *Summary for Policymakers. In: Climate Change 2007: The Physical Science Basis. Contribution of Working Group I to the Fourth Assessment Report of the Intergovernmental Panel on Climate Change; 2007; Vol. Geneva.*

- (164) Khilyuk, L. F.; Chilingar, G. V; Robertson, J. O.; Endres, B. Typical Composition of Natural Gases. In *Gas Migration*; 2000; pp 238–247.
- (165) Overview of Natural Gas: Background, *NaturalGas.org* (accessed April 6, 2017)
- (166) Lunsford, J. H. Catalytic Conversion of Methane to More Useful Chemicals and Fuels: A Challenge for the 21st Century. *Catal. Today* **2000**, *63*, 165–174.
- (167) Ross, J. R. H. Natural Gas Reforming and CO₂ Mitigation. In *Catalysis Today*; 2005; Vol. 100, pp 151–158.
- (168) Gutsol, A.; Rabinovich, A.; Fridman, A. Combustion-Assisted Plasma in Fuel Conversion. *Journal of Physics D: Applied Physics*. 2011, p 274001.
- (169) Petitpas, G.; Rollier, J. D.; Darmon, A.; Gonzalez-Aguilar, J.; Metkemeijer, R.; Fulcheri, L. A Comparative Study of Non-Thermal Plasma Assisted Reforming Technologies. *International Journal of Hydrogen Energy*. 2007, pp 2848–2867.
- (170) Snoeckx, R.; Setareh, M.; Aerts, R.; Simon, P.; Maghari, A.; Bogaerts, A. Influence of N₂ Concentration in a CH₄/N₂ Dielectric Barrier Discharge Used for CH₄ Conversion into H₂. *Int. J. Hydrogen Energy* **2013**, *38*, 16098–16120.
- (171) Snoeckx, R.; Aerts, R.; Tu, X.; Bogaerts, A. Plasma-Based Dry Reforming: A Computational Study Ranging from the Nanoseconds to Seconds Time Scale. *J. Phys. Chem. C* **2013**, *117*, 4957–4970.
- (172) Gong, X.-Q.; Selloni, A.; Batzill, M.; Diebold, U. Steps on Anatase TiO₂(101). *Nat. Mater.* **2006**, *5*, 665–670.

- (173) Chen, H. L.; Lee, H. M.; Chen, S. H.; Chang, M. B.; Yu, S. J.; Li, S. N. Removal of Volatile Organic Compounds by Single-Stage and Two-Stage Plasma Catalysis Systems: A Review of the Performance Enhancement Mechanisms, Current Status, and Suitable Applications. *Environ. Sci. Technol.* **2009**, *43* (7), 2216–2227.
- (174) Bradford, M. C. J.; Vannice, M. A. CO₂ Reforming of CH₄ over Supported Pt Catalysts. *J. Catal.* **1998**, *173* (1), 157–171.
- (175) Bradford, M. C. J.; Vannice, M. A. Metal-Support Interactions during the CO₂ reforming of CH₄ over Model TiO₂/Pt Catalysts. *Catal. Letters* **1997**, *48* (1–2), 31.
- (176) Bitter, J. H.; Hally, W.; Seshan, K.; van, O. J. G.; Lercher, J. A. The Role of the Oxidic Support on the Deactivation of Pt Catalysts during the CO₂ Reforming of Methane. *Catal. Today* **1996**, *29* (1–4), 349–353.
- (177) Nagaoka, K.; Okamura, M.; Aika, K. I. Titania Supported Ruthenium as a Coking-Resistant Catalyst for High Pressure Dry Reforming of Methane. *Catal. Commun.* **2001**, *2* (8), 255–260.
- (178) Nagaoka, K.; Takahabe, K.; Aika, K. I. Modification of Co/TiO₂ for Dry Reforming of Methane at 2 MPa by Pt, Ru or Ni. *Appl. Catal. A Gen.* **2004**, *268* (1–2), 151–158.
- (179) Ferreira-aparicio, P.; Rodr, I. Mechanistic Aspects of the Dry Reforming of Methane over Ruthenium Catalysts. *Appl. Catal.* **2000**, *202* (2), 183–196.
- (180) Wang, Y.; Sun, H.; Tan, S.; Feng, H.; Cheng, Z.; Zhao, J.; Zhao, A.; Wang, B.; Luo, Y.; Yang, J.; et al. Role of Point Defects on the Reactivity of Reconstructed Anatase Titanium Dioxide (001) Surface. *Nat Commun* **2013**, *4*, 2214.

- (181) Sorescu, D. C.; Lee, J.; Al-Saidi, W. A.; Jordan, K. D. CO₂ Adsorption on TiO₂ (110) Rutile: Insight from Dispersion-Corrected Density Functional Theory Calculations and Scanning Tunneling Microscopy Experiments. *J. Chem. Phys.* **2011**, *134*, 104707.
- (182) Golberg-Oster, O.; Bar-Ziv, R.; Yardeni, G.; Zilbermann, I.; Meyerstein, D. On the Reactions of Methyl Radicals with TiO₂ Nanoparticles and Granular Powders Immersed in Aqueous Solutions. *Chem. Eur. J.* **2011**, *17* (33), 9226–9231.
- (183) Bar-Ziv, R.; Zilbermann, I.; Oster-Golberg, O.; Zidki, T.; Yardeni, G.; Cohen, H.; Meyerstein, D. On the Lifetime of the Transients (NP)-(CH₃)_n (NP=Ag⁰, Au⁰, TiO₂ Nanoparticles) Formed in the Reactions Between Methyl Radicals and Nanoparticles Suspended in Aqueous Solutions. *Chem. – A Eur. J.* **2012**, *18* (15), 4699–4705.
- (184) Karunakaran, C.; Dhanalakshmi, R.; Gomathisankar, P.; Manikandan, G. Enhanced Phenol-Photodegradation by Particulate Semiconductor Mixtures: Interparticle Electron-Jump. *J. Hazard. Mater.* **2010**, *176* (1–3), 799–806.
- (185) Karunakaran, C.; Dhanalakshmi, R. Semiconductor-Catalyzed Degradation of Phenols with Sunlight. *Sol. ENERGY Mater. Sol. CELLS* **2008**, *92* (11), 1315–1321.
- (186) Kresse, G.; Furthmüller, J. Efficiency of Ab-Initio Total Energy Calculations for Metals and Semiconductors Using a Plane-Wave Basis Set. *Comput. Mater. Sci.* **1996**, *6* (1), 15–50.
- (187) Kresse, G.; Furthmüller, J. Efficient Iterative Schemes for Ab Initio Total-Energy Calculations Using a Plane-Wave Basis Set. *Phys. Rev. B* **1996**, *54* (16), 11169–11186.

- (188) Blöchl, P. E. Projector Augmented-Wave Method. *Phys. Rev. B* **1994**, *50*, 17953–17979.
- (189) Govender, A.; Curulla Ferré, D.; Niemantsverdriet, J. W. (Hans). A Density Functional Theory Study on the Effect of Zero-Point Energy Corrections on the Methanation Profile on Fe(100). *ChemPhysChem* **2012**, *13* (6), 1591–1596.
- (190) Monkhorst, H. J.; Pack, J. D. Special Points for Brillouin-Zone Integrations. *Phys. Rev. B* **1976**, *13* (12), 5188–5192.
- (191) Henkelman, G.; Arnaldsson, A.; Jónsson, H. A Fast and Robust Algorithm for Bader Decomposition of Charge Density. *Comput. Mater. Sci.* **2006**, *36* (3), 354–360.
- (192) Sanville, E.; Kenny, S. D.; Smith, R.; Henkelman, G. Improved Grid-Based Algorithm for Bader Charge Allocation. *J. Comput. Chem.* **2007**, *28* (5), 899–908.
- (193) Bader, R. F. W. *Atoms in Molecules: A Quantum Theory*; Oxford University Press: New York, 1994.
- (194) Gordy, W. Dependence of Bond Order and of Bond Energy Upon Bond Length. *J. Chem. Phys.* **1947**, *15* (5).
- (195) Linh, N. H.; Nguyen, T. Q.; Dio, W. A.; Kasai, H. Effect of Oxygen Vacancy on the Adsorption of O₂ on Anatase TiO₂ (001): A DFT-Based Study. *Surf. Sci.* **2014**.
- (196) Frenkel, J. Theorie Der Adsorption Und Verwandter Erscheinungen. *Zeitschrift für Phys.* **1924**, *26*, 117–138.
- (197) Inoue, T.; Fujishima, A.; Konishi, S.; Honda, K. Photoelectrocatalytic Reduction of Carbon Dioxide in Aqueous Suspensions of Semiconductor Powders. *Nature*. **1979**, 637–638.

- (198) Yu, J.; Low, J.; Xiao, W.; Zhou, P.; Jaroniec, M. Enhanced Photocatalytic CO₂-Reduction Activity of Anatase TiO₂ by Coexposed {001} and {101} Facets. *J. Am. Chem. Soc.* **2014**, *136*, 8839–8842.
- (199) Onal, I.; Soyer, S.; Senkan, S. Adsorption of Water and Ammonia on TiO₂-Anatase Cluster Models. *Surf. Sci.* **2006**, *600* (12), 2457–2469.
- (200) Vittadini, A.; Selloni, A.; Rotzinger, F. P.; Grätzel, M. Structure and Energetics of Water Adsorbed at TiO₂ Anatase (101) and (001) Surfaces. *Phys. Rev. Lett.* **1998**, *81* (14), 2954–2957.
- (201) Mino, L.; Ferrari, A. M.; Lacivita, V.; Spoto, G.; Bordiga, S.; Zecchina, A. CO Adsorption on Anatase Nanocrystals: A Combined Experimental and Periodic DFT Study. *J. Phys. Chem. C* **2011**, *115* (15), 7694–7700.
- (202) Mino, L.; Spoto, G.; Ferrari, A. M. CO₂ Capture by TiO₂ Anatase Surfaces: A Combined DFT and FTIR Study. *J. Phys. Chem. C* **2014**, *118* (43), 25016–25026.
- (203) Metiu, H.; Chrétien, S.; Hu, Z.; Li, B.; Sun, X. Chemistry of Lewis Acid-Base Pairs on Oxide Surfaces. *J. Phys. Chem. C* **2012**, *116*, 10439–10450.
- (204) Huygh, S.; Neyts, E. C. Adsorption of C and CH_x Radicals on Anatase (001) and the Influence of Oxygen Vacancies. *J. Phys. Chem. C* **2015**, *119* (9), 4908–4921.
- (205) Barzan, C.; Groppo, E.; Bordiga, S.; Zecchina, A. Defect Sites in H₂-Reduced TiO₂ Convert Ethylene to High Density Polyethylene without Activator. *ACS Catal.* **2014**, *4* (3), 986–989.

- (206) Liu, L.; Jiang, Y.; Zhao, H.; Chen, J.; Cheng, J.; Yang, K.; Li, Y. Engineering Coexposed {001} and {101} Facets in Oxygen-Deficient TiO₂ Nanocrystals for Enhanced CO₂ Photoreduction under Visible Light. *ACS Catal.* **2016**, *6* (2), 1097–1108.
- (207) Ramesha, G. K.; Brennecke, J. F.; Kamat, P. V. Origin of Catalytic Effect in the Reduction of CO₂ at Nanostructured TiO₂ Films. *ACS Catal.* **2014**, *4* (9), 3249–3254.
- (208) Huygh, S.; Bogaerts, A.; van Duin, A. C. T. T. T.; Neyts, E. C. Development of a ReaxFF Reactive Force Field for Intrinsic Point Defects in Titanium Dioxide. *Comput. Mater. Sci.* **2014**, *95*, 579–591.
- (209) Tkatchenko, A.; Scheffler, M. Accurate Molecular van Der Waals Interactions from Ground-State Electron Density and Free-Atom Reference Data. *Phys. Rev. Lett.* **2009**, *102*, 73005.
- (210) Al-Saidi, W. A.; Voora, V. K.; Jordan, K. D. An Assessment of the vdW-TS Method for Extended Systems. *J. Chem. Theory Comput.* **2012**, *8* (4), 1503–1513.
- (211) Ghysels, A.; Verstraelen, T.; Hemelsoet, K.; Waroquier, M.; Van Speybroeck, V. TAMkin: A Versatile Package for Vibrational Analysis and Chemical Kinetics. *J. Chem. Inf. Model.* **2010**, *50* (9), 1736–1750.
- (212) Hirshfeld, F. L. Bonded-Atom Fragments for Describing Molecular Charge Densities. *Theor. Chim. Acta* **1977**, *44*, 129–138.
- (213) Sheppard, D.; Xiao, P.; Chemelewski, W.; Johnson, D. D.; Henkelman, G. A Generalized Solid-State Nudged Elastic Band Method. *J. Chem. Phys.* **2012**, *136* (7).
- (214) Sheppard, D.; Henkelman, G. Paths to Which the Nudged Elastic Band Converges. *J. Comput. Chem.* **2011**, *32* (8), 1769–1771.

- (215) Sheppard, D.; Terrell, R.; Henkelman, G. Optimization Methods for Finding Minimum Energy Paths. *J. Chem. Phys.* **2008**, *128* (13), 134106.
- (216) Henkelman, G.; Jónsson, H. Improved Tangent Estimate in the Nudged Elastic Band Method for Finding Minimum Energy Paths and Saddle Points. *J. Chem. Phys.* **2000**, *113* (22), 9978–9985.
- (217) Jónsson, H.; Mills, G.; Jacobsen, K. W.; Jonsson, H.; Mills, G.; Jacobsen, K. W. Nudged Elastic Band Method for Finding Minimum Energy Paths of Transitions. In *Classical and Quantum Dynamics in Condensed Phase Simulations*; **1998**; 385–404.
- (218) Indrakanti, V. P.; Kubicki, J. D.; Schobert, H. H. Quantum Chemical Modeling of Ground States of CO₂ Chemisorbed on Anatase (001), (101), and (010) TiO₂ Surfaces. *Energy & Fuels* **2008**, *22*, 2611–2618.
- (219) Pipornpong, W.; Wanbayor, R.; Ruangpornvisuti, V. Adsorption CO₂ on the Perfect and Oxygen Vacancy Defect Surfaces of Anatase TiO₂ and Its Photocatalytic Mechanism of Conversion to CO. *Appl. Surf. Sci.* **2011**, *257*, 10322–10328.
- (220) Fonseca Guerra, C.; Handgraaf, J.-W.; Baerends, E. J.; Bickelhaupt, F. M. Voronoi Deformation Density (VDD) Charges: Assessment of the Mulliken, Bader, Hirshfeld, Weinhold, and VDD Methods for Charge Analysis. *J. Comput. Chem.* **2004**, *25* (2), 189–210.
- (221) Lee, J.; Sorescu, D. C.; Deng, X. Electron-Induced Dissociation of CO₂ on TiO₂ (110). *J. Am. Chem. Soc.* **2011**, *133* (26), 10066–10069.
- (222) Subramani, V.; Gangwal, S. K. A Review of Recent Literature to Search for an Efficient Catalytic Process for the Conversion of Syngas to Ethanol. *Energy and Fuels*. **2008**, 814–839.

- (223) Lee, M. C.; Seo, S. Bin; Chung, J. H.; Kim, S. M.; Joo, Y. J.; Ahn, D. H. Gas Turbine Combustion Performance Test of Hydrogen and Carbon Monoxide Synthetic Gas. *Fuel* **2010**, *89* (7), 1485–1491.
- (224) Huygh, S.; Bogaerts, A.; Neyts, E. C. How Oxygen Vacancies Activate CO₂ Dissociation on TiO₂ Anatase (001). *J. Phys. Chem. C* **2016**, *120* (38), 21659–21669.
- (225) Sun, C.; Liao, T.; Lu, G. Q.; Smith, S. C. The Role of Atomic Vacancy on Water Dissociation over Titanium Dioxide Nanosheet: A Density Functional Theory Study. *J. Phys. Chem. C* **2012**, *116* (3), 2477–2482.
- (226) Schaub, R.; Thostrup, P.; Lopez, N.; Laegsgaard, E.; Stensgaard, I.; Norskov, J. K.; Besenbacher, F. Oxygen Vacancies as Active Sites for Water Dissociation on Rutile TiO₂ (110). *Phys Rev Lett* **2001**, *87* (26), 266104.
- (227) Nakamura, I.; Negishi, N.; Kutsuna, S.; Ihara, T.; Sugihara, S.; Takeuchi, K. Role of Oxygen Vacancy in the Plasma-Treated TiO₂ Photocatalyst with Visible Light Activity for NO Removal. *J. Mol.* **2000**, *161* (1–2), 205–212.
- (228) Campbell, C. T.; Árnadóttir, L.; Sellers, J. R. V. Kinetic Prefactors of Reactions on Solid Surfaces. *Zeitschrift für Phys. Chemie* **2013**, *227* (9–11), 1435–1454.
- (229) Hussain, A.; Gracia, J.; E., N. Ben; Niemantsverdriet, J. W. (Hans). Chemistry of O- and H-Containing Species on the (001) Surface of Anatase TiO₂: A DFT Study. *ChemPhysChem* **2010**, *11* (11), 2375–2382.
- (230) Liu, H.; Wang, X.; Pan, C.; Liew, K. M. First-Principles Study of Formaldehyde Adsorption on TiO₂ Rutile (110) and Anatase (001) Surfaces. *J. Phys. Chem. C* **2012**, *116* (14), 8044–8053.

- (231) Xiao, P.; Sheppard, D.; Rogal, J.; Henkelman, G. Solid-State Dimer Method for Calculating Solid-Solid Phase Transitions. *J. Chem. Phys.* **2014**, *140* (17).
- (232) Bal, K. M.; Neyts, E. C. Merging Metadynamics into Hyperdynamics: Accelerated Molecular Simulations Reaching Time Scales from Microseconds to Seconds. *J. Chem. Theory Comput.* **2015**, *11* (10), 4545–4554.
- (233) Du, Y.; Deskins, N. A.; Zhang, Z.; Dohnalek, Z.; Dupuis, M.; Lyubinetsky, I. Formation of O Adatom Pairs and Charge Transfer upon O₂ Dissociation on Reduced TiO₂ (110). *Phys. Chem. Chem. Phys.* **2010**, *12* (24), 6337–6344.
- (234) Du, Y.; Deskins, N. A.; Zhang, Z.; Dohnálek, Z.; Dupuis, M.; Lyubinetsky, I. Imaging Consecutive Steps of O₂ Reaction with Hydroxylated TiO₂ (110): Identification of HO₂ and Terminal OH Intermediates. *J. Phys. Chem. C* **2009**, *113* (2), 666–671.
- (235) Ortega, Y.; Hevia, D. F.; Oviedo, J.; San-Miguel, M. a. A DFT Study of the Stoichiometric and Reduced Anatase (001) Surfaces. *Appl. Surf. Sci.* **2014**, *294*, 42–48.
- (236) Lutfalla, S.; Shapovalov, V.; Bell, A. T. Calibration of the DFT/GGA+U Method for Determination of Reduction Energies for Transition and Rare Earth Metal Oxides of Ti, V, Mo, and Ce. *J. Chem. Theory Comput.* **2011**, *7* (7), 2218–2223.
- (237) Cohen, A. J.; Mori-Sánchez, P.; Yang, W. Insights into Current Limitations of Density Functional Theory. *Science*. **2008**, *321* (5890), 792–794.
- (238) Anisimov, V. I.; Zaanen, J.; Andersen, O. K. Band Theory and Mott Insulators: Hubbard U instead of Stoner I. *Phys. Rev. B* **1991**, *44* (3), 943–954.

- (239) Furche, F.; Perdew, J. P. The Performance of Semilocal and Hybrid Density Functionals in 3d Transition-Metal Chemistry. *J. Chem. Phys.* **2006**, *124* (4).
- (240) Morgan, B. J.; Watson, G. W. A DFT+U Description of Oxygen Vacancies at the TiO₂ Rutile (110) Surface. *Surf. Sci.* **2007**, *601* (21), 5034–5041.

Appendix

Reactive MD-force field: TiO₂-surface defects Stijn Huygh

39 ! Number of general parameters
50.0000 !Overcoordination parameter
9.5469 !Overcoordination parameter
1.6725 !Valency angle conjugation parameter
1.7224 !Triple bond stabilisation parameter
6.8702 !Triple bond stabilisation parameter
60.4850 !C2-correction
1.0588 !Undercoordination parameter
4.6000 !Triple bond stabilisation parameter
12.1176 !Undercoordination parameter
13.3056 !Undercoordination parameter
-70.5044 !Triple bond stabilization energy
0.0000 !Lower Taper-radius
10.0000 !Upper Taper-radius
2.8793 !Not used
33.8667 !Valency undercoordination
6.0891 !Valency angle/lone pair parameter
1.0563 !Valency angle
2.0384 !Valency angle parameter
6.1431 !Not used
6.9290 !Double bond/angle parameter
0.3989 !Double bond/angle parameter: overcoord
3.9954 !Double bond/angle parameter: overcoord
-2.4837 !Not used
5.7796 !Torsion/BO parameter
10.0000 !Torsion overcoordination
1.9487 !Torsion overcoordination
-1.2327 !Conjugation 0 (not used)
2.1645 !Conjugation
1.5591 !vdWaals shielding
0.1000 !Cutoff for bond order (*100)
1.7602 !Valency angle conjugation parameter
0.6991 !Overcoordination parameter
50.0000 !Overcoordination parameter
1.8512 !Valency/lone pair parameter
0.5000 !Not used
20.0000 !Not used
5.0000 !Molecular energy (not used)

0.0000 !Molecular energy (not used)
0.7903 !Valency angle conjugation parameter
12 ! Nr of atoms; cov.r; valency;a.m;Rvdw;Evdw;gammaEEM;cov.r2;#
alfa;gammavdW;valency;Eunder;Eover;chiEEM;etaEEM;n.u.
cov r3;Elp;Heat inc.;n.u.;n.u.;n.u.;n.u.
ov/un;val1;n.u.;val3,vval4

C	1.3817	4.0000	12.0000	1.8903	0.1838	0.9000	1.1341	4.0000
	9.7559	2.1346	4.0000	34.9350	79.5548	5.9666	7.0000	0.0000
	1.2114	0.0000	202.2908	8.9539	34.9289	13.5366	0.8563	0.0000
	-2.8983	2.5000	1.0564	4.0000	2.9663	0.0000	0.0000	0.0000
H	0.8930	1.0000	1.0080	1.3550	0.0930	0.8203	-0.1000	1.0000
	8.2230	33.2894	1.0000	0.0000	121.1250	3.7248	9.6093	1.0000
	-0.1000	0.0000	55.1878	3.0408	2.4197	0.0003	1.0698	0.0000
	-19.4571	4.2733	1.0338	1.0000	2.8793	0.0000	0.0000	0.0000
O	1.2450	2.0000	15.9990	2.3890	0.1000	1.0898	1.0548	6.0000
	9.7300	13.8449	4.0000	37.5000	116.0768	8.5000	8.3122	2.0000
	0.9049	0.4056	68.0152	3.5027	0.7640	0.0021	0.9745	0.0000
	-3.5500	2.9000	1.0493	4.0000	2.9225	0.0000	0.0000	0.0000
N	1.2333	3.0000	14.0000	1.9324	0.1376	0.7921	1.1748	5.0000
	10.0667	7.8431	4.0000	32.2482	100.0000	7.5795	6.3952	2.0000
	1.0433	27.4290	119.9837	1.9457	4.2874	3.4869	0.9745	0.0000
	-4.3875	2.6192	1.0183	4.0000	2.8793	0.0000	0.0000	0.0000
S	1.9405	2.0000	32.0600	2.0677	0.2099	1.0336	1.5479	6.0000
	9.9575	4.9055	4.0000	52.9998	112.1416	5.7824	8.2545	2.0000
	1.4601	9.7177	71.1843	5.7487	23.2859	12.7147	0.9745	0.0000
	-11.0000	2.7466	1.0338	6.2998	2.8793	0.0000	0.0000	0.0000
Mg	1.8315	2.0000	24.3050	2.2464	0.1806	0.5020	1.0000	2.0000
	10.9186	27.1205	3.0000	38.0000	0.0000	0.9499	5.6130	0.0000
	-1.3000	0.0000	127.9160	49.9248	0.3370	0.0000	0.0000	0.0000
	-1.0823	2.3663	1.0564	6.0000	2.9663	0.0000	0.0000	0.0000
P	1.5994	3.0000	30.9738	1.7000	0.1743	1.0000	1.3000	5.0000
	9.1909	14.9482	5.0000	0.0000	0.0000	1.6676	7.0946	0.0000
	-1.0000	25.0000	125.6300	0.2187	21.4305	15.1425	0.0000	0.0000
	-3.9294	3.4831	1.0338	5.0000	2.8793	0.0000	0.0000	0.0000
Na	1.8000	1.0000	22.9898	2.8270	0.1872	0.4000	-1.0000	1.0000
	10.0000	2.5000	1.0000	0.0000	0.0000	-0.9871	6.7728	0.0000
	-1.0000	0.0000	23.0445	100.0000	1.0000	0.0000	0.8563	0.0000
	-2.5000	3.9900	1.0338	8.0000	2.5791	0.0000	0.0000	0.0000
Ti	2.0298	4.0000	47.8800	2.3425	0.1850	0.3241	0.1000	4.0000
	12.8848	14.4614	4.0000	0.0730	-0.0829	4.3230	6.9663	0.0000
	-1.0000	0.0000	143.1511	20.6967	-0.8712	0.0192	0.8208	0.0000
	-13.2347	1.6267	0.9024	13.1697	2.4417	0.0000	0.0000	0.0000
Cl	1.7140	1.0000	35.4500	1.9139	0.2000	0.3500	-1.0000	7.0000

	11.5345	10.1330	1.0000	0.0000	0.0000	9.9704	6.1703	0.0000	
	-1.0000	1.2769	143.1770	6.2293	5.2294	0.1542	0.8563	0.0000	
	-10.2080	2.9867	1.0338	6.2998	2.5791	0.0000	0.0000	0.0000	
F	1.2100	1.0000	18.9984	1.8601	0.1200	0.3000	-0.1000	7.0000	
	11.5000	7.5000	4.0000	9.2533	0.2000	9.0000	15.0000	0.0000	
	-1.0000	35.0000	1.5000	6.9821	4.1799	1.0561	0.0000	0.0000	
	-7.3000	2.6656	1.0493	4.0000	2.9225	0.0000	0.0000	0.0000	
X	-0.1000	2.0000	1.0080	2.0000	0.0000	1.0000	-0.1000	6.0000	
	10.0000	2.5000	4.0000	0.0000	0.0000	8.5000	1.5000	0.0000	
	-0.1000	0.0000	-2.3700	8.7410	13.3640	0.6690	0.9745	0.0000	
	-11.0000	2.7466	1.0338	4.0000	2.8793	0.0000	0.0000	0.0000	
58	! Nr of bonds; Edis1;LPpen;n.u.;pbe1;pbo5;13corr;pbo6								
	pbe2;pbo3;pbo4;Etrip;pbo1;pbo2;ovcorr								
1	1	158.2004	99.1897	78.0000	-0.7738	-0.4550	1.0000	37.6117	0.4147
		0.4590	-0.1000	9.1628	1.0000	-0.0777	6.7268	1.0000	0.0000
1	2	169.4760	0.0000	0.0000	-0.6083	0.0000	1.0000	6.0000	0.7652
		5.2290	1.0000	0.0000	1.0000	-0.0500	6.9136	0.0000	0.0000
2	2	153.3934	0.0000	0.0000	-0.4600	0.0000	1.0000	6.0000	0.7300
		6.2500	1.0000	0.0000	1.0000	-0.0790	6.0552	0.0000	0.0000
1	3	164.4303	82.6772	60.8077	-0.3739	-0.2351	1.0000	10.5036	1.0000
		0.4475	-0.2288	7.0250	1.0000	-0.1363	4.8734	0.0000	0.0000
3	3	143.0904	69.5599	50.8329	0.2665	-0.1170	1.0339	30.7245	0.0175
		0.8976	-0.1244	8.7321	1.0000	-0.1993	6.2940	1.0474	0.0000
1	4	134.1215	140.2179	79.9745	0.0163	-0.1428	1.0000	27.0617	0.2000
		0.1387	-0.3681	7.1611	1.0000	-0.1000	5.0825	1.0000	0.0000
3	4	130.8596	169.4551	40.0000	0.3837	-0.1639	1.0000	35.0000	0.2000
		1.0000	-0.3579	7.0004	1.0000	-0.1193	6.8773	1.0000	0.0000
4	4	157.9384	82.5526	152.5336	0.4010	-0.1034	1.0000	12.4261	0.5828
		0.1578	-0.1509	11.9186	1.0000	-0.0861	5.4271	1.0000	0.0000
2	3	160.0000	0.0000	0.0000	-0.5725	0.0000	1.0000	6.0000	0.5626
		1.1150	1.0000	0.0000	0.0000	-0.0920	4.2790	0.0000	0.0000
2	4	185.3171	0.0000	0.0000	-0.3689	0.0000	1.0000	6.0000	0.2854
		7.6517	1.0000	0.0000	1.0000	-0.0408	6.0255	0.0000	0.0000
1	5	128.7959	56.4134	39.0716	0.0688	-0.4463	1.0000	31.1766	0.4530
		0.1955	-0.3587	6.2148	1.0000	-0.0770	6.6386	1.0000	0.0000
2	5	136.1049	0.0000	0.0000	-0.4669	0.0000	1.0000	6.0000	0.3803
		10.5730	1.0000	0.0000	1.0000	-0.1000	7.0000	1.0000	0.0000
3	5	135.6998	220.0000	40.0000	0.5848	-0.2406	1.0000	22.1005	0.2335
		0.7069	-0.2681	8.3465	1.0000	-0.0922	5.4651	1.0000	0.0000
4	5	0.0000	0.0000	0.0000	0.5000	-0.2000	1.0000	40.0000	0.3000
		0.4000	-0.2500	9.0000	1.0000	-0.1000	6.0000	1.0000	0.0000
5	5	0.0000	0.0000	0.0000	0.2500	-0.5000	1.0000	20.0000	1.0000
		0.2500	-0.2500	10.0000	1.0000	-0.1000	8.0000	1.0000	0.0000

2	6	58.6896	0.0000	0.0000	-0.0203	-0.1418	1.0000	13.1260	0.0230
		8.2136	-0.1310	0.0000	1.0000	-0.2692	6.4254	0.0000	24.4461
3	6	87.0227	0.0000	43.3991	0.0030	-0.3000	1.0000	36.0000	0.0250
		0.0087	-0.2500	12.0000	1.0000	-0.0439	6.6073	1.0000	24.4461
6	6	32.3808	0.0000	0.0000	-0.0076	-0.2000	0.0000	16.0000	0.2641
		4.8726	-0.2000	10.0000	1.0000	-0.0729	4.6319	0.0000	0.0000
1	7	110.0000	92.0000	0.0000	0.2171	-0.1418	1.0000	13.1260	0.6000
		0.3601	-0.1310	10.7257	1.0000	-0.0869	5.3302	1.0000	0.0000
2	7	0.1466	0.0000	0.0000	0.2250	-0.1418	1.0000	13.1260	0.6000
		0.3912	-0.1310	0.0000	1.0000	-0.1029	9.3302	0.0000	0.0000
3	7	201.0058	194.1410	0.0000	1.0000	-0.5000	1.0000	25.0000	0.4873
		0.4358	-0.1571	15.8745	1.0000	-0.2431	6.3823	1.0000	0.0000
4	7	130.0000	0.0000	0.0000	0.2171	-0.1418	1.0000	13.1260	0.6000
		0.3601	-0.1310	10.7257	1.0000	-0.0869	5.3302	1.0000	0.0000
6	7	0.1000	0.0000	0.0000	0.2500	-0.5000	1.0000	35.0000	0.6000
		0.5000	-0.5000	20.0000	1.0000	-0.2000	10.0000	1.0000	0.0000
7	7	0.0000	0.0000	0.0000	0.2171	-0.5000	1.0000	35.0000	0.6000
		0.5000	-0.5000	20.0000	1.0000	-0.2000	10.0000	1.0000	0.0000
1	8	0.0000	0.0000	0.0000	-1.0000	-0.3000	1.0000	36.0000	0.7000
		10.1151	-0.3500	25.0000	1.0000	-0.1053	8.2003	1.0000	0.0000
2	8	0.0000	0.0000	0.0000	-1.0000	-0.3000	1.0000	36.0000	0.7000
		10.1151	-0.3500	25.0000	1.0000	-0.1053	8.2003	1.0000	0.0000
3	8	45.8933	0.0000	0.0000	-0.1511	-0.3000	1.0000	36.0000	0.3105
		5.8448	-0.3500	25.0000	1.0000	-0.0659	7.9140	1.0000	0.0000
4	8	0.0000	0.0000	0.0000	-1.0000	-0.3000	1.0000	36.0000	0.7000
		10.1151	-0.3500	25.0000	1.0000	-0.1053	8.2003	1.0000	0.0000
5	8	0.0000	0.0000	0.0000	-1.0000	-0.3000	1.0000	36.0000	0.7000
		10.1151	-0.3500	25.0000	1.0000	-0.1053	8.2003	1.0000	0.0000
6	8	0.0000	0.0000	0.0000	0.2500	-0.5000	1.0000	35.0000	0.6000
		0.5000	-0.5000	20.0000	1.0000	-0.2000	10.0000	1.0000	0.0000
7	8	0.0000	0.0000	0.0000	0.2500	-0.5000	1.0000	35.0000	0.6000
		0.5000	-0.5000	20.0000	1.0000	-0.2000	10.0000	1.0000	0.0000
8	8	64.4508	0.0000	0.0000	-0.3738	0.3000	0.0000	25.0000	0.2158
		0.9915	-0.4000	12.0000	1.0000	-0.0515	5.0000	0.0000	0.0000
4	6	50.0000	10.0901	0.0000	-1.0000	-0.3000	1.0000	36.0000	0.7058
		0.8567	-0.3487	17.4990	1.0000	-0.0794	8.2232	1.0000	0.0000
1	9	0.0000	0.0000	0.0000	-0.2872	-0.3000	1.0000	36.0000	0.0082
		1.7973	-0.2500	20.0000	1.0000	-0.2578	6.5219	1.0000	0.0000
2	9	0.0000	0.0000	0.0000	-0.2872	-0.3000	1.0000	36.0000	0.0082
		1.7973	-0.2500	20.0000	1.0000	-0.2578	6.5219	1.0000	0.0000
3	9	178.8033	119.5547	0.0135	-0.1386	-0.2423	0.0008	39.9934	0.2743
		0.7868	-0.3382	16.0702	1.1200	-0.0991	6.7394	-0.0235	0.0000
4	9	0.0000	0.0000	0.0000	-0.2872	-0.3000	1.0000	36.0000	0.0082

		1.7973	-0.2500	20.0000	1.0000	-0.2578	6.5219	1.0000	0.0000
5	9	0.0000	0.0000	0.0000	-0.2872	-0.3000	1.0000	36.0000	0.0082
		1.7973	-0.2500	20.0000	1.0000	-0.2578	6.5219	1.0000	0.0000
6	9	0.0000	0.0000	0.0000	-0.2872	-0.3000	1.0000	36.0000	0.0082
		1.7973	-0.2500	20.0000	1.0000	-0.2578	6.5219	1.0000	0.0000
7	9	0.0000	0.0000	0.0000	-0.2872	-0.3000	1.0000	36.0000	0.0082
		1.7973	-0.2500	20.0000	1.0000	-0.2578	6.5219	1.0000	0.0000
8	9	0.1000	0.0000	0.0000	0.2500	-0.5000	1.0000	35.0000	0.6000
		0.5000	-0.5000	20.0000	1.0000	-0.2000	10.0000	1.0000	0.0000
9	9	106.1844	-0.0243	0.0184	-1.2501	-0.1500	-0.0257	15.0845	0.0713
		0.2141	-0.2271	15.0298	0.9660	-0.0480	5.0336	-0.0179	0.0000
1	10	0.0000	0.0000	0.0000	0.5000	-0.2000	0.0000	16.0000	0.5000
		1.0001	-0.2000	15.0000	1.0000	-0.1000	10.0000	0.0000	0.0000
2	10	98.9788	0.0000	0.0000	-0.0572	-0.2000	0.0000	16.0000	1.1523
		2.2822	-0.2000	15.0000	1.0000	-0.1093	5.1686	0.0000	0.0000
3	10	0.0000	0.0000	0.0000	0.5000	-0.2000	0.0000	16.0000	0.5000
		1.0001	-0.2000	15.0000	1.0000	-0.1000	10.0000	0.0000	0.0000
4	10	0.0000	0.0000	0.0000	0.5000	-0.2000	0.0000	16.0000	0.5000
		1.0001	-0.2000	15.0000	1.0000	-0.1000	10.0000	0.0000	0.0000
5	10	0.0000	0.0000	0.0000	0.5000	-0.2000	0.0000	16.0000	0.5000
		1.0001	-0.2000	15.0000	1.0000	-0.1000	10.0000	0.0000	0.0000
6	10	0.0000	0.0000	0.0000	0.5000	-0.2000	0.0000	16.0000	0.5000
		1.0001	-0.2000	15.0000	1.0000	-0.1000	10.0000	0.0000	0.0000
7	10	0.0000	0.0000	0.0000	0.5000	-0.2000	0.0000	16.0000	0.5000
		1.0001	-0.2000	15.0000	1.0000	-0.1000	10.0000	0.0000	0.0000
8	10	0.0000	0.0000	0.0000	0.5000	-0.2000	0.0000	16.0000	0.5000
		1.0001	-0.2000	15.0000	1.0000	-0.1000	10.0000	0.0000	0.0000
9	10	0.0000	0.0000	0.0000	0.5000	-0.2000	0.0000	16.0000	0.5000
		1.0001	-0.2000	15.0000	1.0000	-0.1000	10.0000	0.0000	0.0000
10	10	0.2500	0.0000	0.0000	0.1803	-0.2000	0.0000	16.0000	0.3356
		0.9228	-0.2000	15.0000	1.0000	-0.1178	5.6715	0.0000	0.0000
1	11	237.8781	0.0000	0.0000	-0.7438	-0.5000	1.0000	35.0000	1.0460
		3.6661	-0.2500	15.0000	1.0000	-0.0800	5.4719	1.0000	0.0000
2	11	0.0000	0.0000	0.0000	-0.4643	0.0000	1.0000	6.0000	0.6151
		12.3710	1.0000	0.0000	1.0000	-0.1008	8.5980	0.0000	0.0000
3	11	0.0000	0.0000	0.0000	-0.4643	0.0000	1.0000	6.0000	0.6151
		12.3710	1.0000	0.0000	1.0000	-0.1008	8.5980	0.0000	0.0000
4	11	0.0000	0.0000	0.0000	-0.4643	0.0000	1.0000	6.0000	0.6151
		12.3710	1.0000	0.0000	1.0000	-0.1008	8.5980	0.0000	0.0000
5	11	0.0000	0.0000	0.0000	-0.4643	0.0000	1.0000	6.0000	0.6151
		12.3710	1.0000	0.0000	1.0000	-0.1008	8.5980	0.0000	0.0000
11	11	250.0765	0.0000	0.0000	0.2298	-0.3500	1.0000	25.0000	0.8427
		0.1167	-0.2500	15.0000	1.0000	-0.1506	7.3516	1.0000	0.0000

22 !Nr of off-diagonal terms; Ediss;Ro;gamma;rsigma;rpi;rpi2

1	2	0.1239	1.4004	9.8467	1.1210	-1.0000	-1.0000
2	3	0.0283	1.2885	10.9190	0.9215	-1.0000	-1.0000
2	4	0.0687	1.5130	10.0094	0.9412	-1.0000	-1.0000
1	3	0.1345	1.8422	9.7725	1.2835	1.1576	1.0637
1	4	0.1447	1.8766	9.7990	1.3436	1.1885	1.1363
3	4	0.1048	2.0003	10.1220	1.3173	1.1096	1.0206
1	5	0.1408	1.8161	9.9393	1.7986	1.3021	1.4031
2	5	0.0895	1.6239	10.0104	1.4640	-1.0000	-1.0000
3	5	0.1962	1.7872	10.2319	1.4622	1.4025	-1.0000
4	5	0.1505	1.9000	10.5104	1.8000	1.4000	-1.0000
2	6	0.0100	1.6000	13.2979	1.8670	-1.0000	-1.0000
3	6	0.0809	1.7000	11.4606	1.5177	-1.0000	-1.0000
3	7	0.0534	1.7520	10.4281	1.8000	1.4498	-1.0000
6	7	0.1801	1.8566	9.8498	0.1000	-1.0000	-1.0000
3	8	0.0825	1.5904	11.3396	1.5905	-1.0000	-1.0000
2	9	0.1488	1.8047	13.4826	0.0100	-1.0000	-1.0000
3	9	0.1431	1.6041	10.1194	1.7060	1.4678	-1.0000
1	9	0.2035	1.7007	11.4530	0.0100	-1.0000	-1.0000
2	10	0.0376	1.6671	9.6285	1.2123	-1.0000	-1.0000
3	10	0.1945	2.2766	11.2353	-1.0000	-1.0000	-1.0000
1	11	0.1071	1.6243	11.0402	1.3176	-1.0000	-1.0000
2	11	0.0431	1.7204	10.3632	0.5386	-1.0000	-1.0000

83 !Nr of angles;at1;at2;at3;Theta;o;ka;kb;pv1;pv2

1	1	1	59.0573	30.7029	0.7606	0.0000	0.7180	6.2933	1.1244
1	1	2	65.7758	14.5234	6.2481	0.0000	0.5665	0.0000	1.6255
2	1	2	70.2607	25.2202	3.7312	0.0000	0.0050	0.0000	2.7500
1	2	2	0.0000	0.0000	6.0000	0.0000	0.0000	0.0000	1.0400
1	2	1	0.0000	3.4110	7.7350	0.0000	0.0000	0.0000	1.0400
2	2	2	0.0000	27.9213	5.8635	0.0000	0.0000	0.0000	1.0400
1	1	3	53.9517	7.8968	2.6122	0.0000	3.0000	58.6562	1.0338
3	1	3	76.9627	44.2852	2.4177	-25.3063	1.6334	-50.0000	2.7392
1	1	4	78.5538	21.4381	7.4715	0.0000	1.1046	50.0000	1.5275
3	1	4	73.9544	12.4661	7.0000	0.0000	1.1046	0.0000	1.1880
4	1	4	89.3168	20.2660	7.5000	0.0000	1.1046	0.0000	1.5403
2	1	3	65.0000	16.3141	5.2730	0.0000	0.4448	0.0000	1.4077
2	1	4	74.2929	31.0883	2.6184	0.0000	0.1000	0.0000	1.0500
1	2	4	0.0000	0.0019	6.3000	0.0000	0.0000	0.0000	1.0400
1	3	1	72.6199	42.5510	0.7205	0.0000	2.9294	0.0000	1.3096
1	3	3	81.9029	32.2258	1.7397	0.0000	0.9888	68.1072	1.7777
1	3	4	82.4890	31.4554	0.9953	0.0000	3.0000	0.0000	1.0783
3	3	3	80.7324	30.4554	0.9953	0.0000	3.0000	50.0000	1.0783
3	3	4	84.3637	31.4554	0.9953	0.0000	3.0000	0.0000	1.0783

4	3	4	89.7071	31.4554	0.9953	0.0000	3.0000	0.0000	1.1519
1	3	2	70.1101	13.1217	4.4734	0.0000	0.8433	0.0000	3.0000
2	3	3	75.6935	50.0000	2.0000	0.0000	1.0000	0.0000	1.1680
2	3	4	75.6201	18.7919	0.9833	0.0000	0.1000	0.0000	1.0500
2	3	2	85.8000	9.8453	2.2720	0.0000	2.8635	0.0000	1.5800
1	4	1	81.4699	7.2318	1.2608	0.0000	3.0000	0.0000	1.2127
1	4	3	103.3204	33.0381	0.5787	0.0000	3.0000	0.0000	1.2127
1	4	4	50.0000	25.0250	4.7651	0.0000	3.0000	0.0000	1.2028
3	4	3	74.1978	42.1786	1.7845	-18.0069	3.0000	0.0000	1.2127
3	4	4	74.8600	43.7354	1.1572	-0.9193	3.0000	0.0000	1.2127
4	4	4	75.0538	14.8267	5.2794	0.0000	3.0000	0.0000	1.2127
1	4	2	68.2294	29.6576	1.0533	0.0000	0.3481	0.0000	1.5443
2	4	3	81.3686	40.0712	2.2396	0.0000	0.3481	0.0000	1.5443
2	4	4	83.0104	43.4766	1.5328	0.0000	0.3481	0.0000	1.5443
2	4	2	79.6336	17.7917	3.7832	0.0000	0.0222	0.0000	2.0238
1	2	3	0.0000	25.0000	3.0000	0.0000	1.0000	0.0000	1.0400
1	2	4	0.0000	0.0019	6.0000	0.0000	0.0000	0.0000	1.0400
1	2	5	0.0000	0.0019	6.0000	0.0000	0.0000	0.0000	1.0400
3	2	3	0.0000	15.0000	2.8900	0.0000	0.0000	0.0000	2.8774
3	2	4	0.0000	0.0019	6.0000	0.0000	0.0000	0.0000	1.0400
4	2	4	0.0000	0.0019	6.0000	0.0000	0.0000	0.0000	1.0400
2	2	3	0.0000	8.5744	3.0000	0.0000	0.0000	0.0000	1.0421
2	2	4	0.0000	0.0019	6.0000	0.0000	0.0000	0.0000	1.0400
1	1	5	74.4180	33.4273	1.7018	0.1463	0.5000	0.0000	1.6178
1	5	1	79.7037	28.2036	1.7073	0.1463	0.5000	0.0000	1.6453
2	1	5	63.3289	29.4225	2.1326	0.0000	0.5000	0.0000	3.0000
1	5	2	85.9449	38.3109	1.2492	0.0000	0.5000	0.0000	1.1000
1	5	5	85.6645	40.0000	2.9274	0.1463	0.5000	0.0000	1.3830
2	5	2	83.8555	5.1317	0.4377	0.0000	0.5000	0.0000	3.0000
2	5	5	97.0064	32.1121	2.0242	0.0000	0.5000	0.0000	2.8568
3	5	3	81.0926	30.2268	6.4132	-5.4471	2.5968	0.0000	3.0000
1	5	3	70.0000	35.0000	3.4223	0.0000	1.3550	0.0000	1.2002
1	3	5	57.3353	41.0012	1.0609	0.0000	1.3000	0.0000	3.0000
3	3	5	83.9753	31.0715	3.5590	0.0000	0.8161	0.0000	1.1776
2	3	5	89.8843	17.5000	3.3660	0.0000	2.0000	0.0000	2.0734
2	6	2	0.0000	49.8261	0.2093	0.0000	2.0870	0.0000	2.2895
2	2	6	0.0000	40.0366	3.1505	0.0000	1.1296	0.0000	1.1110
6	2	6	0.0000	0.5047	0.8000	0.0000	0.8933	0.0000	4.6650
2	6	6	0.0000	8.7037	0.0827	0.0000	3.5597	0.0000	1.1198
3	6	3	0.0000	9.2317	0.1000	0.0000	1.0000	0.0000	1.0920
6	3	6	0.0008	25.0000	8.0000	0.0000	1.0000	0.0000	3.0000
2	3	6	66.0423	5.0000	1.0000	0.0000	1.0000	0.0000	1.2500
2	6	3	0.0000	0.5000	0.1000	0.0000	1.0000	0.0000	3.0000

3	3	6	70.0000	20.0000	1.0000	0.0000	1.0000	0.0000	1.2500	
3	7	3	90.0000	18.4167	0.6799	-8.0000	0.1310	0.0000	2.2321	
2	3	7	72.6004	9.6150	0.8905	0.0000	3.5473	0.0000	1.0400	
3	3	7	60.0000	40.0000	4.0000	0.0000	1.0000	0.0000	1.0400	
3	2	7	0.0000	10.0000	1.0000	0.0000	1.0000	0.0000	1.0400	
6	3	7	41.0995	3.2207	7.3523	0.0000	0.1101	0.0000	1.0947	
7	3	7	62.1312	7.5931	0.1000	0.0000	0.5154	0.0000	2.1744	
1	3	7	74.1394	8.5687	1.7132	0.0000	-0.6553	0.0000	2.2323	
2	7	3	75.0000	25.0000	2.0000	0.0000	1.0000	0.0000	1.2500	
3	7	7	70.0000	25.0000	2.0000	0.0000	1.0000	0.0000	1.2500	
3	9	3	78.9012	22.4222	2.9317	0.0000	-1.5371	0.0000	0.9661	
9	3	9	82.8138	10.4735	6.0000	0.0000	0.9879	0.0000	10.0000	
3	3	9	48.9276	13.2995	7.0000	0.0000	0.5508	0.0000	4.7792	
3	9	9	19.4109	10.8247	1.7252	0.0000	-3.8844	0.0000	1.4936	
2	3	9	83.8242	10.8643	5.4198	0.0000	0.3191	0.0000	1.4992	
1	3	9	90.0000	7.6430	0.2869	0.0000	1.8647	0.0000	4.0000	
3	2	10	0.0000	0.0100	0.0100	0.0000	0.0000	0.0000	1.1456	
11	1	11	77.8443	49.0744	5.9913	0.0000	0.7835	0.0000	2.3020	
1	11	1	0.0000	19.9962	3.2299	0.0000	2.1012	0.0000	1.1537	
1	11	11	0.0000	25.0000	1.0000	0.0000	1.0000	0.0000	1.0400	
11	1	2	69.6421	10.0000	2.0000	0.0000	1.0000	0.0000	1.0400	
57 ! Nr of torsions;at1;at2;at3;at4;;V1;V2;V3;V2(BO);vconj;n.u;n										
1	1	1	1	-0.2500	34.7453	0.0288	-6.3507	-1.6000	0.0000	0.0000
1	1	1	2	-0.2500	29.2131	0.2945	-4.9581	-2.1802	0.0000	0.0000
2	1	1	2	-0.2500	31.2081	0.4539	-4.8923	-2.2677	0.0000	0.0000
1	1	1	3	1.2799	20.7787	-0.5249	-2.5000	-1.0000	0.0000	0.0000
2	1	1	3	1.9159	19.8113	0.7914	-4.6995	-1.0000	0.0000	0.0000
3	1	1	3	-1.4477	16.6853	0.6461	-4.9622	-1.0000	0.0000	0.0000
1	1	3	1	0.4816	19.6316	-0.0057	-2.5000	-1.0000	0.0000	0.0000
1	1	3	2	1.2044	80.0000	-0.3139	-6.1481	-1.0000	0.0000	0.0000
2	1	3	1	-2.5000	31.0191	0.6165	-2.7733	-2.9807	0.0000	0.0000
2	1	3	2	-2.4875	70.8145	0.7582	-4.2274	-3.0000	0.0000	0.0000
1	1	3	3	-0.3566	10.0000	0.0816	-2.6110	-1.9631	0.0000	0.0000
2	1	3	3	-1.4383	80.0000	1.0000	-3.6877	-2.8000	0.0000	0.0000
3	1	3	1	-1.1390	78.0747	-0.0964	-4.5172	-3.0000	0.0000	0.0000
3	1	3	2	-2.5000	70.3345	-1.0000	-5.5315	-3.0000	0.0000	0.0000
3	1	3	3	-2.0234	80.0000	0.1684	-3.1568	-2.6174	0.0000	0.0000
1	3	3	1	1.1637	-17.3637	0.5459	-3.6005	-2.6938	0.0000	0.0000
1	3	3	2	-2.1289	12.8382	1.0000	-5.6657	-2.9759	0.0000	0.0000
2	3	3	2	2.5000	-22.9397	0.6991	-3.3961	-1.0000	0.0000	0.0000
1	3	3	3	2.5000	-25.0000	1.0000	-2.5000	-1.0000	0.0000	0.0000
2	3	3	3	-2.5000	-2.5103	-1.0000	-2.5000	-1.0000	0.0000	0.0000
3	3	3	3	-2.5000	-25.0000	1.0000	-2.5000	-1.0000	0.0000	0.0000

0	1	2	0	0.0000	0.0000	0.0000	0.0000	0.0000	0.0000	0.0000
0	2	2	0	0.0000	0.0000	0.0000	0.0000	0.0000	0.0000	0.0000
0	2	3	0	0.0000	0.1000	0.0200	-2.5415	0.0000	0.0000	0.0000
0	1	1	0	0.0000	50.0000	0.3000	-4.0000	-2.0000	0.0000	0.0000
0	1	4	0	1.7932	141.5515	0.9686	-4.2368	-1.9727	0.0000	0.0000
0	2	4	0	-1.5000	0.1032	0.0100	-5.0965	0.0000	0.0000	0.0000
0	3	4	0	1.1397	61.3225	0.5139	-3.8507	-3.0000	0.0000	0.0000
0	4	4	0	0.7265	44.3155	1.0000	-4.4046	-2.0000	0.0000	0.0000
4	1	4	4	-0.0949	8.7582	0.3310	-7.9430	-2.0000	0.0000	0.0000
0	1	5	0	3.3423	30.3435	0.0365	-2.7171	0.0000	0.0000	0.0000
0	5	5	0	-0.0555	-5.0000	0.1515	-2.2056	0.0000	0.0000	0.0000
0	2	5	0	0.0000	0.0000	0.0000	0.0000	0.0000	0.0000	0.0000
2	3	5	3	2.5000	2.5000	0.2237	-10.0000	-1.0000	0.0000	0.0000
0	3	5	0	-2.5000	50.0000	-0.5000	-10.0000	-1.0000	0.0000	0.0000
0	6	6	0	0.0000	0.0000	0.1200	-2.4426	0.0000	0.0000	0.0000
0	2	6	0	0.0000	0.0000	0.1200	-2.4847	0.0000	0.0000	0.0000
0	3	6	0	0.0000	0.0000	0.1200	-2.4703	0.0000	0.0000	0.0000
1	1	3	3	-0.0002	20.1851	0.1601	-9.0000	-2.0000	0.0000	0.0000
1	3	3	1	0.0002	80.0000	-1.5000	-4.4848	-2.0000	0.0000	0.0000
3	1	3	3	-0.1583	20.0000	1.5000	-9.0000	-2.0000	0.0000	0.0000
1	1	1	7	-0.3232	14.3871	0.1823	-9.8682	-1.7255	0.0000	0.0000
7	1	1	7	-0.1452	50.0000	-0.1915	-8.0773	-1.7255	0.0000	0.0000
0	1	7	0	4.0000	45.8264	0.9000	-4.0000	0.0000	0.0000	0.0000
0	7	7	0	4.0000	45.8264	0.9000	-4.0000	0.0000	0.0000	0.0000
2	1	3	7	-1.5000	18.9285	0.3649	-6.1208	0.0000	0.0000	0.0000
2	3	7	3	1.5000	-1.0000	0.2575	-6.2100	0.0000	0.0000	0.0000
1	3	7	3	-1.4375	-0.8700	0.9861	-2.5424	0.0000	0.0000	0.0000
7	3	7	3	-1.5000	21.5086	-1.0000	-4.8869	0.0000	0.0000	0.0000
2	1	3	9	0.0000	84.3556	0.1000	-3.1953	0.0000	0.0000	0.0000
1	1	3	9	0.0000	51.0461	0.1059	-7.2043	0.0000	0.0000	0.0000
2	3	9	3	-0.2500	0.2975	-0.1915	-5.5113	0.0000	0.0000	0.0000
1	1	1	11	0.5000	0.1000	0.4683	-11.5274	-1.7255	0.0000	0.0000
2	1	1	11	0.0000	49.3871	0.2000	-10.5765	-1.7255	0.0000	0.0000
11	1	1	11	-0.5000	95.4727	-0.2080	-4.8579	-1.7255	0.0000	0.0000
0	1	11	0	4.0000	45.8264	0.9000	-4.0000	0.0000	0.0000	0.0000
0	11	11	0	4.0000	45.8264	0.8897	-4.0000	0.0000	0.0000	0.0000
9 !Nr of hydrogen bonds;at1;at2;at3;Rhb;Dehb;vhb1										
3	2	3		2.1200	-3.5800	1.4500	19.5000			
3	2	4		1.6787	-3.9601	1.4500	19.5000			
4	2	3		1.5585	-3.9305	1.4500	19.5000			
4	2	4		1.9336	-5.8831	1.4500	19.5000			
3	2	5		1.5000	-2.0000	1.4500	19.5000			
4	2	5		1.5000	-2.0000	1.4500	19.5000			

5 2 3 1.5000 -2.0000 1.4500 19.5000
5 2 4 1.5000 -2.0000 1.4500 19.5000
5 2 5 1.5000 -2.0000 1.4500 19.5000